Volume 31, Number 2 April 2023
ISSN:1521-1398 PRINT,1572-9206 ONLINE

Journal of Computational Analysis and Applications

EUDOXUS PRESS,LLC

Journal of Computational Analysis and Applications
ISSNno.'s:1521-1398 PRINT,1572-9206 ONLINE

SCOPE OF THE JOURNAL

An international publication of Eudoxus Press, LLC
(published quarterly) www.eudoxuspress.com.

Editor in Chief: George Anastassiou
Department of Mathematical Sciences,
University of Memphis, Memphis, TN 38152-3240, U.S.A
ganastss@memphis.edu, ganastss2@gmail.com
http://web0.msci.memphis.edu/~ganastss/jocaaa/

The main purpose of "J.Computational Analysis and Applications" is to publish high quality research articles from all subareas of Computational Mathematical Analysis and its many potential applications and connections to other areas of Mathematical Sciences. Any paper whose approach and proofs are computational,using methods from Mathematical Analysis in the broadest sense is suitable and welcome for consideration in our journal, except from Applied Numerical Analysis articles. Also plain word articles without formulas and proofs are excluded. The list of possibly connected mathematical areas with this publication includes, but is not restricted to: Applied Analysis, Applied Functional Analysis, Approximation Theory, Asymptotic Analysis, Difference Equations, Differential Equations, Partial Differential Equations, Fourier Analysis, Fractals, Fuzzy Sets, Harmonic Analysis, Inequalities, Integral Equations, Measure Theory, Moment Theory, Neural Networks, Numerical Functional Analysis, Potential Theory, Probability Theory, Real and Complex Analysis, Signal Analysis, Special Functions, Splines, Stochastic Analysis, Stochastic Processes, Summability, Tomography, Wavelets, any combination of the above, e.t.c.

"J.Computational Analysis and Applications" is a peer-reviewed Journal. See the instructions for preparation and submission **of articles to JOCAAA.**

Journal of Computational Analysis and Applications(JoCAAA) is published by **EUDOXUS PRESS,LLC**,1424 Beaver Trail Drive,Cordova,TN38016,USA,anastassioug@yahoo.com http://www.eudoxuspress.com. **Annual Subscription Prices**:For USA and Canada,Institutional:Print $500, Electronic OPEN ACCESS. Individual:Print $250. For any other part of the world add $150 more(handling and postages) to the above prices for Print. No credit card payments.

JoCAAA is reviewed and abstracted by Elsevier-Scopus, available also via EBSCO publishing and EBSCO.

Editorial Board
Associate Editors of Journal of Computational Analysis and Applications

George Cybenko
Thayer School of Engineering
Dartmouth College
8000 Cummings Hall,
Hanover, NH 03755-8000
603-646-3843 (X 3546 Secr.)
e-mail:george.cybenko@dartmouth.edu
Approximation Theory and Neural Networks

Sever S. Dragomir
School of Computer Science and Mathematics, Victoria University,
PO Box 14428,
Melbourne City,
MC 8001, AUSTRALIA
Tel. +61 3 9688 4437
Fax +61 3 9688 4050
e-mail: sever.dragomir@vu.edu.au
Inequalities, Functional Analysis, Numerical Analysis, Approximations, Information Theory, Stochastics.

Oktay Duman
TOBB University of Economics and Technology,
Department of Mathematics, TR-06530, Ankara, Turkey,
e-mail: oduman@etu.edu.tr
Classical Approximation Theory, Summability Theory, Statistical Convergence and its Applications

J .A. Goldstein
Department of Mathematical Sciences
The University of Memphis
Memphis, TN 38152
901-678-3130
e-mail: jgoldste@memphis.edu
Partial Differential Equations, Semigroups of Operators

H. H. Gonska
Department of Mathematics
University of Duisburg
Duisburg, D-47048
Germany
011-49-203-379-3542
e-mail: heiner.gonska@uni-due.de
Approximation Theory, Computer Aided Geometric Design

John R. Graef
Department of Mathematics
University of Tennessee at Chattanooga
Chattanooga, TN 37304 USA
e-mail: John-Graef@utc.edu
Ordinary and functional differential equations, difference equations, impulsive systems, differential inclusions, dynamic equations on time scales, control theory and their applications

Weimin Han
Department of Mathematics
University of Iowa
Iowa City, IA 52242-1419
319-335-0770
e-mail: whan@math.uiowa.edu
Numerical analysis, Finite element method, Numerical PDE, Variational inequalities, Computational mechanics

Tian-Xiao He
Department of Mathematics and Computer Science
P.O. Box 2900, Illinois Wesleyan University
Bloomington, IL 61702-2900, USA
Tel (309)556-3089
Fax (309)556-3864
e-mail: the@iwu.edu
Approximations, Wavelet, Integration Theory, Numerical Analysis, Analytic Combinatorics

Margareta Heilmann
Faculty of Mathematics and Natural Sciences, University of Wuppertal
Gaußstraße 20
D-42119 Wuppertal, Germany,
heilmann@math.uni-wuppertal.de
Approximation Theory (Positive Linear Operators)

Xing-Biao Hu
Institute of Computational Mathematics
AMSS, Chinese Academy of Sciences
Beijing, 100190, CHINA
e-mail: hxb@lsec.cc.ac.cn
Computational Mathematics

Seda Karateke
Department of Computer Engineering, Faculty of Engineering,
Istanbul Topkapi University,
Istanbul, Zeytinburnu 34087, Turkey
e-mail: sedakarateke@topkapi.edu.tr
Approximation Theory, Neural Networks

Instructions to Contributors
Journal of Computational Analysis and Applications

An international publication of Eudoxus Press, LLC, of TN.

Editor in Chief: George Anastassiou
Department of Mathematical Sciences
University of Memphis
Memphis, TN 38152-3240, U.S.A.

1. Manuscripts files in Latex and PDF and in English, should be submitted via email to the Editor-in-Chief:

Prof.George A. Anastassiou
Department of Mathematical Sciences
The University of Memphis
Memphis,TN 38152, USA.
Tel. 901.678.3144
e-mail: ganastss@memphis.edu

Authors may want to recommend an associate editor the most related to the submission to possibly handle it.

Also authors may want to submit a list of six possible referees, to be used in case we cannot find related referees by ourselves.

2. Manuscripts should be typed using any of TEX,LaTEX,AMS-TEX,or AMS-LaTEX and according to EUDOXUS PRESS, LLC. LATEX STYLE FILE. (Click HERE to save a copy of the style file.)They should be carefully prepared in all respects. Submitted articles should be brightly typed (not dot-matrix), double spaced, in ten point type size and in 8(1/2)x11 inch area per page. Manuscripts should have generous margins on all sides and should not exceed 24 pages.

3. Submission is a representation that the manuscript has not been published previously in this or any other similar form and is not currently under consideration for publication elsewhere. A statement transferring from the authors(or their employers,if they hold the copyright) to Eudoxus Press, LLC, will be required before the manuscript can be accepted for publication.The Editor-in-Chief will supply the necessary forms for this transfer.Such a written transfer of copyright,which previously was assumed to be implicit in the act of submitting a manuscript,is necessary under the U.S.Copyright Law in order for the publisher to carry through the dissemination of research results and reviews as widely and effective as possible.

4. The paper starts with the title of the article, author's name(s) (no titles or degrees), author's affiliation(s) and e-mail addresses. The affiliation should comprise the department, institution (usually university or company), city, state (and/or nation) and mail code.

The following items, 5 and 6, should be on page no. 1 of the paper.

5. An abstract is to be provided, preferably no longer than 150 words.

6. A list of 5 key words is to be provided directly below the abstract. Key words should express the precise content of the manuscript, as they are used for indexing purposes.

The main body of the paper should begin on page no. 1, if possible.

7. All sections should be numbered with Arabic numerals (such as: 1. INTRODUCTION) .
Subsections should be identified with section and subsection numbers (such as 6.1. Second-Value Subheading).
If applicable, an independent single-number system (one for each category) should be used to label all theorems, lemmas, propositions, corollaries, definitions, remarks, examples, etc. The label (such as Lemma 7) should be typed with paragraph indentation, followed by a period and the lemma itself.

8. Mathematical notation must be typeset. Equations should be numbered consecutively with Arabic numerals in parentheses placed flush right, and should be thusly referred to in the text [such as Eqs.(2) and (5)]. The running title must be placed at the top of even numbered pages and the first author's name, et al., must be placed at the top of the odd numbed pages.

9. Illustrations (photographs, drawings, diagrams, and charts) are to be numbered in one consecutive series of Arabic numerals. The captions for illustrations should be typed double space. All illustrations, charts, tables, etc., must be embedded in the body of the manuscript in proper, final, print position. In particular, manuscript, source, and PDF file version must be at camera ready stage for publication or they cannot be considered.

Tables are to be numbered (with Roman numerals) and referred to by number in the text. Center the title above the table, and type explanatory footnotes (indicated by superscript lowercase letters) below the table.

10. List references alphabetically at the end of the paper and number them consecutively. Each must be cited in the text by the appropriate Arabic numeral in square brackets on the baseline.
References should include (in the following order):
initials of first and middle name, last name of author(s)
title of article,

name of publication, volume number, inclusive pages, and year of publication.

Authors should follow these examples:

<u>Journal Article</u>

1. H.H.Gonska,Degree of simultaneous approximation of bivariate functions by Gordon operators, (journal name in italics) *J. Approx. Theory*, 62,170-191(1990).

<u>Book</u>

2. G.G.Lorentz, (title of book in italics) *Bernstein Polynomials* (2nd ed.), Chelsea,New York,1986.

<u>Contribution to a Book</u>

3. M.K.Khan, Approximation properties of beta operators,in(title of book in italics) *Progress in Approximation Theory* (P.Nevai and A.Pinkus,eds.), Academic Press, New York,1991,pp.483-495.

11. All acknowledgements (including those for a grant and financial support) should occur in one paragraph that directly precedes the References section.

12. Footnotes should be avoided. When their use is absolutely necessary, footnotes should be numbered consecutively using Arabic numerals and should be typed at the bottom of the page to which they refer. Place a line above the footnote, so that it is set off from the text. Use the appropriate superscript numeral for citation in the text.

13. After each revision is made please again submit via email Latex and PDF files of the revised manuscript, including the final one.

14. Effective 1 Nov. 2009 for current journal page charges, contact the Editor in Chief. Upon acceptance of the paper an invoice will be sent to the contact author. The fee payment will be due one month from the invoice date. The article will proceed to publication only after the fee is paid. The charges are to be sent, by money order or certified check, in US dollars, payable to Eudoxus Press, LLC, to the address shown on the Eudoxus <u>homepage</u>.

No galleys will be sent and the contact author will receive one (1) electronic copy of the journal issue in which the article appears.

15. This journal will consider for publication only papers that contain proofs for their listed results.

Two step Newton's method with multiplicative calculus to solve the non-linear equations

Gurjeet Singh[1,a], **Sonia Bhalla**[1,b]

[1] Department of Mathematics, Chandigarh University, Gharuan, Punjab, India, 140413

[a] Corresponding author: gs42477@gmail.com

[b] sonia.e8843@cumail.in

Abstract

For solving non-linear equations, iterative root-finding methods are important because of the broad range of applications in science and engineering. We have constructed an iterative method based on multiplicative calculus in this paper. Some numerical results are performed to exposed the efficiency of proposed and earlier method.

Keywords: Multiplicative calculus, Non linear equations, Iterative methods, Newton's-Raphson method, Order of convergence

1 Introduction

In the field of engineering and sciences, solving nonlinear equations effectively is one of the interesting task. Sometimes it is difficult to solve these problems. Then, we rely on iterative schemes to execute the root of non-linear function $g(t) = 0$. One of the popular methods for approximating the root of a non-linear function is the Newton's method [14] defined as

$$t_{q+1} = t_q - \frac{g(t_q)}{g'(t_q)}, \quad q = 0, 1, 2, 3... \tag{1}$$

The convergence order of Newton's method is two for the simple root. Several variants of Newton's method are developed to improve the convergence order in the literature such as Halley method [23], super-Halley method [16], Euler's method [21], Weerakoon and Fernando [22] etc. All of the above mentioned methods consist second-order derivatives except Weerakoon and Fernando. From 1964 to 2012, researchers [1],[9],[15],[24] has developed fourth-order methods to find the non-linear equations roots like Traub and Ostrowski [15], Chun and Ham [9], Cordero and Torregrosa [1], Kanwar et al. [24] etc. Out of them, Kanwar et. al. introduced a method which consists second-order derivatives while other listed methods have first-order derivative. Sometime it is difficult to achieve the second-order derivative at each step of the method. So some authors [10-11] developed second-order derivative free methods to solve the non-linear equations.

But still handling of first-order or second-order derivative in iterative techniques is difficult task. Nowdays, non-linear equations $g(t)+1=1$ are solved using multiplicative calculus instead of function $g(t)=0$. Initially, in 2008 Bashirov et al. [3] discussed the theoretical foundations and various applications of multiplicative calculus. In 2009 and 2011 Misirli and Gurefe [12], Riza et al. [18], and Ozyapici & Misirli [13] used multiplicative calculus to develop multiplicative numerical methods and in 2010 Filip and Piatecki [11] used it to examine economic growth and Uzer [8] extended the multiplicative calculus to include complex valued functions of complex variables, which was previously applicable only to positive real valued functions of real variables. In 2011 Bashirov et al. [4] used it to develop multiplicative differential equations. Bashirov & Riza [5] and in 2012 Florack and van Assen [17] used in biomedical image analysis. Currently, in 2016 Ozyapici, Sensoy and Karanfiller constructed a Multiplicative Newton's method. Keeping the same fact in mind, we consider the joint four-order multiplicative Newton's method.

This paper is structured as follows. Some basic terms of Multiplicative Calculus forms Section 2. As described in Section 3, a convergence analysis is conducted to determine the fourth-order of convergence of the proposed method. In Section 4, we presents comparisons of results obtained by proposed method with some other fourth-order methods. Finally, the conclusions form Section 5.

2 Some basic terms of Multiplicative Calculus

Definition: Let $g(t)$ be a real positive valued function in the open interval (a,b). Assume function be changes in $t \in (a,b)$ s.t. $g(t)$ changes in $g(t+h)$. Then [13] multiplicative forward operator denoted as Δ^* defined as follows

$$\Delta^* g(t) = \frac{g(t+h)}{g(t)} \tag{2}$$

By considring the operator Δ^* in (2), multiplicative derivative can be defined as below

$$g^*(t) = \lim_{h \to 0} (\Delta^* g)^{1/h} \tag{3}$$

The function $g^*(t)$ is said to be multiplicative differentiable at t if the limit on R.H.S exists.

If g is positive function and the derivative of g at t exist, then q^{th} multiplicative derivatives of g exist and

$$g^{*(q)}(t) = exp\left\{(ln \circ g)^{(q)}(t)\right\} \tag{4}$$

2

Theorem 1: (Multiplicative Taylor Theorem in one variable) [5] Let $g(t)$ be a function in open interval (a, b) s.t the functions is $q+1$ times $*$ differentiable on (a, b). Then for any $t, t+h \in A(a, b)$, there is a number $\theta \in (a, b)$ such that

$$g(t+h) = \prod_{p=0}^{n} \left(g^{*(p)}(t)\right)^{\frac{h^p}{p!}} . \left(g^{*(q+1)}(t+\theta h)\right)^{\frac{h^{q+1}}{(q+1)!}} \tag{5}$$

Theorem 2: (Multiplicative Newton's-Raphson method) [7] Assume that $g \in \mathcal{C}^2[a, b]$ and there exist a number $p \in [a, b]$ such that $g(p) = 1$. If $g^*(p) \neq 1$ and $h(t) = t - \dfrac{ln\ g(t)}{ln\ g^*(t)}$ then there exist a $\delta > 0$ such that the sequence $pk_{k=1}^{\infty}$ defined by iteration will converge to m for any initial value $p_0 \in [p-\delta, p+\delta]$

$$p_k = p_{k-1} - \frac{ln\ g(p_{k-1})}{ln\ g^*(p_{k-1})} \tag{6}$$

with error $e_{q+1} = b_2 e_q^2 + 2(b_3 - b_2^2)e_q^3 + \mathcal{O}(e_q^4)$

3 The Proposed Method and Analysis of Convergence

Here we constructed two step iterative method by considering first step as multiplicative Newton's-Raphson method and second step as considering ordinary Newton's-Raphson Scheme.

$$y_q = t_q - \frac{ln\ g(t_q)}{ln\ g^*(t_q)},$$

$$t_{q+1} = y_q - \frac{g(y_q)}{g'(y_q)}. \tag{7}$$

Where $q = 1, 2, 3, ...$ is the iteration level .
For convergence analysis, we have proved the following theorem.

Theorem 3: Suppose that for an open interval I, the function $g : I \subseteq \mathbb{R} \to \mathbb{R}$ has only one root, $s \in I$. Let $g(t)$ be a sufficiently ordinary differentiable and then multiplicative differentiable in the neighborhood of s. Then the proposed method (7) has fourth-order of convergence.
Proof: Let s be the simple root of $g(t)$ and $e_q = t_q - s$. Consider the function $H(t) = t_{q+1}$ defined by

$$H(t) = y_q - \frac{g(y_q)}{g'(y_q)},$$

where

$$y_q = t_q - \frac{ln\ g(t_q)}{ln\ g^*(t_q)} \tag{8}$$

By using Mathematica version 11.1.1 with the fact that $y'(s) = 0$ from Theorem 2, the function $H(t)$ satisfies

$$H(s) = r \quad and \quad H^{(q)}(s) = 0, q = 1, 2, 3. \tag{9}$$

Thus, $H^{(4)}(s)$ can be given as

$$H^{(4)}(s) = \frac{3(g'(t)^2 - g''(t))^2 g''(t)}{g'(t)^3}$$

By Taylor expansion of $H(t_n)$ around s with condition (9), one obtain

$$t_{q+1} = H(t_q) = H(s) + \frac{H^{(4)}}{4!} e_q^4 + \mathcal{O}(e_q^5).$$

Hence,

$$e_{q+1} = \frac{H^{(4)}(s)}{4!} e_q^4 + \mathcal{O}(e_q^5)$$

Hence, the method (8) has fourth-order of convergence.

4 Numerical Examples

Several examples are given in this section to illustrate the applicability of the proposed method. The results of proposed method denoted as (PM) is also compared with earlier methods such as two-step Newton's Method [19] denoted as (NM), Chun method [10] denoted as (CM) and Maheshwari method [6] denoted as (MM) reprsented in Table 1 - Table 4. All computations can be done in Mathematica version 11.1.1 software and the stopping criteria $|t_{q+1} - t_q| < \epsilon$ and $\epsilon = 10^{-14}$ is used. The obtained results are compared for first three iterations. Moreover, the Approximated computational order of convergence(ACOC) is computed by using the following.

$$\rho \cong \frac{ln\left|\dfrac{t_{q+1} - s}{t_q - s}\right|}{ln\left|\dfrac{t_q - s}{t_{q-1} - s}\right|}.$$

4

Example 1: A fraction conversion problem is considered firstly, in which nitrogen-hydrogen feed is converted to ammonia fractionally. A temperature of 500°C and a pressure of 250 atm have been used in this problem. The nonlinear form of this problem is as follows::

$$g_1(t) = -0.186 - \frac{8t^2(t-4)^2}{9(t-2)^3}, \tag{10}$$

The simplified form of equation (10) is reduces to non-linear function as

$$g_1(t) = t^4 - 7.79075t^3 + 14.7445t^2 + 2.511t - 1.674 \tag{11}$$

Since the polynomial above has a degree of four, there must be exactly four roots. Due to its definition, fraction conversion lies in the interval (0,1), so there can be only one root in this interval, and that is 0.2777595428. Using the initial guess $t_0 = 0.4$ in Table 1, it is clear that our suggested method takes fewer iterations than others.

Example 2: Consider a Kepler's Equation

$$g_2(t) = t - \alpha_1 Sin(t) - K, \tag{12}$$

where $0 \leq \alpha_1 < 1$ and $0 \leq K \leq \pi$. We solve the equation by taking $K = 0.1$ and $\alpha_1 = 0.25$. For this set of values the root is 0.13320215082857313... which is approximated by proposed and earlier methods at the initial root $t_0 = 2$ and results are shown in Table 2.

Example 3: Problems of transcendental and algebraic nature. The following equations are used to numerically analyze the proposed technique:

$$(a) \qquad g_3(t) = e^{-t} + Cost, with\ exact\ root\ s = 1.7461. \tag{13}$$

$$(b)\ g_4(t) = te^{t^2} - Sin^2 t + 3Cost - 4, with\ exact\ root\ s = 1.0651. \tag{14}$$

Table 3 and Table 4 shows the numerical outcomes starting with the initial guess 2.0 and 1.0 respectively. According to the numerical results, the proposed method requires fewer steps and reduces computation time.

5

Method	q	$\|t_q - t_{q-1}\|$	$\|g(t_q)\|$	ρ
NM	1	2.7402×10^{-1}	22.441	4.000
	2	2.7338×10^{-2}	9.6722×10^{-1}	
	3	3.4387×10^{-4}	4.3475×10^{-15}	
CM	1	2.5637×10^{-1}	22.4486	3.9987
	2	4.4424×10^{-2}	1.7056	
	3	5.9249×10^{-4}	1.8635×10^{-2}	
MM	1	2.5941×10^{-1}	22.4486	4.000
	2	4.1567×10^{-2}	1.5720	
	3	4.0948×10^{-4}	1.2868×10^{-2}	
PM	1	5.46149×10^{-1}	23.4486	3.999
	2	3.07797×10^{-2}	2.13315	
	3	3.44644×10^{-4}	1.0109	

Table 1: Fraction Conversion of Nitrogen-Hydrogen to Ammonia

Method	q	$\|t_q - t_{q-1}\|$	$\|g(t_q)\|$	ρ
NM	1	1.6621	1.5227	4.000
	2	6.5678×10^{-3}	5.0169×10^{-3}	
	3	2.8775×10^{-13}	2.1973×10^{-13}	
CM	1	1.6495	1.5226	4.000
	2	1.9131×10^{-2}	1.4623×10^{-2}	
	3	3.3555×10^{-10}	-2.5622×10^{-10}	
MM	1	1.6490	1.5226	4.000
	2	1.9652×10^{-2}	1.5022×10^{-2}	
	3	3.2303×10^{-10}	-2.4667×10^{-10}	
PM	1	1.66756	2.5226	4.000
	2	1.12051×10^{-3}	1.0008	
	3	9.0489×10^{-15}	1.0000	

Table 2: Kepler's Equation

6

Method	q	$\lvert t_q - t_{q-1}\rvert$	$\lvert g(t_q)\rvert$	ρ
NM	1	2.5389×10^{-1}	-2.8081×10^{-1}	4.000
	2	3.2728×10^{-5}	3.7935×10^{-5}	
	3	3.9104×10^{-21}	4.5325×10^{-21}	
CM	1	2.5424×10^{-1}	-2.8081×10^{-1}	4.000
	2	3.7917×10^{-4}	4.3955×10^{-4}	
	3	7.1375×10^{-16}	8.2731×10^{-16}	
MM	1	2.5418×10^{-1}	-2.8081×10^{-1}	4.000
	2	3.2177×10^{-4}	3.7299×10^{-4}	
	3	3.3377×10^{-16}	3.8688×10^{-16}	
PM	1	2.5398×10^{-1}	7.1919×10^{-1}	4.000
	2	1.1458×10^{-4}	1.0001	
	3	4.7761×10^{-18}	1.0000	

Table 3: $e^{-t} + Cost$

Method	q	$\lvert t_q - t_{q-1}\rvert$	$\lvert g(t_q)\rvert$	ρ
NM	1	4.2454×10^{-1}	103.12	3.8484
	2	3.6870×10^{-1}	13.838	
	3	1.3811×10^{-1}	1.3718	
CM	1	3.4554×10^{-1}	103.121	3.9221
	2	3.3105×10^{-1}	20.3079	
	3	2.1605×10^{-1}	3.4207	
MM	1	3.6468×10^{-1}	103.121	3.9615
	2	3.4233×10^{-1}	18.5257	
	3	2.0077×10^{-1}	2.7788	
PM	1	9.2639×10^{-1}	104.12	4.000
	2	8.4709×10^{-3}	1.0580	
	3	7.6367×10^{-9}	1.0000	

Table 4: $te^{t^2} - Sin^2 t + 3Cost - 4$

5 Conclusion

Here, we developed the Joint Multiplicative Newton's method which is mixture of multiplicative Newton's method and Ordinary Newton's method. We tested the proposed method for approximating the roots of nonlinear equations and compared it with ordinary methods. The obtained results are efiicient as compared with earlier ones in terms of residual error, consecutive error and order of convergence.

References

[1] A. Cordero, J. L. Hueso, E. M. Juan, R. Torregrosa, Steffensen type methods for solving nonlinear equations, J. Comput. Appl. Math. 236(12) 3058-3064 (2012).

[2] A. Cordero, N. Garrido, J. R. Torregrosa, P. T. Nvarro, Iterative schemes for finding all roots simultaneously of nonlinear equations, Appl. Math. Lett., Volume 134,(2022)

[3] A.E. Bashirov, E.M.Kurpınar, A.Ozyapıcı, Multiplicative calculus and its applications, J. Math. Anal. Appl. 337(1), 36–48 (2008)

[4] A.E. Bashirov, E. Mısırlı, Y. Tandogdu, A. Ozyapıcı, On modeling with multiplicative differential equations. Appl. Math. J Chin. Univ. 26(4), 425–438 (2011)

[5] A.E. Bashirov, M. Riza, On complex multiplicative differentiation. TWMS J. Appl. Eng. Math. 1(1), 51–61 (2011)

[6] A. K. Maheshwari, A fourth order iterative method for solving nonlinear equations, Appl. Math. Comput. 211(2) 383 –391 (2009)

[7] A Ozyapıcı, Effective Root-Finding Methods for Nonlinear Equations Based on Multiplicative Calculi, J. Math. (2016)

[8] A. Uzer, Multiplicative type complex calculus as an alternative to the classical calculus. Comput. Math. Appl. 60(10), 2725–2737 (2010)

[9] C. Chun and Y. Ham, Some fourth-order modifications of Newton's method, Appl. Math. Comput. 197(2) 654-658 (2008).

[10] C. Chun, M. Y. Lee, B. Neta, and J. Dzunic, On optimal fourth-order iterative methods free from second derivative and their dynamics, Appl. Math. Comput. 218(11) 6427–6438 (2012).

[11] D.A. Filip, C. Piatecki, A non-Newtonian examination of the theory of exogenous economic growth, CNCSIS-UEFISCSU (project number PNII IDEI 2366/2008) and Laboratoire d'Economie d'Orleans (LEO) (2010)

[12] E. Mısırlı, Y. Gurefe, Multiplicative Adams–Bashforth–Moulton methods. Numer. Algo. 57(4), 425–439 (2011)

[13] E. Mısırlı, A. Ozyapıcı, Exponential approximations on multiplicative calculus. Proc. Jangjeon Math. Soc. 12(2), 227–236 (2009)

[14] E. Suli and D. Mayers, An Introduction to Numerical Analysis. Cambridge University Press. ISBN 0-521-00794-1. (2003).

[15] J. F. Traub, Prentice-Hall, Iterative methods for the solution of equations, Englewood Cliffs, New Jersey, 1964.

[16] J. Gutierrez and M. Hernandez, An accerlation of Newton's method, Appl. Math. Comput. 117(2-3) 223-239 (2001).

[17] L. Florack, H. van Assen, Multiplicative calculus in biomedical image analysis, J. Math. Imaging Vis. 42(1), 64–75 (2012)

[18] M. Riza, A. Ozyapıcı, E. Mısırlı, Multiplicative finite difference methods. Q. Appl. Math. 67(4),745 (2009)

[19] M. Ruiz, A. Alberto, I. K. Argyros, Two-step Newton methods. J. Complex, 30(4), 533–553 (2014)

[20] M. Shams, N. Rafiq, N. Kausar, On iterative techniques for estimating all roots of nonlinear equation and its system with application in differential equation. Adv Differ Equ 2021, 480 (2021)

[21] S. Amat, S. Busquier, and J. M. Gutierrez,Geometric Construction of Iterative Functions to Solve Nonlinear Equations, J. Comput. Appl. Math. 157(1), 197-205 (2003).

[22] S. Weekaroon and TGI. Fernando, A variant of Newton's method with accelerated third-order convergence, Appl. Math. Lett. 13 87-93 (2002).

[23] V. Kanwar and S.K. Tomar, Modified families of Newton, Halley and Chebyshev methods, Appl. Math. Comput. 192 20-26 (2007).

[24] V. Kanwar, R. Behl and K. K. Sharma, Simply constructed family of a Ostrowski's method with optimal order of convergence, J. Comput. Appl. Math. 62(11) 4021-4027 (2011).

Analysis of Tripled System of Fractional Differential Equation using Certain Fixed Points Theorems with Fractional Boundary Condition

Ashok Kumar Badsara[1], Jagdev Singh[2], Richa Sharma[3]
and Virendra Singh Chouhan[4]

December 26, 2022

Abstract

This paper presents the tripled system of differential equations of fractional type with fractional integral boundary conditions as well as integer and fractional derivative. Here the Banach fixed points theorem and Scheafer's fixed points theorem are used as a main tool. To justify the results we illustrate some examples.

Key Words and Phrases: Fixed points theorem, Banach fixed point, Fractional differential equations, Fractional integral boundary conditions.
2010 AMS Subject Classification: 47H10, 26A33.

[1]

1 Introduction

Fractional differential equation are applicable in many streams of science and engineering like as fitting of experimental data, e electromagnetics, physics, viscoelasticity, lectro chemistry, biophysics, blood flow phenomena,porous media,biology, electrical circuits, etc. Therefore compare to models of integer order, fractional order model become more practical and realistic. Thus there has been

[1]Corresponding author: [4]Virendra Singh Chouhan,
[1,4]Department of Mathematics and Statistics, Manipal University Jaipur, Rajasthan
[1]Email-ashokkumarbadsra1995@gmail.com
[2]Department of Mathematics, JECRC University, Jaipur (Rajasthan)
Email- jagdevsingh05@gmail.com
[3]Department of Mathematics, Chandigarh University, Mohali (Punjab)
Email-richa.tuknait@gmail.com
[4]Email-darbarvsingh@yahoo.com(Corresponding Author)

a significant developments in problems of boundary value for the existence and uniqueness of fractional differential equations; see [1, 4, 5, 6, 8, 9, 10, 12]. and the references therein. Many authors have worked on existence and uniqueness of solution of tripled system of fractional differential equations [2, 3, 7, 11, 13, 14]. The tripled systems of fractional differential equation often exits in numerous models such as Chemostats and Microorganism Culturing, Brine Tanks, Irregular Heartbeats, Chemical Kinetics, Lidocaine and Pesticides, Predator Prey etc. [8] study fractional differential equations for Boundary value problems of nonlinear type and include nonlocal and integral boundary condition of fractional type. Inspired by the problem [9],

$$\begin{cases} {}^C D^{a_1} x_1(\alpha) = e_1(\alpha, x_2(\alpha), x_3(\alpha)), \alpha \in [0,1] \\ {}^C D^{a_2} x_2(\alpha) = e_2(\alpha, x_1(\alpha), x_3(\alpha)), \alpha \in [0,1] \\ {}^C D^{a_1} x_3(\alpha) = e_3(\alpha, x_1(\alpha), x_2(\alpha)), \alpha \in [0,1] \\ x_1(0) = x_1'(0) = x_1"(0) = 0, \\ {}^C D^{p_1} x_1(1) = \gamma_1 (J^{q_1} x_1)(1), \\ x_2(0) = x_2'(0) = x_2"(0) = 0, \\ {}^C D^{p_2} x_2(1) = \gamma_2 (J^{q_2} x_2)(1) \\ x_3(0) = x_3'(0) = x_3"(0) = 0, \\ {}^C D^{p_3} x_3(1) = \gamma_3 (J^{q_3} x_3)(1) \end{cases}$$

Where ${}^C D^{a_i}$ Caputo fractional derivative with order a_i, J^q represent the Riemann-Liouville fractional integral whose order $a_1, a_2 \in (4,5], p_1, p_2, p_3 \in (0,4]$ $q_1, q_2, q_3 > 0, e_1, e_2, : [0,1] \times R \to R$ are smooth functions and $\gamma_i \neq \frac{\Gamma(q_i+5)}{\Gamma(5-p_i)}, i = 1,2,3.$
Existence and uniqueness of solution for the mentioned above tripled system of nonlinear fractional order differential equations is main focus of the paper.

2 Preliminaries

Firstly we introduce some notation, lemmas and definitions.
Definition 2.1 [6] Caputo derivative whose fractional order is a for smooth function $e : [0,\infty) \to R$ is define as

$${}^C D^a e(\alpha) = \frac{1}{\Gamma(n-a)} \int_0^\alpha (\alpha - t)^{n-a-1} e^{(n)}(t) dt$$

gives $e(n)(\alpha)$ exist, where [a] represents the integer part of the real number a and Γ is the Euler's Gamma function.
Definition 2.2 [12] Riemann-Liouville fractional integral of the order $a > 0$ for a smooth function

$$J^a e(\alpha) = \frac{1}{\Gamma(a)} \int_0^\alpha (\alpha - t)^{a-1} e(t) dt.$$

Lemma 2.1 [2] Let $f, g > 0$ and $e \in L_1[a,b]$ then $J^f J^g e = J^{f+g} e$

2

Lemma 2.2 [**2**] If e is continuous and $n \geq 0$, then

$$^{C}D^{n}J^{n}e = e$$

It follows from Lemmas 2.1 and 2.2 that if e is continuous and $\gamma > a$, then $^{C}D^{a}e = J^{\gamma - a}e$.
Lemma 2.3 [**2**] Let $\gamma > -1$ and $n > 0$. Then

$$J^{n}z^{\gamma} = \frac{\Gamma(\gamma+1)}{\Gamma(n+\gamma+1)}z^{n+\gamma}$$

Lemma 2.4 [**2**] Let $\gamma \geq 0$ and $m = [n] + 1$, then

$$^{C}D^{n}x^{\gamma} = \begin{cases} 0, & \text{if} \gamma \in 0, 1, 2, \dots m-1 \\ \frac{\Gamma(\gamma+1)}{\Gamma(\gamma+1-n)}(z-a)^{\gamma-n}, & \text{if} \gamma \epsilon N \text{and} \gamma \geq m \\ & \text{or} \gamma \notin N, \gamma > m-1 \end{cases}$$

Lemma 2.5 [**7**] Let $a > 0$ then,

$$J^{a\,C}D^{a}V(\alpha) = V(\alpha) + h_0 + h_1\alpha + h_2\alpha^2 + \cdots + h_{n-1}\alpha^{n-1}$$

for some $h_i \in \mathbb{R}, i = 0, 1, 2, \dots n-1$, n is smallest integer grater than or equal to a.

3 Supporting Result

In this part, we establish the result required in our main proofs.
Lemma 3.1 Let $y \in H([0,1], \mathbb{R})$ and $\gamma \neq \frac{\Gamma(q+5)}{\Gamma(5-p)}$. Then the problem

$$\begin{cases} ^{C}D^{a}x(\alpha) = y(\alpha)\alpha \in [0,1] \\ x(0) = x'(0) = x''(0) = x'''(0) = 0,^{C} D^{p}x(1) = \gamma(J^{q}x)(1) \end{cases} \tag{3.1}$$

has unique solution

$$\begin{aligned} x(\alpha) &= \frac{1}{\Gamma a}\int_0^{\alpha}(\alpha-t)^{\alpha-1}y(t)dt \\ -\frac{\gamma\Gamma(5-p)\Gamma(5+q)\alpha^3}{24\Gamma(a-p)[\gamma\Gamma(5-p)-\Gamma(q+4)}&\int_0^1(1-t)^{q+a-1}y(t)dt \\ +\frac{\Gamma(5-p)\Gamma(q+5)\alpha^3}{24\Gamma(a-p)[\gamma\Gamma(5-p)-\Gamma(q+5)]}&\int_0^1(1-t)^{a-p-1}y(t)dt \end{aligned} \tag{3.2}$$

Proof: From Lemma 2.2, (3.2) is similar to

$$x(\alpha) = J^{a}y(\alpha) - h_0 - h_1\alpha - h_2\alpha^2 - h_3\alpha^3 - h_4\alpha^4 \tag{3.3}$$

3

for some $h_i \in \mathbb{R}, i$ from $0 to 4$.
from $x(0) = 0$ it follows $h_0 = 0$ also $x'(0) = 0 \implies h_1 = 0, x''(0) = 0 \implies h_2 = 0$ and $x'''(0) = 0 \implies h_3 = 0$. Thus (3.3) becomes

$$x(\alpha) = J^a y(\alpha) - h_4 \alpha^4 \tag{3.4}$$

Now

$$({}^C D^p x) = J^{a-p} y(\alpha) - c_4 \frac{\Gamma 5}{\Gamma(5-p)} \alpha^{4-p}$$
$$J^q x(\alpha) = J^{p+q} y(\alpha) - c_4 \frac{\Gamma 5}{\Gamma(5+q)} \alpha^{4+q}$$

From the boundary condition,

$$\begin{aligned} & ({}^C D^p x)(1) = (J^q x)(1) \\ \implies & J^{a-p} y(1) - c_4 \frac{\Gamma 5}{\Gamma(5-p)} = \gamma J^{p+q} y(1) - c_4 \frac{\Gamma 5}{\Gamma(5+q)} \\ \implies & c_4 \left[\frac{\Gamma 5(\gamma \Gamma(5-p) - \Gamma(5+q))}{\Gamma(5+q)\Gamma(5-q)} \right] = \gamma J^{p+q} y(1) - J^{a-p} y(1) \\ \implies & c_4 = \frac{\Gamma(5-q)\Gamma(5+q)}{24(\gamma\Gamma(5-p) - \Gamma(5+q)} \left[\gamma J^{p+q} y(1) - J^{a-p} y(1) \right]. \end{aligned}$$

On substituting the value of c_4 in (3.4) we find solution (3.2). It clear from lemma (3) that solution of the tripled system (1.1) is given by the integral equation,

$$\begin{aligned} x_1(\alpha) &= \frac{1}{\Gamma a_1} \int_0^\alpha (\alpha - t)^{a_1 - 1} e_1(t, x_2(t), x_3(t)) dt \\ &- \frac{\gamma_1 R_1 \alpha^3}{24\Gamma(q_1 + a_1)} \int_0^1 (1-t)^{q_1 + a_1 - 1} e_1(t, x_2(t), x_3(t)) dt \\ &+ \frac{R_1 \alpha^3}{\Gamma(a_1 - p_1)} \int_0^1 (1-t)^{a_1 - p_1 - 1} e_1(t, x_2(t), x_3(t)) dt \end{aligned}$$

$$\begin{aligned} x_2(\alpha) &= \frac{1}{\Gamma a_2} \int_0^\alpha (\alpha - t)^{a_2 - 1} e_2(t, x_2(t), x_3(t)) dt \\ &- \frac{\gamma_2 R_2 \alpha^3}{24\Gamma(q_2 + a_2)} \int_0^1 (1-t)^{q_2 + a_2 - 1} e_2(t, x_2(t), x_3(t)) dt \\ &+ \frac{R_2 \alpha^3}{\Gamma(a_2 - p_2)} \int_0^1 (1-t)^{a_2 - p_2 - 1} e_2(t, x_2(t), x_3(t)) dt \end{aligned}$$

$$\begin{aligned} x_3(\alpha) &= \frac{1}{\Gamma a_3} \int_0^\alpha (\alpha - t)^{a_3 - 1} e_3(t, x_2(t), x_3(t)) dt \\ &- \frac{\gamma_3 R_3 \alpha^3}{24\Gamma(q_3 + a_3)} \int_0^1 (1-t)^{q_3 + a_3 - 1} e_3(t, x_2(t), x_3(t)) dt \\ &+ \frac{R_3 \alpha^3}{\Gamma(a_3 - p_3)} \int_0^1 (1-t)^{a_3 - p_3 - 1} e_3(t, x_2(t), x_3(t)) dt \end{aligned}$$

Where

$$R_i = \frac{\Gamma(5-p_i)\Gamma(q_i+5)}{\gamma_i\Gamma(5-p_i)-\Gamma(q_i+4)},$$

for i =1, 2, 3.
Let $X = H[0,1]$ then $(X, \|.\|_X)$ is Banach space fit out with the norm.

$$\|X\|_X = (sup|x(\alpha)|\colon \alpha \in [0,1])$$

Let $B = X \times X \times X$ then $(B, \|.\|_B)$ is also a Banach space equipped with the norm.

$$\|(x_1, x_2, x_3)\|_B = \|x_1\|_X + \|x_2\|_X + \|x_3\|_X$$

Let us define an operation $F : B \to B$

$$f(x_1,x_2,x_3)(\alpha) = (f_1x_2(\alpha)x_3(\alpha), f_2x_1(\alpha)x_3(\alpha), f_3x_1(\alpha)x_2(\alpha)$$

Where

$$\begin{aligned}
f_1x_2(\alpha)x_3(\alpha) &= \frac{1}{\Gamma a_1}\int_0^\alpha (\alpha-t)^{a_1-1}e_1(t,x_2(t),x_3(t))dt\\
&-\frac{\gamma_1R_1\alpha^3}{24\Gamma(q_1+a_1)}\int_0^1(1-t)^{q_1+a_1-1}e_1(t,x_2(t),x_3(t))dt\\
&+\frac{R_1\alpha^3}{\Gamma(a_1-p_1)}\int_0^1(1-t)^{a_1-p_1-1}e_1(t,x_2(t),x_3(t))dt\\
f_2x_1(\alpha)x_3(\alpha) &= \frac{1}{\Gamma a_2}\int_0^\alpha (\alpha-t)^{a_2-1}e_2(t,x_2(t),x_3(t))dt\\
&-\frac{\gamma_2R_2\alpha^3}{24\Gamma(q_2+a_2)}\int_0^1(1-t)^{q_2+a_2-1}e_2(t,x_2(t),x_3(t))dt\\
&+\frac{R_2\alpha^3}{\Gamma(a_2-p_2)}\int_0^1(1-t)^{a_2-p_2-1}e_2(t,x_2(t),x_3(t))dt\\
f_3x_1(\alpha)x_2(\alpha) &= \frac{1}{\Gamma a_3}\int_0^\alpha (\alpha-t)^{a_3-1}e_3(t,x_2(t),x_3(t))dt\\
&-\frac{\gamma_3R_3\alpha^3}{24\Gamma(q_3+a_3)}\int_0^1(1-t)^{q_3+a_3-1}e_3(t,x_2(t),x_3(t))dt\\
&+\frac{R_3\alpha^3}{\Gamma(a_3-p_3)}\int_0^1(1-t)^{a_3-p_3-1}e_3(t,x_2(t),x_3(t))dt
\end{aligned}$$

We see fixed point of F are solution of tripled system(1.1). To simplify and our convenience we put.

$$\Lambda_i = \frac{1}{\Gamma(a_i+1)} + \frac{\gamma|R_i|}{24\Gamma(q_i+a_i+1)} + \frac{|R_i|}{24\Gamma(a_i-p_i+1)}$$

for i = 1, 2, 3

4 Main Theorem

We will use well know Banach fixed points theorem to prove our first result.
Theorem 4.1 Suppose that $\gamma_i \neq \frac{\Gamma(q_i+5)}{\Gamma(5-p_i)}, i = 1,2,3$ and the following hypothesis holds. (H 1) Assume that a non-negative continuous functions $k_i \in C[0,1], i = 1,2$ exist such that

$$\begin{aligned} |e_i(\alpha,y_1) - e_i(\alpha,y_2)| &\leq k_i(\alpha)|y_1 - y_2| \\ |e_i(\alpha,y_2) - e_i(\alpha,y_3)| &\leq k_i(\alpha)|y_2 - y_3| \\ |e_i(\alpha,y_3) - e_i(\alpha,y_1)| &\leq k_i(\alpha)|y_3 - y_1| \\ \forall y_1,y_2,y_3 \in \mathbb{R}&\text{and}\forall\alpha \in [0,1] \end{aligned}$$

with $I_i = \sup k_i(\alpha) i = 1,2,3\ \alpha \in [0,1]$ and $I = \underset{i}{max} I_i$ and if $I(\eta_1+\eta_2+\eta_3) < 1$ where $\eta_i, i = 1,2,3$ and defined by (7) then on $[0,1]$ the tripled system (1) has a unique. We shall show F is contraction.
Proof. Let $(x_1,x_2,x_3),(x'_1,x'_2,x'_3) \in B$ then $\forall\alpha \in [0,1]$

$$\begin{aligned} |f_1(x_2)(x_3)(\alpha) - f_1(x'_2)(x'_3)(\alpha)| &\leq \frac{1}{\Gamma a_1}\int_0^\alpha (\alpha-t)^{a_1-1} \\ |e_1(t,x_2(t),x_3(t) - e_1(t,x'_2(t),x'_3(t)|dt &+ \frac{|R_1|\gamma_1}{24\Gamma(q_1+a_1)} \\ \int_0^1 (1-t)^{q_1+a_1-1}|e_1(t,x_2(t),x_3(t) &- e_1(t,x'_2(t),x'_3(t)|dt \\ +\frac{|R_1|}{\Gamma(a_1-p_1)}\int_0^1 &(1-t)^{a_1-p_1-1}|e_1(t,x_2(t),x_3(t) \\ &-e_1(t,x'_2(t),x'_3(t)|dt \\ \leq I\|x_2x_3 - x'_2x'_3\|\Bigg[\frac{1}{\Gamma a_1}&\int_0^\alpha (\alpha-t)^{a_1-1}dt + \frac{|R_1|\gamma_1}{24\Gamma(q_1+a_1)} \\ \int_0^1 (1-t)^{q_1+a_1-1}dt &+ \frac{|R_1|}{\Gamma(a_1-p_1)}\int_0^1 (1-t)^{a_1-p_1-1}dt\Bigg] \\ \leq \|x_2x_3 - x'_2x'_3\| &\times \left[\frac{1}{\Gamma a_1} + \frac{|R_1|}{24\Gamma(q_1+a_1)} + \frac{|R_1|\gamma_1}{\Gamma(a_1-p_1)}\right] \end{aligned}$$

Thus

$$\|f_1(x_2)(x_3) - f_1(x'_2)(x'_3)\| \leq I\eta_1\|x_2x_3 - x'_2x'_3\|_x$$

Similarly

$$\|f_2(x_1)(x_3) - f_2(x'_1)(x'_3) \leq I\eta_2\|x_1x_3 - x'_1x'_3\|$$

and

$$\|f_2(x_1)(x_2) - f_2(x'_1)(x'_2) \leq I\eta_2\|x_1x_2 - x'_1x'_2\|$$

6

$$\|f(x_1,x_2,x_3)-f(x_1',x_2',x_3')\|_B\leq I(\eta_1+\eta_2+\eta_3)\|(x_1,x_2,x_3)-(x_1',x_2',x_3')\|_B$$

As $I(\eta_1+\eta_2+\eta_3)<1$ therefore f is a contradiction and by Banach fixed point result, f must have unique fixed point i.e. the tripled system (1.1) has unique solution.

Theorem 4.2 Assume $\gamma_i \neq \frac{\Gamma(q_i+5)}{\Gamma(5-p_i)}, i=1,2,3$ and the following hypothesis holds.

(H 2) there exist non negative continuous function $l_1,l_2,l_3 \in C[0,1]$ such that $|e_i(\alpha,y)|\leq l_i(\alpha)$ $\forall y\in\mathbb{R}$ and $\forall\alpha\in[0,1]$ with $L_i = \underset{\alpha\in[0,1]}{sup}\, l_i(\alpha), i=1,2,3.$

Then the tripled system (1.1) defined on [0, 1] has at least one solution

Proof: To prove this result we take help of Schaefer fixed point theorems.

Step-1 F is smooth.

Since e_1,e_2 and e_3 are smooth therefore f is also smooth.

Step-2 Under the mapping f bounded set of B are mapped into bounded sets of B.

Let $\omega_\xi=(x_1,x_2,x_3)\in B; \|(x_1,x_2,x_3)\|_B\leq \xi$

where $\xi>0$ Now for $(x_1,x_2,x_3)\in\omega_\xi$ and $\forall\alpha\in[0,1]$

$$\begin{aligned}
|f_1(x_1)(x_2)(x_3)|\leq{}& \frac{1}{\Gamma a_1}\int_0^\alpha(\alpha-t)^{a_1-1}|e_1(t,x_2(t),x_3(t)|dt\\
&+\frac{|R_1|\gamma_1}{24\Gamma(q_1+a_1)}\int_0^1(1-t)^{q_1+a_1-1}|e_1(t,x_2(t),x_3(t)|dt\\
&+\frac{|R_1|}{\Gamma(a_1-p_1)}\int_0^1(1-t)^{a_1-p_1-1}|e_1(t,x_2(t),x_3(t)|dt\\
\leq{}& \omega_1\left[\frac{1}{\Gamma a_1}\int_0^\alpha(\alpha-t)^{a_1-1}dt+\frac{|R_1|\gamma_1}{24\Gamma(q_1+a_1)}\right.\\
&\left.\int_0^1(1-t)^{q_1+a_1-1}dt+\frac{|R_1|}{\Gamma(a_1-p_1)}\int_0^1(1-t)^{a_1-p_1-1}dt\right]\\
\leq{}& \omega_1\left[\frac{1}{\Gamma a_1}+\frac{|R_1|\gamma_1}{24\Gamma(q_1+a_1)}+\frac{|R_1|}{\Gamma(a_1-p_1)}\right]
\end{aligned}$$

Thus

$$\|f_1(x_2)(x_3)\|_X\leq\omega_1\eta_1$$

similar

$$\|f_1(x_1)(x_3)\|_X\leq\omega_2\eta_2$$

and

$$\|f_1(x_1)(x_2)\|_X\leq\omega_3\eta_3$$

$$\implies \|f_1(x_1,x_2,x_3)\|_X\leq\omega_1\eta_1+\omega_2\eta_2+\omega_3\eta_3$$

7

i.e. $\|f_1(x_1,x_2,x_3)\|_X \leq \infty$ Step-3. $F : B \to B$ is completely continuous operator. Let $(x_1,x_2,x_3) \in \omega_\xi$ and $\alpha_1,\alpha_2,\alpha_3 \in [0,1]$ with $\alpha_1 < \alpha_2 < \alpha_3$, then

$$|f_1(x_2)(\alpha_2) - f_1(x_2)(\alpha_1)| \leq \frac{\omega_1}{\Gamma a_1}\int_0^{\alpha_1}\left[(\alpha_2 - t)^{a_1-1} - (\alpha_1 - t)^{a_1-1}\right]dt$$
$$+\frac{\omega_1}{\Gamma a_1}\int_0^{\alpha_1}(\alpha_2 - t)^{a_1-1} + \frac{\omega_1\gamma_1|R_1|\|\alpha_2^3-\alpha_1^3\|}{24\Gamma(q_1+a_1)}\int_0^1(1-t)^{q_1+a_1-1}dt$$
$$+\frac{\omega_1\gamma_1|R_1|\|\alpha_2^3-\alpha_1^3\|}{24\Gamma(q_2-p_1)}\int_0^1(1-t)^{a_1-p_1-1}dt \leq \frac{\omega_1}{\Gamma(a_1+1)}\left[(\alpha_2-\alpha_1)^{a_1}\right. \tag{4.1}$$
$$\left.+(\alpha_2^{a_1}-\alpha_1^{a_1})\right] + \frac{(\alpha_2-\alpha_1)^{a_1}}{\Gamma(a_1+1)} + \frac{\omega_1\gamma|R_1|\|\alpha_2^3-\alpha_1^3\|}{24\Gamma(q_1+a_1+1)} + \frac{\omega|R_1|\|\alpha_2^3-\alpha_1^3\|}{24\Gamma(a_1-p_1+1)} \tag{4.2}$$

right- hand side tends to zero when $\alpha_1 \to \alpha_2$.
Thus $\|f_1x_2(\alpha_2) - f_1x_2(\alpha_1)\|_X \to 0$ as $\alpha_1 \to \alpha_2$.
Similarly $\|f_2x_1(\alpha_2) - f_2x_1(\alpha_1)\|_X \to 0$ as $\alpha_1 \to \alpha_2$
$\|f_3x_1(\alpha_2) - f_3x_1(\alpha_1)\|_X \to 0$ as $\alpha_1 \to \alpha_2$.
Thus $\|f(x_1,x_2,x_3)(\alpha_2) - f(x_1,x_2,x_3)(\alpha_1)\|_B \to 0$ as $\alpha_1 \to \alpha_2$
Similarly $\|f(x_1,x_2,x_3)(\alpha_3) - f(x_1,x_2,x_3)(\alpha_1)\|_B \to 0$ as $\alpha_1 \to \alpha_3$
Combining step 1 to 3 and by reaction of Arzela - Ascoli theorem, $F : B \to B$ is completely continuous operation.
Step-4
Let

$$\psi = \{(x_1,x_2,x_3) \in B : (x_1,x_2,x_3) = \phi F(x_1,x_2,x_3)$$

for some $\phi \in (0,1)$ we shall show that set ψ is bounded. Let $(x_1,x_2,x_3) \in \psi \implies (x_1,x_2,x_3)(\alpha) = \phi f(x_1,x_2,x_3)(\alpha)$ for some $\phi \in (0,1)$. Then we have

$$\begin{aligned} x_1(\alpha) &= \phi f_1 x_2 x_3(\alpha) \\ x_2(\alpha) &= \phi f_2 x_2 x_3(\alpha) \\ x_3(\alpha) &= \phi f_3 x_2 x_3(\alpha), \forall \alpha \in [0,1] \end{aligned}$$

$$\|x_1(\alpha)\| = |\phi f_1 x_2 x_3(\alpha)| \leq \phi\omega_1\left[\frac{1}{\Gamma a_1}\int_0^\alpha(\alpha-t)^{a_1-1}dt\right.$$
$$+\frac{\gamma_1|R_1|}{24\Gamma(q_1+a_1)}\int_0^1(1-t)^{q_1+a_1-1}dt + \frac{|R_1|}{24\Gamma(a_1-p_1)}$$
$$\left.\int_0^1(1-t)^{a_1-p_1-1}dt\right]$$
$$\leq \omega_1\left[\frac{1}{\Gamma(a_1+1)} + \frac{\gamma_1|R_1|}{24\Gamma(q_1+a_1+1)} + \frac{|R_1|}{24\Gamma(a_1-p_1+1)}\right] \tag{4.3}$$

Thus

$$\|x_1\|_X \leq \omega_1\eta_1$$

8

Similarly

$$\|x_2\|_X \leq \omega_2 \eta_2$$

and

$$\|x_3\|_X \leq \omega_3 \eta_3$$

Hence, we get

$$\begin{aligned}
\|(x_1, x_2, x_3)\|_X &\leq \omega_1 \eta_1 + \omega_2 + \omega_3 \eta_3 \eta_2 \\
\|(x_1, x_2, x_3)\|_B &\leq \infty
\end{aligned}$$

Thus Scheafer's fixed point result present ϕ is bounded set. f must have minimum one fixed point which is solution of tripled system (1.1).

Example 4.1. Take the following tripled system

$$\begin{cases}
{}^C D^{\frac{17}{4}} x_1(\alpha) = \frac{1}{\alpha^2+16} \frac{|x_2(\alpha) x_3(\alpha|)}{1+|x_2(\alpha) x_3(\alpha)|} \\
{}^C D^{\frac{9}{2}} x_2(\alpha) = \frac{1}{\alpha^2+25} \tan^{-1}(x_1(\alpha) x_3(\alpha)), \alpha \in [0,1] \\
{}^C D^{\frac{13}{2}} x_3(\alpha) = \frac{1}{\alpha^2+49} \cot^{-1}(x_1(\alpha) x_3(\alpha)), \alpha \in [0,1] \\
x_1(0) = x_1'(0) = x_1''(0) = 0, {}^C D^{\frac{1}{2}} x_1(1) = \frac{15}{16} (J^{\frac{5}{2}} x_1)(1) \\
x_2(0) = x_2'(0) = x_2''(0) = 0, {}^C D^{\frac{3}{2}} x_2(1) = \frac{16}{17} (J^{\frac{7}{2}} x_2)(1) \\
x_3(0) = x_3'(0) = x_3''(0), {}^C D^{\frac{4}{3}} x_3(1) = \frac{17}{18} (J^{\frac{9}{2}} x_3)(1) \\
a_1 = \frac{17}{4}, p_1 = \frac{1}{2}, q_1 = \frac{5}{2}, \gamma_1 = \frac{15}{16} \neq \frac{\Gamma(q_1+5)}{\Gamma(5-p_1)} = 160.875 \\
a_2 = \frac{9}{2}, p_2 = \frac{3}{2}, q_2 = \frac{7}{2}, \gamma_2 = \frac{16}{7} \neq \frac{\Gamma(q_2+5)}{\Gamma(5-p_2)} = 422.96 \\
a_3 = \frac{13}{2}, p_3 = \frac{4}{3}, q_3 = \frac{9}{2}, \gamma_3 = \frac{17}{8} \neq \frac{\Gamma(q_3+5)}{\Gamma(5-p_3)} = 4558.125
\end{cases} \tag{4.4}$$

for $\alpha \in [0,1]$ and $y_1, y_2, y_3 \in \mathbb{R}$.

$$|e_i(\alpha, y_1) - e_i(\alpha, y_2)| \leq \frac{1}{\alpha^2 + 16} |y_1 - y_2|$$

$$|e_i(\alpha, y_2) - e_i(\alpha, y_3)| \leq \frac{1}{\alpha^2 + 25} |y_2 - y_3|$$

$$|e_i(\alpha, y_3) - e_i(\alpha, y_1)| \leq \frac{1}{\alpha^2 + 49} |y_3 - y_1|$$

So, we can take $K_1 = \frac{1}{\alpha^2+16}, K_2 = \frac{1}{\alpha^2+25}, K_3 = \frac{1}{\alpha^2+49}$

$$I_1 = \sup_{\alpha \in [0,1]} K_1(\alpha) = \frac{1}{16}$$

$$I_2 = \sup_{\alpha \in [0,1]} K_2(\alpha) = \frac{1}{25}$$

$$I_3 = \sup_{\alpha \in [0,1]} K_3(\alpha) = \frac{1}{49}$$

and then, we have

$$I = \max\{I_1, I_2, I_3\} = \frac{1}{16}$$

Further,

$$\begin{aligned}
|R_1| &= \frac{\Gamma(5-p_1)\Gamma(q_1+5)}{|\Gamma(5-p_1)-\Gamma(q_1+5)|} = \frac{2786582\sqrt{\pi}}{1467322} = 3.37 \\
|R_2| &= \frac{\Gamma(5-p_2)\Gamma(q_2+5)}{|\Gamma(5-p_2)-\Gamma(q_2+5)|} = \frac{8968428\sqrt{\pi}}{9624241} = 1.65 \\
|R_3| &= \frac{\Gamma(5-p_3)\Gamma(q_3+5)}{|\Gamma(5-p_3)-\Gamma(q_3+5)|} = \frac{7525863\sqrt{\pi}}{9569341} = 1.39 \\
I\eta_1 &= I\left[\frac{1}{\Gamma(a_1+1)} + \frac{\alpha_1|R_1|}{24\Gamma(q_1+a_1+1)} + \frac{R_1}{24\Gamma(a_1-p_1+1)}\right] \\
&= \frac{1}{16}[0.078 + 0.0034 + 0.0007] \\
&= \frac{1}{16}[0.08211] \\
&= 0.00513 \\
I\eta_2 &= I\left[\frac{1}{\Gamma(a_2+1)} + \frac{\alpha_2|R_2|}{24\Gamma(q_2+a_2+1)} + \frac{R_2}{24\Gamma(a_2-p_2+1)}\right] \\
&= \frac{1}{16}[0.4357 + 0.0046 + 0.0036] \\
&= \frac{1}{16}[0.44066] \\
&= 0.027 \\
I\eta_3 &= I\left[\frac{1}{\Gamma(a_3+1)} + \frac{\alpha_3|R_3|}{24\Gamma(q_3+a_3+1)} + \frac{R_3}{24\Gamma(a_3-p_3+1)}\right] \\
&= \frac{1}{16}[0.00742 + 0.0000127 + 0.00332] \\
&= \frac{1}{16}[0.010752] \\
&= 0.005376
\end{aligned}$$

and then

$$I(\eta_1 + \eta_2 + \eta_3) = 0.005131 + 0.027 + 0.005376 = 0.0375087 < 1$$

Hence all assumptions of Theorem 4.1 are justify and consequently the tripled system (4.4) must have unique solution defined on $[0, 1]$.

Example 4.2. Now consider the following tripled system

$$\begin{cases} {}^{C}D^{\frac{5}{2}}x_1(\alpha) = \frac{\cos x_2 x_3(\alpha)}{7+\alpha} \\ {}^{C}D^{\frac{11}{4}}x_2(\alpha) = \frac{\sin x_1 x_3(\alpha)}{4+\alpha^2} \\ {}^{C}D^{\frac{17}{4}}x_3(\alpha) = \frac{\cos 2\pi x_2 x_3(\alpha)}{7+\alpha^3} \\ x_1(0) = x_1'(0) = x_1'''(0) = 0, {}^{C}D^{\frac{1}{2}}x_1(1) = \frac{13}{4}(J^{\frac{13}{2}}x_1)(1) \\ x_2(0) = x_2'(0) = x_2'''(0) = 0, {}^{C}D^{\frac{3}{2}}x_2(1) = \frac{9}{8}(J^{\frac{9}{2}}x_2)(1) \\ x_3(0) = x_3'(0) = x_3'''(0), {}^{C}D^{\frac{5}{2}}x_3(1) = \frac{6}{7}(J^{\frac{7}{2}}x_3)(1) \\ a_1 = \frac{5}{2}, p_1 = \frac{1}{2}, q_1 = \frac{13}{2}, \alpha_1 = \frac{13}{4} \neq \frac{\Gamma(q_1+5)}{\Gamma(5-p_1)} = 1023014.17 \\ a_2 = \frac{11}{4}, p_2 = \frac{3}{2}, q_2 = \frac{9}{2}, \alpha_2 = \frac{9}{8} \neq \frac{\Gamma(q_2+5)}{\Gamma(5-p_2)} = 35.895.23 \\ a_3 = \frac{17}{4}, p_3 = \frac{5}{2}, q_3 = \frac{7}{2}, \alpha_3 = \frac{6}{7} \neq \frac{\Gamma(q_3+5)}{\Gamma(5-p_3)} = 10557.42 \end{cases} \tag{4.5}$$

for $\alpha \in [0,1]$ and $B \in R$, we get

$$|e_1(\alpha, B)| = |\frac{\cos B}{7+\alpha}| \leq \frac{1}{7+\alpha}$$
$$|e_2(\alpha, B)| = |\frac{\sin B}{4+\alpha^2}| \leq \frac{1}{4+\alpha^2}$$
$$|e_3(\alpha, B)| = |\frac{\cos 2\pi B}{7+\alpha}| \leq \frac{1}{9+\alpha^3}$$

so we can take $l_1(\alpha) = \frac{1}{7+\alpha}, l_2(\alpha) = \frac{1}{4+\alpha^2}, l_3(\alpha) = \frac{1}{9+\alpha^3}$ and then, we have

$$w_1 = \sup_{\alpha \in [0,1]} l_1(\alpha) = \frac{1}{7}$$
$$w_2 = \sup_{\alpha \in [0,1]} l_2(\alpha) = \frac{1}{4}$$
$$w_3 = \sup_{\alpha \in [0,1]} l_3(\alpha) = \frac{1}{9}$$

Hence all assumption of Theorem 4.2 are satisfied therefor the tripled solution (4.5).

Acknowledgement

For the helpful comments and suggestions the authors of the manuscript express sincere thanks to the editors and reviewers.

References

[1] S. Sunder, S. Bhatter, K. Jangid, S.D. Purohit, *Fractionalized mathematical models for drug diffusion*, Chaos, Solitons and Fractals, Volume 165, https://doi.org/10.1016/j.chaos.2022.112810.

[2] K. Diethelm, N. J. Ford, *Analysis of fractional differential equations*, Journal of Mathematical Analysis and Applications 265 (2) (2002) 229–248.

[3] V. Gafiychuk, B. Datsko, V. Meleshko, D. Blackmore, *Analysis of the solutions of coupled nonlinear fractional reaction diffusion equations*, Chaos Solitons and Fractals 41 (3) (2009) 1095–1104.

[4] A. Guezane-Lakoud, R. Khaldi, *Solvability of a three-point fractional nonlinear boundary value problem*, Differential Equations and Dynamical Systems 4 (20) (2012) 395–403.

[5] M. Houas, M. Benbachir, *Existence solutions for three point boundary value problem for differential equations*, J. Fract. Calc. Appl 6 (1) (2015) 160–174.

[6] R. W. Ibrahim, A. Killcman, F. H. Damag, *Existence and uniqueness for a class of iterative fractional differential equations*, Advances in Difference Equations 2015 (1) (2015) 1–13.

[7] A. Kilbas, A. Anatoli, H. Srivastava, and J. Juan, *Theory and applications of fractional differential equation*, Elsvier Publication 204, 2006.

[8] A. K. Nain, R. K. Vats, S. K. Verma, V. Sihag, *Existence of solutions of a non linear fractional differential equations with fractional derivative and fractional integral boundary conditions*,Advances and Applications in Mathematical Sciences 18 (1) (2018) 75–84.

[9] S. K. Ntouyas, *Boundary value problems for nonlinear fractional differential equations and inclusions with nonlocal and fractional integral boundary conditions*, Mathematica 33 (1) (2013) 117–138.

[10] J. Singh, A.M. Alshehri , S. Momani , S. Hadid,D. Kumar, *Computational Analysis of Fractional Diffusion Equations Occurring in Oil Pollution*, Mathematics. 2022; 10(20):3827. https://doi.org/10.3390/math10203827

[11] X.Su, *Boundary value problem for a coupled system of nonlinear fractional differential equations*,Applied Mathematics Letters 22 (1) (2009) 64–69.

[12] M. P. Yadav, R. Agarwal, S. D. Purohit, D. Kumar, D. L. Suthar, (2022) *Groundwater flow in karstic aquifer: analytic solution of dual-porosity fractional model to simulate groundwater flow*, Applied Mathematics in Science and Engineering, 30:1, 598-608, DOI: 10.1080/27690911.2022.2117913

[13] W. Yang *Positive solutions for a coupled system of nonlinear fractional differential equations with integral boundary conditions*, Computers and Mathematics with Applications 63 (1) (2012) 288–297.

[14] Y. Zhang, Z. Bai, T. Feng, *Existence results for a coupled system of nonlinear fractional three-point boundary value problems at resonance*, Computers and Mathematics with Applications 61 (4) (2011) 1032–1047.

J. COMPUTATIONAL ANALYSIS AND APPLICATIONS, VOL. 31, NO. 2, 2023, COPYRIGHT 2023 EUDOXUS PRESS, LLC

L^1-Convergence of Newly Defined Trigonometric Sums Under Some New Class of Fourier Coefficients

Priyanka, Karannvir Singh
Maharaja Ranjit Singh Punjab Technical University, Bathinda, India
priyanka.baghla@gmail.com

Tough difficulties in the trigonometric series convergence in L^1 norm is appearance of trigonometric series as Fourier series, and its L^1- convergence. Many academics investigated trigonometric series separately by examining the cosine & sine series , so as a result, modified cosine sums and sine sums were developed to assess the sharp consequences on trigonometric series's integrability & L^1-convergence, as improved sums approach respective limits closer than traditional trigonometric sums. This work presents 'KP', a new class of Fourier Coefficients, as well as advanced cosine and sine sums of trigonometric series with real coefficients. As a result, necessary & sufficient criterion for Integrability and L^1-normed convergence for trigonometric functions is achieved. Here, authors also discuss about L^1-convergence of r^{th} differential of newly defined improved trigonometric sums with Fourier coefficients are from an enlarged class KP_r.

Keywords: L^1- convergence; Integrability; Modified Sums; Dirichlet Kernel
Mathematics Subject Classifications: 42A20; 42A32

1 Introduction

Take a look at sine & cosine series

$$\sum_{\kappa=1}^{\infty} c_\kappa^* \sin \kappa y \tag{1.1}$$

$$\frac{c_0^*}{2} + \sum_{\kappa=1}^{\infty} c_\kappa^* \cos \kappa y \tag{1.2}$$

and these equations collectively written as

$$\sum_{\kappa=1}^{\infty} c_\kappa^* \psi y \tag{1.3}$$

where ψy is $\sin \kappa y$ or $\cos \kappa y$ respectively.
η^{th} sum of $\sum_{\kappa=1}^{\infty} c_\kappa^* \psi y$ is represented as $S_\eta(y)$. So $\lim_{\eta\to\infty} S_\eta(y) = Z(y)$.
Kano's[1] outcome is popularly known as sequence $\{c_\kappa^*\}$ fulfilling $\{c_\kappa^*\} \to 0$ as $\kappa \to \infty$ & $\sum_{\kappa=1}^{\infty} \kappa^2 |\Delta^2 \left(\frac{c_\kappa^*}{\kappa}\right)| < \infty$ then $\sum_{\kappa=1}^{\infty} c_\kappa^* \sin \kappa y$ and $\frac{c_0^*}{2} + \sum_{\kappa=1}^{\infty} c_\kappa^* \cos \kappa y$ are known to us as Fourier Series.

Definitions:

Convex Sequence: $\{c_\tau^*\}$ is called a convex sequence(seq.) satisfying

$$\Delta^2 c_\tau^* \geq 0, \quad \text{where} \quad \Delta c_\tau^* = c_\tau^* - c_{\tau+1}^* \quad \text{and} \quad \Delta^2 c_\tau^* = \Delta c_\tau^* - \Delta c_{\tau+1}^*.$$

Quasi-Convex Sequence([2],Vol.2, page 204): A seq. $\{c_\tau^*\}$ is called quasi-convex satisfying

$$\sum_{\tau=1}^{\infty} (\tau+1)|\Delta^2 c_\tau^*| < \infty.$$

Sequence $\{c_\tau^*\}$ is known as generalised quasi-convex satisfying

$$\sum_{\tau=1}^{\infty} \tau^{\varkappa} |\Delta^2 c_\tau^*| < \infty : \varkappa = 0, 1, 2, ...$$

'S' Class([4]: sequence $\{c_\tau^*\}$ follow class S by satisfying $c_\tau^* = 0(1)$, τ monotonically decreasing seq. converging to $0 \to \infty$ and $\exists$ a sequence $\{A_\tau^*\}$ s.t.
(a) A_τ^* is monotonically decreasing seq. converging to 0, as$\tau \to \infty$, (b) $\sum\limits_{\tau=0}^{\infty} A_\tau^* < \infty$,
(c) $|\Delta c_\tau^*| \leq A_\tau^* \quad \forall \quad \tau$.
Convergence in L^1-norm: The series L^1-converges in $(0,\pi)$ if $||f^* - S_\tau^*|| = o(1), \tau \to \infty$.
Young[5] began to work on this issue in 1913 by examining a class of convex seq., which was followed by Kolmogorov[6] in 1923 by addressing a general class of quasi-convex seq.Then Telyakovskii[4] analysed Sidon's significantly weaker class S rather than the previously defined classes for L^1- normed convergence(cgs.) of trigonometric series. Following theorems are famous about the L^1- normed cgs. of Fourier series:

Theorem 1.1:[2], Vol.2, page 204

If $\{c_\kappa^*\}$ is monotonically decreasing and $\{c_\kappa^*\}$ is convex/quasi-convex seq. , then necessary & sufficient condition for L^1-normed convergence of $\frac{c_0^*}{2} + \sum_{\kappa=1}^{\infty} c_\kappa^* \cos \kappa y$ is $c_\kappa^* \log \kappa = o(1) \quad \kappa \to \infty$.
Telyakovsk˘ii generalised Theorem 1.1 for expression (1.2) where the coefficients of series (1.2) satisfy the requirements of class S[7] as follows:

Theorem 1.2:[4]

When coefficients of $\frac{c_0^*}{2} + \sum_{\kappa=1}^{\infty} c_\kappa^* \cos \kappa y$ satisfying criterion of class S[7] then criterion of its L^1 convergence is that $c_\kappa^* \log \kappa = o(1)$ as $\kappa \to \infty$

Many writers examined and generalised these findings by examining various generalisations of seq. classes.Recently,the coefficient seq. SJ[8] was introduced to study the integrability and L^1-cgs. of modified cosine and sine sums, which was further generalied by Krasniqi[9]. A contemporary class of Fourier coefficients is formulated in this study as:

Definition 1.3: A monotonically decreasing seq. $\{c_\eta^*\}$ with $c_\eta^* \to 0$ as $\eta \to \infty$ is follow a new class KP if $\exists$ a seq. $\{A_\eta^*\}$ satisfying

$$(i) A_\eta^* \downarrow 0 \tag{1.4}$$

$$(ii) \sum \eta A_\eta^* < \infty \tag{1.5}$$

$$(iii) \left| \Delta \left(\frac{c_\eta^*}{\eta^2} \right) \right| \leq \frac{A_\eta^*}{\eta^2} \tag{1.6}$$

Here, coefficient sequence KP_r will be formulated that is enlargement of coefficient sequence KP.

Definition 1.4:: A monotonically decreasing seq. $\{c_\eta^*\}$ with $c_\eta^* \to 0$ as $\eta \to \infty$ is from a new class KP_r if $\exists$ seq. $\{A_\eta^*\}$ satisfying

$$(i) A_\eta^* \downarrow 0 \tag{1.7}$$

$$(ii) \sum \eta^{r+1} A_\eta^* < \infty \tag{1.8}$$

$$(iii) \left| \Delta \left(\frac{c_\eta^*}{\eta^2} \right) \right| \leq \frac{A_\eta^*}{\eta^2} \tag{1.9}$$

Obviously, KP = KP_r when r = 0. It is obvious that $KP_{r+1} \subseteq KP_r$, but its reverse does not hold.

Example. Define $b_\eta = \frac{1}{\eta^{r+3}},$ r = 0,1,2,... Firstly we are going to demonstrate that$\{b_\eta\} \notin KP_{r+1}$

As, $b_\eta = \frac{1}{\eta^{r+3}} \to 0$ as $\eta \to \infty$.

Let $\exists$ $A_\eta = \frac{1}{\eta^{r+3}}, r = 0, 1, 2, 3, ... s.t. \sum_{\eta=1}^{\infty} \eta^{r+2} A_\eta = \sum_{\eta=1}^{\infty} \frac{1}{\eta}$ is divergent, means $\{b_\eta\}$ does not belong to KP_{r+1}.

But, A_η is monotonically decreasing and converging to 0 $\eta \to \infty$, &

$\sum_{\eta=1}^{\infty} \eta^{r+1} A_\eta^* = \sum_{\eta=1}^{\infty} \frac{1}{\eta^2} < \infty$,

Also $|\Delta(\frac{b_\eta}{\eta^2})| \leq \frac{A_\eta^*}{\eta^2}, \forall \eta$.

Therefore, $\{b_\eta\} \in KP_r$.

3

2 Main Results:

Now we will give proof of the succeeding statement:

Theorem 2.1: If the coefficients of series (1.3) meet the class KP criteria, then it will be a Fourier series.

Explanation

$$\sum_{\kappa=1}^{\infty}\kappa^2\left|\Delta^2\left(\frac{c_\kappa^*}{\kappa}\right)\right| = \sum_{\kappa=1}^{\infty}\kappa^2\left|\Delta\left(\frac{c_\kappa^*}{\kappa}\right)-\Delta\left(\frac{c_{\kappa+1}^*}{\kappa+1}\right)\right|$$

$$= \sum_{\kappa=1}^{\infty}\kappa^2\left|\frac{c_\kappa^*}{\kappa}-\frac{c_{\kappa+1}^*}{\kappa+1}-\frac{c_{\kappa+1}^*}{\kappa+1}+\frac{c_{\kappa+2}^*}{\kappa+2}\right|$$

$$\left\{\begin{array}{l} c_{\kappa+2}^*<c_{\kappa+1}^* \quad and \quad \kappa+2>\kappa+1 \quad \text{therefore} \quad \dfrac{1}{\kappa+2}<\dfrac{1}{\kappa+1} \\ \qquad\qquad\qquad\qquad\qquad\qquad\qquad \Rightarrow \dfrac{c_{\kappa+2}^*}{\kappa+2}<\dfrac{c_{\kappa+1}^*}{\kappa+1} \end{array}\right\}$$

$$\leq \sum_{\kappa=1}^{\infty}\kappa^2\left|\frac{c_\kappa^*}{\kappa}-\frac{c_{\kappa+1}^*}{\kappa+1}\right|$$

$$= \sum_{\kappa=1}^{\infty}\kappa^2\left|\kappa\frac{c_\kappa^*}{\kappa^2}-(\kappa+1)\frac{c_{\kappa+1}^*}{(\kappa+1)^2}\right|$$

$$< \sum_{\kappa=1}^{\infty}\kappa^3\left|\frac{c_\kappa^*}{\kappa^2}-\frac{c_{\kappa+1}^*}{\kappa+1^2}\right|$$

$$= \sum_{\kappa=1}^{\infty}\kappa^3\left|\Delta\left(\frac{c_\kappa^*}{\kappa^2}\right)\right|$$

$$\leq \sum_{\kappa=1}^{\infty}\kappa^3\frac{A_\kappa^*}{\kappa^2} \quad \text{by} \quad \text{defined} \quad \text{class KP of Fourier Coefficients.}$$

$$= \sum_{\kappa=1}^{\infty}\kappa A_\kappa^*<\infty$$

As c_κ^* is null sequence, So by the result given by Kano[1], Theorem 1 holds. In this study, we provide latest improved trigonometric sums.

$$Z_\eta(y) = \frac{c_0^*}{2} + \sum_{\kappa=1}^{\eta}\left[\sum_{j=\kappa}^{\eta}\Delta\left(\frac{c_j^*\cos jy}{j^2}\right)\right]\kappa^2,$$

$$r_\eta(y) = \sum_{\kappa=1}^{\eta}\left[\sum_{j=\kappa}^{\eta}\Delta\left(\frac{c_j^*\sin jy}{j^2}\right)\right]\kappa^2.$$

4

Also investigated their L^1-convergence following the newly established class KP of coefficient sequences

Theorem 2.2: Suppose that coefficients of series (1.3) follow class KP, then

$$\lim_{\eta\to\infty} Z_\eta(y) = Z(y), exists \quad for \quad y \in (o,\pi] \tag{2.2.1}$$

$$Z(y) \in L^1(0,\pi] \tag{2.2.2}$$

$$||Z(y) - S_\eta(y)|| = o(1), \eta \to \infty \tag{2.2.3}$$

Theorem 2.3: If coefficients of a sequence (1.3) are from a class KPr, then

$$\lim_{\eta\to\infty} Z^r{}_\eta(y) = Z^r(y), exists \quad for \quad y \in (o,\pi] \tag{2.3.1}$$

$$Z^r(y) \in L^1(0,\pi], \qquad (r = 0,1,2,...) \tag{2.3.2}$$

$$||Z^r(y) - S^r{}_\eta(y)|| = o(1), \eta \to \infty. \tag{2.3.3}$$

3 Lemmas:

The subsequent lemmas are required to prove our main results.

Lemma 3.1[3]

Let $\eta \geq 1$ & $r \in \mathbb{Z}^+ \cup 0$, y $\in$ [s,π] So $|\tilde{D}^r_\eta(y)| \leq C_s \frac{\eta^r}{y}$ Where C_s is +ve constant rely upon s, $0<s<\pi$ & $\tilde{D}^r_\eta(y)$ is conjugate Dirichlet kernel.

Lemma 3.2[4]

Suppose $\{c^*_\eta\}$ is a sequence of $\Re$ s.t. $|c^*_\eta| \leq 1$ forall η. So the relation

$$\int_{\frac{\pi}{\eta+1}}^{\pi} |\sum_{\kappa=0}^{\eta} c^*_\kappa \tilde{D}_\kappa(y)|dy \leq N(\eta+1)$$

exists, where N is perfectly constant.
By Bernstein's inequality,

$$\int_{\frac{\pi}{\eta+1}}^{\pi} |\sum_{\kappa=0}^{\eta} c^*_\kappa \tilde{D}^r_\kappa(y)|dx \leq N(\eta+1)^{s+1} \quad \text{for s = 0,1,2,...}$$

lemma 3.3[3]

$||D^s_\eta(y)||_{L^1} = o(\eta^s \log\eta) + o(\eta^s)$, $s = 0,1,2,....$, and $D^r_\eta(y)$ shows the r^{th} differentials of Dirichlet Kernel.

4 Proof of Main results:

4.1 Solution of theorem 2.1:

We will just show the evidence for cosine sums here, while the argument for sine sums will be shown on parallel paths.
To prove (2.2.1), we notice that

$$\begin{aligned}
Z_\eta(y) &= \frac{c_0^*}{2} + \sum_{\kappa=1}^{\eta}\left[\sum_{j=\kappa}^{\eta}\Delta\left(\frac{c_j^*\cos jy}{j^2}\right)\right]\kappa^2 \\
&= \frac{c_0^*}{2} + \sum_{\kappa=1}^{\eta}\left[\sum_{j=\kappa}^{\eta}\left(\frac{c_j^*\cos jy}{j^2} - \frac{c_{j+1}^*\cos(j+1)y}{(j+1)^2}\right)\right]\kappa^2 \\
&= \frac{c_0^*}{2} + \sum_{\kappa=1}^{\eta} c_\kappa^*\cos\kappa y - \sum_{\kappa=1}^{\eta}\kappa^2\frac{c_{\eta+1}^*\cos(\eta+1)y}{(\eta+1)^2} \\
&= S_\eta(y) - \frac{c_{\eta+1}^*\cos(\{\eta+1\}y)\eta(\eta+1)(2\eta+1)}{6(\eta+1)^2}
\end{aligned}$$

$$\lim_{\eta\to\infty} Z_\eta(y) = \lim_{\eta\to\infty} S_\eta(y) - \lim_{\eta\to\infty}\frac{c_{\eta+1}^*\eta(2\eta+1)\cos((\eta+1)y)}{6(\eta+1)}$$

Since $\cos(\eta+1)y$ is bounded in $(0,\pi]$ and $\lim_{\eta\to\infty}\frac{2\eta+1}{\eta+1} = 2$ and

$$\begin{aligned}
\eta\left|c_\eta^*\right| = \frac{\eta^3 c_\eta^*}{\eta^2} &= \eta^3\sum_{\kappa=\eta}^{\infty}\left|\Delta\left(\frac{c_\kappa^*}{\kappa^2}\right)\right| \\
&\le \sum_{\kappa=\eta}^{\infty}\kappa^3\left|\Delta\left(\frac{c_\kappa^*}{\kappa^2}\right)\right| \\
&\le \sum_{\kappa=\eta}^{\infty}\kappa^3\frac{A_\kappa^*}{\kappa^2} = \sum_{\kappa=\eta}^{\infty}\kappa A_\kappa^* = 0(1) \\
&as \quad \eta\to\infty
\end{aligned}$$

$\{if \sum c_\eta^*$ is convergent then $\lim_{\eta\to\infty} c_\eta^* = 0\}$

$$\text{So,} \quad \lim_{\eta\to\infty} Z_\eta(y) = \lim_{\eta\to\infty} S_\eta(y) = Z(y) \quad where$$

$$\begin{aligned}
Z(y) &= \frac{c_0^*}{2} + \lim_{\eta\to\infty}\sum_{\kappa=1}^{\eta} c_\kappa^*\cos\kappa y \\
&= \lim_{\eta\to\infty} Z_\eta(y) = \lim_{\eta\to\infty} S_\eta(y) \\
&= \lim_{\eta\to\infty}(\frac{c_0^*}{2} + \sum_{\kappa=1}^{\eta} c_\kappa^*\cos\kappa y)
\end{aligned}$$

6

$$\text{Now} \lim_{\eta\to\infty}(\sum_{\kappa=1}^{\eta} c_\kappa^* \cos\kappa y)$$

$$\begin{aligned}
&= \lim_{\eta\to\infty}(\sum_{\kappa=1}^{\eta} \frac{c_\kappa^*}{\kappa^2}\kappa^2 \cos\kappa y) \\
&= \lim_{\eta\to\infty}(\sum_{\kappa=1}^{\eta-1} \Delta(\frac{c_\kappa^*}{\kappa^2}(-D_\kappa^{''}(y)) + \frac{c_\eta^*}{\eta^2}(-D_\eta^{''}(y))) \\
&= \sum_{\kappa=1}^{\infty} \Delta(\frac{c_\kappa^*}{\kappa^2})(-D_\kappa^{''}(y)) \\
&\le \sum_{\kappa=1}^{\infty} \Delta(\frac{A_\kappa^*}{\kappa^2})(-D_\kappa^{''}(y))
\end{aligned}$$

According to the provided hypothesis & lemma 1, $\sum_{\kappa=1}^{\infty} \Delta(\frac{A_\kappa^*}{\kappa^2})(-D_\kappa^{''}(y))$ converges. Therefore Z(y)exists for y $\in$ (0,π]
This brings the proof of (2.2.1).

$$\begin{aligned}
\text{Now}||Z(y) - Z_\eta(y)|| &= \int_0^\pi |Z(y) - Z_\eta(y)|dy \\
&= \int_0^\pi |\sum_{\kappa=\eta+1}^{\infty} c_\kappa^* \cos\kappa y + \frac{\eta(2\eta+1)c_{\eta+1}^* \cos(\eta+1)y}{6(\eta+1)}|dy \\
&= \lim_{m\to\infty}\int_0^\pi |\sum_{\kappa=\eta+1}^{m} \frac{c_\kappa^*\kappa^2 \cos\kappa y}{\kappa^2} + \frac{\eta(2\eta+1)c_{\eta+1}^* \cos(\eta+1)y}{6(\eta+1)}|dy
\end{aligned}$$

We obtain by employing Abel's Transformation

$$\begin{aligned}
&= \int_0^\pi |\sum_{\kappa=\eta+1}^{\infty} \Delta\left(\frac{c_\kappa^*}{\kappa^2}\right)\left(-D_\kappa^{''}(y)\right) + \frac{c_{\eta+1}^* D_\eta^{''}(y)}{(\eta+1)^2} \\
&+ \frac{\eta(2\eta+1)c_{\eta+1}^* \cos(\eta+1)y}{6(\eta+1)}|dy \\
&\le \int_0^\pi |\sum_{\kappa=\eta+1}^{\infty} \Delta\left(\frac{c_\kappa^*}{\kappa^2}\right)\left(-D_\kappa^{''}(y)\right)|dy + \int_0^\pi |\frac{c_{\eta+1}^* D_\eta^{''}(y)}{(\eta+1)^2}|dy \\
&+ \int_0^\pi |\frac{\eta(2\eta+1)c_{\eta+1}^* \cos(\eta+1)y}{6(\eta+1)}|dy \\
&= (i) + (ii) + (iii)
\end{aligned}$$

Evidence of part (i)

$$\int_0^\pi |\sum_{\kappa=\eta+1}^{\infty} \Delta\left(\frac{c_\kappa^*}{\kappa^2}\right)\left(-D_\kappa^{''}(y)\right)|dy = \int_0^\pi |\sum_{\kappa=\eta+1}^{\infty} \frac{\frac{A_\kappa^*}{\kappa^2}\Delta\left(\frac{c_\kappa^*}{\kappa^2}\right)\left(-D_\kappa^{''}(y)\right)}{\frac{A_\kappa^*}{\kappa^2}}|dy$$

7

Implementing Abel's Transformation Once More

$$
\begin{aligned}
&= \int_0^{\pi} |\sum_{\kappa=\eta+1}^{\infty} \Delta \frac{A_\kappa^*}{\kappa^2}) \sum_{j=1}^{\kappa} \frac{\Delta \frac{c_j^*}{j^2}}{(\frac{A_j}{j^2})} (-D_j^{''}(x))|dy \\
&\leq \sum_{\kappa=\eta+1}^{\infty} \Delta \left(\frac{A_\kappa^*}{\kappa^2}\right) \int_0^{\pi} |\sum_{j=1}^{\kappa} \left(\frac{\Delta\left(\frac{c_j^*}{j^2}\right)}{\frac{A_j^*}{j^2}}\right) \left(D_j^{''}(y)\right)|dy
\end{aligned}
$$

Now by given assumption

$$
\begin{aligned}
&\leq \sum_{\kappa=\eta+1}^{\infty} \Delta \left(\frac{A_\kappa^*}{\kappa^2}\right) M(\kappa+1)^3 \\
&= o\left(\sum_{\kappa=\eta+1}^{\infty} (\kappa+1)^3 \Delta \left(\frac{A_\kappa^*}{\kappa^2}\right)\right) \\
&= o(1) \quad \text{as} \quad \{c_\kappa^*\} \in \quad \text{new defined class.}
\end{aligned}
$$

Validation of (ii) component

$$
\begin{aligned}
\frac{c_{\eta+1}^*}{(\eta+1)^2} \int_0^{\pi} |D_\eta^{''}(y)|dy &= \frac{c_{\eta+1}^*}{(\eta+1)^2} \left(\frac{4}{\pi}(\eta^2 \log \eta) + O(\eta^2)\right) \\
&\leq c_{\eta+1}^* \left(\frac{4}{\pi} \frac{\eta^2 \log \eta}{(\eta+1)^2} + \frac{1}{(\eta+1)^2} o(\eta^2)\right) \\
&\leq c_{\eta+1}^* \left(\frac{4}{\pi} \frac{\eta^2 \log \eta}{(\eta+1)^2} + o(1)\right) \\
&= o\left(c_{\eta+1}^* \log \eta\right)
\end{aligned}
$$

Now $\log \eta \leq \eta \quad \forall \quad \eta \geq 1$

And $\eta c_\eta^* = o(1) \quad as \quad \eta \to \infty$ as already proved above.

Proof of (iii)part

(iii) part is equal to $o(\eta c_{\eta+1}^*)$ which is equal to $o(1) \quad$ as $\quad \eta \to \infty$.

Therefore $||Z(y) - Z_\eta(y)|| = o(1)$ as $\eta \to \infty$

Therefore $Z(y) \in L^1(0, \pi]$

This concludes (2.2.2).

Now we shall provide evidence of (2.2.3)

$$
\begin{aligned}
||Z - S_\eta|| &= ||Z - Z_\eta + Z_\eta - S_\eta|| \\
&\leq ||Z - Z_\eta|| + ||Z_\eta - S_\eta|| \\
&= ||Z - Z_\eta|| + ||\frac{\eta(2\eta+1)}{6(\eta+1)} c_{\eta+1}^* \cos{(\eta+1)y}|| \\
&\leq ||Z - Z_\eta|| + \frac{\eta(2\eta+1)}{6(\eta+1)} c_{\eta+1}^* \int_0^{\pi} |\cos{(\eta+1)y}|dy \\
&\to \quad o(1) \quad as \quad \eta \to \infty
\end{aligned}
$$

by employing the assertion (2.2.1) and (2.2.2). This brings the proof of (2.2.3) to a close. Apparently theorem 2 is developed for feeble class than class S, yet conclusions are produced for L^1 -convergence by not employing condition like $c^*_\eta \log\eta = o(1), \quad as \quad \eta \to \infty$.

4.2 Explanation of theorem 2.3:

We will just show the evidence for cosine sums here, while the argument for sine sums will be shown on parallel paths.

$$Z_\eta(y) = S_\eta(y) - \frac{c^*_{\eta+1}\cos((\eta+1)y)(\eta)(2\eta+1)}{6(\eta+1)}$$

$$Z^r_\eta(y) = S^r{}_\eta(y) - \frac{c^*_{\eta+1}\cos(((\eta+1)y)+r\frac{\pi}{2})(\eta)(2\eta+1)(\eta+1)^r}{6(\eta+1)}$$

Since A_κ is monotonically decreasing and converging to 0 as $\kappa\to\infty$ & $\sum\limits_{\kappa=1}^{\infty}\kappa^{r+1}A_\kappa<\infty$,
So, we got $\kappa^{r+2}A_\kappa \to 0$, as $\kappa\to\infty$ and

$$\eta^{r+1}c^*_\eta = \eta^{r+3}\sum_{\kappa=\eta}^{\infty}|\Delta(\frac{a_\kappa}{\kappa^2})| \le \sum_{\kappa=\eta}^{\infty}\kappa^{r+3}|\Delta(\frac{c^*_\kappa}{\kappa^2})| \le \sum_{\kappa=\eta}^{\infty}\kappa^{r+3}(\frac{A^*_\kappa}{\kappa^2}) = o(1), \eta\to\infty. \tag{4.2.1}$$

As $\cos((\eta+1)y+r\frac{\pi}{2})$ is finite in (0,π]. So,

$$\begin{aligned} z^r(y) &= \lim_{\eta\to\infty} z_\eta{}^r(y) \\ &= \lim_{\eta\to\infty} S_\eta{}^r(y) \\ &= \lim_{\eta\to\infty}(\sum_{\kappa=1}^{\eta}\kappa^r c^*_\kappa\cos(\kappa y + r\frac{\pi}{2})) \end{aligned}$$

After using Abel's Transformation, obtained as

$$\begin{aligned} \lim_{\eta\to\infty}(\sum_{\kappa=1}^{\eta}\kappa^r c^*_\kappa\cos(\kappa y + r\frac{\pi}{2})) &= \lim_{\eta\to\infty}[\sum_{\kappa=1}^{\eta-1}\Delta(\frac{c^*_\kappa}{\kappa^2})(-D^{r+2}{}_\kappa(y)) + \frac{c^*_\eta}{\eta^2}D^{r+2}{}_\eta(y)] \\ &= \sum_{\kappa=1}^{\infty}\Delta(\frac{c^*_\kappa}{\kappa^2})(-D^{r+2}{}_\kappa(y)) + \lim_{\eta\to\infty}\frac{c^*_\eta}{\eta^2}D^{r+2}{}_\eta(y) \\ &\le \sum_{\kappa=1}^{\infty}\frac{A^*_\kappa}{\kappa^2}(-D^{r+2}{}_\kappa(y)) + \lim_{\eta\to\infty}\frac{c^*_\eta}{\eta^2}D^{r+2}{}_\eta(y) \end{aligned}$$

Using the provided assumptions, lemma 1 & (4.2.1), the series $\sum\limits_{\kappa=1}^{\infty}\frac{A^*_\kappa}{\kappa^2}(-D^{r+2}{}_\kappa(y))$ converges.

So, the limit $z^r(y)$ exists for $y \in (0,\pi]$ and (2.3.1) follows.
Take the following consideration to establish (2.3.2).

$$\begin{aligned}
z^r(y) - {z_\eta}^r(y) &= \sum_{\kappa=\eta+1}^{\infty} \kappa^r c^*_\kappa \cos(\kappa y + r\frac{\pi}{2}) + \frac{c^*_{\eta+1}\cos{(\eta+1)y + r\frac{\pi}{2}}\eta(2\eta+1)(\eta+1)^r}{6(\eta+1)} \\
&= \sum_{\kappa=\eta+1}^{\infty} \Delta(\frac{c^*_\kappa}{\kappa^2})(-{D_\kappa}^{r+2}(y)) + \frac{c^*_{\eta+1}}{(\eta+1)^2} D_\eta^{r+2}(y) \\
&+ \frac{\eta(\eta+1)^r(2\eta+1)}{6(\eta+1)} c^*_{\eta+1}\cos((\eta+1)y + r\frac{\pi}{2}) \\
&= \sum_{\kappa=\eta+1}^{\infty} \frac{A^*_\kappa}{\kappa^2} \frac{\Delta(\frac{c^*_\kappa}{\kappa^2})}{\frac{A^*_\kappa}{\kappa^2}}(-{D_\kappa}^{r+2}(y)) + \frac{c^*_{\eta+1}}{(\eta+1)^2} D_\eta^{r+2}(y) \\
&+ \frac{\eta(\eta+1)^r(2\eta+1)}{6(\eta+1)} c^*_{\eta+1}\cos((\eta+1)y + r\frac{\pi}{2}) \\
&= \sum_{\kappa=\eta+1}^{\infty} \Delta(\frac{A^*_\kappa}{\kappa^2}) \sum_{j=1}^{\kappa} \frac{\Delta(\frac{c^*_j}{j^2})}{\frac{A^*_j}{j^2}}(-{D_j}^{r+2}(y)) + (\frac{A^*_{\eta+1}}{\eta+1}) \sum_{j=1}^{\eta} \frac{\Delta(\frac{c^*_j}{j^2})}{\frac{A^*_j}{j^2}}(-{D_j}^{r+2}(y)) \\
&+ \frac{c^*_{\eta+1}}{(\eta+1)^2} D_\eta^{r+2}(y) + \frac{\eta(\eta+1)^r(2\eta+1)}{6(\eta+1)} c^*_{\eta+1}\cos((\eta+1)y + r\frac{\pi}{2})
\end{aligned}$$

After applying the lemma 2 & lemma 3

$$\begin{aligned}
||z^r(y) - {z_\eta}^r(y)|| &\leq \sum_{\kappa=\eta+1}^{\infty} \Delta(\frac{A^*_\kappa}{\kappa^2}) \int_0^\pi |\sum_{j=1}^{\kappa} \frac{\Delta(\frac{c^*_j}{j^2})}{\frac{A^*_j}{j^2}}(-{D_j}^{r+2}(y))|dy \\
&+ (\frac{A^*_{\eta+1}}{\eta+1}) \int_0^\pi |\sum_{j=1}^{\eta} \frac{\Delta(\frac{c^*_j}{j^2})}{\frac{A^*_j}{j^2}}(-{D_j}^{r+2}(y))|dy + \int_0^\pi |\frac{c^*_{\eta+1}}{(\eta+1)^2} D_\eta^{r+2}(y)|dy \\
&+ \frac{\eta(\eta+1)^r(2\eta+1)}{6(\eta+1)} |c^*_{\eta+1}| \int_0^\pi |\cos((\eta+1)y + r\frac{\pi}{2})|dy \\
&= O(\sum_{\kappa=\eta+1}^{\infty} \kappa^{r+3}\Delta(\frac{A^*_\kappa}{\kappa^2})) + O(\eta^{r+3}(\frac{A^*_{\eta+1}}{\eta+1^2})) + O(\eta^r c^*_{\eta+1}\log\eta) \\
&+ \frac{\eta(\eta+1)^r(2\eta+1)}{6(\eta+1)} \left| c^*_{\eta+1} | \int_0^\pi |\cos\left((\eta+1)y + r\frac{\pi}{2}\right)\right| dy
\end{aligned}$$

Using the reasoning provided in the explanation of theorem 2, researchers may conclude that $\sum\limits_{\kappa=\eta+1}^{\infty} \kappa^{r+3}\Delta(\frac{A_\kappa}{\kappa^2})$ converges.
$\int_0^\pi |\cos((\eta+1)y + r\frac{\pi}{2})|dy \leq \frac{2}{\eta+1}$ and for $\eta \geq 1, \eta^{r+1}c^*_\eta \log\eta \leq \eta^{r+2}c^*_\eta = o(1)$ as $\eta \to \infty$. This implies that

$$||z^r(y) - {z_\eta}^r(y)|| = 0(1) \qquad as \qquad \eta \to \infty. \tag{4.2.2}$$

10

Because,${z_\eta}^r(y)$ is a monomial, so $z^r(y) \in L^1(0,\pi]$ which completes (2.3.2). We are now proceeding on to the evidence of (2.3.3)

$$\begin{aligned}
||z^r - {S_\eta}^r|| &= ||z^r - {z_\eta}^r + {z_\eta}^r - {S_\eta}^r|| \\
&\le ||z^r - {z_\eta}^r|| + ||{z_\eta}^r - {S_\eta}^r|| \\
&= ||z^r - {z_\eta}^r|| + ||\frac{\eta(\eta+1)^r(2\eta+1)}{6(\eta+1)}|c^*_{\eta+1}\cos((\eta+1)y + r\frac{\pi}{2})|| \\
&\le ||z^r - {z_\eta}^r|| + \frac{\eta(\eta+1)^r(2\eta+1)}{6(\eta+1)}|c^*_{\eta+1}|\int_0^\pi |\cos((\eta+1)y + r\frac{\pi}{2})|dy
\end{aligned}$$

Further $||z^r(y) - {z_\eta}^r(y)|| = 0(1) \quad as \quad \eta \to \infty$ by using (1.11),$\int_0^\pi |\cos((\eta+1)y + r\frac{\pi}{2})|dy \le \frac{2}{\eta+1}$ and c^*_η is a seq. converging to 0,so the (2.3.3)part of theorem 2.3 holds.

Note The scenario r = 0 in main result 2.3 gives output of main result 2.2.

Acknowledgment

Authors are thankful to MRSPTU Bathinda for enabling opportunities in paper preparation process.

References

[1] T.Kano,Coefficients of some trigonometric series,*Jour. Frac. Sci. Shihshu University*,**3**,153-621(968).

[2] N.K.Bary,*A Treatise on Trigonometric Veries* (vol 1 and vol 2),London,1964.

[3] S.Sheng,The extension of the theorems of C.V.Stanojevic and V.B.Stanojevic,*Proc. Amer. Math. Soc.*,**14**,158-60,(1939).

[4] S.A.Telyakovskii,A sufficient condition of Sidon for the integrability of trigonometric series,*Mat.Zametki*,**14**,317-28,(1973).

[5] W.H.Young, On the Fourier series of bounded functions,*Proc. London Math. Soc.*,**12**,41-70,(1993).

[6] A.N. Kolmogorov,Sur l'ordere de grandeur des coefficients de la sėrie de Fourier-Lebsque,*Bull. Acad. Polon. Sci. Ser. Sci. Math. Astronom. Phys.*,83-86,(1923).

[7] S.Sidon, Hinreichende Bedingungen f ur den Fourier-Charakter einer trigonometrischen Reihe,*J. London Math. Soc.*,**14**,579-86,(1939).

[8] J.Kaur and S.S. Bhatia,Convergence of new modified trigonometric sums in metric space L, *The journal of Non Linear Sciences and applications*,**1(3)**,179-188,(2008).

[9] Xh.Z. Krasniqi, Further results on L^1-convergence of some modified complex trigonometric sums, *J. Numer. Anal. Approx. Theory*,**44(2)**,180-189,(2015).

Numerical Study of Heat and Mass Transfer of MHD Casson Fluid Flow with Cross-Diffusion and Heat Source Impacts in presence of Radiation

Shilpa[1], *Ruchika Mehta*[1*], *Sushila*[2] *and Renu Sharma*[3]
[1] *Department of Mathematics and Statistics*,
Manipal University Jaipur, Jaipur(Raj.), India
[2] *Department of Physics*,
Vivekananda Global University, Jaipur(Raj.), India
[3] *Department of Physics*,
JECRC University, Jaipur(Raj.), India
[1*] *ruchika.mehta*1981@*gmail.com*

Abstract

The current research analyzes Soret and Dufour effects on magneto hydrodynamic natural convection viscous-elastic radiative Casson fluid flow across a non-linear stretchy sheet. First, the PDEs (partial differential equations) are changed using similarity analysis into non-linear paired ODEs (ordinary differential equations). Then, using the BVP4C technique, ordinary differential equations are numerically solved. Engineering interest of substantial quantities like skin-friction coefficient, Nusselt parameter, and Sherwood parameter debated in the table with multiple significant characteristics. The current study describes that the temperature profile increases with rising thermal radiation and the Dufour effect. A declining Sherwood impression of Soret number is depicts in current study. An increasing radiation impact declines the Nusselt number.In addition, the concentration field enhances due to an increasing Soret effect.

Key words: Non-linear stretchy sheet, Soret and Dufour effects, Casson fluid, Radiation Parameter, BVP4C technique.

1 Introduction

When most organic and commercial fluids, including hemoglobin, printer inks, greasing heavy oils, watercolors, gypsum pastes, fluid cleansers, multigrade oils, ceramic materials, fruit drinks, polymeric materials and others are pressured, they modify their initial fluid properties or viscosity nature. The traditional Newton's law of viscosity is significantly deviated by these non-Newtonian fluids. Many Researchers have explore a variety of non-Newtonian viscous-elastic flow samples through evaluate their unique flow movement in order to estimate these conventional fluids' features of flow, temperature and concentration dispensation in a suitable way.

Thermal radiation is the process through which energy or heat is conveyed by electromagnetic waves. Thermal radiation is important when there is a large temperature difference between the boundary surface and the surrounding fluid. In physics and engineering, radiative impacts are essential. The effects of radiation heat transfer on various flows are critical when performing activities requiring high temperatures and space technologies. For instance, the effects of radiation are essential for observing heat transfer in the polymer sectors, where heat regulating elements have a mild influence on the quality of the finished product. Relevant are also the effects of radiation on nuclear power plants, aircraft, gas turbines, spacecraft, liquid metal fluids, and solar radiation.A comprehensive examination of mixture convective flow of Casson and Oldroyd-B fluids through a linearly stratified stretchy sheet was reported by Kumam, P.et al. [1]. Additionally Thermal radiation, chemical reactivity, and magnetization are all properties of Casson and Oldroyd-B fluids. The property of slide boundary circumstances and chemical reactive on heat and mass transport via mix convective boundary stratum flow of a non-Newtonian fluid over a non-linear stretchy sheet are studied by Ahemed et al. [2]. Ahmad. et al. [3] studied the free convection slippage flow of fractional viscous fluid by considering the thermal radiation, heat generation, chemical reaction of order first, and Newtonian heating through a porous medium by considering single-wall carbon nanotube (SWCNT).The Casson fluid form is used to explain the performance of non-Newtonian fluids. Basha et al. [4] investigated the MHD convective heat transport viscous-elastic boundary layer of the Casson fluid with Joule and viscous dissipation characteristics under the impact of chemical process and in the presence of Lorentz forces, a non-linear stretched sheet was utilized. Basha et al. [5] developed a 2D numerical form to explore the result of buoyancy forces on magnetized free convective Walters-B fluid flow across a stretched sheet with Soret impact, heat radiative, heat source/sink, and viscous dissipation. The stretchy sheet geometry is used to generate the present physical model. The electromagnetic force on a charged particle, effect on a non-linear structure is analyzed. The work focuses exclusively on contributions to the utilization of non-Newtonian Casson fluid entropy generation across an exponentially stretched sheet. Entropy generation and homogeneous–heterogeneous reactions are explored by Das et al. [6]. Instead of no-slip situation at the boundary, motion and thermal slips are measured. The buoyancy influence on 2D Casson fluid flow and mix convection over a non-linear stretched sheet is detected from Gangadhar et al. [7].

The Soret effect is related to mass flow phenomena caused by heat diffusion, while the Dufour effect is tied to the energy flux generated by the solute difference. The Soret impact is used to cope with gas concentrations with lighter and medium molecular weights. The Soret and Dufour phenomena are used to transfer heat and mass in a variety of industrial and engineering applications, such as multicomponent melts in geosciences, groundwater pollutant migration, solidification of binary alloys, chemical reactors, space cooling, isotope separation, oil reservoirs, and mixtures of gases.An unsteady free convection slip flow of second grade fluid over an infinite heated inclined plate solved with Caputo-Fabrizio fractional derivativeis studied by Haq et al. [8].Hussanan et al. [9] explored the heat transfer from a Casson fluid to a non-linearly expanding sheet using Newtonian heating and the magneto hydrodynamic flow of that fluid. Ibrahim et al. [10] constructed a mathematical model for the investigation of mixed convection on MHD Casson fluid flow through a non-linearly permeable extended sheet with radiative, viscous dispersion, heat source/sink, chemical reaction, and suction. They also used the Buogiorno's type Nano-fluid form, which includes Brownian motion and thermophoresis. The impacts of radiation parameter and chemical reactions on time dependent MHD free convection flow in a porous plate were analyzed by Matta et al. [11].Mehta. et al. [12] discussed magnetohydrodynamics varied convective stagnation point stream with a vertically extended sheet embedded in a permeable material with generation/absorption, radiation impacts, and viscous dissipation. The MHD flow stalling at the point of Casson fluid across a non-linearly extending sheet with viscous dispersion was studied from Medicare et al. [13].The MHD flow and heat transmission of Casson nano particles across a non-linear (temperature variation throughout) stretchable sheet is studied by Mustafa et al. [14]. Mukhopadhyay, s. [15] explored a boundary layer investigation for non-Newtonian fluid flow and heat transport across a non-linearly stretchy sheet. The motion field is suppressed when the Casson constraint is rised. However, as the Casson parameter is enhanced, the temperature rises. In the existence of a chemical reaction, Naduvinamani et al.[16] explored the heat and mass transport characteristics of a time dependent MHD squeeze flow of Casson fluid between two parallel plates with viscous and Joule dissipation influences. Compress flow is affected by Soret and Dufour impacts, as well as radiation parameter and heat source/sink impacts are explored. Panigrahi et al. [17] assessed the effects of Soret and Dufour on the properties of heat and mass transport in a mixture Powell-Erying fluid boundary layer flow on a non-linear stretch sheet. In the existence of thermal radiation and chemical reaction, Reddy et al.[18] studied the time independent 2D MHD convective boundary layer flow of a Casson fluid over an increasingly slope porous stretchy sheet.

Aside from the flow caused by an unstable or steady extending/shrinking sheet, the influence of the buoyant force caused by the stretching sheets could not be ignored. The importance of thermal radiation with mixed convective boundary layer (BL) flow in geothermal engineering, space technology, and nuclear reactor cooling has increased interest in the topic.Singh et al. [19] investigate thin film flow of a third-grade fluid down a inclined planeusing an effective well organized computational scheme namely homotopy perturbation Elzaki transform method.Singh et al. [20] studied the local fractional linear transport equations (LFLTE) in fractal porous media.Sumalatha and Bandari [21] investigated the impact of radiation impact and heat source/sink on the flow across a non-linearly expanding sheet of Casson fluid. Sreedevi et al. [22] studied the convective heat and mass transport flow of an electrical conducting fluid over a porous vertically stretched sheet under the assorted property of the magnetic parameter, Joule heating, thermal radiation absorption, viscous dissipation, buoyancy forces, Soret, and Dufour. Tak et al. [23] examined the impressions of radiation parameter and magnetic impact on the heat and mass transport features of natural convection around an upright surface embedded in a dripping wet Darcian porous media, taking into account the Soret and Dufour impacts. Ullah et al. [24] explored the impact of slip effects on MHD free convection flow of non-Newtonian fluid across a non-linear stretched sheet wringing wet in porous media with Newtonian heating. Ullah et al. [25] investigated a time dependent mix convection flow of Casson fluid for a non-linear extending sheet with slip and convective boundary circumstances. Furthermore explored are the impacts of thermo-diffusion, diffusion-thermo, viscous dissipation, and heat Source/Sink. The flow and heat transport characteristics of a viscous fluid over a non-linear extending sheet are investigated through studied by Vajravelu, K. [26].

Basha, H. et al. [4] are investigated the Casson fluid flow natural convection viscous-elastic boundary layer in MHD over a non-linear stretched sheet with Joule and viscous dissipation impacts under chemical reaction influence in the presence of Lorentz forces. The current work fills the gap of Basha, H. et al. [4] by involving the Soret and Dufour impacts in existence of radiation parameter, and the numerical result discussed through graphs along with table using MATLAB software.

2 Problem Structure:

The current study examines the movement of 2D; time-independent, laminar, viscous, incompressible boundary layer carrying a MHD Non-Newtonian Casson fluid across a non-linear stretched sheet. Based on the geometry that is taken into consideration, the current physical condition is modeled. On the other hand, Figure 1 gives clear clarification of the measured problems flow configuration completed with all required criteria. The contemplated flow design is consistent with the $y = 0$ plane and stream are restricted to just $y > 0$. Still, exterior forces are used in combination with axial flow side in which the surface is enhanced and the origin is fixed. In order to clearly give details the problem, the authors also established a rectangular system where the y-direction is taken perpendicular to the stretchy surface and the x-coordinate is measured along the flow direction. Also, B_0 strength is applied to the Y-coordinate, as is seen in Fig. 1. Furthermore; the free flow velocity, thermal, and volume fraction are represented by U_∞, T_∞, and C_∞.

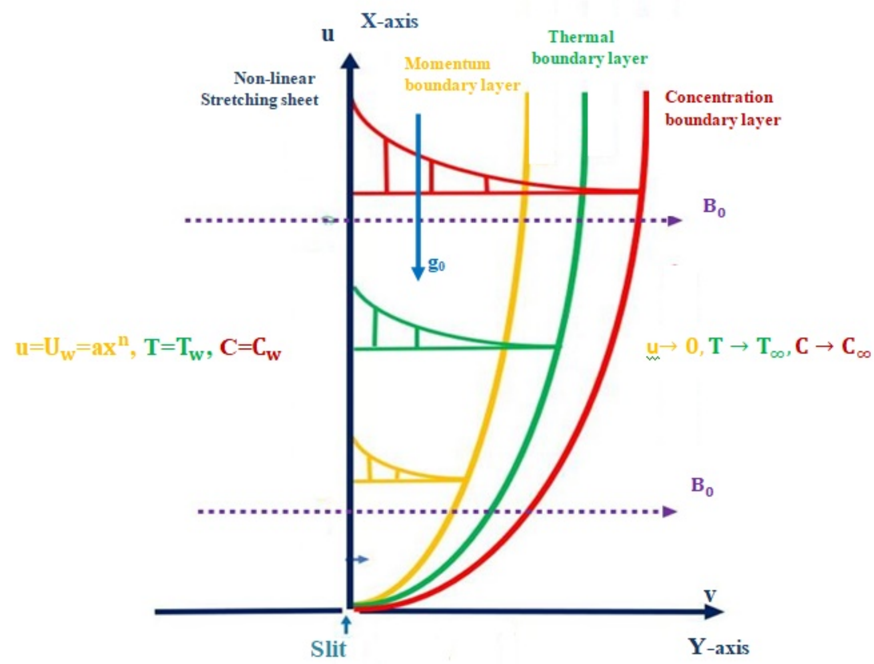

Figure 1: Physical structure and coordinate system of the topic under investigation.

The established equation of a Casson fluid is inscribed by used Ref [4], [7], [9], and [15]

$$\tau_{mn} = \begin{cases} 2(\mu_B + \frac{\tau_y}{\sqrt{2\pi}})e_{mn} & \text{if } \pi > \pi_c \\ 2(\mu_B + \frac{\tau_y}{\sqrt{2\pi}})e_{mn} & \text{if } \pi < \pi_c \ . \end{cases} \tag{1}$$

Where $\pi = e_{mn}e_{mn}$ and e_{mn} is the $(m,n)^{th}$ section of the rate of deformation, π is the multiple of the sections of defacement rate, π_c is critical worth of the multiply founded by the non-Newtonian fluid form, μ_B is the plastic movable viscosity of the non-Newtonian fluid and τ_y is the yield stress of the fluid.

The following criteria define the controlling relations for the proposed study Ref. [4], [17], [18]

$$\frac{\partial u}{\partial x} + \frac{\partial v}{\partial y} = 0, \tag{2}$$

4

$$u\frac{\partial u}{\partial x}+v\frac{\partial v}{\partial y}=\nu(1+\frac{1}{\beta})\frac{\partial^2 u}{\partial y^2}-\frac{\sigma {B_0}^2 u}{\rho}+g\beta_T(T-T_\infty)+g\beta_C(C-C_\infty), \tag{3}$$

$$u\frac{\partial T}{\partial x}+v\frac{\partial T}{\partial y}=\frac{k}{\rho c_p}\frac{\partial^2 T}{\partial y^2}+\frac{Q_0}{\rho c_p}(T-T_\infty)+\frac{\mu}{\rho c_p}(1+\frac{1}{\beta})(\frac{\partial u}{\partial y})^2+\frac{\sigma {B_0}^2 u^2}{\rho c_p}$$
$$-\frac{1}{\rho c_p}\frac{\partial q_r}{\partial y}+\frac{D_m K_T}{c_s c_p}\frac{\partial^2 C}{\partial y^2}, \tag{4}$$

$$u\frac{\partial C}{\partial x}+v\frac{\partial C}{\partial y}=D_m\frac{\partial^2 C}{\partial y^2}+\frac{D_m K_T}{T_m}\frac{\partial^2 T}{\partial y^2}-k_1(C-C_\infty). \tag{5}$$

Earlier, equations (2) to (5) are in paired form, $\beta=\mu_B\frac{\sqrt{2\pi_C}}{\tau_y}$ is a parameter for the Casson fluid. And motion factors are u and v. and ν denotes kinematic viscosity, β is a number of the shear thinning Casson fluid, σ shows the electro conductivity, B_0 signifies the magneto field strength, ρ symbol for the density, k denotes thermal conductivity, T pointed for temperature, Q_0 characterizes inside heat source (>0)/sink (<0) amount, C is the occurrence of concentration, D_m defines diffusivity, and k_1 shows the chemical reactive parameter, μ symbol for the dynamic viscosity, C_p represents for the specific heat capacity, C_s is the volume fraction susceptibility, g is the gravitational force, β_T and β_C are the coefficients of thermal and mass expansion. Where the non-linear stretchy surface speed is represented by the parameters a ($a>0$) and n. further the terms $\rho-\rho_\infty=-(\beta_T(T-T_\infty)+\beta_C(C-C_\infty))$ is buoyancy effects. Furthermore, the boundary-layer supposition suggests that corporally the conditions on a particular location are directly dependent upon those upstream. From a mathematical standpoint, the behavior of the system was converted from an elliptical to a parabola form, additionally; this change would significantly simplify the mathematical studies of the problem.

The limitations are composed by used Ref. [4]

$$u=u_w=ax^n,\ v=0,\ T=T_w,\ C=C_w,\ \ at\ y=0.$$
$$u\to 0, \qquad T\to T_\infty, \qquad C\to C_\infty, \qquad at\ \ y\to\infty. \tag{6}$$

the Roseland approximation of the radiation heat flow is defined by Ref. [18], [21]

$$q_r=\frac{-4\sigma}{3k^*}\frac{\partial T^4}{\partial y}, \tag{7}$$

Inscribe the T^4 as a linear connection of thermal with Taylor's series extension regarding expansion about T_∞ and deleting greater terms, we get

$$T^4\approx 4{T_\infty}^3 T-{T_\infty}^4. \tag{8}$$

In view of the similarity transformation, we change the dimensional governing equation into non-dimensional equations and similarity transformation are written as

$$u=ax^n f'(\eta), \qquad v=-x^{(n-1)/2}\sqrt{\frac{\nu a(n+1)}{2}}[f(\eta)+\frac{(n-1)}{(n+1)}\eta f'(\eta)], \tag{9a}$$

$$where \quad \eta = y\sqrt{\frac{a(n+1)}{2\nu}}x^{(n-1)/2}, \quad \theta(\eta) = \frac{T-T_\infty}{T_w-T_\infty}, \quad \phi(\eta) = \frac{C-C_\infty}{C_w-C_\infty}. \tag{9b}$$

With the help of equations (7) to (9b), equations (2) to (6) are diminished to the following regime with rejecting pressure gradient.

$$(1+\frac{1}{\beta})f''' = \frac{2n}{(n+1)}(f')^2 - ff'' + 2Mf' - G_T\theta - G_C\phi = 0, \tag{10}$$

$$((1+Nr))\theta'' + 2QPr\theta + Prf\theta' + (1+\frac{1}{\beta})PrEc(f'') + 2PrMEc(f')^2 + Dupr\phi'' = 0, \tag{11}$$

$$(1+ScSr)\phi'' + Scf\phi' - 2ScKr\phi = 0. \tag{12}$$

With suitable boundary circumstances

$$f(0)=0, \quad f'(0)=1, \quad \theta(0)=1, \quad \phi(0)=0, \quad at \;\; \eta=0. \tag{13a}$$

$$f'(\infty)\to 0, \quad \theta(\infty)\to 0, \quad \phi(\infty)\to 0, \quad at \;\; \eta\to\infty. \tag{13b}$$

Where,M shows the magnetic parameter or Hartman number $M = \frac{\sigma B^2(0)}{\rho a(n+1)x^{n-1}}$, G_T and G_C represent the local Temperature Grashof number $G_T = \frac{g\beta_T(T_w-T_\infty)}{a^2x^{2n-1}\frac{(n+1)}{2}}$ and local Concentration Grashof number $G_C = \frac{g\beta_C(C_w-C_\infty)}{a^2x^{2n-1}\frac{(n+1)}{2}}$ respectively, Pr shows the Prandtl number $Pr = \frac{\nu\rho C_p k}{}$, Nr denotes the Radiation parameter $Nr = \frac{16\sigma {T_\infty}^3}{3kk^*}$, Ec denotes the Eckert number $Ec = \frac{a^2x^{2n}}{c_p(T_w-T_\infty)}$, Du specifies the Dufour number $Du = \frac{D_mK_T(C_w-C_\infty)}{c_sc_p\nu(T_w-T_\infty)}$, Sc denotes the Schmidt number $Sc = \frac{\nu}{D_m}$, Sr represents the Soret number $Sr = \frac{D_mK_T(C_w-C_\infty)}{T_m\nu(T_w-T_\infty)}$, β denotes the non-Newtonian Casson parameter$\beta = \mu_B\frac{\sqrt{2\pi_C}}{\tau_y}$, Kr shows that the chemical reaction $Kr = \frac{K_1}{a(n+1)x^{n-1}}$, where K_1 stands for porosity parameter$K_1 = \frac{\nu}{kc}$, and Q denotes the heat sorce sink $Q = \frac{Q_0}{\rho ac_px^{n-1}}$.

Physical Quantities:

Skin Friction Coefficient Cf_x: The physical amount Skin friction Cf_x that getsup due to the viscous stretch in the surroundings of the plate is well-defined as

$$Cf_x = \frac{\tau_w}{\rho u_w^2}, \;\; where \;\; \tau_w = (\mu_B + \frac{\tau_y}{\sqrt{2\pi}})(\frac{\partial u}{\partial y})_{y=0}. \tag{14}$$

Heat Transfer Coefficient: The dimensionless Nusselt number(Nu_x) is specified by

$$Nu_x = \frac{xq_w}{k(T_w-T_\infty)}, \;\; where \;\; q_w = -k(\frac{\partial T}{\partial y})_{y=0}. \tag{15}$$

Mass Transmission factor: The amount of mass transport is resulting through a Sherwood parameter (Sh_x) which is assumed by

$$Sh_x = \frac{xq_m}{D_m(C_w-C_\infty)}, \;\; where \;\; q_m = -D_m(\frac{\partial C}{\partial y})_{y=0}. \tag{16}$$

Here τ_w denotes the shear stress along with the shrinkage wall, q_w signifies heat flux, and q_m is mass transmission quantity at wall.

Therefore, in terms of Equations (9a) to (9b), the following non-dimensional quantities are obtained:

$${Re_x}^{1/2}Cf_x = (\frac{n+1}{2})^{1/2}(1+\frac{1}{\beta})f''(0),$$

local Nusselt

$$Re_x^{-1/2} Nu_x = -(\frac{n+1}{2})^{1/2} \theta'(0),$$

local Sherwood

$$Re_x^{-1/2} Sh_x = -(\frac{n+1}{2})^{1/2} \phi'(0). \tag{18}$$

Where, $Re_x = \frac{u_w x}{\nu}$ is the local Reynolds number, Cf_x is Skin Friction coefficient, Nu_x is Nusselt number, Sh_x is Sherwood parameter,τ_w indicates the wall shear stress, k signifies the thermo nano-fluid conductivity, q_w shows the surface heat flux, and q_m directs the surface mass flux.

We resolve the reduced equations (10) to (12) with limit conditions (13a) and (13b) via BVP4C method.

3 Results and Discussion:

The current research attempts to provide a fundamental physical understanding and industrial level practical significance of the subject under consideration. The rheological equations (10 to 13b)are solved numerically with the BVP4C with rheological quantities heat source/sink parameter, generative/destructive, chemical reactive parameter, transverse magnetic impact, thermal diffusivity, viscous dissipation, chemical reaction, radiation parameter, Dufour and Soret effect.Such as n,G_c,G_T, β, M, Ec, Pr, Kr,Nr,Sr,Q,Du, and Sc.For existing study, The Fig. of different parameters is designed with the service of MATLAB software and shown in Fig. 2 to Fig.25. Fig. (2-4) presents how the effects of β on flow sensibility, temperature, and mass transport characteristics. Additionally, the impacts of β on the dominant motion profile are also seen in Figure 2. The flow velocity in the domain of the solution under consideration is significantly reduced by the increasing under the impression of the magnetic and non-linear stretchy parameters, like shown in Figure 2.Flow velocities are decreased for increasingβ because an enhance in β rises the dynamic viscosity when stresses are present, that significantly increases the resistance to the movement of fluid near the wall. Therefore, flow velocity was decreased.Figure 3 also displays the effect ofβ thermal dispersion. This figure shows that the thermal graph decomposes as β rises. The thermal layer is also seen to be thinning.The temperature profile drops to zero until it is close to the surface.Like this, Figure 4 depicts the effect of the Casson fluid parameter on the mass distribution field.The concentration distribution increases near the stretching surface as β increases. Greater β values result in stronger molecular scale contacts, which increase molecular mobility and, ultimately, enhance the fluid's mass distribution. A thicker concentration boundary layer is subsequently observed.Figure 5 shows that the thermal distribution enlarges at greater values of the Dufour impact Du. this can be decoded that rise in the Dufour effect Du, which reason an enhancement in the concentration gradient and a faster rate of mass diffusion. The rate of heat transport associated to the particles rises as an outcome. The thermal profiles improve as a result. Velocity and Temperature decreases with increasing Eckert parameter Ec which is shown in Fig.-6 and 7, respectively. The purpose of Figs. 8 and 9 is to see how local concentration (local concentration Grashof number G_c) affects velocity and concentration. As G_c rises, an enhancement in fluid velocity is seen. As G_c increases, the buoyant force increasingly outweighs the viscous force. As a result, the Grashof number improves fluid flow, raising both the velocity and thickness of the motion barrier layer.Additionally, since the buoyancy force tends to make the concentration gradient higher, the concentration is reduced.

Fig.10-12 shows that the influence of local temperature Grashof number G_T on motion, thermal and volume fraction. For the decrease in the thickness of the boundary layer the motion reduces with rising values of the local temperature Grashof effect. For increasing the local temperature Grashof parameter, the thermal and volume fraction profiles decrease. This decrease in temperature and concentration profiles is primarily caused by the fact that raising the local temperature uses more energy and causes more heat to flow to the surrounding fluid, which lowers the thermal and volume fraction profiles. Figure 13 shows that the mass distribution degraded at increasing Kr parameters. This decline in Solutal graph is mostly caused by the increased mass distribution that also reduces the concentration distribution. The decreased velocity profile for the increasing Magnetic field M values is depicted in Fig. 14. The resistance grows as the Lorentz forces increase, which causes the velocity distribution close to the surface to flatten. Additionally, for an increasing magnetic impact in the flow field, the factor of the velocity distribution along the axial side decrease to nil at a greater distance from a given point. Consequently, when the magnetic field increased, the velocity field degraded. Figures 15 and 16 explain the impact magnetic parameter M has on thermal and volume fraction flow formulation. The temperature distribution increased for the growing magnetic field M, as seen in Figure 15. Based to the fluid's Joule heating, the temperature field grows as the magnetic field rises since more thermal energy will be liberated into the fluid as an outcome. Even as flexibility stress parameter lowers due to an enhance in the magnetic parameter, the thermal field is augmented in the fluid flow under consideration. Figure 16 also shows how the magnetic field affects the concentration profile. The concentration distribution is seen to react as a decreasing function of magnetic number in this graph.

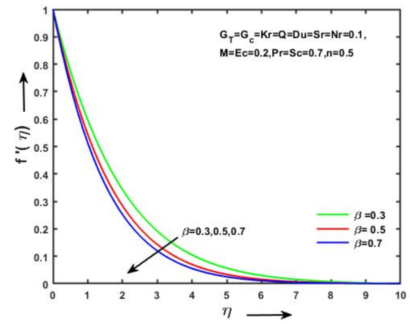

Figure 2: Motion formulation of Casson fluid parameter β.

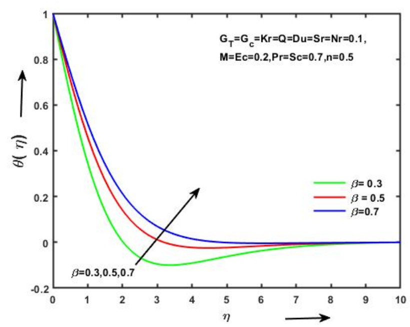

Figure 3: Thermal formulation of Casson fluid parameter β.

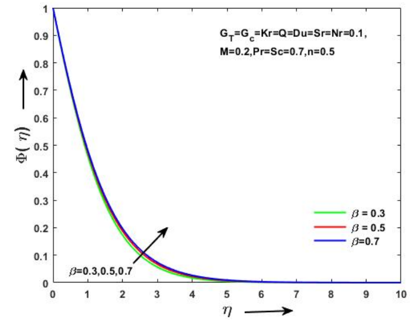

Figure 4: Concentration formulation of Casson parameter β.

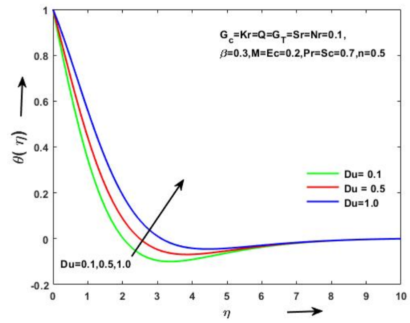

Figure 5: Temperature formulation of Dufour effect Du.

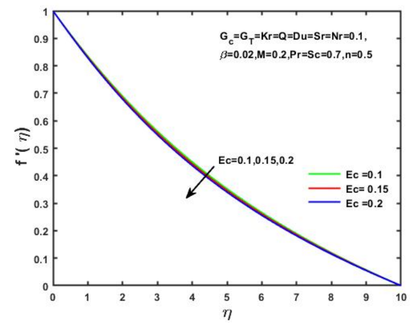

Figure 6: Velocity formulation of Eckert number Ec.

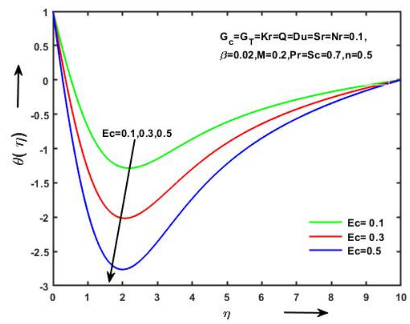

Figure 7: Temperature formulation of Eckert number Ec.

9

Figures (17–19) show how non-linear stretched parameters affect velocity, temperature, and concentration distribution behavior. Figures 17 illustrate how the expanding stretching variable reduces flow velocity. Additionally, at higher n numbers, this decrease in $f^{'}(\eta)$ is quite small. Since $\frac{2n}{n+1}$ is the coefficient in Equation (10) approaches 2 when $n > 1$, and an outcome the velocity profile is reduced. Additionally, the non-linear parameter n causes the velocity profile to be more disconnected. Furthermore, at a greater distance from the fixed value, the velocity profile monotonically decreased to zero. Figures 18 and 19 show, correspondingly, how the non - linear stretched parameter affects thermal and volume fraction profiles. The thermal and Solutal curves are magnified for the enhancing non - linear parameter n, as shown in Figures 18 and 19. Additionally, at a greater distance from the object, temperature and concentration exponentially decrease to zero. Also, as the non - linear stretched number n increases, the temperature and concentration boundary regions get thicker. As seen in figure.20, temperature is rising as the radiation parameter Nr and the boundary layer thickness it depends on both grow. This is because a rise in the radiation parameter heats the fluid more, which raises the temperature and thickens the layer of thermal boundaries

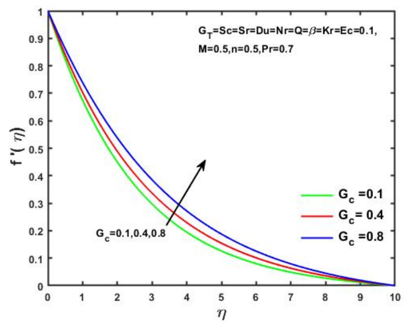

Figure 8: Velocity formulation of concentration Grashof number G_c.

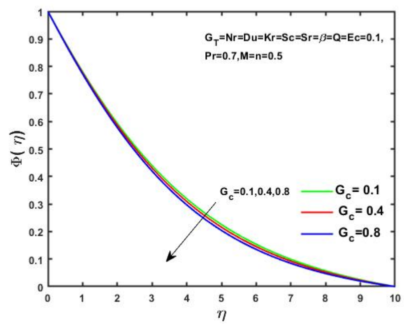

Figure 9: Concentration formulation of concentration Grashof number G_c.

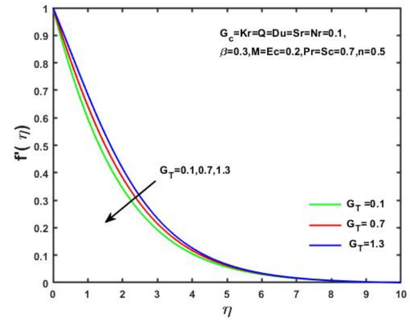

Figure 10: Velocity formulation of local thermal Grashof number G_T.

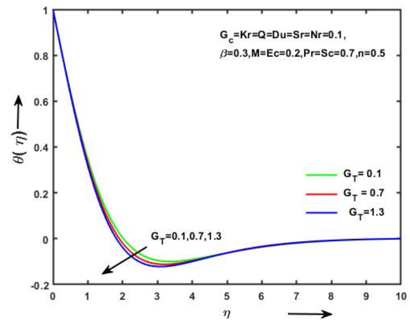

Figure 11: Temperature formulation of local thermal Grashof number G_T.

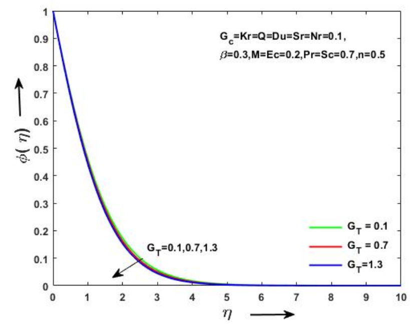

Figure 12: Concentration formulation of local thermal Grashof number G_T.

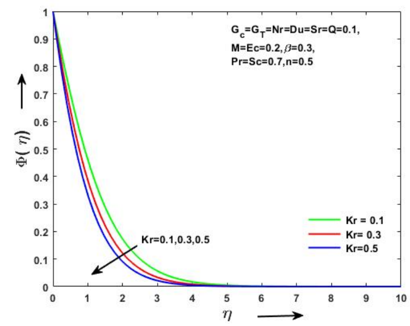

Figure 13: Concentration formulation of chemical reaction parameter Kr.

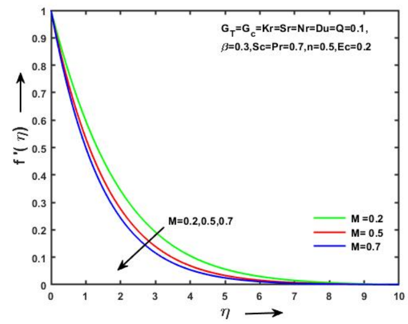

Figure 14: Velocity formulation of magnetic impact M.

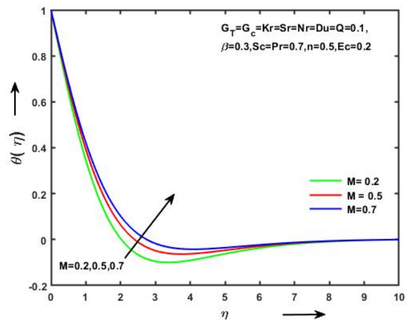

Figure 15: Temperature formulation of magnetic impact M.

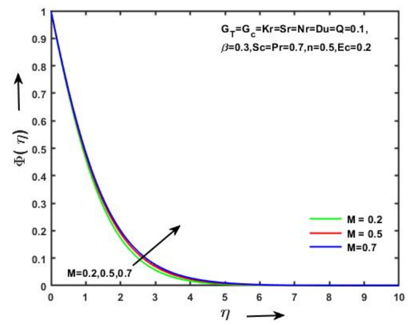

Figure 16: Volume fraction of magnetic impact M.

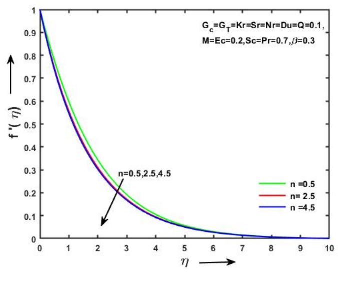

Figure 17: Motion formulation of the nonlinear parameter n.

12

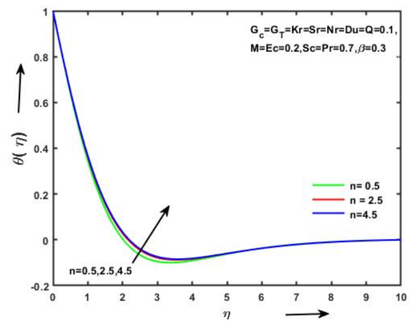

Figure 18: Temperature formulation of the nonlinear parameter n.

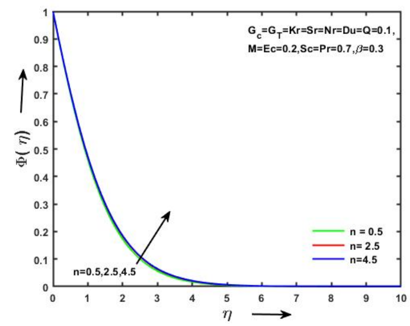

Figure 19: Concentration formulation of the nonlinear parameter n.

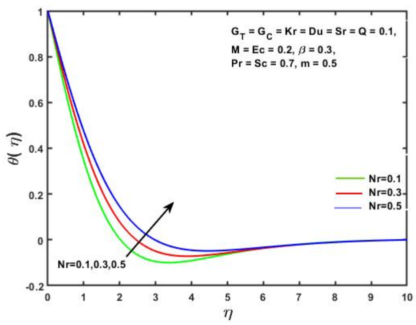

Figure 20: Temperature formulation of the Radiation parameter Nr.

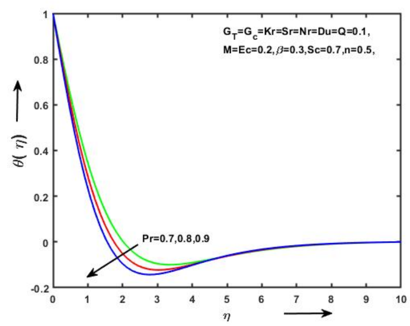

Figure 21: Temperature formulation of the Prandtl parameter Pr.

13

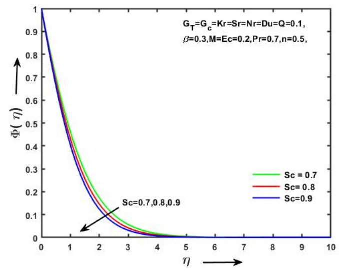

Figure 22: Concentration formulation of the Schmidt parameter Sc.

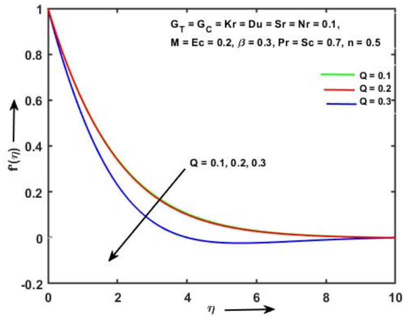

Figure 23: Motion formulations of Heat source sink Q.

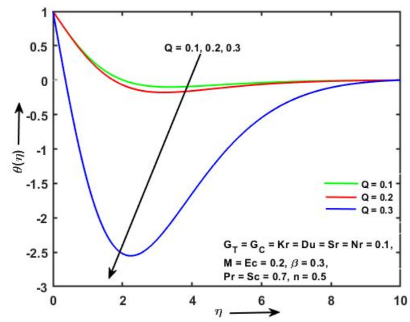

Figure 24: Temperature formulations of Heat source sink Q.

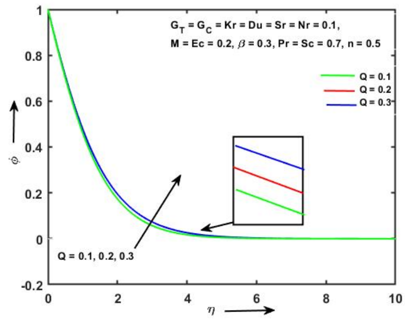

Figure 25: Concentration formulations of Heat source sink Q.

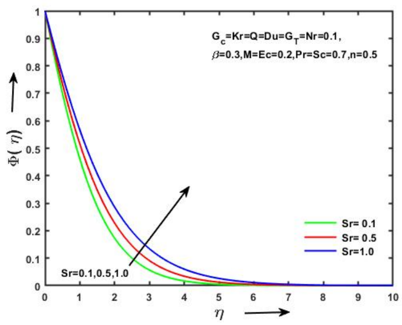

Figure 26: Concentration formulation of Soret effect Sr.

The impact of the thermal graph is displayed in Fig. 21 for various Prandtl number Pr quantities. Temperature distribution is shown to reduce for increasing in this analysis. Physically, Prandtl parameter Pr affects the thickness of the thermal boundary layer and momentum boundary layers. A larger Prandtl number denotes a thickness of the thermal boundary layer that is thinner, maintaining the boundary layer's uniform thermal distribution. The heating-boundary layer is subordinated to the magneto hydrodynamic boundary layer. Heat can dissipate more quickly in reduced Prandtl parameter fluids than in highest Prandtl parameter fluids according to their higher thermal conductivities. The impact of Schmidt parameter Sc on the dispensation of concentrations is shown in Fig.22. The volume fraction field reduces with rising Schmidt number Sc. Schmidt number, though it is constantly connected to velocity and mass diffusivities. Therefore, the fluid concentration diffusion is suppressed by rising values of Schmidt parameter Sc. In Figure 23, the motion profile reduces with the enhancing value of heat source or sink Q. Figure 24 shows how heating source or sink parameter Q affects temperature. The figure shows that as the heat sink's power rises, the non - dimensional temperature lowers, even as the heat source's power rises, the temperature rises. Therefore, as the heat sink parameter is raised, the thermal boundary layer reduces thickness, whereas the heat source effect causes it to rise. Also Fig.25 denotes the increasing concentration profile with the increasing value of heat source or sink Q. Figure 26 provided a visual representation of the consequences of thermal migration or Soret number (Sr). Sr represents the mass transfer rate between lowest to the highest solute concentrations and is essentially a ratio of temperature gradient to concentration. Figure 26 show that the concentration profile is exhibiting a rising behavior along with the rising value of Sr.

Table I: Impression of parameters of notice on skin friction, Nusselt parameter, and Sherwood parameter:

n	G_T	G_C	β	M	Pr	Ec	Sc	Q	Du	Sr	Nr	Kr	$Cf_xRe_x{}^{1/2}$	$-Nu_xRe_x{}^{-1/2}$	$-Sh_xRe_x{}^{-1/2}$
0.5													**-1.85657**	**0.65240**	**0.55783**
2.5	**0.1**	**0.1**	**0.3**	**0.2**	**0.7**	**0.2**	**0.7**	**0.1**	**0.1**	**0.1**	**0.1**	**0.1**	**-2.23135**	**0.65017**	**0.54858**
4.5													**-2.3244**	**0.64932**	**0.54636**
	0.1												**-1.85657**	**0.6524**	**0.55783**
0.5	**0.7**												**-1.59447**	**0.65546**	**0.56157**
	1.3												**-1.33728**	**0.65742**	**0.56520**
			0.3										**-1.85657**	**0.652401**	**0.557836**
	0.1		**0.7**										**-1.43724**	**0.535531**	**0.5621336**
			0.7										**-1.44060**	**0.482280**	**0.5611931**
				0.2									**-1.85657**	**0.652401**	**0.557836**
			0.3	**0.5**									**-2.33732**	**0.928422**	**0.508645**
				0.7									**-2.05587**	**0.571925**	**0.545825**

16

					0.7								-1.85657	0.652401	0.55783
				0.2	0.8								-1.48080	0.727980	.561245
					0.9								-1.53126	0.79666	0.5589154
						0.1							-10.18979	2.044867	0.594878
			0.02		0.7	0.3							-26.32619	10.6900	0.507348
						0.5							-33.7957	18.38017	0.4583266
							0.7						-1.85657	0.652401	0.557836
			0.3			0.2	0.8						-2.01032	0.925019	0.558312
							0.9						-1.42483	0.648136	0.558312
								0.1					-1.85657	0.652401	0.557836
							0.7	0.2					-1.463515	0.626327	0.56106
								0.3					-1.63419	0.691826	0.551289
									0.1				-1.856577	0.652401	0.557836
								0.1	0.5				-1.9724632	0.809687	0.515012
									1				-1.222268	0.336784	0.573077
										0.1			-1.85657	0.652401	0.557836
									0.1	0.5			-1.419446	0.663674	0.494086
										1			-2.0097	0.948055	0.3811412
											0.1		-1.856577	0.652401	0.557836
										0.1	0.3		-1.34829	0.577117	0.56761
											0.5		-1.283884	0.51627	0.570809
												0.1	-1.856577	0.652401	0.557836
											0.1	0.2	-1.42427	0.6509020	0.64566
												0.3	-1.425672	0.645687	0.7180935
		0.1											-3.678953	0.75017	0.200603
		0.4	0.1	0.5		0.1	0.1					0.1	-3.2968876	0.7372915	0.20394816
		0.8											-2.803422	0.720553	0.208056

Table II: validate the current values of various physical parameters to previouslyresults of Basha et al. Ref. [3] andVajraveluk. Ref. [21] respectively.

		Vajraveluk.Ref[21]		Basha et al. Ref. [3]		current values	
n	Pr	$f''(0)$	$\theta'(0)$	$f''(0)$	$\theta'(0)$	$f''(0)$	$\theta'(0)$
1	0.71	-1.0000	-0.4590	-1.00005468353233	-0.45908783553	-1.00001	-0.459033
5	0.71	-1.1945	-0.4394	-1.19449559110388	-0.4395495710690	-1.1945	-0.4394
10	0.71	-1.2348	-0.4357	-1.23488263663213	-0.4356401511209	-1.23488	-0.435641
1	7	-1.0000	-1.8953	-1.00005468353233	-1.8953100096284	-1.00001	-1.89541
5	7	-1.1945	-1.8610	-1.19449559110388	-1.8609911518168	-1.1945	-1.86159
7	7	-1.2348	-1.8541	-1.23488263663213	-1.8540100137230	-1.23488	-1.85464

4 Conclusion:

From the current study we conclude that the mathematical outcomes for diverse physical quantities have been dissolved. The effects of the transfer of mass and heat including Soret and Dufour effects, heat absorption/ generation, Radiation parameter, chemical reaction, have been expressed for a non-linear stretchy surface in the rheology.This problem can be solved for future purpose if sheet is inclined at some angle. The boundary conditions and fluids can also be changed. The ending conclusion is

- An increasing value of Soret effect, grow the concentration of the fluid. And an increasing value of Heat source/ sink, also enhancing the concentration of the fluid

- Temperature profile is increased for an increasing value of Dufour effect
- Motion and thermal profiles of the fluid are decreased due to increased Heat source/sink
- Temperature profile of the fluid is increased when raised thermal radiation
- Motion and thermal profiles of the fluid are decreased due to enhanced Eckert number
- The decreasing skin-friction rate impression is seen for radiation parameters
- For the Soret effect, the diminishing Sherwood parameter impression is observed

References

[1] Ebrahem A Algehyne, Musaad S Aldhabani, Anwar Saeed, Abdullah Dawar, and Poom Kumam. Mixed convective flow of casson and oldroyd-b fluids through a stratified stretching sheet with nonlinear thermal radiation and chemical reaction. *Journal of Taibah University for Science*, 16(1):193–203, 2022.

[2] Sameh E Ahmed, MA Mansour, A Mahdy, and Shadia S Mohamed. Entropy generation due to double diffusive convective flow of casson fluids over nonlinearity stretching sheets with slip conditions. *Engineering Science and Technology, an International Journal*, 20(6):1553–1562, 2017.

[3] Mushtaq Ahmad, Muhammad Imran Asjad, and Jagdev Singh. Application of novel fractional derivative to heat and mass transfer analysis for the slippage flow of viscous fluid with single-wall carbon nanotube subject to newtonian heating. *Mathematical Methods in the Applied Sciences*, 2021.

[4] Hussain Basha, Naresh Kumar Nedunuri, Gudala Janardhana Reddy, and Sreenivasulu Ballem. Thermal analysis of buoyancy-motivated casson fluid flow with time-independent chemical reaction under lorentz forces. *Heat Transfer*, 50(7):7291–7320, 2021.

[5] Hussain Basha, Sreenivasulu Ballem, G Janardhana Reddy, Harish Holla, and Mikhail A Sheremet. Buoyancy-motivated dissipative free convection flow of walters-b fluid along a stretching sheet under the soret effect and lorentz force influence. *Heat Transfer*, 51(4):3512–3539, 2022.

[6] Subrata Das, Hiranmoy Mondal, Prabir Kumar Kundu, and Precious Sibanda. Spectral quasi-linearization method for casson fluid with homogeneous heterogeneous reaction in presence of nonlinear thermal radiation over an exponential stretching sheet. *Multidiscipline Modeling in Materials and Structures*, 2018.

[7] K Gangadhar, R Edukondala Nayak, and M Venkata Subba Rao. Buoyancy effect on mixed convection boundary layer flow of casson fluid over a non linear stretched sheet using the spectral relaxation method. *International Journal of Ambient Energy*, 43(1):1994–2002, 2022.

[8] Sami Ul Haq, Saeed Ullah Jan, Syed Inayat Ali Shah, Ilyas Khan, and Jagdev Singh. Heat and mass transfer of fractional second grade fluid with slippage and ramped wall temperature using caputo-fabrizio fractional derivative approach. *AIMS Mathematics*, 5(4):3056–3088, 2020.

[9] Abid Hussanan, Mohd Zuki Salleh, Hamzeh Taha Alkasasbeh, and Ilyas Khan. Mhd flow and heat transfer in a casson fluid over a nonlinearly stretching sheet with newtonian heating. *Heat transfer research*, 49(12), 2018.

[10] SM Ibrahim, G Lorenzini, P Vijaya Kumar, and CSK Raju. Influence of chemical reaction and heat source on dissipative mhd mixed convection flow of a casson nanofluid over a nonlinear permeable stretching sheet. *International Journal of Heat and Mass Transfer*, 111:346–355, 2017.

[11] Sweta Matta, Appidi L BalaSidduluMalga, and P Pramod Kumar. Radiation and chemical reaction effects on unsteady mhd free convention mass transfer fluid flow in a porous plate. *Indian Journal of Science and Technology*, 14(8):707–717, 2021.

[12] Ruchika Mehta, Ravindra Kumar, Himanshu Rathore, and Jagdev Singh. Joule heating effect on radiating mhd mixed convection stagnation point flow along vertical stretching sheet embedded in a permeable medium and heat generation/absorption. *Heat Transfer*, 51(8):7369–7386, 2022.

[13] Monica Medikare, Sucharitha Joga, Kishore Kumar Chidem, et al. Mhd stagnation point flow of a casson fluid over a nonlinearly stretching sheet with viscous dissipation. *American Journal of Computational Mathematics*, 6(01):37, 2016.

[14] M Mustafa and Junaid Ahmad Khan. Model for flow of casson nanofluid past a non-linearly stretching sheet considering magnetic field effects. *AIP advances*, 5(7):077148, 2015.

[15] Swati Mukhopadhyay. Casson fluid flow and heat transfer over a nonlinearly stretching surface. *Chinese Physics B*, 22(7):074701, 2013.

[16] NB Naduvinamani and Usha Shankar. Thermal-diffusion and diffusion-thermo effects on squeezing flow of unsteady magneto-hydrodynamic casson fluid between two parallel plates with thermal radiation. *Sādhanā*, 44(8):1–16, 2019.

[17] Satyaban Panigrahi, Motahar Reza, and Akshya Kumar Mishra. Mixed convective flow of a powell-eyring fluid over a non-linear stretching surface with thermal diffusion and diffusion thermo. *Procedia Engineering*, 127:645–651, 2015.

[18] P Bala Anki Reddy. Magnetohydrodynamic flow of a casson fluid over an exponentially inclined permeable stretching surface with thermal radiation and chemical reaction. *Ain Shams Engineering Journal*, 7(2):593–602, 2016.

[19] Jagdev Singh, Devendra Kumar, Dumitru Baleanu, et al. A hybrid analytical algorithm for thin film flow problem occurring in non-newtonian fluid mechanics. *Ain Shams Engineering Journal*, 12(2):2297–2302, 2021.

[20] Jagdev Singh, Devendra Kumar, and Sunil Kumar. An efficient computational method for local fractional transport equation occurring in fractal porous media. *Computational and Applied Mathematics*, 39(3):1–10, 2020.

[21] Chenna Sumalatha, Shankar Bandari, et al. Effects of radiations and heat source/sink on a casson fluid flow over nonlinear stretching sheet. *World Journal of Mechanics*, 5(12):257, 2015.

[22] Gandluru Sreedevi, DRV Rao, Oluwole Daniel Makinde, and G Reddy. Soret and dufour effects on mhd flow with heat and mass transfer past a permeable stretching sheet in presence of thermal radiation. 2017.

[23] Shyam Sunder Tak, Rajeev Mathur, Rohit Kumar Gehlot, and Aiyub Khan. Mhd free convection-radiation interaction along a vertical surface embedded in darcian porous medium in presence of soret and dufour's effects. *Thermal Science*, 14(1):137–145, 2010.

[24] Imran Ullah, Sharidan Shafie, and Ilyas Khan. Effects of slip condition and newtonian heating on mhd flow of casson fluid over a nonlinearly stretching sheet saturated in a porous medium. *Journal of King Saud University-Science*, 29(2):250–259, 2017.

[25] Imran Ullah, Ilyas Khan, and Sharidan Shafie. Soret and dufour effects on unsteady mixed convection slip flow of casson fluid over a nonlinearly stretching sheet with convective boundary condition. *Scientific Reports*, 7(1):1–19, 2017.

[26] K Vajravelu. Viscous flow over a nonlinearly stretching sheet. *Applied mathematics and computation*, 124(3):281–288, 2001.

J. COMPUTATIONAL ANALYSIS AND APPLICATIONS, VOL. 31, NO. 2, 2023, COPYRIGHT 2023 EUDOXUS PRESS, LLC

M/M/1 Retrial Queueing Model with Server Breakdown and Feedback

M.SEENIVASAN,
Mathematics Wings - DDE, Annamalai University,
Annamalainagar-608002, India.
Email: emseeni@yahoo.com
J.SHINY EPCIYA,
Department of Mathematics, Annamalai University,
Annamalainagar-608002, India.
Email: epciyashinydoss@gmail.com

December 28, 2022

In this article, we present M/M/1 retrial queueing system with feedback and Server breakdown. Arrival follows Poisson process. An arrival finds the system is full, the arrival enters into an orbit of size infinity. From the orbit the customers try their luck. The time between two successive retrials is called retrial time, it follows negative exponential distribution. Service time is exponentially distributed. Once the server experiences an unanticipated failure, it should be repaired and returned to normal functioning. Feedback is when unsatisfied customers join the orbit again for a service. Matrix geometric method is engaged to determined performance measures. Some graphical representations are also acquired.

AMS subject classification number— 90B22, 60K30 and 60K25
Key Words —- Retrial Queue, Arrival Rate, Server Breakdown, Feedback, Matrix Geometric Method (MGM).

1 Introduction

Queueing model can be found in variety of real-life scenarios. Queueing system with feedback have several uses in the manufacturing, computing and telecommunications systems. In queueing theory in which customer arrives who finds the sever and waiting places are engaged, may retry after an irregular measurement of time is known as retrial queue. During the period of getting service the server may get sudden breakdown and send to repair, at that time the customer wait to get complete service. After getting a service the customer has to decide to leave the system or to continue the service. The unsatisfied customer goes to the orbit for another service is called feedback. Artalejo (2012) determined M/M/1 retrial queue with finite population. A survey of retrial queues was explored by Falin (1990). M/M/1 retrial queueing system with variable service rates in priority service was analyzed by Ayyappan Govindan et al (2011). Neuts (1981) discussed several matrix geometric stochastic model solutions. Praveen Deora et al (2021) analyzed the cost analysis and optimization of machine repair model with working vacation and feedback policy.

This model has been investigated by Choi, et al (1998) analyzed multi-server retrial queue with feedback and loss. Choi and Kulkarni (1992) explored feedback retrial queueing model. Chuen-Horng Lin and Jau-Chuan Ke (2011) determined multi server retrial queue with loss and feedback. Retrial queue with server breakdown has been investigated by Kalyanaraman and Seenivasan (2011) analyzed multi-server retrial queue with breakdown and geometric loss. Seenivasan et al investigated different type of queueing models and their characteristics behavior. With the help of that research criteria we developed the concept using in retrial queueing model.

Following is an overview of the remaining sections of this article. Construction of our model is presented in section 2. Section 3 includes some numerical examples. Section 4 describes the system performance measures, as well as the summary follows in the end part of this article. [1]

2 Construction of the model

In this article, we concentrated on retrial queue with server breakdown and Feedback. Arriving customer follows Poisson process with rate λ. Assuming that the server is free, the incoming customer will be served instantly, and if the server is occupied, he will joining the orbit. After certain uneven estimations of time, customers from orbit attempt their luck. In retrial, each customer is viewed as equivalent to a primary customer. The retrial time is exponentially distributed with rate ν. The service time is exponential distributed with service rate μ. Eventually when the server could open to unforeseen breakdown with rate α and after it ought to be fixed and goes to normal service with rate ϕ. Server will wait unless there is no queue at the ending of the vacation. Assuming that the served customer decide to leaves the framework forever with rate $\beta^{'} = (1-\beta)$ (or) he rejoins the orbit again for another service at a rate β (it is called feedback). Our model's transition diagram is depicted in (Figure. 1).

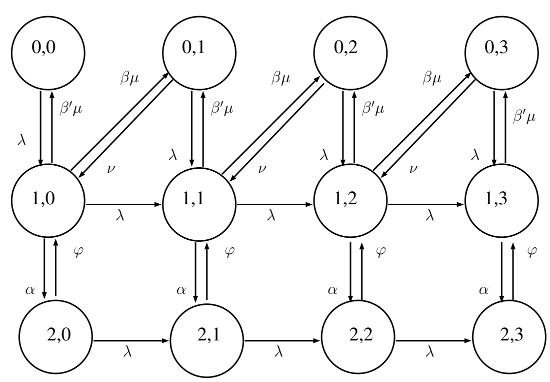

[1]Corresponding Author: M.Seenivasan, Mathematics Wings - DDE, Annamalai University, Annamalainagar - 608002, Tamilnadu, India.
Email: emseeni@yahoo.com

2

Figure 1. Transition Diagram

Let $A(t), B(t) : t \geq 0$ be a stochastic process with state space at time t,
A(t) = 0, server is idle,
A(t) = 1, server is working,
A(t) = 2, server gets breakdown.
B(t) indicates no. of customers in the orbit.
Lexicographical series is given by:
$\Omega = (0,0)U(1,0)U(i,j); i = 0,1, j = 1,2, ..., n \geq 1$
Infinitesimal generated matrix Q:

$$Q = \begin{pmatrix} K_{00} & L_{00} & \cdots & \cdots & \cdots & \cdots & \cdots & \cdots \\ N_{00} & M_{00} & L_{00} & \cdots & \cdots & \cdots & \cdots & \cdots \\ 0 & N_{00} & M_{00} & L_{00} & \cdots & \cdots & \cdots & \cdots \\ 0 & \cdots & N_{00} & M_{00} & \cdots & \cdots & \cdots & \cdots \\ 0 & \cdots & \cdots & N_{00} & \cdots & \cdots & \cdots & \cdots \\ \cdots & \cdots & \cdots & \cdots & \cdots & \cdots & \cdots & \cdots \end{pmatrix}$$

Where

$$K_{00} = \begin{pmatrix} -(\lambda) & \lambda & 0 \\ \beta' \mu & -(\lambda+\alpha+\mu) & \alpha \\ 0 & \varphi & -(\lambda+\varphi) \end{pmatrix}; \; L_{00} = \begin{pmatrix} 0 & 0 & 0 \\ \beta\mu & \lambda & 0 \\ 0 & 0 & \lambda \end{pmatrix};$$

$$N_{00} = \begin{pmatrix} 0 & \nu & 0 \\ 0 & 0 & 0 \\ 0 & 0 & 0 \end{pmatrix}; \; M_{00} = \begin{pmatrix} -(\lambda+\nu) & \lambda & 0 \\ \beta' \mu & -(\lambda+\alpha+\mu) & \alpha \\ 0 & \varphi & -(\lambda+\varphi) \end{pmatrix};$$

We define $\pi_{ij} = \{A = i, B = j\}$=$\lim_{t\to\infty} Pr\{A(t) = i, B(t) = j\}$, where j indicates no. of customers in the orbit & i indicates the server state.
From the balance equation $\Pi Q = 0$. (1)
$\pi_0 K_{00} + \pi_1 N_{00} = 0$ (2)
$\pi_0 L_{00} + \pi_1 M_{00} + \pi_2 N_{00} = 0$ (3)
$\pi_1 L_{00} + \pi_2 M_{00} + \pi_3 N_{00} = 0$ (4)
.
.
.
$\pi_i L_{00} + \pi_{i+1} M_{00} + \pi_{i+2} N_{00} = 0$ (5)
And $\pi_j = \pi_0 R^j$ for$j \geq 1$. (6)
We can assuming that R is a rate matrix.
$\pi_0[K_{00} + RN_{00}] = 0$ (7)
$\pi_0[R^2 N_{00} + RM_{00} + L_{00}] = 0$ (8)
The normalizing condition is
$\Pi_0 \,[I-R]^{-1}\, e = 1$ (9)
'e' is a column vector with all elements equal to 1.
Π partitioned as $\Pi = (\Pi_0, \Pi_1, \Pi_2)$ is a static prob. vector of the (reducible) generator matrix is $D = L_{00} + M_{00} + N_{00}$.

$$D = \begin{pmatrix} -(\lambda+\nu) & (\lambda+\nu) & 0 \\ \mu & -(\mu+\alpha) & \alpha \\ 0 & \varphi & -\varphi \end{pmatrix} \tag{10}$$

And Π could be displayed to be stationary in order that $\Pi D = 0$ & $\Pi e = 1$.

$$\Pi_0 = [1 + \frac{\lambda+\nu}{\mu} + \frac{\alpha(\lambda+\nu)}{\varphi\mu}]^{-1}; \Pi_1 = \frac{\lambda+\nu}{\mu}\Pi_0; \Pi_2 = \frac{\alpha(\lambda+\nu)}{\varphi\mu}\Pi_0.$$

The static condition adopts the format actually determined by the drift condition. $\Pi L_{00}e < \Pi N_{00}e$. Equation (10) determines D's static probability. After obtaining rate matrix R, our probability vectors Πj's ($j \geq 1$) are calculated using Eqs. (6) and (9).

3 Numerical Study

By changing the values of the parameter λ & fixing all other parameters

Case i

If $\lambda = 0.10$, $\mu = 2.0$, $\beta = 0.4$,$\beta' = 0.6$,$\alpha = 0.30$, $\varphi = 0.50$, $\nu = 0.05$ & $R = \begin{pmatrix} 0.3950 & 0.2226 & 0.0247 \\ 0.5926 & 0.1838 & 0.0370 \\ 0.4938 & 0.1868 & 0.1975 \end{pmatrix}$

Table 1. Probability vectors

Π_j	π_{0j}	π_{1j}	π_{2j}	Total
π_0	0.2436	0.0203	0.0361	0.3000
π_1	0.1261	0.0647	0.0139	0.2047
π_2	0.0950	0.0426	0.0083	0.1459
π_3	0.0668	0.0305	0.0056	0.1029
π_4	0.0472	0.0215	0.0039	0.0726
π_5	0.0333	0.0152	0.0027	0.0512
π_6	0.0235	0.0107	0.0019	0.0316
π_7	0.0166	0.0076	0.0014	0.0256
π_8	0.0117	0.0053	0.0010	0.0180
π_9	0.0083	0.0038	0.0007	0.0128
π_{10}	0.0058	0.0027	0.0005	0.0090
π_{11}	0.0041	0.0012	0.0003	0.0063
π_{12}	0.0029	0.0008	0.0002	0.0044
π_{13}	0.0020	0.0006	0.0002	0.0031
π_{14}	0.0014	0.0004	0.0001	0.0022
π_{15}	0.0010	0.0003	0.0001	0.0016
π_{16}	0.0007	0.0002	0.0001	0.0011

π_{17}	0.0005	0.0001	0.0000	0.0007
π_{18}	0.0004	0.0001	0.0000	0.0006
π_{19}	0.0003	0.0001	0.0000	0.0004
π_{20}	0.0002	0.0001	0.0000	0.0003
Total				0.9999

The prob. vectors in table 1 were calculated by using the matrix R in Equation (7) and Equation (9), we get the vector $\Pi_0 = (0.2436\ 0.0203\ 0.0361)$. Utilizing Π_0 in Equation (6), the rest of the vectors are obtained. Hence the sum of the probability is affirmed to be $0.9999 \approx 1$.

Case ii

If $\lambda = 0.15$, $\mu = 2.0$, $\beta = 0.4$,$\beta^{'} = 0.6$, $\alpha = 0.30$, $\varphi = 0.50$, $\nu = 0.05$ & $R = \begin{pmatrix} 0.4548 & 0.2665 & 0.0394 \\ 0.6064 & 0.2264 & 0.0525 \\ 0.4665 & 0.2100 & 0.2711 \end{pmatrix}$

Table 2. Probability vectors

Π_j	π_{0j}	π_{1j}	π_{2j}	Total
π_0	0.1364	0.0171	0.0338	0.1873
π_1	0.0882	0.0473	0.0154	0.1509
π_2	0.0760	0.0375	0.0101	0.1236
π_3	0.0621	0.0309	0.0077	0.1006
π_4	0.0505	0.0251	0.0062	0.0818
π_5	0.0411	0.0204	0.0050	0.0665
π_6	0.0334	0.0166	0.0040	0.0540
π_7	0.0272	0.0135	0.0033	0.0440
π_8	0.0221	0.0110	0.0027	0.0358
π_9	0.0179	0.0089	0.0022	0.0290
π_{10}	0.0146	0.0073	0.0018	0.0237
π_{11}	0.0119	0.0059	0.0014	0.0192
π_{12}	0.0096	0.0048	0.0012	0.0156
π_{13}	0.0078	0.0039	0.0009	0.0126
π_{14}	0.0064	0.0032	0.0008	0.0104
π_{15}	0.0052	0.0026	0.0006	0.0084
π_{16}	0.0042	0.0021	0.0005	0.0068
π_{17}	0.0034	0.0017	0.0004	0.0055
π_{18}	0.0028	0.0014	0.0003	0.0045

π_{19}	0.0023	0.0011	0.0003	0.0037
π_{20}	0.0018	0.0009	0.0002	0.0029
π_{21}	0.0015	0.0007	0.0002	0.0024
π_{22}	0.0012	0.0006	0.0001	0.0019
π_{23}	0.0010	0.0005	0.0001	0.0021
π_{24}	0.0008	0.0004	0.0001	0.0013
π_{25}	0.0007	0.0003	0.0001	0.0011
π_{26}	0.0005	0.0003	0.0001	0.0009
π_{27}	0.0004	0.0002	0.0001	0.0007
π_{28}	0.0004	0.0002	0.0000	0.0006
π_{29}	0.0003	0.0001	0.0000	0.0004
π_{30}	0.0002	0.0001	0.0000	0.0003
Total				0.9998

The prob. vectors in table 2 were calculated by using the matrix R in Equation (7) and Equation (9), we get the vector $\Pi_0 = (0.1364\ 0.0171\ 0.0338)$. Utilizing Π_0 in Equation (6), the rest of the vectors are obtained. Hence the sum of the probability is affirmed to be $0.9998 \approx 1$.

Case iii

If $\lambda = 0.20$, $\mu = 2.0$, $\beta = 0.4$,$\beta' = 0.6$, $\alpha = 0.30$, $\varphi = 0.50$, $\nu = 0.05$ & $R = \begin{pmatrix} 0.4827 & 0.2894 & 0.0517 \\ 0.6034 & 0.2543 & 0.0647 \\ 0.4310 & 0.2160 & 0.3319 \end{pmatrix}$

Table 3. Probability vectors

Π_j	π_{0j}	π_{1j}	π_{2j}	Total
π_0	0.0849	0.0142	0.0305	0.1296
π_1	0.0627	0.0348	0.0154	0.1129
π_2	0.0579	0.0303	0.0106	0.0988
π_3	0.0508	0.0268	0.0085	0.0861
π_4	0.0443	0.0233	0.0072	0.0748
π_5	0.0386	0.0203	0.0062	0.0651
π_6	0.0335	0.0177	0.0054	0.0566
π_7	0.0292	0.0154	0.0047	0.0493
π_8	0.0253	0.0133	0.0040	0.0416
π_9	0.0220	0.0116	0.0035	0.0371
π_{10}	0.0192	0.0101	0.0031	0.0324
π_{11}	0.0166	0.0088	0.0027	0.0281
π_{12}	0.0145	0.0076	0.0023	0.0244

π_{13}	0.0126	0.0066	0.0020	0.0212
π_{14}	0.0109	0.0058	0.0017	0.0184
π_{15}	0.0095	0.0050	0.0015	0.0160
π_{16}	0.0083	0.0044	0.0013	0.0140
π_{17}	0.0072	0.0038	0.0011	0.0121
π_{18}	0.0062	0.0033	0.0010	0.0105
π_{19}	0.0054	0.0029	0.0009	0.0092
π_{20}	0.0047	0.0025	0.0008	0.0080
π_{21}	0.0041	0.0022	0.0007	0.0070
π_{22}	0.0036	0.0019	0.0006	0.0061
π_{23}	0.0031	0.0016	0.0005	0.0052
π_{24}	0.0027	0.0014	0.0004	0.0045
π_{25}	0.0023	0.0012	0.0004	0.0039
π_{26}	0.0020	0.0011	0.0003	0.0034
π_{27}	0.0018	0.0009	0.0003	0.0030
π_{28}	0.0015	0.0008	0.0002	0.0025
π_{29}	0.0013	0.0007	0.0002	0.0022
π_{30}	0.0012	0.0006	0.0002	0.0020
π_{31}	0.0010	0.0005	0.0002	0.0017
π_{32}	0.0009	0.0005	0.0001	0.0015
π_{33}	0.0008	0.0004	0.0001	0.0013
π_{34}	0.0007	0.0003	0.0001	0.0011
π_{35}	0.0006	0.0003	0.0001	0.0010
π_{36}	0.0005	0.0003	0.0001	0.0009
π_{37}	0.0004	0.0002	0.0001	0.0007
π_{38}	0.0003	0.0002	0.0001	0.0006
π_{39}	0.0003	0.0002	0.0000	0.0005
π_{40}	0.0002	0.0001	0.0000	0.0003
Total				0.9980

The prob. vectors in table 3 were calculated by using the matrix R in Equation (7) and Equation (9), we get the vector $\Pi_0 = (0.0849\ 0.0142\ 0.0305)$. Utilizing Π_0 in Equation (6), the rest of the vectors are obtained. Hence the sum of the probability is affirmed to be $0.9980 \approx 1$.

Case iv

If $\lambda = 0.25$, $\mu = 2.0$,$\beta = 0.4$,$\beta^{'} = 0.6$, $\alpha = 0.30$, $\varphi = 0.50$, $\nu = 0.05$ & $R = \begin{pmatrix} 0.4938 & 0.3055 & 0.0617 \\ 0.5926 & 0.2768 & 0.0741 \\ 0.3950 & 0.2161 & 0.3827 \end{pmatrix}$

7

Table 4. Probability vectors

Π_j	π_{0j}	π_{1j}	π_{2j}	Total
π_0	0.0570	0.0119	0.0275	0.0964
π_1	0.0416	0.0267	0.0149	0.0877
π_2	0.0444	0.0247	0.0105	0.0796
π_3	0.0407	0.0227	0.0086	0.0720
π_4	0.0369	0.0206	0.0075	0.0650
π_5	0.0334	0.0186	0.0067	0.0587
π_6	0.0301	0.0168	0.0060	0.0529
π_7	0.0272	0.0152	0.0054	0.0478
π_8	0.0245	0.0137	0.0049	0.0431
π_9	0.0221	0.0123	0.0044	0.0388
π_{10}	0.0200	0.0111	0.0040	0.0351
π_{11}	0.0180	0.0100	0.0036	0.0316
π_{12}	0.0163	0.0091	0.0032	0.0286
π_{13}	0.0147	0.0082	0.0029	0.0258
π_{14}	0.0132	0.0074	0.0026	0.0232
π_{15}	0.0119	0.0067	0.0024	0.0210
π_{16}	0.0108	0.0060	0.0021	0.0189
π_{17}	0.0097	0.0054	0.0019	0.0170
π_{18}	0.0088	0.0049	0.0017	0.0154
π_{19}	0.0079	0.0044	0.0016	0.0139
π_{20}	0.0071	0.0040	0.0014	0.0125
π_{21}	0.0064	0.0036	0.0013	0.0113
π_{22}	0.0058	0.0032	0.0012	0.0102
π_{23}	0.0052	0.0029	0.0010	0.0091
π_{24}	0.0047	0.0026	0.0009	0.0082
π_{25}	0.0043	0.0024	0.0008	0.0075
π_{26}	0.0038	0.0021	0.0008	0.0067
π_{27}	0.0035	0.0019	0.0007	0.0061
π_{28}	0.0033	0.0017	0.0006	0.0054
π_{29}	0.0028	0.0016	0.0006	0.0050
π_{30}	0.0025	0.0014	0.0005	0.0044
π_{31}	0.0023	0.0013	0.0005	0.0041
π_{32}	0.0021	0.0012	0.0004	0.0037

π_{33}	0.0019	0.0010	0.0004	0.0033
π_{34}	0.0017	0.0009	0.0003	0.0029
π_{35}	0.0015	0.0008	0.0003	0.0026
π_{36}	0.0014	0.0008	0.0003	0.0025
π_{37}	0.0012	0.0007	0.0002	0.0021
π_{38}	0.0011	0.0006	0.0002	0.0018
π_{39}	0.0010	0.0006	0.0002	0.0018
π_{40}	0.0009	0.0005	0.0002	0.0016
π_{41}	0.0008	0.0005	0.0002	0.0015
π_{42}	0.0007	0.0004	0.0001	0.0012
π_{43}	0.0007	0.0004	0.0001	0.0012
π_{44}	0.0006	0.0003	0.0001	0.0010
π_{45}	0.0005	0.0003	0.0001	0.0009
π_{46}	0.0005	0.0003	0.0001	0.0009
π_{47}	0.0004	0.0002	0.0001	0.0007
Total				0.9990

The prob. vectors in table 4 were calculated by using the matrix R in Equation (7) and Equation (9), we get the vector $\Pi_0 = (0.0570\ 0.0119\ 0.0275)$. Utilizing Π_0 in Equation (6), the rest of the vectors are obtained. Hence the sum of the probability is affirmed to be $0.9990 \approx 1$.

4 Performance Measures

The following performance measures were discovered using steady-state probabilities.

- Pr{server is in idle} $E(I) = \Pi_0$ (11)
- Pr{server is on busy period} $E(B) = \sum_{j=1}^{\infty} j\pi_{1j}$ (12)
- Pr{server gets breakdown} $E(BD) = \sum_{j=1}^{\infty} j\pi_{2j}$ (13)
- Pr{Total no. of customers in the system} $E(N) = E(I) + E(B) + E(BD)$ (14)
- Pr{No customer in the orbit} $PNCO = \sum_{i=0}^{2} \pi_{i0}$ (15)

Table 5. Performance Measures

λ	0.1	0.15	0.2	0.25
E(I)	0.6917	0.6327	0.5954	0.5660
E(B)	0.7077	1.3304	2.0656	3.6330
E(BD)	0.1297	0.3255	0.6596	1.0317
E(N)	2.3764	4.3319	6.6537	9.8917
PNCO	0.3000	0.1873	0.1296	0.0964

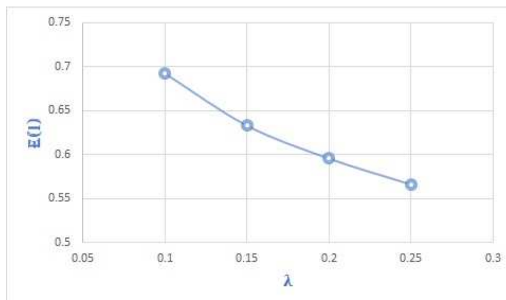

Figure 2. Arrival rate versus E(I)

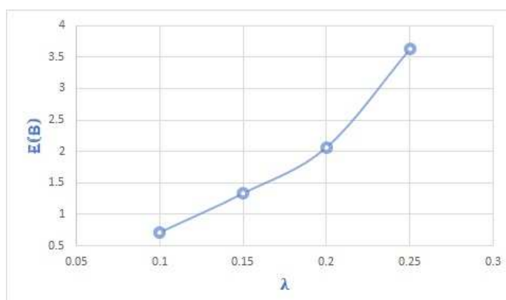

Figure 3. Arrival rate versus E(B)

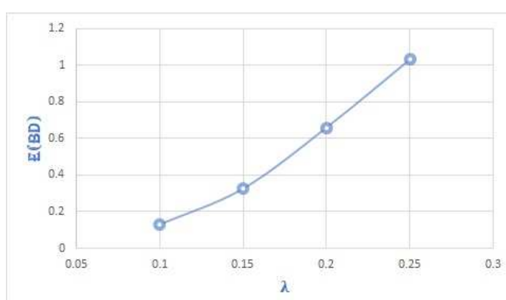

Figure 4. Arrival rate versus E(BD)

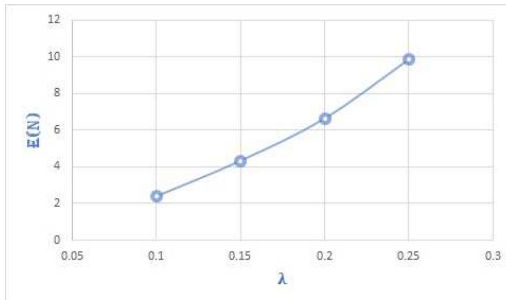

Figure 5. Arrival rate versus E(N)

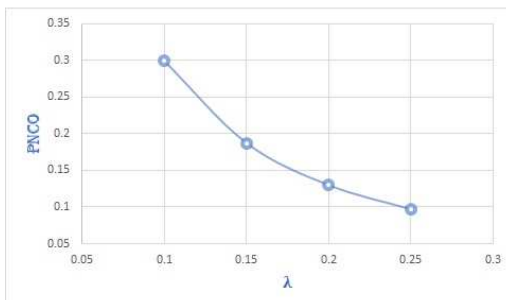

Figure 6. Arrival rate versus PNCO

The values of arrival rate have been varied from 0.1 to 2.5 As the arrival increases, Prob. that server is on idle and Prob. that orbit has no customer are decreases(refer Fig. 2 & Fig. 6). Similarly, if arrival rate increases, then Prob. that server is on busy period, Prob. that server gets breakdown and Prob. that total customers in the system are gradually increases (refer Fig. 3, Fig. 4 & Fig. 5).

5 Summary

This article focused on M/M/1 retrial queue with breakdown & feedback by utilizing Matrix geometric method. Using this type of model we can able to manage the time during the server breakdown and customer who is not satisfied are also able to get a servers again without any issues. By this producing this method the steady state probability vectors are obtained. From that some system performance measures are also determined with graphical representations.

References

[1] Artalejo. J. R. Lopez-Herrero M. J., The single server retrial queue with finite population, A BSDE approach, (2012).

[2] Ayyappan Govindan Muthu Ganapathy Subramanian and Gopal Sekar, Single Server Retrial Queueing System with Variable Service Rates in Priority Service

by Matrix Geometric Method, International Journal of Applied Mathematics & Computation, vol.3, pp. 216-231, (2011).

[3] Choi. B. D. Kim. Y. C. and Lee. Y. W., The M/M/c retrial queue with Geometric loss and Feedback, Computers Math. Applic. vol.36, pp. 41-52, (1998).

[4] Choi. B. D. Kulkarni. V. G., Feedback retrial queueing system, Stochastic Model Relat. Fields, pp. 93-105, (1992).

[5] Chuen-Horng Lin Jau-Chuan Ke., On the multiserver retrial queue with geometric loss and feedback, computational algorithm and parameter optimization, International Journal of Computer Mathematics, vol.88, pp. 1083-1101,(2011).

[6] Falin. G.I., A survey of retrial queues, Queueing Syst.,7, pp. 127-168, (1990).

[7] Kalyanaraman. R. Seenivasan. M., A multi Server Retrial Queue with Breakdown and Geometric loss, International Journal of Computational Cognition, vol. 9, pp. 44 - 48, (2011).

[8] Neuts, M.F., Markov chains with applications queueing theory, which have a matrix geometric invariant probability vector, Adv Appl Prob, Vol. 10, pp. 185-212, (1978).

[9] Neuts. M.F., Matrix-Geometric solutions in stochastic models, vol. 2 of johnsHopkins's series in the mathematical series, Johns HopkinsUniversity Press, Baltimore, USA, (1981).

[10] Praveen Deora, Umesh Kumari, and DC Sharma, Cost analysis and optimization of machine repair model with working vacation and feedback policy, International Journal of Applied Computational Mathematics, Vol. 6, pp. 1-14, (2021).

[11] Praveen Kumar Agrawal, Anamika Jain, and Madhu Jain, M/M/1 queueing model with working vacation and two type of server breakdown, Phys Conf Ser, Vol. 1849, (2021).

[12] Seenivasan, M., Senthilkumar, R., Subasri K S., "M/M/2 Heterogeneous Queueing System Having Unreliable Server with Catastrophes and Restoration", Materials Today: Proceedings Vol. 51(8) Pp. 2332 – 2338, 2021.

[13] Seenivasan, M., Chakravarthy, V J., Abinaya, R., "Markovian Queueing Model with Server Breakdown, Single Working Vacation and Catastrophe", Springer Book Series, vol-881, Pp. 409-421, 2022.

[14] Seenivasan, M., and Shiny Epciya, J. "M/M/1 queue Server Breakdown, Single Working Vacation, Feedback and State Dependent Customer", IEEE Xplore, Pp. 1-5, 2022.

[15] Seenivasan, M., and Chandiraleka. S. "Single Server Queueing Model with Multiple Working Vacation and with Server Breakdown", IEEE Xplore, Pp. 1-5, 2022.

J. COMPUTATIONAL ANALYSIS AND APPLICATIONS, VOL. 31, NO. 2, 2023, COPYRIGHT 2023 EUDOXUS PRESS, LLC

Norm retrieval by vectors and projections

Suman Dowerah[†*] and Saikat Mukherjee[†]

[†]Department of Mathematics, NIT Meghalaya, Shillong 793003, India

December 28, 2022

Abstract

Norm retrieval was introduced for Hilbert space frames for the first time by Bahmanpour et. al. in the year 2015. In order for a subspace as well as its orthogonal complement to do norm retrieval, it was proved by Bahmanpour et. al. that norm retrieval is a necessary requirement. Basically, norm retrieval refers to the process of reconstructing the signal's norm from the intensity measurements. We give a few characterizations for norm retrieval by vectors and subspaces under the action of bounded linear operators.

2020 Mathematics Subject Classification 42C15, 46C15
Keywords: Norm retrieval; Phase retrieval; Frames; Hilbert spaces; Signal reconstruction

1 Introduction

For any orthonormal basis $\{u_1, u_2, u_3, \dots\}$, a vector $v \in \mathcal{H}$ can be explicitly represented as $v = \sum_i \langle v, u_i \rangle u_i$. Thus orthonormal bases help to reconstruct a vector. In a similar manner, frames, having more flexible structure, also help to reconstruct a vector in a stable way. Duffin and Schaeffer [9] for the first time introduced frames for Hilbert spaces in the year 1952. Frames provides us with a reconstruction formula for lost signals. Daubechies et. al. popularized frames through their work in [7]. Over the last few decades, frame theory has become a prestigious area of research. Researchers worked various generalizations of frames, for instance, K-frame [13], fusion frame [5], wavelet frame [6] and many more. Basically, frames help us to recover and reconstruct the signal, that was lost or distorted, in a stable manner.

Reconstruction of signal is one of the important and significant problems in engineering especially in signal processing. Here a signal can be thought as a vector. This process of regaining the original signal becomes challenging when

*Corresponding author. *E-mail address:* sumandowerah@nitm.ac.in

there is a partial loss of information. Sometimes it happens that we only have the intensity measurements or the phaseless measurements of the lost signal. In such case, phase retrieval sequences help to reconstruct or regain the signal from its intensity measurements or phaseless measurements. Phase retrieval was introduced by Balan et al. [2] for Hilbert space frames in the year 2006. Since then mathematicians have started to work in this area. Phase retrieval is one of the challenging engineering problems. It includes a broad range of applications in many fields, such as speech recognition technology, X-ray crystallography, etc.

Norm retrieval means regaining or reconstructing the lost signal's norm from its intensity measurements or phaseless measurements. Norm retrieval for Hilbert spaces was discussed for the first time by Bahmanpour et. al. [1] in the year 2015. It was proved in [1] that norm retrieval is the necessary requirement for a subspace so that the subspace along with its orthogonal complement do phase retrieval. We note that if a sequence does phase retrieval then it will always do norm retrieval. In the last few years, it is observed that researchers have worked on norm retrieval frames [10], norm retrieval subspaces in finite dimensional Hilbert spaces [4]; and in infinite dimensional Hilbert spaces [15]. Apart from these, pertubation of norm retrieval frames is discussed in [11]. Being highly influenced as well as encouraged by the above mentioned work we explore norm retrieval sequences for vectors under the action of bounded linear operators, T. We also provide a method for construction of norm retrieval subspaces.

We stick to the following notations throughout paper. $\mathcal{H}, \mathcal{K}$ represents separable Hilbert spaces, $\mathcal{B}(\mathcal{H})$ represents the space of linear and bounded operators from $\mathcal{H}$ to $\mathcal{H}$. I, Λ, Λ_i represents a countable index set.

The paper is organised as follows. In Section 2, we give some preliminary background on norm retrieval sequences for finite and infinite dimensional spaces and we highlight some of the important results in these fields. We provide characterizations of norm retrieval sequences and and norm retrieval subspaces in Section 3.

2 Preliminaries

We recall the fundamental definitions and basic results that will be helpful for the paper. Frames are mathematical tools that are used to reconstruct signals.

Definition 2.1. [6] Consider a sequence, say $\varphi = \{\varphi_i\}_{i\in I}$, in $\mathcal{H}$. If for all $x \in \mathcal{H}$, there exist constants $0 < A_1 \leq A_2 < \infty$ such that φ satisfies

$$A_1\|x\|^2 \leq \sum_{i\in I} |\langle x, \varphi_i\rangle|^2 \leq A_2\|x\|^2.$$

Then φ is called a frame for $\mathcal{H}$. Here the constants A_1 is known as the lower frame bound, A_2 is known as the upper frame bound. The frame φ is called Parseval frame if $A_1 = A_2 = 1$.

For example, consider an orthonormal basis, say, $\{e_n\}$ for $\mathcal{H}$, then the sequence $\{e_1, e_1, e_2, e_3, e_4, \dots\}$ is a frame for $\mathcal{H}$. The associated frame bounds are $A_1 = 1$, $A_2 = 2$.

The frame operator, S, is a mapping $S : \mathcal{H} \to \mathcal{H}$ defined as

$$Sx = \sum_{i\in I} \langle x, \varphi_i\rangle \varphi_i, \quad \forall x \in \mathcal{H}.$$

The reconstruction formula given by frame operator and frame elements is as follows:

$$x = \sum_{i\in I} \langle x, S^{-1}\varphi_i\rangle \varphi_i = \sum_{i\in I} \langle x, \varphi_i\rangle S^{-1}\varphi_i, \quad \forall x \in \mathcal{H}.$$

We note that this representation is not unique, owing to the fact that frame elements are not necessarily linearly independent. Frames are one of the essential tools for restoring a signal. There are many different types of frames. One special type of frame is the scalable frame [14]. A scalable frame is a frame, φ, for $\mathcal{H}$ such that there exists scalars, say $c_1, c_2, c_3, \dots$ with $c_i \geq 0$ for which $\{c_i\varphi_i\}_{i\in I}$ is a Parseval frame for $\mathcal{H}$. We refer the readers [6] for more information in frame theory.

Definition 2.2. [2] Consider a sequence $\varphi = \{\varphi_i\}_{i\in I} \in \mathcal{H}$. We say φ performs phase retrieval for $\mathcal{H}$, if for $x, y \in \mathcal{H}$, φ satisfies

$$|\langle x, \varphi_i\rangle| = |\langle y, \varphi_i\rangle|, \quad \forall\ i \in I,$$

then $x = cy$ and c satisfies $|c| = 1$.

The sequence of vectors $\{e_i + e_j\}_{i<j}$, where e_i's are standard orthonormal basis, performs phase retrieval for ℓ_2. If a sequence does phase retrieval in a finite dimension space then it is also a frame, but it may not necessarily be a frame in an infinite dimension space.

In [3], Cahill et. al. thoroughly discussed phase retrieval by subspaces or projections.

Definition 2.3. [3] Suppose $W = \{W_i\}_{i\in I} \subset \mathcal{H}$ is a collection of closed subspaces with corresponding projections $P = \{P_i\}_{i\in I}$. Then W or P does phase retrieval whenever $x, y \in \mathcal{H}$, P satisfies

$$\|P_i x\| = \|P_i y\| \qquad \forall\ i \in I,$$

we have $x = cy$ and c satisfies $|c| = 1$.

Bahmanpour et. al. [1] introduced norm retrieval for frames in Hilbert spaces in the year 2015. In his attempt to pass the phase retrieval condition by subspaces to its orthogonal complements, Bahmanpour proved in [1] that the property of norm retrieval is a necessary requirement. A norm retrieval sequence helps to reconstruct partially lost signal's norm.

Definition 2.4. [1] A sequence of vectors $\varphi = \{\varphi_i\}_{i\in I}$ in $\mathcal{H}$ does norm retrieval if for $x, y \in \mathcal{H}$, φ satisfies

$$|\langle x, \varphi_i\rangle| = |\langle y, \varphi_i\rangle| \quad \forall\ i \in I,$$

then $\|x\| = \|y\|$.

It is obvious for scalable frames, parseval frames, tight frames to do norm retrieval. An orthonormal basis will always do norm retrieval for the corresponding space. It is to be noted that if a sequence performs phase retrieval for $\mathcal{H}$ then the sequence also performs norm retrieval for $\mathcal{H}$, however the converse is not true. For example, orthonormal bases do norm retrieval but not phase retrieval.

Norm retrieval by projections is defined as follows.

Definition 2.5. [1] Consider a family of subspaces, say $\{W_i\}_{i\in I}$, in an infinite dimensional Hilbert space $\mathcal{H}$ and define the orthogonal projections, say $\{P_i\}_{i\in I}$, onto $\{W_i\}_{i\in I}$. Then $\{W_i\}_{i\in I}$ (or $\{P_i\}_{i\in I}$) performs norm retrieval for $\mathcal{H}$ if for $x, y \in \mathcal{H}$, $\{P_i\}_{i\in I}$ satisfies $\|P_i x\| = \|P_i y\|, \ \forall\ i \in I$, we have $\|x\| = \|y\|$.

Norm retrieval can be thought as having an advantage of one free measurement when one tries to do phase retrieval.

The next proposition gives us a method to construct norm retrieval subspaces with the help of dimension of the subspaces.

Proposition 2.6. *[4] If $\{W_i\}_{i=1}^m$ are subspaces in $\mathbb{R}^n$ such that they do norm retrieval then $\sum_{i=1}^m \dim W_i \geq n$. Moreover, if $\exists\ k_1, k_2, \dots, k_m \in \mathbb{N}$ with $k_i \leq n$ such that for some $L \in \mathbb{N}$ $\sum_{i=1}^m k_i = Ln$ then there exist subspaces $\{W_i\}_{i=1}^m$ that perform norm retrieval in $\mathbb{R}^n$ where $\dim W_i = k_i$ for $1 \leq i \leq m$.*

The above result can easily be generalized as follows.

Theorem 2.7. *Suppose $\{k_i\}_{i=1}^m$ are natural numbers such that $k_i \leq n$ and $\sum_{i=1}^m k_i \geq n$. If for some $l \in \mathbb{N}$ with $1 \leq l \leq m$, $\sum_{i=1}^l k_i$ is a multiple of n, then there exist subspaces $\{W_i\}_{i=1}^m$ in $\mathbb{R}^n$ satisfying $\dim W_i = k_i$ such that $\{W_i\}_{i=1}^m$ performs norm retrieval.*

We recall the following properties of projection operators.

Lemma 2.8. *[12] Consider any two Hilbert spaces, say, $\mathcal{H}_1$, $\mathcal{H}_2$ and $T \in \mathcal{B}(\mathcal{H}_1, \mathcal{H}_2)$. Consider a closed subspace, say, W_1, of $\mathcal{H}_1$ and another closed subspace, say, W_2, of $\mathcal{H}_2$. Then the following statements are true.*

(i) $P_{W_1} T^* P_{W_2} = P_{W_1} T^*$ *if and only if* $TW_1 \subset W_2$.

(ii) $P_{W_1} T^* P_{\overline{TW_1}} = P_{W_1} T^*$

4

3 Main Results

We begin this section by studying norm retrieval sequences under the action of bounded linear operators.

In [1], it was shown that orthogonal projections preserve the norm retrieval property. However in [4], it is shown that the norm retrieval property is not preserved by invertible operators. For instance, $\varphi = \{(1,0),(0,1)\}$ does norm retrieval for $\mathbb{R}^2$; consider an invertible on $\mathbb{R}^2$ defined by $T(x_1,x_2) = (x_1+x_2, x_2)$; but $T\varphi = \{(1,0),(1,1)\}$ does not do norm retrieval for $\mathbb{R}^2$.

Remark 3.1. $\varphi = \{\varphi_i\}_{i\in I}$ perform norm retrieval for $\mathcal{H} \iff$ for $c_i \neq 0$, $c\varphi = \{c_i\varphi_i\}_{i\in I}$ perform norm retrieval for $\mathcal{H}$. Indeed, this can be easily verified from the fact that $|\langle x, c_i\varphi_i\rangle| = |\langle y, c_i\varphi_i\rangle| \iff |\langle x, \varphi_i\rangle| = |\langle y, \varphi_i\rangle|, \quad \forall i \in I$.

Theorem 3.2. *Suppose $\{\varphi_i\}_{i\in I}$ performs norm retrieval for $\mathcal{H}$. Consider $T \in \mathcal{B}(\mathcal{H})$, such that T is an isometry. Then $\{T^*\varphi_i\}_{i\in I}$ performs norm retrieval for $\mathcal{H}$.*

Proof. Suppose $x, y \in \mathcal{H}$ such that $|\langle x, T^*\varphi_i\rangle| = |\langle y, T^*\varphi_i\rangle| \implies |\langle Tx, \varphi_i\rangle| = |\langle Ty, \varphi_i\rangle|, \quad \forall \ i \in I$. Using the fact that $\{\varphi_i\}_{i\in I}$ performs norm retrieval for $\mathcal{H}$ and T is an isometry, we get $\|x\| = \|y\|$. □

Corollary 3.3. *Suppose $T \in \mathcal{B}(\mathcal{H})$ is an unitary operator and let $\varphi = \{\varphi_i\}_{i\in I}$ be a sequence of vectors in $\mathcal{H}$. Then, φ doing norm retrieval for $\mathcal{H}$ is equivalent to $T\varphi$ doing norm retrieval for $\mathcal{H}$.*

In [8] it was shown that phase retrieval is preserved by non-zero idempotent operators for the range space. Theorem 3.4 shows that idempotent operators also preserves norm retrieval for the range space.

Theorem 3.4. *Consider $T \in \mathcal{B}(\mathcal{H})$, a non-zero idempotent operator and let $\varphi = \{\varphi_i\}_{i\in I}$ be a sequence of vectors in $\mathcal{H}$. Then φ doing norm retrieval for $R(T^*)$ is equivalent to $\{T\varphi_i\}_{i\in I}$ doing norm retrieval for $R(T^*)$.*

Proof. We note that for every $x_1, x_2 \in R(T^*)$, there exists $y_1, y_2 \in \mathcal{H}$ such that $T^*y_1 = x_1$, $T^*y_2 = x_2$. Then we have,

$$\begin{aligned}
|\langle x_1, T\varphi_i\rangle| = |\langle x_2, T\varphi_i\rangle| &\iff |\langle T^*y_1, T\varphi_i\rangle| = |\langle T^*y_2, T\varphi_i\rangle| \\
&\iff |\langle T^*y_1, \varphi_i\rangle| = |\langle T^*y_2, \varphi_i\rangle| \\
&\iff |\langle x_1, \varphi_i\rangle| = |\langle x_2, \varphi_i\rangle|,
\end{aligned}$$

for all $i \in I$. Hence the theorem holds. □

Theorem 3.5. *Given a closed subspace W of a Hilbert space $\mathcal{H}$, every norm sequence for $\mathcal{H}$ can be uniquely decomposed into norm retrieval sequences for W and $W^\perp$.*

5

Proof. Suppose $\varphi = \{\varphi_i\}_{i\in I}$ does norm retrieval for $\mathcal{H}$ and P_w is the orthogonal projection onto W. Then φ can be uniquely decomposed as $P_w\varphi$ and $(I-P_w)\varphi$, where $P_w\varphi = \{P_w\varphi_i\}_{i\in I}$. The conclusion follows from the facts that for $x, y \in W$,

$$|\langle x, \varphi_i\rangle| = |\langle x, P_w\varphi_i\rangle| = |\langle y, P_w\varphi_i\rangle| = |\langle y, \varphi_i\rangle|,\ \forall\ i \in I;$$

and for $x, y \in W^\perp$,

$$|\langle x, \varphi_i\rangle| = |\langle x, (I-P_w)\varphi_i\rangle| = |\langle y, (I-P_w)\varphi_i\rangle| = |\langle y, \varphi_i\rangle|,\ \forall\ i \in I.$$

□

Corollary 3.3 shows that the norm retrieval property for vectors is preserved by unitary operators. We now show that the norm retrieval property for subspaces is also preserved by unitary operators.

Theorem 3.6. *Consider $W = \{W_i\}_{i\in I}$ is a collection of closed subspaces in $\mathcal{H}$. Further, let $T : \mathcal{H} \to \mathcal{K}$ be unitary. If W does norm retrieval for $\mathcal{H}$, then TW does norm retrieval for $\mathcal{K}$.*

Proof. For $y_1, y_2 \in \mathcal{K}$, let $\|P_{TW_i}y_1\| = \|P_{TW_i}y_2\|$ for all $i \in I$. Since T is surjective, $\exists\ x_1, x_2 \in \mathcal{H}$ such that $Tx_1 = y_1$ and $Tx_2 = y_2$. We note that for $k = 1, 2$, we have $P_{TW_i}y_k = P_{TW_i}Tx_k = P_{TW_i}TP_{W_i}x_k + P_{TW_i}TP_{W_i^\perp}x_k = P_{TW_i}TP_{W_i}x_k = TP_{W_i}x_k$. Thus, we get $\|TP_{W_i}x_1\| = \|TP_{W_i}x_2\|$. Using the fact that T is isometry and $\{W_i\}_{i\in I}$ do norm retrieval, we obtain $\|y_1\| = \|y_2\|$. □

The following two examples show that if we drop the condition that T is isometry or the condition that T is surjective then we may lose the property of norm retrievality of $\{TW_i\}_{i\in I}$.

Example 3.7. Consider the subspaces $W_1 = x$-axis and $W_2 = y$-axis in $\mathbb{R}^2$. Clearly, $\{W_1, W_2\}$ does norm retrieval for $\mathbb{R}^2$. Define $T_1 : \mathbb{R}^2 \to \mathbb{R}^2$ as $T_1(x_1, x_2) = (x_1 + x_2, x_2)$. Thus T_1 is not an isometry. Now $T_1W_1 = x$-axis and $T_1W_2 = \text{span}\{(x, x) : x \in \mathbb{R}\}$. However $\{T_1W_1, T_1W_2\}$ does not do norm retrieval in $\mathbb{R}^2$. This can be easily verified at $(1, 1)$ and $(1, -3)$.

Example 3.8. Consider the subspaces $W_1 = x$-axis and $W_2 = y$-axis in $\mathbb{R}^2$. We note that $\{W_1, W_2\}$ does norm retrieval for $\mathbb{R}^2$. Define $T_2 : \mathbb{R}^2 \to \mathbb{R}^3$ as $T_2(x_1, x_2) = (x_1, x_2, 0)$. Clearly T_2 is not surjective. Now $T_2W_1 = x$-axis and $T_2W_2 = y$-axis in $\mathbb{R}^3$. But $\{T_2W_1, T_2W_2\}$ does not do norm retrieval in $\mathbb{R}^3$. This can be easily verified for $(0, 0, 1)$ and $(0, 0, 2)$.

Let $\{P_i\}_{i=1}^m$ be projections onto subspaces $\{W_i\}_{i=1}^m$ of $\mathbb{C}^n$. Consider any orthonormal bases $\{\varphi_{ij}\}_{j=1}^{I_i}$ of $\{W_i\}_{i=1}^m$ and a sub collection $S \subseteq \{(i, j) : 1 \le i \le m, 1 \le j \le I_i\}$. It was shown in [4] that if $\{P_i\}_{i=1}^m$ does norm retrieval and $x \perp \text{span}\{\varphi_{ij}\}_{(i,j)\in S}$, $y \perp \text{span}\{\varphi_{ij}\}_{(i,j)\in S^c}$ then $\text{Re}\langle x, y\rangle = 0$. In fact $\langle x, y\rangle = 0$ for an arbitrary Hilbert space, this is eveident from the following result. A similar result for weaving norm retrival subspaces was proved in [8].

Theorem 3.9. *Let $\{P_i\}_{i\in\Lambda}$ be projections onto subspaces $\{W_i\}_{i\in\Lambda}$ of $\mathcal{H}$. Given any orthonormal bases $\{\varphi_{ij}\}_{j\in\Lambda_i}$ of $\{W_i\}_{i\in\Lambda}$ and a sub collection $S\subset\{(i,j): i\in\Lambda, j\in\Lambda_i\}$. If $\{P_i\}_{i\in\Lambda}$ does norm retrieval then $\{\varphi_{ij}\}^{\perp}_{(i,j)\in S}\perp\{\varphi_{ij}\}^{\perp}_{(i,j)\in S^c}$.*

Proof. Given $S\subset\{(i,j): i\in\Lambda, j\in\Lambda_i\}$. Let $x\in\{\varphi_{ij}\}^{\perp}_{(i,j)\in S}$ and $y\in\{\varphi_{ij}\}^{\perp}_{(i,j)\in S^c}$. We note that for each $i\in\Lambda$,

$$\begin{aligned}\|P_i(x+y)\|^2 = \sum_{j\in\Lambda_i}|\langle x+y,\varphi_{ij}\rangle|^2 &= \sum_{\substack{j\in\Lambda_i\\(i,j)\in S^c}}|\langle x,\varphi_{ij}\rangle|^2+\sum_{\substack{j\in\Lambda_i\\(i,j)\in S}}|\langle y,\varphi_{ij}\rangle|^2.\\ &=\sum_{j\in\Lambda_i}|\langle x-y,\varphi_{ij}\rangle|^2\\ &=\|P_i(x-y)\|^2.\end{aligned}$$

Therefore, we get $\|x+y\|^2=\|x-y\|^2$ for all $i\in\Lambda$. Thus $\mathrm{Re}\langle x,y\rangle=0$.

Similarly, we obtain $\|P_i(x+iy)\|^2=\|P_i(x-iy)\|^2 \implies \|x+iy\|^2=\|x-iy\|^2 \implies \mathrm{Im}\langle x,y\rangle=0$ for all $i\in\Lambda$. Hence, $x\perp y$. □

Corollary 3.10. *Consider a sequence of vectors $\varphi=\{\varphi_i\}_{i\in I}$ in $\mathcal{H}$. For non-trivial $J\subset I$, let $W_1=span\{\varphi_i\}_{i\in J}$ and $W_2=span\{\varphi_i\}_{i\in J^c}$. If φ does norm retrieval then $W_1^{\perp}\subset W_2$.*

Proof. Since φ does norm retrieval, so by Theorem 3.9 we have $W_1^{\perp}\perp W_2^{\perp}$. Hence the conclusion follows. □

In [4], it has been proved that corollary 3.11 is true for $\mathbb{R}^n$. We extend it to $\mathcal{H}^n$ where $\mathcal{H}^n$ is an n-dimensional Hilbert space.

Corollary 3.11. *Every norm retrieval set with n elements is orthogonal in $\mathcal{H}^n$, where $\mathcal{H}^n$ is an n-dimensional Hilbert space.*

Proof. Consider a norm retrieval collection $\{\varphi_i\}_{i=1}^n$ in $\mathcal{H}^n$. If possible, suppose for some k with $1\le k\le n$, φ_k is not orthogonal to another element of this collection. Let $W_1=\mathrm{span}\{\varphi_i\}_{i\neq k}$ and $W_2=\mathrm{span}\{\varphi_k\}$. Then $W_1^{\perp}$ can not be a subset W_2, a contradiction to Corollary 3.10. □

References

[1] S. Bahmanpour, J. Cahill, P. G. Casazza, J. Jasper and L. Woodland, Phase retrieval and norm retrieval, Trends in Harmonic Analysis and its Applications, *Contemp. Math*, Amer. Math. Soc., Providence, RI, 650, 2015, pp.3–14.

[2] R. Balan, P. Casazza and D. Edidin, On signal reconstruction without phase, *Applied and Computational Harmonic Analysis*, 20(3), 345–356 (2006).

[3] J. Cahill, P. G. Casazza, J. Peterson and L. Woodland, Phase retrieval by projections, *Houstan J. Math.*, 42(2), 537–558 (2016).

[4] P. G. Casazza, D. Ghoreishi, S. Jose and J. C. Tremain, Norm retrieval and Phase retrieval by projections, *Axioms*, 6(1), 6 (2017).

[5] P. Casazza and G. Kutyniok, Frames of subspaces, *Contemp. Math.*, AMS, 345, 2004, pp.87–114.

[6] O. Christensen, *An introduction to frames and Riesz bases*, Boston: Birkhäuser, 2003.

[7] I. Daubechies, A. Grossmann and Y. Meyer, Painless nonorthogonal expansions, *J. Math. Phys.*, 27, 1271–1283 (1986).

[8] S. Dowerah and S. Mukherjee, Weaving phase retrieval and weaving norm retrieval, *Int. J. Appl. and Comput. Math.*, 8(4), 198 (2022).

[9] R. J. Duffin and A. C. Schaeffer, A class of nonharmonic Fourier series, *Trans. Amer. Math. Soc.*, 72(2), 341–366 (1952).

[10] M. A. H. Fard and S. Moazeni, Signal reconstruction without phase by norm retrievable frames, *Linear and Multilinear Algebra*, 69(8), 1484–1499 (2021).

[11] M. A. H. Fard and L. M. Rad, Norm Retrievable Frames and Their Perturbation in Finite Dimensional Complex Hilbert Spaces, *Numerical Functional Analysis and Optimization*, 38(1), 51–57 (2016).

[12] L. Găvruţa, On the duality of fusion frame, *J. Math. Anal. Appl.*, 333(2), 871–879 (2007).

[13] L. Găvruţa, Frames for operators, *Appl. Comput. Harmon. Anal.*, 32, 139–144 (2012).

[14] G. Kutyniok, K. A. Okoudjou, F. Philipp and E. K. Tuley, Scalable frames, *Linear Algebra and its Applications*, 438, 2225–2238 (2013).

[15] Y. Zhou, Norm Retrieval by Projections on Infinite-Dimensional Hilbert Spaces, *Ann. Appl. Math.*, 33, 324–330 (2017).

Non Markovian retrial queue, balking, disaster under working breakdown and working vacation

P. Manoharan[1] and S. Subathra[2]
[1,2]Department of Mathematics, Annamalai University,
Annamalainagar-608002, Tamilnadu, India.
*Corresponding Author E-Mail: manomaths.hari@gmail.com

December 29, 2022

Abstract

Any arriving customer who arrives and finds that the server is free, enters the service station and the remaining customers connect into the orbit. When the normal busy server is running, the system may at any time become defective due to a disaster. All users are forced to quit the system due to a disaster, which also brings about the failure of the main server. When a primary server breaks, it is shipped out for repair, and the repair process starts instantly. The server stops running as soon as the orbit is empty at a typical service finish instant. During the working breakdown or working vacation, the replacement server offers arriving customers a lower level of service. The arriving customer receives service instantly if the server is idle. If not, he will choose whether to leave the system without service or returning to receive service. Using the supplementary variable technique, we calculate the steady state PGF for system and orbit sizes. We generate performance measures and particular cases. With the use of specific numerical examples, we analyse the model.
Keywords: Retrial queue, balking, disaster, working breakdown, working vacation.

Mathematics Subject Classification 2010: 60K25, 90B22

1 Introduction

Previously, various authors investigated queueing models with varying service rates. These models drive almost made the assistance rate subject to the framework's circumstance, like lines in irregular conditions, lines with breakdown, and working breakdown. Retrial lines with repeated tasks are distinguished in a retrial queueing system by the fact that an arriving customer sees the server busy upon arrival and is encouraged to leave the support area and join a retry line

1

known as orbit. After a specific measure of time has elapsed, the client in orbit might make another assistance demand. It makes no difference to the other customers in the orbit if any random customer in the orbit repeats the service request. Such queues assume a novel part in PC and broadcast communications frameworks. Rajadurai [8,9], estimated a Non-Markovian retrial queue including calamity and working breakdown. Kalidass and Ramanath (2012) pioneered "The concept of working breakdowns". If a regular busy server fails due to a disaster at any time, the system ought to be ready with a reinforcement (reserve) server in the event that the primary server falls flat. It makes no difference to the other customers in the orbit if any random customer in the orbit repeats the service request. The main server rejoins the system and becomes operational as soon as the repair is fulfilled. Furthermore, the operational breakdown service can reduce customer complaints as the principal server is being repaired, as well as the cost of customers who are waiting. As a result, a more sensible repair strategy for problematic queueing framework is the working breakdown service. Rajadurai et al [10], considered inconsistent queueing frameworks with different highlights, one of which is that when a server falls flat, it is sent for fix, during which time it stops offering support to essential clients until the assistance channel is fixed, and the client who was simply being served before the server disappointment trusts that the leftover help will finish.

2 Model Description

In this model the arrival follows Poisson process with rate λ and the service discipline is FIFO. Since there is no waiting area, this is assumed. When a customer arrives and determines that the server is busy, they are joined to the orbit. If an orbital customer is permitted access to the server. Laplace-Stieltjes Transforms (LST) represent inter retrial times as $\Upsilon^*(\theta)$ and have an arbitrary distribution function $\Upsilon(t)$. In normal service period (NS period), service time have general distribution function S(t), with LST as $S^*(\theta)$. We assume that the disaster occur only when the main service is in progress and disaster follows a negative exponential distribution with rate δ. When the disaster occurs all customers are clear out and the primary server is dispatched for maintenance. The repair time follows an exponential distribution with parameter η. The server gives a lower rate of service follows an arbitrary distribution function $S_w(t)$ to arriving customers during the working breakdown period, with LST as $S_w^*(\theta)$. The server resumes normal operation after the repair is finished. As soon as the service is finished and the orbit is empty, the server goes on vacation. The duration of the vacation period is determined by an exponential distribution with the parameter θ. If there are still users in the system at the time the vacation ends, the server will begin a new busy period. Otherwise, he awaits the arrival of a customer. The server gives a lesser rate of service follows an arbitrary distribution function $S_w(t)$ to arriving customers during the working vacation period, with LST as $S_w^*(\theta)$. A vacation interruption occurred if the server quits

his vacation to return to the normal busy period after discovering that there is a customer in the orbit. Working breakdown and working vacation are both regarded as low service in this situation (LS period). If the server is idle, the customer arrives and gets served instantly. If not, he will choose whether to leave the system with probability $(1-r)$ or joining the orbit with probability r.
Let $\Upsilon^0(t)$ denotes the elapsed retrial time, $S^0(t)$ denotes the elapsed service time in NS period , $S^0_w(t)$ denotes the elapsed service time in LS period .
Let $F(t)$ denotes the size of the orbit at time "t". and we use the subsequent random variable as follows.
Let's use the subsequent random variables.
$F(t)$- Size of the orbit at time "t".
At time "t" the four distinct states of the server are

$$\Theta(t) = \begin{cases} 0, & \text{if the server is idle in LS period} \\ 1, & \text{if the server is idle in NS period} \\ 2, & \text{if the server is busy in LS period} \\ 3, & \text{if the server is busy in NS period} \end{cases}$$

o generate bivariate Markov Process, $\{(F(t), \Theta(t)); t \geq 0\}$ further supplementary variables $\Upsilon^0(t)$, $S^0(t)$, and $S^0_w(t)$ are introduced. The sequence of periods at which a NS or LS periods completion occurs is $\{t_m, m = 1, 2, 3, ...\}$. The Markov chain that is formed by the random vector sequences $Z_m = \{F(t_m+), \Theta(t_m+)\}$ is incorporated into the retrial queueing system. The concerned embedded Markov chain is ergodic if and only if $\rho < \Upsilon^*(\lambda)\big[$ See Sennott et al.,[12]$\big]$ where $\rho = \dfrac{\lambda r}{\delta}(1 - S^*(\delta))$ pretaining to our model.
Following are the limiting probabilities

$$\begin{aligned}
\Omega_{0,1} &= \lim_{t\to\infty} P\{\Theta(t) = 1,\ F(t) \ = 0\}, \\
\Omega_{0,2} &= \lim_{t\to\infty} P\{\Theta(t) = 0,\ F(t) \ = 0\}, \\
\Upsilon_m(x) &= \lim_{t\to\infty} P\{\Theta(t) = 1,\ F(t) \ = m,\ x \leq \Upsilon^0(t) < x + dx\}, \\
&\qquad\qquad x \geq 0,\ m \geq 1 \\
\Omega_{m,1}(x) &= \lim_{t\to\infty} P\{\Theta(t) = 3,\ F(t) \ = m,\ x \leq S^0(t) < x + dx\}; \\
&\qquad\qquad x \geq 0,\ m \geq 0,
\end{aligned}$$

$$\begin{aligned}
\Omega_{m,2}(x) &= \lim_{t\to\infty} P\{\Theta(t) = 2,\ F(t) \ = m,\ x \leq S^0_w(t) < x + dx\}; \\
&\qquad\qquad x \geq 0,\ m \geq 0.
\end{aligned}$$

Following are the probability generating function

$$\Upsilon(z,x)=\sum_{m=1}^{\infty}\Upsilon_m(x)z^m; \qquad \Upsilon(z,0)=\sum_{m=1}^{\infty}\Upsilon_m(0)z^m;$$
$$\Upsilon^*(\theta)=\int_0^{\infty}e^{-\theta x}r(x)dx; \qquad \Omega_1(z,x)=\sum_{m=0}^{\infty}\Omega_{m,1}(x)z^m;$$
$$\Omega_1(z,0)=\sum_{m=0}^{\infty}\Omega_{m,1}(0)z^m; \qquad S^*(\theta)=\int_0^{\infty}e^{-\theta x}\mu(x)dx;$$
$$\Omega_2(z,x)=\sum_{m=0}^{\infty}\Omega_{m,2}(x)z^m; \qquad \Omega_2(z,0)=\sum_{m=0}^{\infty}\Omega_{m,2}(0)z^m;$$
$$S_w^*(\theta)=\int_0^{\infty}e^{-\theta x}\mu_w(x)dx;$$

We are using the following hazard rate functions. Let $r(x)$ denotes the conditional retrial completion rate of $\Upsilon(x)$

and $r(x)dx=\dfrac{d\Upsilon(x)}{1-\Upsilon(x)}$.
Let $\mu(x)$ denotes the conditional normal service completion rate of $S(x)$

and $\mu(x)dx=\dfrac{dS(x)}{1-S(x)}$.
Let $\mu_w(x)$ denotes the conditional lower service completion rate of $S_w(x)$

and $\mu_w(x)dx=\dfrac{dS_w(x)}{1-S_w(x)}$.
The system was demonstrated in steady state by the following differential difference equations:

$$\lambda\Omega_{0,1} = (\theta+\eta)\Omega_{0,2}, \tag{1}$$
$$(\lambda+\theta+\eta)\Omega_{0,2} = \int_0^{\infty}\Omega_{0,1}(x)\mu(x)dx+\int_0^{\infty}\Omega_{0,2}(x)\mu_w(x)dx +\delta\int_0^{\infty}\Omega_{m,1}(x)dx, m\geq 0, \tag{2}$$
$$\frac{d\Upsilon_m(x)}{dx} = -(\lambda+r(x))\Upsilon_m(x), m\geq 1, \tag{3}$$
$$\frac{d\Omega_{0,1}(x)}{dx} = -(\lambda+\delta+\mu(x))\Omega_{0,1}(x)+\lambda(1-r)\Omega_{0,1}(x), m=0 \tag{4}$$
$$\frac{d\Omega_{m,1}(x)}{dx} = -(\lambda+\delta+\mu(x))\Omega_{m,1}(x)+\lambda(1-r)\Omega_{m,1}(x) +\lambda r\Omega_{m-1,1}(x), m\geq 1, \tag{5}$$

4

$$\frac{d\Omega_{0,2}(x)}{dx} = -(\lambda+\eta+\theta+\mu_w(x))\Omega_{0,2}(x)+\lambda(1-r)\Omega_{0,2}(x), m=0, \quad (6)$$

$$\frac{d\Omega_{m,2}(x)}{dx} = -(\lambda+\eta+\theta+\mu_w(x))\Omega_{m,2}(x)+\lambda(1-r)\Omega_{m,2}(x) + \lambda r\Omega_{m-1,2}(x), m\geq 1. \quad (7)$$

At $x=0$,

$$\Upsilon_m(0) = \int_0^\infty \Omega_{m,1}(x)\mu(x)dx + \int_0^\infty \Omega_{m,2}(x)\mu_w(x)dx, \ m\geq 1, \quad (8)$$

$$\Omega_{0,1}(0) = \int_0^\infty \Upsilon_1(x)r(x)dx + (\theta+\eta)\int_0^\infty \Omega_{0,2}(x)dx + \lambda\Omega_{0,1}, \ m=0, \quad (9)$$

$$\Omega_{m,1}(0) = \int_0^\infty \Upsilon_{m+1}(x)r(x)dx + (\theta+\eta)\int_0^\infty \Omega_{m,2}(x)dx + \lambda\int_0^\infty \Upsilon_m(x)dx, \ m\geq 1, \quad (10)$$

$$\Omega_{m,2}(0) = \begin{cases} \lambda\Omega_{0,2}, & m=0, \\ 0, & m\geq 1, \end{cases} \quad (11)$$

The normalizing condition is

$$1 = \Omega_{0,1}+\Omega_{0,2}+\sum_{m=0}^{\infty}\Big[\int_0^\infty \Omega_{m,1}(x)dx + \int_0^\infty \Omega_{m,2}(x)dx\Big] + \sum_{m=1}^{\infty}\int_0^\infty \Upsilon_m(x)dx$$

Multiply the equations (2) - (8) by the proper powers of z

$$\frac{d\Upsilon(z,x)}{dx} + (\lambda+r(x))\Upsilon(z,x) = 0 \quad (12)$$

$$\frac{d\Omega_1(z,x)}{dx} + (\lambda(1-rz)-\lambda(1-r)+\delta+\mu(x))\Omega_1(z,x) = 0 \quad (13)$$

$$\frac{d\Omega_2(z,x)}{dx} + (\lambda(1-rz)-\lambda(1-r)+\theta+\eta+\mu_w(x))\Omega_2(z,x) = 0 \quad (14)$$

$$\Upsilon(z,0) = \int_0^\infty \Omega_1(z,x)\mu(x)dx + \int_0^\infty \Omega_2(z,x)\mu_w(x)dx - \int_0^\infty \Omega_{0,1}(x)\mu(x)dx - \int_0^\infty \Omega_{0,2}(x)\mu_w(x)dx \quad (15)$$

Using the equation (2) in equation (15), we get

$$\Upsilon(z,0) = \int_0^\infty \Omega_1(z,x)\mu(x)dx + \int_0^\infty \Omega_2(z,x)\mu_w(x)dx + \delta\int_0^\infty \Omega_1(z,x)dx - (\lambda+\theta+\eta)\Omega_{0,2} \quad (16)$$

Multiply the equations $(10)-(11)$ by the proper powers of z

$$\begin{aligned}\Omega_1(z,0) &= \frac{1}{z}\int_0^{\infty}\Upsilon(z,x)r(x)dx+\lambda\int_0^{\infty}\Upsilon(z,x)dx+\lambda\Omega_{0,1}\\ &\quad+(\eta+\theta)\int_0^{\infty}\Omega_2(z,x)dx \qquad (17)\\ \Omega_2(z,0) &= \lambda\Omega_{0,2} \qquad (18)\end{aligned}$$

Solving the first order linear differential equations $(13),(14),(15)$ which yields,

$$\begin{aligned}\Upsilon(z,x) &= \Upsilon(z,0)[1-\Upsilon(x)]e^{-\lambda x} \qquad (19)\\ \Omega_1(z,x) &= \Omega_1(z,0)[1-S(x)]e^{-B(z)x} \qquad (20)\\ \Omega_2(z,x) &= \Omega_2(z,0)[1-S_w(x)]e^{-B_w(z)x} \qquad (21)\end{aligned}$$

where $B(z)=(\lambda r(1-z)+\delta)$, $B_w(z)=(\lambda r(1-z)+\theta+\eta)$.
Substituting the equations (19) and (21)in equation (17), we get

$$\Omega_1(z,0) = \frac{\Upsilon(z,0)}{z}\Big[\Upsilon^*(\lambda)+z(1-\Upsilon^*(\lambda))\Big]+\lambda\Omega_{0,1}+\lambda\Omega_{0,2}U(z) \qquad (22)$$

where, $U(z) = \dfrac{(\eta+\theta)(1-S_w^*(B_w(z))}{B_w(z)}$.
Substituting the equations (20) and (21) in equation (16), we get

$$\Upsilon(z,0) = \Omega_1(z,0)[S^*(B(z))+S(z)]+\Omega_2(z,0)S_w^*(B(z))-(\lambda+\theta+\eta)\Omega_{0,2}. \qquad (23)$$

where $S(z)=\dfrac{\delta(1-S^*(B(z)))}{\delta+\lambda r(1-z)}$
Using equations (18) and (22) in equation (23) and get

$$\begin{aligned}\Upsilon(z,0) &= \frac{z\Omega_{0,2}}{Dr_1(z)}\Big\{[\theta+\eta+\lambda U(z)][S^*(B(z))+S(z)]+\lambda(S_w^*(B_w(z))-1)\\ &\quad-(\theta+\eta)\Big\}, \qquad (24)\end{aligned}$$

Substituting the equation (24) in equation (22), we get

$$\begin{aligned}\Omega_1(z,0) &= \frac{\Omega_{0,2}}{Dr_1(z)}\Big\{[\lambda(S_w^*(B_w(z))-1)-(\theta+\eta)][\Upsilon^*(\lambda)+z(1-\Upsilon^*(\lambda))]\\ &\quad+z[\theta+\eta+\lambda U(z)])\Big\} \qquad (25)\end{aligned}$$

where $Dr_1(z)=z-[S^*(B(z))+S(z)][\Upsilon^*(\lambda)+z(1-\Upsilon^*(\lambda))]$. Using the equations (24), (25) and (18) in equations (19), (20) and (21), then the limiting PGF's are $\Upsilon(z,x)$, $\Omega_1(z,x)$, and $\Omega_2(z,x)$.

6

3 Steady state results

If $\rho < \Upsilon^*(\lambda)$, The PGF's are listed below.
(i) The amount of orbiting customers as the server is not being utilized

$$\begin{aligned}\Upsilon(z) &= \frac{(1-\Upsilon^*(\lambda))}{\lambda Dr_1(z)}\Big\{z\Omega_{0,2}\big[(\lambda U(z)+\theta+\eta)[S^*(B(z))+S(z)] \\ &\quad +\lambda(S_w^*(B_w(z))-1)-(\theta+\eta)\big]\Big\} \qquad (26)\end{aligned}$$

(ii) The amount of orbiting customers as the server is regularly busy

$$\begin{aligned}\Omega_1(z) &= \frac{(1-S^*(B(z)))}{B(z)Dr_1(z)}\Big\{\Omega_{0,2}\big[(\lambda U(z)+\theta+\eta)z+[\lambda(S_w^*(B_w(z))-1) \\ &\quad -(\theta+\eta)][\Upsilon^*(\lambda)+z(1-\Upsilon^*(\lambda))]\big]\Big\} \qquad (27)\end{aligned}$$

(iii) PGF is used to determine the total number of users in orbit ($C_s(z)$).

$$\begin{aligned}C_s(z) &= \Omega_{0,1}+\Omega_{0,2}+\Upsilon(z)+z(\Omega_1(z)+\Omega_2(z)), \\ C_s(z) &= \frac{\Omega_{0,2}}{Dr_1(z)}\Big\{B(z)\Big(z-(S^*(B(z))+S(z))(\Upsilon^*(\lambda)+z(1-\Upsilon^*(\lambda)))\Big) \\ &\quad \times\Big(\frac{\eta+\theta}{\lambda}+1\Big)+\Big((U(z)+\frac{1}{\lambda}(\theta+\eta))(S^*(B(z))+S(z)) \\ &\quad +(S_w^*(B_w(z))-1)-\frac{1}{\lambda}(\theta+\eta)\Big)z(1-\Upsilon^*(\lambda))B(z)+(1-S^*(B(z)) \\ &\quad \times\Big((\lambda U(z)+\theta+\eta)z+(\lambda(S_w^*(B_w(z))-1)-(\theta+\eta))(\Upsilon^*(\lambda) \\ &\quad +z(1-\Upsilon^*(\lambda)))\Big)z+B(z)\Big(z-(S^*(B(z))+S(z))(\Upsilon^*(\lambda) \\ &\quad +z(1-\Upsilon^*(\lambda)))\Big)\frac{\lambda zU(z)}{(\theta+\eta)}\Big\}.\end{aligned}$$

(iv) PGF is used to determine the total number of users in orbit ($C_o(z)$).

$$\begin{aligned}C_o(z) &= \Omega_{0,1}+\Omega_{0,2}+\Upsilon(z)+\Omega_1(z)+\Omega_2(z), \\ C_o(z) &= \frac{\Omega_{0,2}}{Dr_1(z)}\Big\{B(z)\Big(z-(S^*(B(z))+S(z))(\Upsilon^*(\lambda)+z(1-\Upsilon^*(\lambda)))\Big) \\ &\quad \times\Big(\frac{\eta+\theta}{\lambda}+1\Big)+\Big((U(z)+\frac{1}{\lambda}(\theta+\eta))(S^*(B(z))+S(z)) \\ &\quad +(S_w^*(B_w(z))-1)-\frac{1}{\lambda}(\theta+\eta)\Big)z(1-\Upsilon^*(\lambda))B(z)+(1-S^*(B(z)) \\ &\quad \times\Big((\lambda U(z)+\theta+\eta)z+(\lambda(S_w^*(B_w(z))-1)-(\theta+\eta))(\Upsilon^*(\lambda) \\ &\quad +z(1-\Upsilon^*(\lambda)))\Big)+B(z)\Big(z-(S^*(B(z))+S(z))(\Upsilon^*(\lambda) \\ &\quad +z(1-\Upsilon^*(\lambda)))\Big)\frac{\lambda U(z)}{(\theta+\eta)}\Big\}. \qquad (28)\end{aligned}$$

(v) The amount of orbiting customers as the server is lower speed service

$$\Omega_2(z) \quad = \quad \frac{\lambda\Omega_{0,2}U(z)}{\theta+\eta} \tag{29}$$

Using normalizing condition , we find $\Omega_{0,1}$, $\Omega_{0,2}$ by putting $z=1$ and we apply L's hospital rule,
$\Omega_{0,1}+\Omega_{0,2}+\Upsilon(1)+\Omega_1(1)+\Omega_2(1)=1$,

$$\Omega_{0,2} = \frac{\Upsilon^*(\lambda)-\frac{\lambda r}{\delta}(1-S^*(\delta))}{\left[\begin{array}{r}\Upsilon^*(\lambda)(\frac{\eta+\theta}{\lambda}+1)+\frac{\lambda r}{\theta+\eta}(1-S_w^*(\theta+\eta))\\ +\frac{\lambda}{\delta}\Upsilon^*(\lambda)(1-r)(1-S^*(\delta))+\frac{\eta+\theta}{\delta}\Upsilon^*(\lambda)(1-r)\\ \times(1-S^*(\delta))-\frac{\lambda r}{\delta}S_w^*(\theta+\eta)(1-S^*(\delta))-\frac{\lambda}{\delta}S_w^*(\theta+\eta)\\ \times\Upsilon^*(\lambda)(1-r)+\frac{\lambda}{\theta+\eta}\Upsilon^*(\lambda)(1-r)(1-S_w^*(\theta+\eta)\end{array}\right]} \tag{30}$$

$$\Omega_{0,1} = \frac{\Upsilon^*(\lambda)-\frac{\lambda r}{\delta}(1-S^*(\delta))}{\frac{\lambda}{\eta+\theta}\left[\begin{array}{r}\Upsilon^*(\lambda)(\frac{\eta+\theta}{\lambda}+1)+\frac{\lambda r}{\theta+\eta}(1-S_w^*(\theta+\eta))\\ -\frac{\lambda r}{\delta}S_w^*(\theta+\eta)(1-S^*(\delta))+\frac{\eta+\theta}{\delta}\Upsilon^*(\lambda)(1-r)\\ \times(1-S^*(\delta))+\frac{\lambda}{\delta}\Upsilon^*(\lambda)(1-r)(1-S^*(\delta))\\ +\frac{\lambda}{\theta+\eta}\Upsilon^*(\lambda)(1-r)(1-S_w^*(\theta+\eta)\\ -\frac{\lambda}{\delta}S_w^*(\theta+\eta)\Upsilon^*(\lambda)(1-r)\end{array}\right]} \tag{31}$$

4 System Performance Measures

When the server is not being utilized,the steady state probability is $\Upsilon(1)$

$$\Upsilon(1) = \frac{(1-\Upsilon^*(\lambda))\Omega_{0,2}\left[\begin{array}{r}(1-S_w^*(\theta+\eta)[\frac{\lambda r}{\delta}(1-S^*(\delta))+\frac{\lambda r}{\theta+\eta}]\\ +(\frac{(\eta+\theta)r}{\delta})(1-S^*(\delta)\end{array}\right]}{\Upsilon^*(\lambda)-\frac{\lambda r}{\delta}(1-S^*(\delta)} \tag{32}$$

When the server is busy, let $\Omega_1(1)$ be the steady state probability.

$$\Omega_1(1) = \frac{(1-S^*(\delta))\Omega_{0,2}\begin{bmatrix}(\eta+\theta)\Upsilon^*(\lambda)-\Upsilon^*(\lambda)(\lambda(S_w^*(\theta+\eta)-1)) \\ \qquad +\dfrac{\lambda^2 r}{\theta+\eta}(1-S_w^*(\theta+\eta))\end{bmatrix}}{\delta[\Upsilon^*(\lambda)-\dfrac{\lambda r}{\delta}(1-S^*(\delta)]} \tag{33}$$

When the server is providing slower service, let $\Omega_2(1)$ be the steady state probability.

$$\Omega_2(1) = \frac{\lambda\Omega_{0,2}(1-S_w^*(\theta+\eta))}{\theta+\eta} \tag{34}$$

The busy cycle and busy period's expected durations are $E(T_b)$ and $E(T_c)$. Then

$$\begin{aligned} E(T_b) &= \frac{1}{\lambda}\left[\frac{1}{\Omega_{0,1}}-1\right], \\ E(T_c) &= \frac{1}{\lambda\Omega_{0,1}}, \\ E(T_0) &= \frac{1}{\lambda}. \end{aligned}$$

where the duration of the system's empty state is indicated by the time T_0.

$$E(T_b) = \frac{\begin{bmatrix}\Upsilon^*(\lambda)+\dfrac{(\eta+\theta)r}{\delta}(1-S^*(\delta))+\dfrac{\lambda r}{\theta+\eta}(1-S_w^*(\theta+\eta)) \\ +\dfrac{\eta+\theta}{\delta}\Upsilon^*(\lambda)(1-r)(1-S^*(\delta))-\dfrac{\lambda r}{\delta}S_w^*(\theta+\eta) \\ \times(1-S^*(\delta))+\dfrac{\lambda}{\theta+\eta}\Upsilon^*(\lambda)(1-r)(1-S_w^*(\theta+\eta) \\ +\dfrac{\lambda}{\delta}\Upsilon^*(\lambda)(1-r)(1-S^*(\delta))-\dfrac{\lambda}{\delta}S_w^*(\theta+\eta)\Upsilon^*(\lambda)(1-r)\end{bmatrix}}{(\theta+\eta)[\Upsilon^*(\lambda)-\dfrac{\lambda r}{\delta}(1-S^*(\delta))]} \tag{35}$$

$$E(T_c) = \frac{\begin{bmatrix}\Upsilon^*(\lambda)(\dfrac{\eta+\theta}{\lambda}+1)+\dfrac{\lambda r}{\theta+\eta}(1-S_w^*(\theta+\eta)) \\ +\dfrac{\eta+\theta}{\delta}\Upsilon^*(\lambda)(1-r)(1-S^*(\delta))-\dfrac{\lambda r}{\delta}S_w^*(\theta+\eta) \\ \times(1-S^*(\delta))+\dfrac{\lambda}{\theta+\eta}\Upsilon^*(\lambda)(1-r)(1-S_w^*(\theta+\eta) \\ +\dfrac{\lambda}{\delta}\Upsilon^*(\lambda)(1-r)(1-S^*(\delta))-\dfrac{\lambda}{\delta}S_w^*(\theta+\eta)\Upsilon^*(\lambda)(1-r)\end{bmatrix}}{(\theta+\eta)[\Upsilon^*(\lambda)-\dfrac{\lambda r}{\delta}(1-S^*(\delta))]} \tag{36}$$

5 Particular Cases

Case(i) Assuming that $r = 1$ then our model reduces to a non Markovian retrial queue with single working vacation, vacation interruption, disaster and working breakdown.
Case(ii) Assuming that if there is no disaster, then our model reduces to a non Markovian retrial queue with Balking, single working vacation and vacation interruption.
Case(iii) Assuming that if there is no disaster, $r = 1$, and no vacation, then our model reduces to a non Markovian retrial queue.

6 Numerical results

In Figure 1 displays the appropriate line graphs and Table 1 contains the values of $E(T_b)$ by fixing the values of $\mu = 4$, $\mu_w = 2$, $\lambda = 3$, $\theta = 6$, and $r = 0.5$ subject to stability conditions and extending the value of η from 1 to 2 increased with 0.2 and θ from the graph suggests that $E(T_b)$ decreases as η increases as would be predicted.

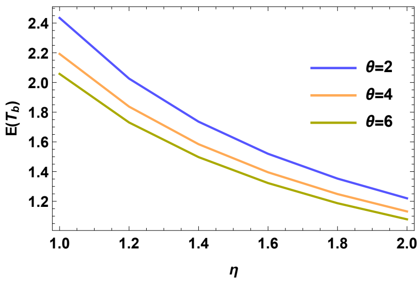

Figure 1: $E(T_b)$ with turn over of η

η	$\theta = 2$	$\theta = 4$	$\theta = 6$
1.0	8.0714	5.1388	4.1767
1.2	6.3738	3.9925	3.2156
1.4	5.3334	3.2963	2.6343
1.6	4.6285	2.8277	2.2444
1.8	4.1185	2.4905	1.9645
2.0	3.7321	2.2361	1.7537

Table 1: $E(T_b)$ with turn over of η

In Figure 2 displays the appropriate line graphs and Table 2 contains the values of $E(T_b)$ subject to stability conditions, by fixing the values of $\mu = 2$, $\mu_w = 1$, $\lambda = 4$, $\theta = 4$, and $r = 0.2$, and extending the values of δ from 1 to 2 increased-with 0.2 and η. The graph suggests that $E(T_b)$ decreases as expected when δ increases.

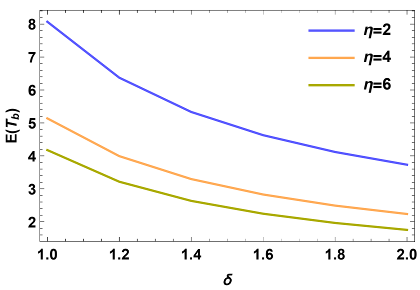

Figure 2: $E(T_b)$ with turn over of δ

δ	$\eta = 2$	$\eta = 4$	$\eta = 6$
1.0	8.0714	5.1388	4.1767
1.2	6.3738	3.9925	3.2156
1.4	5.3334	3.2963	2.6343
1.6	4.6285	2.8277	2.2444
1.8	4.1185	2.4905	1.9645
2.0	3.7321	2.2361	1.7537

Table 2: $E(T_b)$ with turn over of δ

In Figure 3 displays the appropriate line graphs and Table 3 contains the values of $E(T_b)$ by fixing the values of $\mu = 3$, $\mu_w = 2$, $\lambda = 3$, $\theta = 1$, and $r = 0.4$, subject to stability conditions, and extending the values of δ from 1 to 2 incremented with 0.2 and η. From the graph, it can be deduced that $E(T_c)$ decreases as expected when δ increases.

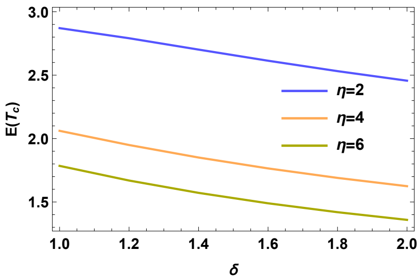

Figure 3: $E(T_c)$ with turn over of δ

δ	$\eta = 2$	$\eta = 4$	$\eta = 6$
1.0	2.8708	2.0610	1.7847
1.2	2.7911	1.9492	1.6691
1.4	2.7016	1.8505	1.5719
1.6	2.6137	1.7646	1.4896
1.8	2.5316	1.6898	1.4194
2.0	2.4564	1.6245	1.3589

Table 3: $E(T_c)$ with turn over of δ

In Figure 4 displays the appropriate line graphs and Table 4 contains the values of $E(T_b)$ subject to stability conditions, by fixing the values of $\mu = 3$, $\mu_w = 2$, $\lambda = 3$, $\theta = 1$, and $r = 0.4$, and extending the values of η from 1 to 2 increased with 0.2 and δ. The graph suggests that $E(T_c)$ decreases as η increases as would be predicted.

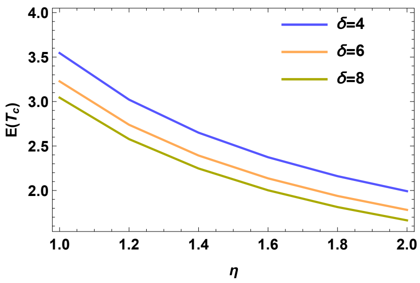

Figure 4: $E(T_c)$ with turn over of η

η	$\delta = 4$	$\delta = 6$	$\delta = 8$
1.0	3.5452	3.2272	3.0440
1.2	3.0212	2.7388	2.5773
1.4	2.6499	2.3931	2.2472
1.6	2.3738	2.1363	2.0022
1.8	2.1609	1.9385	1.8135
2.0	1.9920	1.7818	1.6641

Table 4: $E(T_c)$ with turn over of η

7 Conclusion

In this paper, non Markovian retrial queue, balking, disaster under working breakdown and working vacation is analysed. We discovered the PGF for the total and average number of people in invisible waiting area. We derived some performance measures and deduced some particular cases and illustrated some numerical results.

References

[1] Afthab begum, M.I., Fijy Jose, P., and Bama, S. (2016): An $M^X/G/1$ queue with disasters and working breakdown, Int. Jou. Sci. Res and Pub, Vol. 6, pp. 2250-3153 (2016).

[2] Chandrasekaran, V.M. , Indhira, K. , Saravanarajan, M.C., and Rajadurai, P.: A survey on working vacation queueing models, International Journal of Pure and Applied Mathematics, Vol.106 No.6 ,pp. 33-41 (2016).

[3] Jain, and Sigman.: A Pollaczeck- Khinchine formula for $M/G/1$ queue with disasters, J. Appl. Prob. Vol. 33, pp. 1191-1200 (1996).

[4] Kalidass, K., and Ramanath, K.: A queue with working breakdowns, Computers and Industrial Engineering, Vol 63(4), pp. 779783 (2012).

[5] Kim, B.K., and Lee, D.H.: The $M/G/1$ queue with disasters and working breakdowns, Applied Mathematical Modelling, Vol. 38, pp. 1788-1798 (2014).

[6] Manoharan, P., and Sankarasasi, K.: Analysis of a multitype service of a non-markovian queue with breakdown, delay time and optional vacation, Advances and Applications in Mathematical Sciences, Vol. 20, pp. 975-1001 (2021).

[7] Pazhani Bala Murugan, S., Santhi, K.: An M/G/1 retrial queue with multiple working vacation, International Journal of Mathematics and its Applications, Vol.4, No. 2-D, pp. 35-48 (2016).

[8] Rajadurai P., A study on an M/G/1 retrial G-queue with unreliable server under variant working vacations policy and vacation interruption, *Songklanakarin Journal of Science Technology*, 40(1), pp. 231-242 (2018a).

[9] Rajadurai, P.: Sensitivity analysis of an M/G/1 retrial queueing system with disaster under working vacations and working breakdowns, RAIRO-Operations Res, Vol. 52(1), pp. 35-54 (2018).

[10] Rajadurai P, Chandrasekaran V. M and Saravanarajan M. C., Analysis of an M[X]/G/1 unreliable retrial G-queue with orbital search and feedback under Bernoulli vacation schedule, *OPSEARCH*, 53,pp. 197-223 (2016).

[11] Sennot L. I., Humblet P. A and Tweedi R. L., Mean drifts and the non-Ergodicity of Markov chains. *Oper. Res,* Vol. 31, pp. 783-789 (1983).

[12] Servi, L., Finn, S.: M/M/1 queue with working vacations (M/M/1/WV), Perform. Eval, Vol. 50, pp. 41-52 (2002).

[13] Wu, D., Takagi, H.: M/G/1 queue with multiple working vacations, Perform. Eval, Vol. 63, pp. 654-681 (2006).

J. COMPUTATIONAL ANALYSIS AND APPLICATIONS, VOL. 31, NO. 2, 2023, COPYRIGHT 2023 EUDOXUS PRESS, LLC

A mathematical study of fractional order unsteady natural convective Casson fluid flow past an infinitely vertical plate with heat and mass transfer

Sapna Tyagi [1], Monika Jain [1*], Jagdev Singh[1]

[1] Department of Mathematics, JECRC University, Jaipur-303905, Rajasthan, India

tyagisapna1990@gmail.com, monikaj@gmail.com, jagdevsinghrathore@gmail.com

Abstract. Research on Casson fluid is very important due to its applicability in the progress of industrial and engineering industries. Here, a fractional order model of the Casson fluid over an oscillating plate in the presence of thermal radiation with constant wall temperature and concentration has been considered. The solution of this fractional model is obtained with the help of Laplace transform technique in terms of Wright function. The graphical analysis is also done by making several variations in parametric values including fractional parameter, mass Grashoff number, Prandtl number, velocity, temperature, concentration profiles etc.

1. Introduction

The physical characteristic of non-Newtonian fluid is always a barrier for researchers while solving the problems of non-Newtonian fluid. There is yet no comprehensive model that covers every aspect of a non-Newtonian fluid. Non-Newtonian fluid is widely used in the manufacturing and processing industries, thus researchers are constantly attempting to develop new models. One of the models is the Casson fluid model. In 1959, Casson [22] was the first to present the rheological data of pigment oil suspensions in printing ink.

Khalid et al. [1] studied the Casson fluid across an oscillating vertical plate for Unsteady boundary layer flow with constant wall temperature.

2010 *Mathematics Subject Classification.* 34A34, 26A33.

Key words and phrases. Casson fluid, fractional order, Wright function, Laplace transform.

*Corresponding Author.

1

Mahantesh et al. [4] studied the convective flow of Casson fluid across an oscillating plate using non-coaxial rotation and quadratic density fluctuation as its boundary conditions. Using variables without dimensions, the governing equations were first transformed into a non - dimensional form. Analytical solutions of the dimensionless momentum, heat, and mass equations were achieved using the Laplace transform method.

Using an exponentially permeable decreasing sheet, Nadeem et al. [25] investigated the boundary layer MHD flow of Casson fluid. The Adomian decomposition method was employed to arrive at the analytical answer to the problem. The velocity distributions resulting from a number of fascinating parameters were displayed and investigated.

The role of the magnetic flux on the three-dimensional Casson fluid flow over the boundary layer of a stretching porous sheet was taken into account in the study by Nadeem et al., [26] . It was discovered that the magnetic field, Casson fluid parameter, and porosity parameter all reduced the velocity profiles in the x and y directions.

The effects of chemical processes and heat generation of MHD convection Casson fluid flow model in a porous media using a revolving vertical plate is provided in the study done by Khan et al. [5].

The unstable MHD free convection flow of Casson fluid through a porous medium past a vertical plate that was moving exponentially was explored by Mohan et al.[24] in the presence of thermal radiation, chemical interaction, and a heat source or sink. They discovered that the velocity profiles decrease when the heat flow, magnetic field parameter, prandtl number, heat source, and Casson parameter increase in value.

Deka [3] has conducted studies of an unstable MHD casson fluid in nanopores with heat transfer through an accelerating vertical plate. It has been discovered that the Casson parameter increases skin friction and fluid velocity. Along with the casson parameter, the surface shear stress also rises.

It is assumed that the Casson fluid, a shear-thinning fluid, has infinite viscosity at zero rate of shear, zero viscosity at infinite rate of shear, and a yield stress below which no flow occurs. A fluid behaves like a solid when it is under conditions where the yield stress is greater than the shear stress. When the applied yield stress is greater than the applied shear stress, the fluid starts to flow. Casson fluid can take the form of things like honey, soup, chocolate, tomato sauce, jelly, blood, sludge, fused polymers, etc. These fluid models have been shown to have important uses in the biomechanics, textile, cosmetic, polymer processing, and pharmaceutical industries.

The Casson fluid flow across an oscillating plate with chemical reaction and sliding phenomenon was expressed by Saqib et al. [16]. The investigation concentrated on the mass and heat transport processes. The Laplace transform method was used to analyse the mathematical model once it had been transformed into dimensionless form. The profiles of velocity, temperature, and concentration were plotted.

Fractional derivatives have recently piqued the interest of many scholars due to the extensive coverage of derivatives and integrals of non-integer order. A variety of physical phenomena or natural circumstances have been studied with the help of fractional calculus, together with the rheological properties of winding polymers, traffic modelling, electric circuits, signal and image processing, electrical networks, stochastic processes and bioengineering.

Imran et al. [18] used two distinct fractional derivatives known as Caputo and Caputo-Fabrizio to study the convection flow of Newtonian fluid.The solutions to the concentration , temperature and velocity profiles were discovered by using the Laplace transform approach. The results were graphically depicted to compare and contrast the two fractional derivatives.

Also, the Caputo time-fractional derivatives are used by Imran et al. [19] to formulate fluid flows with Newtonian heating and arbitrary velocities.It was possible to obtain the dimensionless form of the governing equations by using the specified dimensionless variables. Using the Laplace transform approach, the dimensionless equations were solved.

Numerous scholars have noted the impact of fractional parameters on temperature and velocity characteristics. The computational analysis of fractional diffusion equations occurring in oil pollution has been done by Singh et al., [12].Research by Khan et al.,[11]gives the effect of fractional Caputo time derivatives of general Cassonian fluids with oscillating boundary conditions.

Ali et al. [9] employed the Caputo fractional derivative to examine the blood flow in a horizontal cylinder that was simulated by a Casson fluid. Magnetic particles were present in the fluid flow that was being driven by an oscillating pressure gradient. With the use of finite Hankel and Laplace transformations, the effects of magnetodynamics on Casson's fluids have been investigated and described.

The researchers observed that the fractional order fluid model performs noticeably differently from the conventional model. Several recent important analytical investigations on fluid problems can be found in preceding study [7], [8], [24], and [24].

Atangana-Baleanu and Caputo-Fabrizio are two fractional derivatives that are compared in Sheikh et al. comparative analysis for the convection of Casson's liquid across an infinite vertical flat plate, together with heat and mass transfer[20].

The researchers discovered that for a given unit of time, the velocities calculated using the Caputo-Fabrizio and Atangana-Baleanu operators are the same. Exact solutions for both situations were discovered using the Laplace transform methodology, and the outcomes were compared graphically and in tabular form.On the other hand, when time is less than unity, variance occurs and further differences increase as time increases.
For more definitions and results about the fractional operators, the reader can referes to [5], [13], [14].

2. Mathematical formulation of the problem

The present study takes into account the in compressible Casson fluid flow past an infinitely vertical plate in a free convection flow that is unsteady. Here, the flow range is $y > 0$, and y is the plate's coordinate normal.Primarily, at a time $\tau = 0$, the fluid and the plate are both at rest with a uniform surface concentration of C_∞^* and temperature T_∞^*. The plate begins to accelerate in its plane at time $\tau > 0$ according to a velocity $A\tau$, where unvarying A represents the plate's acceleration. Both the concentration and plate temperature are increased simultaneously to $T_\infty^*$and C_∞^* respectively, and then kept constant. The spatial variable y and the time variable t affect the velocity and temperature.

Following the use of the Boussinesq approximation and unidirectional flow, the momentum, energy, and concentration equations acquire the following forms.

$$\rho \frac{\partial \mathrm{u}^*}{\partial \tau^*} = \mu \left(1 + \frac{1}{\beta}\right) \frac{\partial^2 \mathrm{u}^*}{\partial \mathrm{y}^{*2}} + \rho \mathrm{g} \gamma \left(\mathrm{T}^* - \mathrm{T}_\infty^*\right) + \rho \mathrm{g} \beta' \left(\mathrm{C}^* - \mathrm{C}_\infty^*\right), \tag{2.1}$$

$$\rho \mathrm{c_p} \frac{\partial \mathrm{T}^*}{\partial \tau^*} = \mathrm{k} \frac{\partial^2 \mathrm{T}^*}{\partial \mathrm{y}^{*2}} - \frac{\partial \mathrm{q_r^*}}{\partial \mathrm{y}^*}, \tag{2.2}$$

$$\frac{\partial \mathrm{C}^*}{\partial \tau^*} = \frac{1}{\mathrm{S_c}} \frac{\partial^2 \mathrm{C}^*}{\partial \mathrm{y}^{*2}}. \tag{2.3}$$

Here, β refers Casson parameter, u^* represent fluid in the y-direction, and time variable is denoted by τ^*. The fluid temperature near the plate is T^*, while T_∞^* refers plate's temperature. ρ denotes fluid density,μ is dynamic viscosity, Y refers to coefficients of the thermal expansion, q_r^* present radiative heat flux, c_p is the heat constant pressure, S_c is Schmidt number, k denotes thermal conductivity.

C^* is the concentration of the fluid near the plate, while C^*_∞ refers concentration of the plate associated with initial and boundary conditions:

$$\left.\begin{array}{c} u^*\left(y^*,0\right)=0, u^*\left(0,\tau^*\right)=\mathrm{F}\tau^{**}; u^*\left(\infty,\tau^*\right)=0 \\ \mathrm{T}^*\left(\mathrm{y}^*,0\right)=\mathrm{T}^*_\infty, \mathrm{T}^*\left(0,\tau^*\right)=\mathrm{T}^*_\mathrm{w}, \mathrm{T}^*\left(\infty,\tau^*\right)=\mathrm{T}^*_\infty \\ \mathrm{C}^*\left(\mathrm{y}^*,0\right)=\mathrm{C}^*_\infty, \mathrm{C}^*\left(0,\tau^*\right)=\mathrm{C}^*_\mathrm{w}, \mathrm{C}^*\left(\infty,\tau^*\right)=\mathrm{C}^*_\infty \end{array}\right\} \tag{2.4}$$

q_r^* is the radiative heat flux in equation (2.2). When q_r^* is differentiated in terms of y using Rosseland's approximation [2],[10],[27],[28], equation (2.2) becomes:

$$\rho c_p \frac{\partial T^*}{\partial \tau^*} = k\frac{\partial^2 T^*}{\partial y^{*2}} - \left(-\frac{16\sigma {T^*_\infty}^3}{3k^*}\right)\frac{\partial^2 T^*}{\partial y^{*2}}. \tag{2.5}$$

3. Problem Solution

The fundamental dimensional equations (2.1), (2.3), and (2.5) are changed into dimensionless equations. The solutions are then derived by employing the Laplace transform approach.
By employing appropriate dimensionless variables,

$$\mathrm{u}=\frac{\mathrm{u}^*}{(\vartheta\mathrm{A})^{\frac{1}{3}}}, \mathrm{t}=\frac{\tau^*(\mathrm{A})^{\frac{2}{3}}}{(\vartheta)^{\frac{1}{3}}}, \mathrm{y}=\frac{\mathrm{y}^*(\mathrm{A})^{\frac{1}{3}}}{(\vartheta)^{\frac{2}{3}}}, \mathrm{T}=\frac{\mathrm{T}^*-\mathrm{T}^*_\infty}{\mathrm{T}^*_\mathrm{w}-\mathrm{T}^*_\infty}\, and\, \mathrm{C}=\frac{\mathrm{C}^*-\mathrm{C}^*_\infty}{\mathrm{C}^*_\mathrm{w}-\mathrm{C}^*_\infty}. \tag{3.1}$$

The governing momentum (2.1), concentration (2.3) and energy (2.5) equations in the dimensionless form in view of (3.1) are

$$\frac{\partial \mathrm{u}}{\partial \mathrm{t}} = \left(1+\frac{1}{\beta}\right)\frac{\partial^2 \mathrm{u}}{\partial \mathrm{y}^2} + \mathrm{GrT} + \mathrm{GmC}, \tag{3.2}$$

$$\mathrm{S_c}\frac{\partial \mathrm{C}}{\partial \mathrm{t}} = \frac{\partial^2 \mathrm{C}}{\partial \mathrm{y}^2}, \tag{3.3}$$

$$\frac{\partial \mathrm{T}}{\partial \mathrm{t}} = \left(\frac{1+\mathrm{N}}{\mathrm{Pr}}\right)\frac{\partial^2 \mathrm{T}}{\partial \mathrm{y}^2}. \tag{3.4}$$

Also the boundary conditions (2.4) takes the form

$$\left.\begin{array}{c} \mathrm{u}\left(\mathrm{y},0\right)=0, \mathrm{u}\left(0,\tau\right)=\mathrm{t}; \mathrm{u}\left(\infty,\tau\right)=0 \\ \mathrm{T}\left(\mathrm{y},0\right)=0, \mathrm{T}\left(0,\tau\right)=1, \mathrm{T}\left(\infty,\tau\right)=0 \\ \mathrm{C}\left(\mathrm{y},0\right)=0, \mathrm{C}\left(0,\tau\right)=1, \mathrm{C}\left(\infty,\tau\right)=0. \end{array}\right\} \tag{3.5}$$

Next, equations (3.2), (3.3), and (3.4) are defined in terms of Caputo fractional derivatives as:

$$\mathrm{D}^\alpha_\mathrm{t}\mathrm{u} = \left(1+\frac{1}{\beta}\right)\frac{\partial^2 \mathrm{u}}{\partial \mathrm{y}^2} + \mathrm{GrT} + \mathrm{GmC}, \tag{3.6}$$

$$\mathrm{S_c D_t^\alpha C} = \frac{\partial^2 \mathrm{C}}{\partial \mathrm{y}^2}, \tag{3.7}$$

$$\left(\frac{\mathrm{Pr}}{1+\mathrm{N}}\right) \mathrm{D_t^\alpha T} = \frac{\partial^2 \mathrm{T}}{\partial \mathrm{y}^2}, \tag{3.8}$$

where D denotes the differential operator, the fractional operator is α, whereas Gr, N, Pr and Gm are the thermal Grashof number, radiation and Prandtl number and mass Grashof number respectively.

4. Laplace Transform Technique

Unsteady differential equations are frequently solved using the Laplace transform, an integral transform technique. The second order differential equations for the partial differential equations (3.2), (3.3), and (3.4)are generated on using the Laplace transform technique.

$$\left(1+\frac{1}{\beta}\right) \frac{\mathrm{d}^2 \bar{u}}{\mathrm{dy}^2} - \mathrm{s}^\alpha \bar{u}\left(\mathrm{y},\mathrm{s}\right) + \mathrm{Gr}\bar{T} + \mathrm{Gm}\bar{C} = 0, \tag{4.1}$$

$$\frac{\mathrm{d}^2 \bar{C}}{\mathrm{dy}^2} - \mathrm{s}^\alpha \mathrm{S_c} \bar{C}\left(\mathrm{y},\mathrm{s}\right) = 0, \tag{4.2}$$

$$\frac{\mathrm{d}^2 \bar{T}}{\mathrm{dy}^2} - \left(\frac{\mathrm{Pr}}{1+\mathrm{N}}\right) \mathrm{s}^\alpha \bar{T}\left(\mathrm{y},\mathrm{s}\right) = 0. \tag{4.3}$$

Eq. (4.1), (4.2) and (4.3) are then solved by using the undetermined coefficient method and the solutions are presented as

$$\bar{u}\left(\mathrm{y},\mathrm{s}\right) = \frac{1}{\mathrm{s}^2}\mathrm{e}^{-\mathrm{y}\sqrt{\frac{\mathrm{s}^\alpha}{\mathrm{z}}}} + \frac{\mathrm{Gr_0}}{\mathrm{s}^{\alpha+1}}\mathrm{e}^{-\mathrm{y}\sqrt{\frac{\mathrm{s}^\alpha}{\mathrm{z}}}} + \frac{\mathrm{Gm_0}}{\mathrm{s}^{\alpha+1}}\mathrm{e}^{-\mathrm{y}\sqrt{\frac{\mathrm{s}^\alpha}{\mathrm{z}}}} - \frac{\mathrm{Gr_0}}{\mathrm{s}^{\alpha+1}}\mathrm{e}^{-\mathrm{y}\sqrt{\mathrm{as}^\alpha}} - \frac{\mathrm{Gm_0}}{\mathrm{s}^{\alpha+1}}\mathrm{e}^{-\mathrm{y}\sqrt{\mathrm{S_c s}^\alpha}}, \tag{4.4}$$

$$\bar{T}\left(\mathrm{y},\mathrm{s}\right) = \frac{1}{\mathrm{s}}\mathrm{e}^{-\mathrm{y}\sqrt{\mathrm{as}^\alpha}}, \tag{4.5}$$

$$\bar{C}\left(\mathrm{y},\mathrm{s}\right) = \frac{1}{\mathrm{s}}\mathrm{e}^{-\mathrm{y}\sqrt{\mathrm{S_c s}^\alpha}}, \tag{4.6}$$

where $\mathrm{z} = \left(1+\frac{1}{\beta}\right), \mathrm{a} = \left(\frac{\mathrm{Pr}}{1+\mathrm{N}}\right), \mathrm{Gr_0} = \frac{\mathrm{Gr}}{(\mathrm{az}-1)}$ and $\mathrm{Gm_0} = \frac{\mathrm{Gm}}{(\mathrm{S_c z}-1)}$. The final solution to the problem is provided by taking inverse Laplace of equations (4.4), (4.5), and (4.6).

$$\begin{aligned}\mathrm{u}\left(\mathrm{y},\mathrm{t}\right) = {} & \mathrm{t}\varphi\left(2,-\tfrac{\alpha}{2};-\mathrm{y}\sqrt{\tfrac{\mathrm{s}^\alpha}{\mathrm{z}}}\mathrm{t}^{-\frac{\alpha}{2}}\right) + \tfrac{\mathrm{Gr_0}}{\Gamma(\alpha)}\mathrm{t}^{\alpha-1}\varphi\left(1,-\tfrac{\alpha}{2};-\mathrm{y}\sqrt{\tfrac{\mathrm{s}^\alpha}{\mathrm{z}}}\mathrm{t}^{-\frac{\alpha}{2}}\right)\\ & + \tfrac{\mathrm{Gm_0}}{\Gamma(\alpha)}\mathrm{t}^{\alpha-1}\varphi\left(1,-\tfrac{\alpha}{2};-\mathrm{y}\sqrt{\tfrac{\mathrm{s}^\alpha}{\mathrm{z}}}\mathrm{t}^{-\frac{\alpha}{2}}\right) - \tfrac{\mathrm{Gr_0}}{\Gamma(\alpha)}\mathrm{t}^{\alpha-1}\varphi\left(1,-\tfrac{\alpha}{2};-\mathrm{y}\sqrt{\mathrm{a}}\mathrm{t}^{-\frac{\alpha}{2}}\right)\\ & - \tfrac{\mathrm{Gm_0}}{\Gamma(\alpha)}\mathrm{t}^{\alpha-1}\varphi\left(1,-\tfrac{\alpha}{2};-\mathrm{y}\sqrt{\mathrm{S_c}}\mathrm{t}^{-\frac{\alpha}{2}}\right),\end{aligned} \tag{4.7}$$

$$\mathrm{C}\left(\mathrm{y},\mathrm{t}\right)=\varphi\left(1,-\frac{\alpha}{2};-\mathrm{y}\sqrt{\mathrm{S_c}}\mathrm{t}^{-\frac{\alpha}{2}}\right), \tag{4.8}$$

$$\mathrm{T}\left(\mathrm{y},\mathrm{t}\right)=\varphi\left(1,-\frac{\alpha}{2};-\mathrm{y}\sqrt{\mathrm{a}}\mathrm{t}^{-\frac{\alpha}{2}}\right), \tag{4.9}$$

where $\varphi\left(a,-\varrho;\zeta\right)=\sum\limits_{n=0}^{\infty}\frac{(\zeta)^n}{n!\Gamma(a-n\varrho)}$ is the Wright function.
Equations (4.7)–(4.9) are bounded by boundary conditions as in (3.5).

5. Result and Discussion

For the free convection flow of a generalised fractional Casson fluid over an accelerating plate, equations (4.4), (4.5), and (4.6) show the closed form. The graphs are generated with varied values of embedded parameters to study how different parameters affect the profiles of velocity, concentration, and temperature. The purpose of the graphs 1-3 is to investigate the impact of the fractional parameter, Prandtl number Pr, and N radiation on temperature profiles with different values.Figures 4–7 display the velocity profile graphs, which were plotted with various fractional parameters, Casson fluid parameters, mass Grashoff number Gm, and time t. In the meantime, Figure 8 shows validation of current solutions.

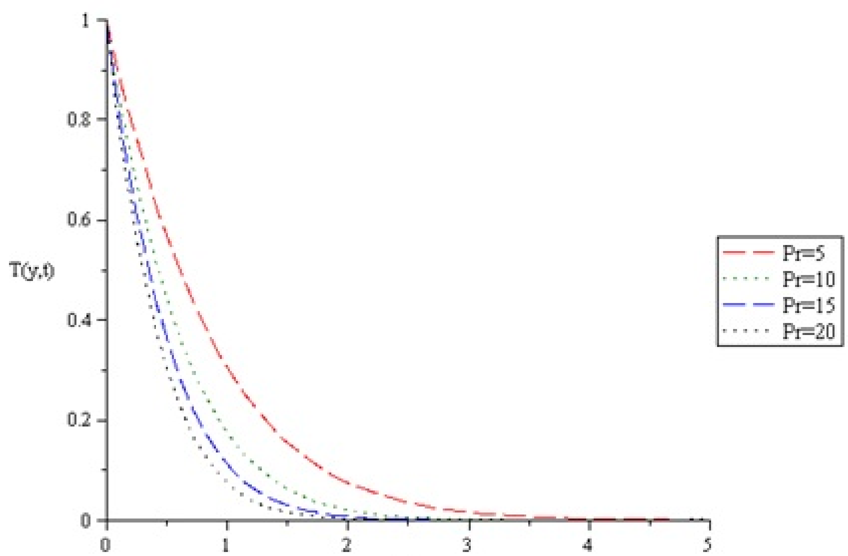

Fig1. Temperature profile with different Pr

The Prandtl number's impact on the temperature distribution is shown in Figure 1. The graph shows that as the value of Pr rises, the temperature profile rapidly falls. The thermal and momentum diffusivity relationship is defined by Prandtl number. Further, the thermal boundary layer thickness is more than the thickness of the momentum boundary layer when Pr , the Prandtl number is small because the fluid travels more slowly than heat transfer. Therefore, for higher Pr fluids, heat can flow from the sheet more quickly. However, a bigger Prandtl number might result in a thinner thermal boundary layer, which would then result in a weaker thermal force for transport and a lower temperature profile.

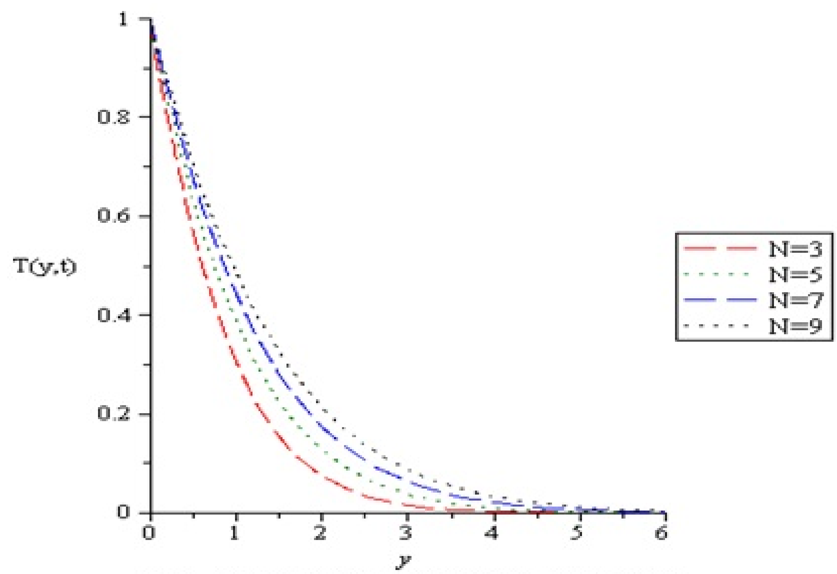

Fig2. Temperature profile with different N

Figure 2 displays the temperature profile of thermal radiation for constant values of Pr and t and various values of N. It is evident that a rise in temperature causes a rise in thermal radiation. The fluid temperature rises as a result of the growing radiation parameter's rising temperatures absorption.

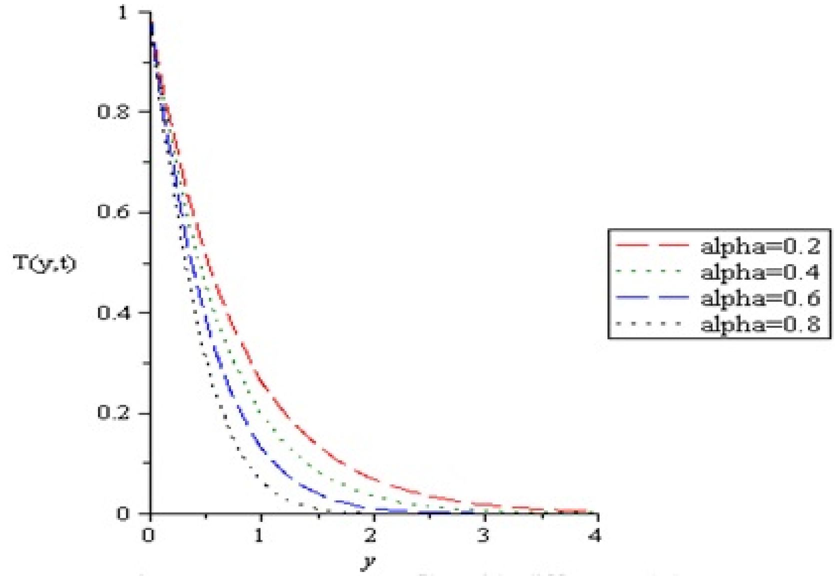

Fig3. Temperature profile with different alpha

Figure 3 illustrates the effect of fractional parameters on temperature. As shown in the figure, the temperature increases monotonically as falls. The outcome here can be helpful for a few real-world issues. By using the computed theoretical results and a suitable fractional mathematical model, the expected outcome and the range for an experimental design are assessed.

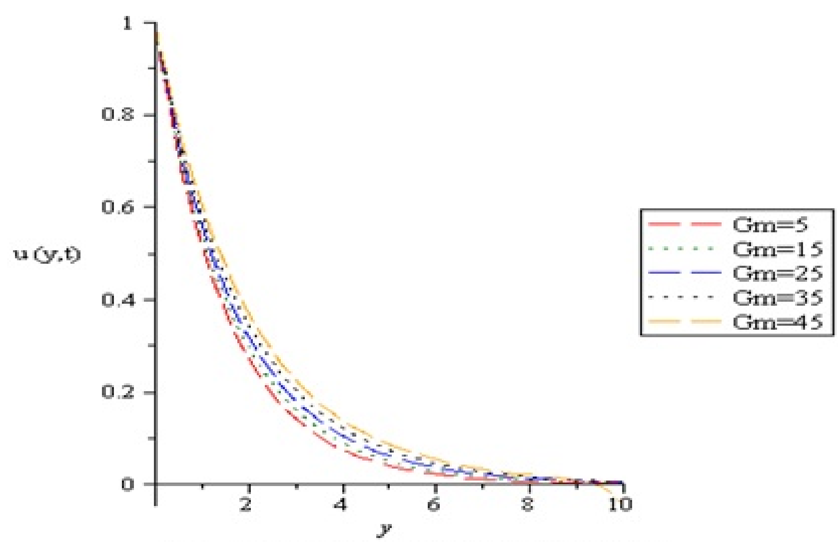

Fig4. Velocity profile with different Gm

The impact of the Grashoff number Gm on the velocity profile is depicted in Figure 4. It is possible to claim that when the value of Gm has been increased, the velocity value also goes up gradually.

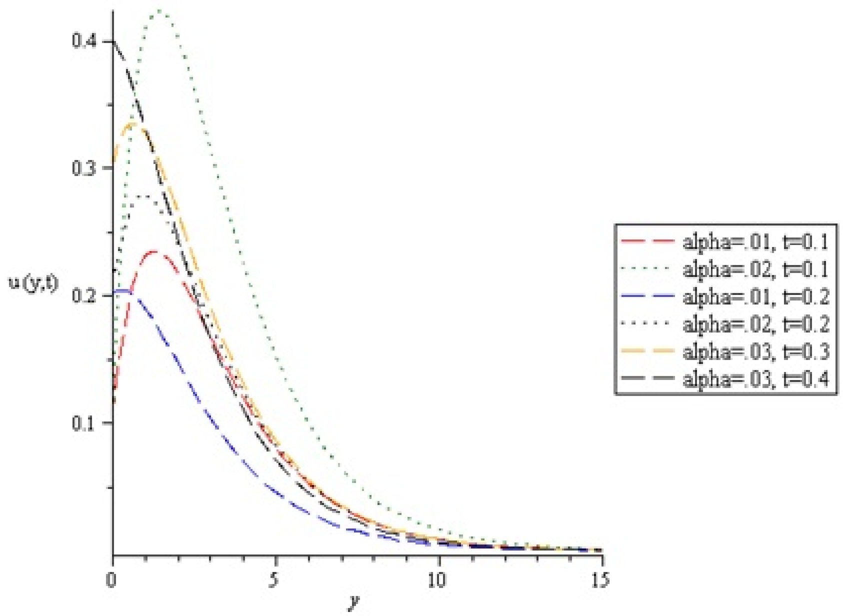

Fig5. Velocity profile with different t & alpha

Figure 5 effects of time and alpha toward the velocity. The velocity increases dramatically in figure 5.

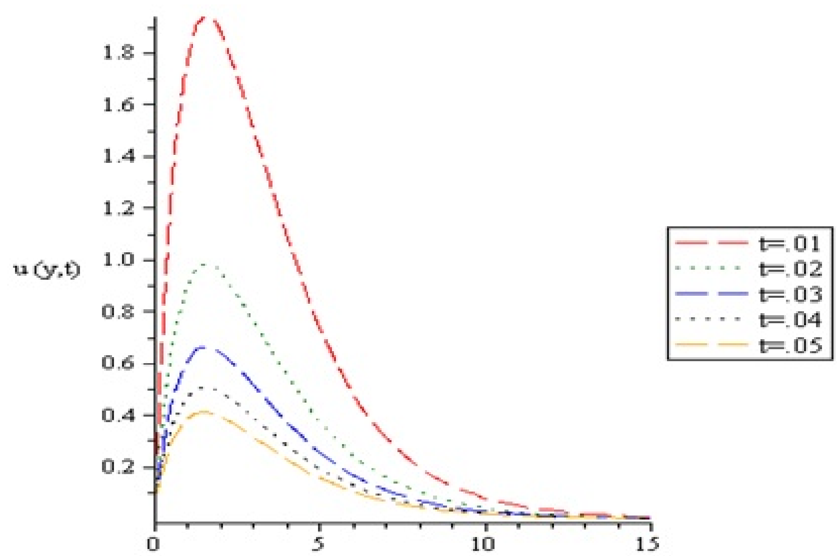

Fig 6. Velocity profile with different t

The impact of time t on velocity profiles is shown in Figure 6. The velocity declines but at a different rate as the value of t rises. The velocity decreases sharply in Figure 6. This tendency can be explained by the graphs' trend which indicates that as t increases, the energy produced by the fluid flow will eventually fall as well.

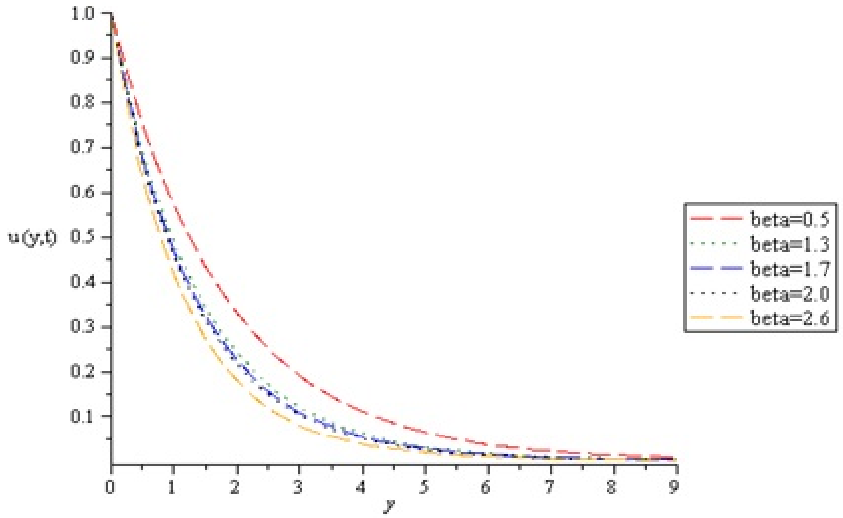

Fig 7. Velocity profile with different beta

The impact of the velocity profile by the Casson parameter is depicted in Figure 7. The velocity initially suffers a falling tendency before progressively increasing.

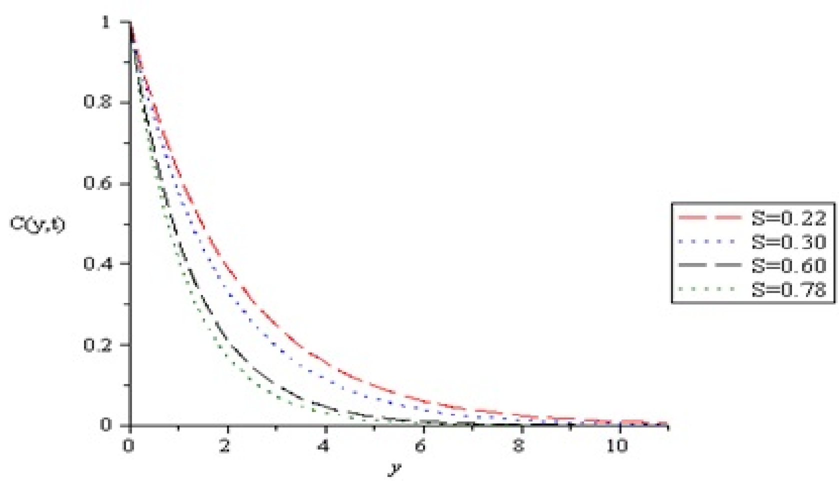

Fig 8. Concentration profile with different Schmidt number (S)

Schmidt number S's impact on the concentration profile may be seen in Figure 8.The value of concentration decrease progressively as the value rise up.

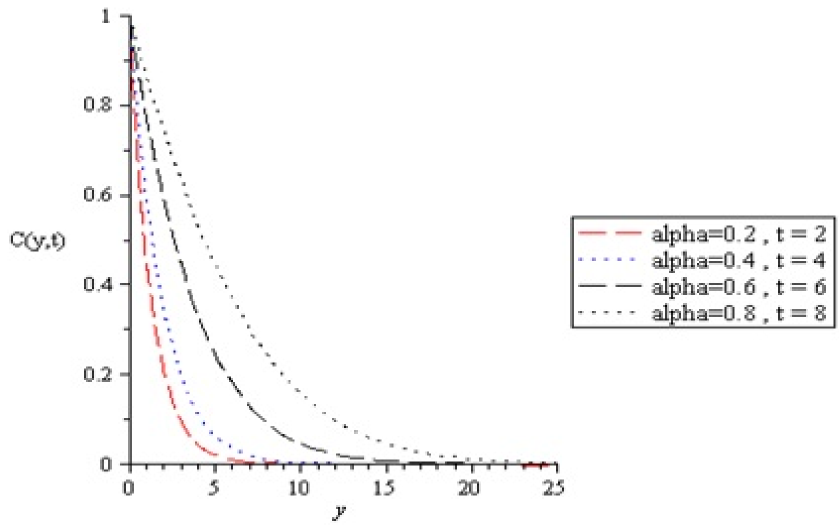

Fig 9. Concentration profile with different alpha and t

Figure 9 shows the effect of t and alpha on the concentration profile. As the value of t and alpha increases, the value of concentration raised steadily.

6. Conclusion

An accelerating plate's free convection flow of fractional order Casson fluid flow has been investigated in the present study. The solutions for velocity and temperature were obtained using the Laplace transform approach.The impact of several parameters on fluid flow, including the Casson fluid parameter, fractional parameter, time, Schmidt number (S), thermal radiation (N), and Prandtl number, is explored. Additionally, it is considered that the obtained results are reliable and provide a new points of view on Casson fluid flow.

References

[1] A. Khalid, I .Khan and S. Shafie, "Unsteady boundary layer flow of a casson fluid past an oscillating vertical plate with constant wall temperature." Malaysian Journal of Fundamental and Applied Science 11, no.1, 28-32(2015).

[2] A.B.M. Raju., P.R. Chandra, B. Malikarjuna and C.S.K. Raju, "Radiation absorption and Soret effects on MHD conducting fluid flow past an exponentially accelerated vertical plate." South East Asian J. Math . Math. Sci., vol. 2'1, no. 1, 1-9 (2020).

[3] A.K. Deka, "In the presence of thermal radiation through porous medium unsteady MHD casson fluid flow past an accelerated vertical plate." International Journal of Statistics and Applied Mathematics 5, no. 4, 213-228 (2020).

[4] B. Mahanthesh, T. Brizlyn, S. Shehzad and B. J. Gireesha, "Nonlinear Thermo-Solution Convective Flow of Casson Fluid over an Oscillating Plate Due to Non-Coaxial Rotation with Quadratic Density Fluctuation Exact Solutions." Multidiscipline Modeling in Materials and Structures 15, 818–8424 (2018).

[5] C. Li, D. Qian and Y. Chen, "On Riemann- Liouville and Caputo Derivative.", Discrete Dynamics in Nature and Society, vol.2011, Article Id 562494, (2011).

[6] D. Khan, A. Khan, I. Khan, F. Ali, F. ul. Karim and I. Tlili, "Effects of relative magnetic field, chemical reaction, heat generation and newtonian heating on convection flow of casson fluid over a moving vertical plate embedded in a porous medium." Scientific Reports 9, no. 1, 1–18(2019).

[7] E.K. Ghiasi and R. Saleh, "Analytical and numerical solutions to the 2d sakiadis flow of casson fluid with cross diffusion, inclined magnetic force, viscous dissipation and thermal radiation based on buongiorno's mathematical model." CFD Letters 11, no. 1, 40–54(2019).

[8] E.K. Mahmoud, "Analytical solution of modified bingham fluid flow through parallel plates channel subjected to forchheimer medium and hall current using linearized differential transformation method." Journal of Advanced Research in Numerical Heat Transfer 4, no. 1, 14–31(2021).

[9] F. Ali, N.A. Sheikh, I. Khan and M. Saqib, "Magnetic field effect on blood flow of Casson fluid in axisymmetric cylindrical tube: A fractional model." Journal of Magnetism and Magnetic Materials 423, 327-336 (2017).

[10] F.S. Ibrahim, A.M. Elaiw and A.A. Bakar, "Effects of the chemical reaction and radition absorption on the unsteady MHD free convection flow past a semi infinite vertical permeable moving plate with heat source and suction." Commun. Nonlinear Sci. Numer. Simul., vol. 13, no. 6, 1056-1066 (2008).

[11] I. Khan, N.A.Shah and D.Vieru, "Unsteady flow of generalized Casson fluid with fractional derivative due to an infinite plate." The European Physical Journal Plus 131, no. 6, 1-12(2016).

[12] J. Singh, A.M. Alshehri, S. M. Momaniand S.B. Hadid, " Computational Analysis of Fractional Diffusion Equations Occurring in Oil Pollution." Mathematics, 10, 20 (2022).

[13] J. Singh, B. Ganbari, D. Kumar and D. Baleanu, "Analysis of fractional model of guava for biological pest control with memory effect." Journal of Advanced Research, 32, 99-108 (2021).

[14] J. Singh, D. Kumar and D. Baleanu, "A new analysis of fractional fish farm model associated with Mittag-Leffler type kernel." International Journal of Biomathematics, vol 13, no. 2(2020).

[15] M. A. Qushairi, N.A. Jaafar, S. Shafie, Z. Ismail and M. Qasim, "Theoretical study on rotating casson fluid in moving channel disk." In Journal of Physics: Conference Series, vol. 1366, no. 1, p. 012039. IOP Publishing, (2019).

[16] M. Saqib, F. Ali, I. Khan and N. A. Sheikh, "Heat and mass transfer phenomena in the flow of Casson fluid over an infinite oscillating plate in the presence of first-order chemical reaction and slip effect.' Neural Computing and Applications 30, no.7, 2159-2172(2018).

[17] M.A. Imran, M. Aleem, M.B. Riaz, R.Ali and I. Khan, "A comprehensive report on convective flow of fractional (ABC) and (CF) MHD viscous fluid subject to generalized boundary conditions." Chaos, Solutions & Fractals, 118, 274-289(2019).

[18] M.A. Imran, N. A.Shah, I. Khan, and M. Aleem, "Applications of non-integer Caputo time fractional derivatives to natural convection flow subject to arbitrary velocity and Newtonian heating." Neural Computing and Applications 30, no. 5, 1589-1599(2018).

[19] M.A. Imran, S. Sarwar, M. Abdullah and I. Khan, "An analysis of the semi-analytic solutions of a viscous fluid with old and new definitions of fractional derivatives." Chinese journal of physics 56, no. 5, 1853-1871(2018).

[20] M.G. Reddy, P.V. Kumari and P. Padma, "Effects of thermal radiation on MHD Casson fluid over a cylinder." J. Nanofluids, vol. 7, 428-438(2018).
[21] N. A. Sheikh, F. Ali, M. Saqib, I. Khan A.S. Alshomrani and M. S Alghamdi, "Comparison and analysis of the atangana–baleanu and caputo–fabrizio fractional derivatives for generalized casson fluid model with heat generation and chemical reaction." Results in Physics 7, 789–800(2017).
[22] N. Casson, "A flow equation for pigment –oil-suspensions of the printing ink type." Rhealogy of Disperse systems (1959).
[23] N. S. Wahid, M. E.H. Hafidzuddin, N. Md. Arifin, M. Turkyilmazoglu and N. A. Abd Rahmin, "Magnetohydrodynamic (MHD) slip darcy flow of viscoelastic fluid over a stretching sheet and heat transfer with thermal radiation and viscous dissipation." CFD Letters 12, no. 1 (2020).
[24] S.Mohan, G.V. Reddy and S. Balakrishna,"An unsteady MHD free convection flow of casson fluid past an exponentially accelerated infinite vertical plate through porous medium in the presence of the thermal radiation, chemical reaction and heat source or sink." International journal of engineering and techniques 4, no. 4, 16-27(2018).
[25] S. Nadeem, R. Ul Haq and C. Lee, "MHD flow of a Casson fluid over an exponentially shrinking sheet." Scientia Iranica 19, no. 6, 1550-1553(2012).
[26] S. Nadeem, R. Ul Haq, N.S. and Z. H. Khan, "MHD three-dimensional Casson fluid flow past a porous linearly stretching sheet." Alexandria Engineering Journal 52, no. 4, 577–882(2013).
[27] S. Pramanik, "Casson fluid flow and heat transfer past exponentially porous stretching surface in presence of thermal radiation." Ain Shams Eng. J., Vol. 5, no. 1, 205-212 (2014).
[28] S.R.Mohan,"Dufour and radiation absorption effects on unsteady MHD free convection casson fluid flow past an exponentially infinite vertical plate through porous medium." Vol. 6, no. 2, 485-512(2019).
[29] V.P. Dubey, J. Singh, A.M. Alshehri and S. Dubey, "Analysis of local fractional coupled Helmholtz and coupled Burgers' equations in fractal media." AIMS Mathematics, 7,5, 8080-8111 (2022).

Effect of the Couple-Stress on Micro Polar Rotating Fluid Flow Saturating a Porous Medium

Devilal Kumawat[1*], Ram Dayal Pankaj[1], and Vijay Mehta[1]

[1]Department of Mathematics and Statistics, Jai Narain Vyas University, Jodhpur, Rajasthan (INDIA).
[*]E-mail: devilalkumawat225@gmail.com

December 27, 2022

Abstract - Effect of the couple-stress on micro polar rotating fluid layer heated from below in the presence of varying gravitational field in a porous medium is studied, using normal mode, the problem has been analyzed and it is found that the permeability has destabilizing effect. The rotation, couple-stress parameter and micro-polar parameters have stabilizing effect. The condition of over stability has been found.
Keywords - Micro-Polar Fluid; Couple-Stress; Porous Medium; Rotation

1 Introduction

There are some important classes of fluid in technology areas, one of them being micro-polar fluid. The general theory of micro polar fluid was introduced Eringen[3] . Sharma and Gupta [8] investigated the thermal convection on micro polar fluid in porous medium. Sunil [12] et al. analyzed rotation and different parameters on a micro-polar ferromagnetic fluid flow. Mittal and Rana [5] investigated the medium permeability, suspended particles and other parameters on the micro-polar ferromagnetic fluid.
Stokes [11] study the classical concept of couple-stress fluid. Kumar Pardeep [4] et al. study the rotation on thermal instability in couple-stress viscous elastic fluid. Banyal and Singh [2] investigated the rotation on the couple-stress fluid in a porous medium. Shivakumara et al. [10] used the Galerkin method to investigate the convection in a couple-stress fluid flow. Pundir [6] et al. analyzed the effect of permeability, couple-stress parameter and magnetization. Shah Zahir et al. [7] discussed the effect of couple stress on micro polar fluid flow with hall current. Sharma K. Bhupendra et al. [9] study the effect of porosity, magnetic field and electrically conducting. Aparna P. et al. [1] investigated

the couple stress fluid on rotating permeable sphere. Xiong Pei-Ying et al. [13] analyzed the couple stress fluid flow between parallel plates with thermal convection.
Application of this work in geophysics, engineering science, chemical science and industry like as liquid crystal, blood flows, colloids suspensions and clean engine lubricants. In this paper, I attempt to study the couple-stress on micro-polar rotating fluid flow saturating a porous medium. To my knowledge this problem has not yet been investigated using the generalized Darcys model.

2 Mathematical Formulation

An infinite, horizontal, incompressible micro-polar fluid layer of thickness d is assumed and has porosity $\in$ and medium permeability k_1. The upper limit $z = d$ and lower limit $z = 0$ are maintained at constant but varying temperatures T_0 and T_1 such that a study adverse temperature gradient $\beta = \left|\frac{dT}{dz}\right|$ has been continued. The rotation and gravity are applied along z-axis to the system.

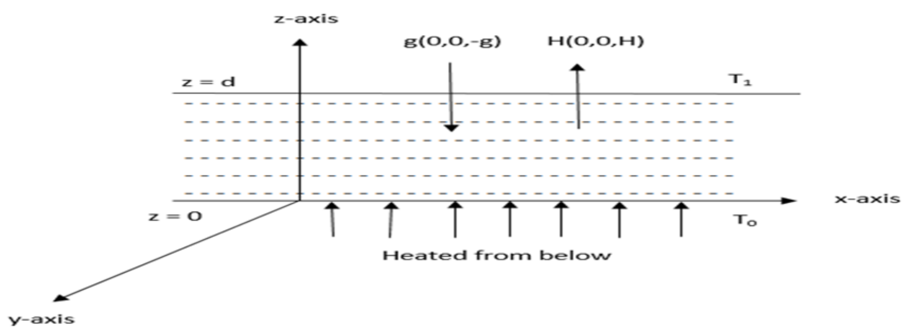

The equation of continuity, momentum, internal angular momentum, temperature and state is

$$\nabla.\vec{q} = o \tag{1}$$

$$\frac{\rho_0}{\in}\left[\frac{\partial \vec{q}}{\partial t} + \frac{1}{\in}(\vec{q}.\nabla)\vec{q}\right] = -\nabla P - \rho g \hat{e}_z + \left(\mu - \frac{\mu'}{\rho_0}\nabla^2\right)\nabla^2 \vec{q} - \frac{1}{k_1}(\mu + \varsigma)\vec{q} + \varsigma(\nabla \times \vec{v}) + \frac{2\rho_0}{\in}(\vec{q} \times \Omega) \tag{2}$$

$$\rho_0 J\left[\frac{\partial \vec{v}}{\partial t} + \frac{1}{\in}(\vec{v}.\nabla)\vec{v}\right] = (\alpha' + \beta')\nabla(\nabla.\vec{v}) + \gamma'\nabla^2\vec{v} + \frac{\varsigma}{\in}(\nabla \times \vec{q}) - 2\varsigma\vec{v} \tag{3}$$

$$[\in \rho_0 C_v + (1-\in)\rho_s C_s]\frac{\partial T}{\partial t} + \rho_0 C_v(\vec{q}.\nabla)T = \chi\nabla^2 T + \delta(\nabla \times \vec{v}).\nabla T \tag{4}$$

$$\rho = \rho_0[1 - \alpha(T - T_a)] \tag{5}$$

Where ρ - Fluid density, ρ_0 Reference density, $\vec{q}$ Filter velocity, $\vec{v}$ Spin (micro rotation), μ - Shear kinematic viscosity coefficient, ς - Coupling viscosity coefficient, P - Pressure, μ' - Couple stress viscosity, $\hat{e}_z$ - Unit vector in z-direction, α' - Bulk spin viscosity coefficient, β' - Shear spin viscosity coefficient, γ' - Micro-polar viscosity coefficient, J - Micro inertia constant, t - time, C_v - Specific heat at constant volume, C_s - Specific heat of solid (Porous Material Matrix), ρ_s - Density of solid matrix, χ - Thermal conductivity, T - Temperature, δ - Micro-polar heat conduction coefficient, α - Coefficient of thermal expansion.

3 Basic State of Problem

The basic state is

$$\vec{q} = \vec{q}_b\,(0,0,0)\,,\ \vec{v} = \vec{v}_b\,(0,0,0)\,,\ \rho = \rho = \rho_b\,(z)\ and\, P = P_b\,(z)$$

From equation (1) to (5)

$$\frac{dP_b}{dz} + \rho_b g = 0 \tag{6}$$

$$T = T_b\,(z) = -\beta z + T_a \tag{7}$$

$$\rho_b = \rho_0\,(1 + \alpha\beta z) \tag{8}$$

4 Linearize Perturbation Equations

$$\nabla.\vec{q}' = o \tag{9}$$

$$\frac{\rho_0}{\in}\frac{\partial \vec{q}'}{\partial t} = -\nabla P' + \alpha\theta g\hat{e}_z + \left(\mu - \frac{\mu'}{\rho_0}\nabla^2\right)\nabla^2\vec{q}' - \frac{1}{k_1}\,(\mu + \varsigma)\,\vec{q}' + \varsigma\,(\nabla \times \vec{v}') + \frac{2\rho_0}{\in}\,(\vec{q}' \times \Omega) \tag{10}$$

$$\rho_0 J\frac{\partial \vec{v}'}{\partial t} = (\alpha' + \beta')\,\nabla\,(\nabla.\vec{v}') + \gamma'\nabla^2\vec{v}' + \frac{\varsigma}{\in}\,(\nabla \times \vec{q}') - 2\varsigma\vec{v}' \tag{11}$$

$$E\frac{\partial \theta}{\partial t} + (\vec{q}.\nabla)\,T_b = k_T\nabla^2\theta - \frac{\delta}{\rho_0 C_v}(\nabla \times \vec{v}')_z\beta + \beta(\vec{q}')_z \tag{12}$$

$$\rho' = -\rho_0\alpha\theta \tag{13}$$

Converting equation (9) to (13) by the following transform $x = dx*, y = dy*, z = dz*, \vec{q}' = \frac{k_T}{d}\vec{q}*, P' = \frac{\mu k_T}{d^2}P*, \vec{v}' = \frac{k_T}{d^2}\vec{v}*, t = \frac{\rho_0 d^2}{\mu}t*, \nabla = \frac{\nabla*}{d}, \theta = \beta d\,\theta*$, then we have

$$\nabla.\vec{q} = o \tag{14}$$

$$\frac{1}{\in}\frac{\partial \vec{q}}{\partial t} = -\nabla P + R\theta\hat{e}_z + \left(1 - F\nabla^2\right)\nabla^2\vec{q} - \frac{1}{K_1}\,(1 + K)\,\vec{q} + K\,(\nabla \times \vec{v}) + \frac{2}{\in}\,(\vec{q} \times \Omega) \tag{15}$$

$$\bar{J}\frac{\partial \vec{v}}{\partial t} = C_1\,\nabla\,(\nabla.\vec{v}) - C_0\,\nabla\,(\nabla \times \vec{v}) + K\left\{\frac{1}{\in}\,(\nabla \times \vec{q}) - 2\vec{v}\right\} \tag{16}$$

$$EP_r\frac{\partial\theta}{\partial t} = \nabla^2\theta - \bar{\delta}(\nabla\times\vec{v})_z + (\vec{q})_z \tag{17}$$

Where $R = \frac{\rho_0 g\alpha\beta d^4}{\mu k_T}$ - Thermal Rayleigh number, $P_r = \frac{\mu}{\rho_0 k_T}$ - Prandtl number, $F = \frac{\mu'}{\rho_0 d^2}$, $E = \in + \frac{(1-\in)\rho_s C_s}{\rho_0 C_v}$, $\bar{J} = \frac{J}{d^2}$, $K_1 = \frac{k_1}{d^2}$, $\bar{\delta} = \frac{\delta}{\rho_0 C_v d^2}$, $C_0 = \frac{\gamma'}{\mu d^2}$, $C_1 = \frac{\alpha'+\beta'+\gamma'}{\mu d^2}$, and $W = \vec{q}.\hat{e}_z$.

5 Boundary conditions

$$W = \frac{d^2W}{dz^2} = 0,\, \theta = 0\, at\, z = 0\, and\, z = d \tag{18}$$

6 Dispersion Relation

Taking curl on both side equation (15) then we have

$$\left[\frac{1}{\in}\frac{\partial}{\partial t} + \left(\frac{1+K}{K_1}\right) - \left(1 - F\nabla^2\right)\nabla^2\right](\nabla\times\vec{q}) = R\left(\frac{\partial\theta}{\partial x}\hat{e}_x + \frac{\partial\theta}{\partial x}\hat{e}_y\right) + K\nabla\times(\nabla\times\vec{v}) + \frac{2}{\in}\nabla\times(\vec{q}\times\Omega) \tag{19}$$

Let $\nabla^2 = \frac{\partial^2}{\partial x^2} + \frac{\partial^2}{\partial y^2} + \frac{\partial^2}{\partial z^2}$, $\nabla_1^2 = \frac{\partial^2}{\partial x^2} + \frac{\partial^2}{\partial y^2}$, $D = \frac{\partial}{\partial z}$, $\zeta_z = (\nabla\times\vec{q})_z$, ${\Omega_z}' = (\nabla\times\vec{v})_z$
Taking curl and z-component of equation (19), (16), then we have

$$\left[\frac{1}{\in}\frac{\partial}{\partial t} + \left(\frac{1+K}{K_1}\right) - \left(1 - F\nabla^2\right)\nabla^2\right]\nabla^2 W = R\nabla_1^2\theta + K\nabla^2\,{\Omega_z}'\,\hat{e}_z - \frac{2}{\in}\Omega\left(D\zeta_z\right) \tag{20}$$

$$\bar{J}\frac{\partial{\Omega_z}'}{\partial t} = C_0\nabla^2{\Omega_z}' - K\left[\frac{1}{\in}\nabla^2 W + 2{\Omega_z}'\right] \tag{21}$$

Taking z-component of equation (19) and (17) then we have

$$\left[\frac{1}{\in}\frac{\partial}{\partial t} + \left(\frac{1+K}{K_1}\right) - \left(1 - F\nabla^2\right)\nabla^2\right]\zeta_z = \frac{2}{\in}\Omega DW \tag{22}$$

$$EP_r\frac{\partial\theta}{\partial t} = \nabla^2\theta - \bar{\delta}\,{\Omega_z}' + W \tag{23}$$

1. Normal Mode Analysis

Let $\left[W,\, \zeta_z,\, \theta,\, {\Omega_z}'\right] = \left[W(z),\, X(z),\, \Theta(z),\, G(z)\right]\exp.\left[i\,k_x x + i\,k_y y + \sigma t\right]$
Applying normal mode of equation (20) to (23), becomes

$$\left[\frac{\sigma}{\in} + \left(\frac{1+K}{K_1}\right) + F\left(D^2-a^2\right)^2 - \left(D^2-a^2\right)\right]\left(D^2-a^2\right)W = -Ra^2\Theta + K\left(D^2-a^2\right)G - \frac{2}{\in}\Omega DX \tag{24}$$

4

$$\left[\frac{\sigma}{\in}+\left(\frac{1+K}{K_1}\right)+F\left(D^2-a^2\right)^2-\left(D^2-a^2\right)\right]X=\frac{2}{\in}\Omega DW \tag{25}$$

$$\left[m\sigma+2A-\left(D^2-a^2\right)\right]G=-\frac{A}{\in}\left(D^2-a^2\right)W \tag{26}$$

$$\left[EP_r\sigma-\left(D^2-a^2\right)\right]\Theta=-\bar{\delta}G+W \tag{27}$$

Where $a^2=k_x^2+k_y^2$ - wave number, $\sigma=\sigma_r+i\,\sigma_r$ - stability parameter and $m=\frac{\bar{J}A}{K}$, $A=\frac{K}{C_0}$, A - ratio between the micro-polar viscous effect and micro-polar diffusion effects.

$$W=D^2W=0=X=DX=G,\Theta=0\,at\,z=0\,to\,z=1 \tag{28}$$

$$D^{2n}W=0\,at\,z=0\,to\,z=1,\text{ Where } n>0.$$

The solution of equation (28) is

$$W=W_0\sin\pi z$$

Eliminating Θ, G, Φ , X from (24) to (27) and put the value of W *and* $b=\pi^2+a^2$, then we have

$$\begin{aligned}
b\left[\frac{\sigma}{\in}+\left(\frac{1+K}{K_1}\right)+Fb^2+b\right]^2&[m\sigma+2A+b]\,[EP_r\sigma+b]\\
=Ra^2&\left[\frac{\sigma}{\in}+\left(\frac{1+K}{K_1}\right)+Fb^2+b\right]\left[(m\sigma+2A+b)-\frac{\bar{\delta}Ab}{\in}\right]\\
&+\frac{KAb^2}{\in}\left[\frac{\sigma}{\in}+\left(\frac{1+K}{K_1}\right)+Fb^2+b\right][EP_r\sigma+b]\\
&-\frac{4\Omega^2\pi^2}{\in^2}(m\sigma+2A+b)\,[EP_r\sigma+b]
\end{aligned} \tag{29}$$

7 Stationary Convection

Put the $\rho=0$ in equation (29), then we have

$$R=\frac{1}{a^2\left[2A+b-\frac{\bar{\delta}Ab}{\in}\right]}\left[b^2(2A+b)\left(\frac{1+K}{K_1}+Fb^2+b\right)-\frac{KAb^3}{\in}+\frac{\frac{4\Omega^2\pi^2}{\in^2}b\,(2A+b)}{\left(\frac{1+K}{K_1}+Fb^2+b\right)}\right] \tag{30}$$

To study the behavior of permeability, rotation, couple-stress parameter coupling parameter, micro-polar coefficient, micro-polar heat transfer parameter and find the nature of $\frac{dR}{dK_1}$, $\frac{dR}{d\Omega}$, $\frac{dR}{dF}$, $\frac{dR}{dK}$, $\frac{dR}{dA}$ *and* $\frac{dR}{d\delta}$ respectively, then

$$\frac{dR}{dK_1}=\frac{-b\,(2A+b)\,(1+K)}{a^2{K_1}^2\left[2A+b-\frac{\bar{\delta}Ab}{\in}\right]}\left[b-\frac{\frac{4\Omega^2\pi^2}{\in^2}}{\left(\frac{1+K}{K_1}+Fb^2+b\right)}\right] \tag{31}$$

5

$$\frac{dR}{dK_1} < 0\, if\, \frac{4\Omega^2\pi^2}{b} < \in^2 \left(\frac{1+K}{K_1} + Fb^2 + b\right) \, and\, \bar{\delta} < \frac{\in}{A}$$

From equation (31), we can say that the permeability has destabilizing effect when $\frac{4\Omega^2\pi^2}{b} < \in^2 \left(\frac{1+K}{K_1} + Fb^2 + b\right) \, and\, \bar{\delta} < \frac{\in}{A}$.

$$\frac{dR}{d\Omega} = \frac{8\Omega\pi^2\in^{-2}b\,(2A+b)}{a^2\left(\frac{1+K}{K_1} + Fb^2 + b\right)\left[2A + b - \frac{\bar{\delta}Ab}{\in}\right]} \tag{32}$$

$$\frac{dR}{d\Omega} < 0\, if\;\bar{\delta} < \frac{\in}{A}$$

From equation (32) shows that the rotation has stabilizing effect when $\bar{\delta} < \frac{\in}{A}$.

$$\frac{dR}{dF} = \frac{b^3\,(2A+b)\left[b\left(\frac{1+K}{K_1} + Fb^2 + b\right)^2 - \frac{4\Omega^2\pi^2}{\in^2}\right]}{a^2\left(\frac{1+K}{K} + Fb^2 + b\right)^2\left[2A + b - \frac{\bar{\delta}Ab}{\in}\right]} \tag{33}$$

$$\frac{dR}{dF} > 0\, if\;\left(\frac{1+K}{K_1} + Fb^2 + b\right) > \frac{2\Omega\pi}{\in\sqrt{b}}$$

It is clear that the couple-stress parameter has stabilizing effect when $\left(\frac{1+K}{K_1} + Fb^2 + b\right) > \frac{2\Omega\pi}{\in\sqrt{b}}$.

$$\frac{dR}{dK} = \frac{b\left[Ab\left(\frac{2}{K_1} - \frac{b}{\in}\right)\left(\frac{1+K}{K_1} + Fb^2 + b\right)^2 + \left\{b^2\left(\frac{1+K}{K_1} + Fb^2 + b\right)^2 - \frac{4\Omega^2\pi^2(2A+b)}{\in^2}\right\}\frac{1}{K_1}\right]}{a^2\left(\frac{1+K}{K} + Fb^2 + b\right)^2\left[2A + b - \frac{\bar{\delta}Ab}{\in}\right]} \tag{34}$$

$$\frac{dR}{dK} > 0\, if\, \frac{2}{K_1} > \frac{b}{\in}\, and\;\left(\frac{1+K}{K_1} + Fb^2 + b\right) > \frac{2\Omega\pi\sqrt{(2A+b)}}{\in}$$

Hence the coupling parameter has stabilizing effect when $\frac{2}{K_1} > \frac{b}{\in}\, and\;\left(\frac{1+K}{K_1} + Fb^2 + b\right) > \frac{2\Omega\pi\sqrt{(2A+b)}}{\in}$.

$$\frac{dR}{dA} = \frac{\frac{b^4}{\in}\left(\frac{1+K}{K_1} + Fb^2 + b\right)^2\left[\bar{\delta} - K\left(\frac{1+K}{K_1} + Fb^2 + b\right)\right] + \frac{4\Omega^2\pi^2\bar{\delta}b^3}{\in^3}}{a^2\left(\frac{1+K}{K_1} + Fb^2 + b\right)\left[(2A+b) - \frac{\bar{\delta}Ab}{\in}\right]^2} \tag{35}$$

$$\frac{dR}{dA} > 0\;if\,\bar{\delta} > K\left(\frac{1+K}{K_1} + Fb^2 + b\right)$$

From equation (35), we can say that the micro-polar coefficient has stabilizing effect when $\bar{\delta} > K\left(\frac{1+K}{K_1} + Fb^2 + b\right)$.

$$\frac{dR}{d\bar{\delta}} = \frac{\frac{Ab}{\in}}{a^2\left[(2A+b) - \frac{\bar{\delta}Ab}{\in}\right]^2}\left[b^3\left\{\left(\frac{1+K}{K_1} + Fb^2 + b\right) - \frac{KA}{\in}\right\}\right.$$
$$\left. + 2Ab^2\left(\frac{1+K}{K_1} + Fb^2 + b\right) + \frac{4\Omega^2\pi^2\in^{-2}b\,(2A+b)}{\left(\frac{1+K}{K_1} + Fb^2 + b\right)}\right] \quad (36)$$

$$\frac{dR}{d\delta} > 0\, if\ \left(\frac{1+K}{K_1} + Fb^2 + b\right) > \frac{KA}{\in}$$

From equation (36), shows that the micro-polar heat transfer parameter has stabilizing effect when $\left(\frac{1+K}{K_1} + Fb^2 + b\right) > \frac{KA}{\in}$

8 Oscillatory Convection

Putting $\sigma = i\,\sigma_i$ in equation (29) then we get real and imaginary part, eliminating R between them, then we have

$$f_0\sigma_i^4 + f_1\sigma_i^2 + f_2 = 0$$

Put $s = \sigma_i^2$then we have

$$f_0 s^2 + f_1 s + f_2 = 0 \quad (37)$$

Where

$$f_0 = a_1 q_1 - p_1 b_1$$
$$f_1 = a_2 q_1 - p_2 b_1 - p_1 b_2$$
$$f_2 = a_3 q_1 - p_2 b_2$$
$$b_1 = -\frac{ma^2}{\in},\ a_1 = \frac{EP_r mb}{\in^2} \text{ and } b_2 = a^2\,(2A+b)\left\{\frac{1+K}{K_1} + Fb^2 + b\right\}$$

$$a_2 = -\left[\frac{\left\{(2A+b)\,b^2\right\}}{\in^2} + \frac{2b}{\in}\left(\frac{1+K}{K_1} + Fb^2 + b\right)\left\{(2A+b)\,EP_r + mb\right\}\right.$$
$$\left. + \left(\frac{1+K}{K_1} + Fb^2 + b\right)^2 EP_r mb\right] + \frac{KAb^2EP_r}{\in^2} - \frac{4\Omega^2\pi^2EP_r m}{\in^2}$$

$$a_3 = (2A+b)\,b^2\left(\frac{1+K}{K_1} + Fb^2 + b\right)^2 - \frac{KAb^3}{\in}\left(\frac{1+K}{K_1} + Fb^2 + b\right) + \frac{4\Omega^2\pi^2(2A+b)b}{\in^2}$$
$$P_1 = -\frac{1}{\in}\left[\frac{b}{\in}\left\{(2A+b)\,EP_r + mb\right\} + 2EP_r mb\left(\frac{1+K}{K_1} + Fb^2 + b\right)\right]$$

$$P_2 = \Bigg[2\left(2A+b\right)b^2 \in^{-1} \left(\frac{1+K}{K_1} + Fb^2 + b \right) + \left\{ \left(2A+b\right)EP_r + mb \right\} b \left(\frac{1+K}{K_1} + Fb^2 + b \right)^2 \Bigg] - \frac{KAb^2}{\in} \left(\frac{b}{\in} + EP_r \right) + \frac{4\Omega^2\pi^2}{\in^2} \left[\left(2A+b\right)EP_r + mb \right]$$

$$q_1 = a^2 \left[\frac{(2A+b)}{\in} + m\left(\frac{1+K}{K_1} + Fb^2 + b \right) - \frac{\bar{\delta}Ab}{\in^2} \right]$$

From (37), we saying that $s = \sigma_i^2$ is positive, equation (37) for the sum of roots is positive, it is not possible if $f_0 > 0$ and $f_1 > 0$.
If $f_0 > 0$ and $f_1 > 0$ when $\bar{\delta} < \frac{\in}{A}$, $K < 4Fb \in$, $KEP_r < 4b \, and \, AKb^2 < 2\pi^2\Omega^2 m$.
Above conditions of the overstability.

9 Numerical Calculation

Now we show numerically effect of different parameter from equation (29)

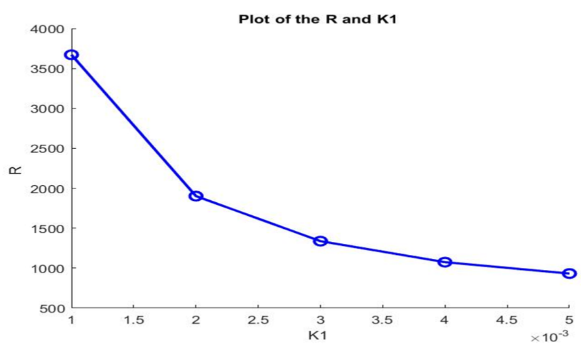

Figure 1:
$E = 1$, $P_r = 2$, $\in = 0.5$, $A = 0.1$, $F = 2$, $K = 0.2$, $\Omega = 10 \, and \, \bar{\delta} = 0.05$.

Fig 1 shows the variation of Rayleigh number R with respect to medium permeability K_1 i.e. medium permeability K_1 increases then the Rayleigh number R decreases.

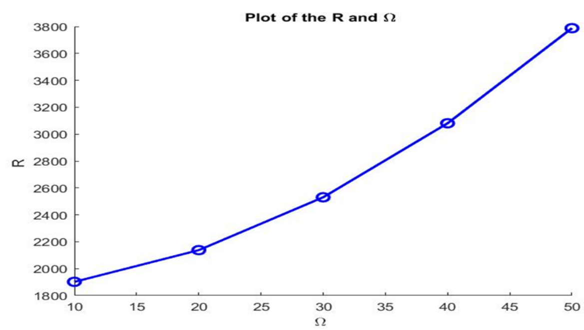

Figure 2:
$E = 1,\ \mathrm{P}_r = 2,\ \in= 0.5,\ A = 0.1,\ F = 2,\ K = 0.2,\ K_1 = 0.002\, and\, \bar{\delta} = 0.05.$

Fig 2 represent the plot of Rayleigh number R versus rotation ω i.e. rotation increases ω then the Rayleigh number R increases.

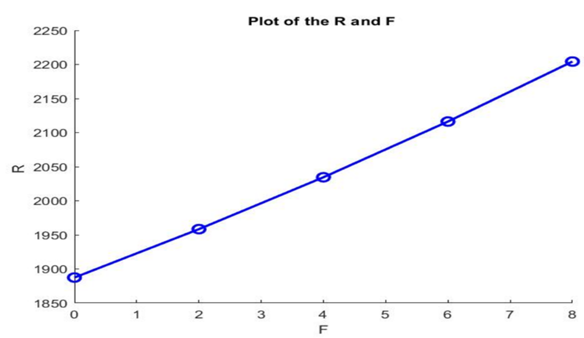

Figure 3:
$E = 1,\ \mathrm{P}_r = 2,\ \in= 0.5,\ A = 0.1,\ \Omega = 10,\ K = 0.2,\ K_1 = 0.002\, and\, \bar{\delta} = 0.05.$

Fig 3 plot between Rayleigh number R and couple-stress parameter F i.e. couple-stress parameter F increases then the Rayleigh number R increases.

9

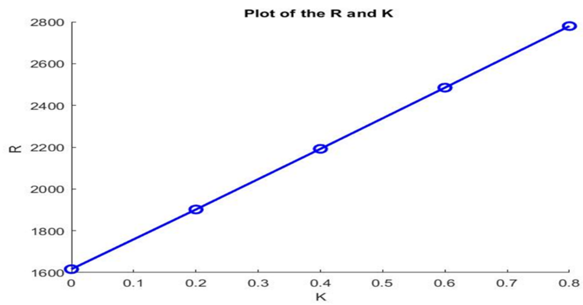

Figure 4:
$E = 1,\ \mathrm{P}_r = 2,\ \in= 0.5,\ A = 0.1,\ \Omega = 10,\ F = 2,\ K_1 = 0.002\, and\, \bar{\delta} = 0.05.$

Fig 4 shows the variation of Rayleigh number R with respect to coupling parameter K i.e. coupling parameter K increases then the Rayleigh number R increases.

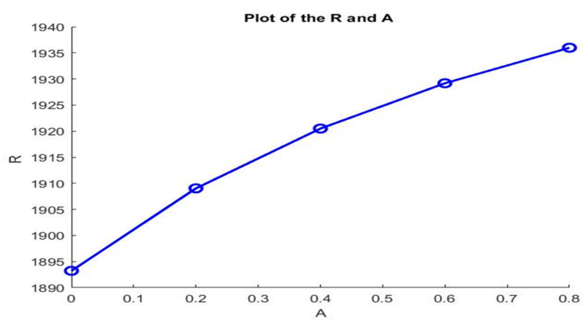

Figure 5:
$E = 1,\ \mathrm{P}_r = 2,\ \in= 0.5,\ K = 0.2,\ \Omega = 10,\ F = 2,\ K_1 = 0.002\, and\, \bar{\delta} = 0.05.$

Fig 5 represent the plot of Rayleigh number R versus micro-polar coefficient i.e. micro-polar coefficient A increases then the Rayleigh number R increases.

10 Conclusions

According to the stationary convection and numerically discussion we found that the effect of permeability is destabilizing. The effect of couple-stress parameter, rotation, coupling parameter, micro-polar coefficient and micro-polar heat conduction are stabilizing. Among them the most important result that the effect of rotation stabilize on the system. The condition of over stability is $\bar{\delta} < \frac{\in}{A}$, $K < 4Fb \in$, $KEP_r < 4b\, and\, AKb^2 < 2\pi^2\Omega^2 m$.

10

References

[1] Aparna P., Murthy Ramana J.V., Couple on a rotating permeable sphere in a couple stress fluid, Ain shams engineering journal, 2018; 9:665-673.

[2] Banyal S.A. and Singh Kamal A characterization of couple-stress fluid heated from below in a porous medium in the presence of a rotation, International journal of advanced computer and mathematical science, 2012; 3(3): 310-320.

[3] Eringen A.C., Simple microfluids, International journal of engineering science, 1964; 2(2): 205-217.

[4] Kumar pardeep, Lal Roshan and Sharma Poonam, Effect of rotation on thermal instability in couple-stress elastio-viscous fluid, Zeitschrift fur Naturforschung, 2004; 59(a): 407-411.

[5] Mittal Reena and Rana U.S., Effect of dust particles on a layer of micropolar ferromagnetic fluid heated from below saturating a porous medium, Applied Mathematics and computation, 2009; 215:2591-2607.

[6] Pundir K.S., Nadiam K.P. and Pundir R, Effect of hall current on hydromagnetic instability of a couple-stress ferromagnetic fluid in the presence of varying gravitational field through a porous medium, International journal of Statistics and applied mathematics, 2021; 6(4): 01-15.

[7] Shah Zahir, Kumam Poom, Dawar Abdullah, Alzahrani O. Ebraheem and Thounthong Phatiphat, study of the couple stress convective micropolar fluid flow in a hall MHD generator system, Frontiers in physics; 2019, 7:171.

[8] Sharma C.R. and Gupta Urvashi, Thermal convection in micropolar fluids in porous medium, International journal of engineering science, 1995; 33(13): 1887-1892.

[9] Sharma K. Bhupendra, Sharma Kumar Pawan and Chauhan Kumar Sudhir, Effect of MHD on unsteady oscillatory couette flow through porous media, Int. J. of applied mechanics and engineering, 2022; 24(1):188-202

[10] Shivakumara S. Sureshkumar S. and Devaraju N., Effect of Non-uniform temperature gradients on the onset of convection in a couple-stress fluid-saturated porous medium, Journal of applied fluid mechanics, 2012; 5(1): 49-55.

[11] Stokes Kumar Vijay, Couple-stress in fluid, Physics of fluid, 1966; 9(9):1709-1715.

[12] Sunil, Sharma Anu, Bharti K.P., Shandil G.R., Effect of rotation on a layer of micropolar ferromagnetic fluid heated from below saturating a porous medium, International Journal of engineering science, 2006; 44:683-698.

[13] Xiong Pie-Ying, Nazeer Mubbashar, Hussain Farooq, Khan Ijaz M., Saleem Adila, Qayyum Sumaira and Chu Yu-Ming, Two-phase flow of couple stress fluid thermally effected slip boundary conditions: Numerical analysis with variable liquids properties, Alexandria Engineering journal, 2022; 61:3821-3830.

Mathematical Analysis of SEITR Model for Influenza Dynamics

K. Arun Kumar [1] and A.Venkatesh[2*]

[1,2]Department of Mathematics,
AVVM Sri Pushpam College (Affiliated to Bharathidasan University),
Poondi, Thanjavur(Dt), Tamilnadu, India-613 503.

December 28, 2022

Abstract

In order to give timely hospitalisation for infections that are dangerously ill, our primary goal is to reduce the interaction between susceptibles and infections. For this we add treatment T as a fifth compartment to the SEIR model, converting it from SEIR to SEITR. The stabilities of endemic equilibrium and disease-free equilibrium were tested. The next generation matrix method was used to calculate the SEITR model's basic reproduction number. Numerical simulations were also presented to validate our analytic findings. A graphic depicted the impact of parameters on infected populations. It was perceived that, anytime the treatment rate increased, the infected population, exposed population, and treated population all declined but the susceptible population increased.

Keywords: SEITR model, basic reproduction number, stability and numerical simulation.
AMS Subject Classification: 34D20

1 Introduction

Kermack and McKendrick [21] introduced the first mathematical model, SIR (Susceptible-Infectious-Recovered), early in the 20th century. Later Anderson and May[1] were proposed the SEIR model by adding Exposed (E) as fourth compartment to SIR model to define the spread of epidemic. Many authors introduced a numerous extended SEIR models to define the infectious diseases spread and their preventions [7]. ZhilanFeng (2007) [31] developed a SEIR model which has been used to evaluate the electiveness of different control strategies for the size of endemic with separation and isolation. Rafiqul Islam et al [16] was proposed an SEIR model to analysis the influenza in Bangladesh. Vinod kumar bais and Deepak kumar [29] was introduced a model SITR emphasized the condition of the dynamical classic to the transmission populace of H1N1 virus. By combining these two SEIR and SITR models we developed an new SEITR model by including treatment T as a fifth compartment to investigate the dynamics of the influenza epidemic's transmission. Hethcote and Yorke [14] were charity models to analyze the gonorrhea controller techniques, such as showing, outling infectors, post treatment and vaccination.

*Corresponding author: avenkateshmaths@gmail.com

Chinviriyasit (2007) was introduced a dynamic SIRC model [6] to study the Numerical exhibiting modeling of the spread dynamics of influenza. Samuel Abubakar (2013) was proposed a model [25] to investigation the spread of infectious disease and stability of disease in population. Various researchers such as Andreasen et al. (1997)[2], Hethcote (2000), Earn et al. (2002)[15], Casagrandi et al. (2006)[10], Murray et al. (2008) [23] have been studied the dynamics of influenza and they recommended mathematical models to revision the spread of H1N1 and control the influenza epidemic. Over the past several decades, the field of FDEs has made considerable advancements. To examine the dynamical behaviour of a fish farm in relation to an arbitrary order Atangana-Baleanu derivative, Jagdev et al. [19] suggested a fraction fish farm model. By Jagdev Singh [18], a fractional guava fruit model with memory outcome was introduced. To analyse the COVID-19 trend, Supriya, Yadav et al [28] created the FDE model. A fractional model was created by Jagdev Singh and Arpita Gupta[17] to analyse the results of nonlinear partial modified. To study malaria transmission, Rehman, Attiq ul, et al [**?**] proposed a 9 compartment FDE model. A simple influenza(H1N1) model by means of optimal control studied by Srivastav. A. K et al. (2016) [27], Also Mishra et al. (2013) [22], consume suggested a mathematical model to analyze the spread and control of influenza between two economic groups. Christian Quirouette et al[24] developed to unfolding the localization and spread of influenza virus inside the human breathing area. The Mathematical model [3], plays a crucial role to learning the spread dynamics of the Contagious Disease Influenza, and control the virus through isolation, treatment and vaccination of infected population. Environmental contaminations, global warming, ecosystems, roving etc. are main reasons to spread the contagious diseases. So that certain assumptions and parameters are considered to formulate the model. Influenza is a breathing contagious disease instigated by influenza virus[18], which is also known as flu and it has three kinds A, B and C. This virus spreads easily in the population very fast through the air from coughing, sneezing and through contact by the hands touching our eyes, nose or mouth etc. Communal symptoms of H1N1 are high fever, pain, sore gorge, muscle pain, coughing and weariness [11]. The symptoms were appeared after two days and it has been at most one week [12] but cough may last more than two weeks. Each year individuals are infected by this virus an outbreak particularly in the winter session. The formulation and analysis of the SEITR model were briefly detailed in this article. The analyses of the model, together with the findings on local and global stability, as well as the presence of endemic equilibrium, were investigated. Numerical evidence was used to establish an analytical conclusion. It was seen that if the rate of treatment increased, the susceptible population rose while the infected, exposed, and treated populations all decreased. The limitations of the SEITR model is that it oversimplifies complicated disease processes while still being easily calculable. The SEITR model does take this parameter into account, however additional model extensions would be required.

2 Model Formation

In this study we proposed a new model SEITR by adding treatment T as fifth compartment to SEIR model to analyze the spread dynamics of epidemic Influenza in India. The total populace $N(t)$ at time t is separated into five different populaces , namely, Susceptible populace $S(t)$ at time t, Exposed populace $E(t)$ at time t, Infected inhabitants $I(t)$ at time t, Treatment populace $T(t)$ at time t, and Recovered populace $R(t)$ at time t. The susceptible $(S(t))$ populace are those who are at possibility to become infected by virus. The exposed $(E(t))$ populace are those who are infested by virus but not yet infectious that is not able to infect others. The infected populaces are those who

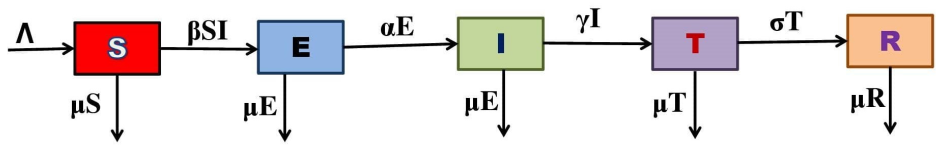

Figure 1: Schematic diagram of SEITR model

are diseased and able to infect others. The treatment populations are those who are infected and taking treatment in hospitals. The recovered populations are those who are recovered after treatment.
The flow diagram of influenza model was presented in fig1.

The susceptible human populace is created by the inflow rate of humans into the populace (at the rate $\wedge$) and the natural death rate μ. Therefore the incidence rate βSI incorporate the transmission frequency at which susceptible individuals becomes exposed and entered exposed populace without being infectious. Thus the rate of change of susceptible human populace is given by

$$\frac{dS}{dt} = \wedge - \beta SI - \mu S$$

The exposed human populace at the rate α be the exposed rate which exposed individuals becomes infected but not infectious and entered into infected populace and the natural death rate μ. Thus the rate of variation of exposed human populace is specified by

$$\frac{dE}{dt} = \beta SI - (\alpha + \mu) E$$

The infected human populace at the rate γ be the people are joined in hospital for treatment populace and the natural death rate μ. Thus the rate of variation of infected human populace is specified by

$$\frac{dI}{dt} = \alpha E - (\gamma + \mu) I$$

The treatment human populace at the rate σ be a rate at which the treatment individuals recovered and entered into recovered populace. Hence the rate of variation of treatment human populace is specified by

$$\frac{dT}{dt} = \gamma I - (\sigma + \mu) T$$

Finally, the rate of variation of recovered human populace is specified by

$$\frac{dR}{dt} = \sigma T - \mu R$$

By using all above assumptions, a nonlinear structure of five differential equations for

Table 1: Complete Description of relative parameters of the SEITR model

Parameter	Depiction
$\wedge$	inflow rate of susceptible individuals
μ	Normal death rate
β	Rate at which susceptible populace becomes exposed
α	Rate at which exposed populace becomes infected
γ	Rate at which infected populace getting treatment
σ	Rate at which treatment populace getting recovered

SEITR model is formed as follows

$$\begin{cases} \frac{dS}{dt} &= \wedge - \beta SI - \mu S \\ \frac{dE}{dt} &= \beta SI - (\alpha+\mu)E \\ \frac{dI}{dt} &= \alpha E - (\gamma+\mu)I \\ \frac{dT}{dt} &= \gamma I - (\sigma+\mu)T \\ \frac{dR}{dt} &= \sigma T - \mu R \end{cases} \tag{1}$$

Where the primary conditions $S(0) \geq 0$, $E(0) \geq 0$, $I(0) \geq 0$, $T(0) \geq 0$ and $R(0) \geq 0$. The total population $N(t) = S(t) + E(t) + I(t) + T(t) + R(t)$ will be assumed as constant.

3 Analysis of the SEITR model

In the segment, the elementary belongings of SEITR model 1 such as positivity and boundedness of the solution, basic reproduction number and stability analysis were discorsed.

3.1 Positivity and boundedness

Theorem 1. *All the solutions $(S(t), E(t), I(t), T(t), R(t)) \in R^5_+$ of the sturcture 1 with primary condition $S(t) \geq 0$, $E(t) \geq 0$, $I(t) \geq 0$, $T(t) \geq 0$, and $R(t) \geq 0$ are nonnegative and uniformly bounded for all $t \geq 0$.*

Proof 1. *Assume that $(S(t), E(t), I(t), T(t), R(t)) \in R^5_+$ is a solution of 1 for $t \in [0, t_0)$, where $t_0 > 0$.*
Through 1^{st} equation of system 1, we get

$$\frac{dS}{dt} = \wedge - \beta^* S^* I - \mu^* S \geq \wedge - \phi(t)^* S.$$

where $\phi(t) = \beta^* I + \mu$
After integration, we get

$$S(t) = S_0 \exp\left(-\int_0^t \phi(s)ds\right) + \wedge \exp\left(-\int_0^t \phi(s)ds\right) \int_0^t e^{\int_0^s \phi(u)du} ds \geq 0 \geq 0.$$

$\Rightarrow S(t) \geq 0$.
From the 2^{nd} equation of system 1, we develop

$$\frac{dE}{dt} = \beta SI - (\alpha+\mu)E \geq -(\alpha+\mu)E$$

Which leads

$$E(t) = E_0 \exp\left(-\int_0^t (\alpha+\mu)\, ds\right) \geq 0$$

$\Rightarrow E(t) \geq 0$
From the 3^{rd} *equation of system 1, we acquire*

$$\frac{dI}{dt} = \alpha E - (\gamma+\mu) \geq -(\gamma+\mu)\, I$$

Which leads

$$I(t) = I_0 \exp\left(-\int_0^t (\gamma+\mu)\, ds\right) \geq 0.$$

$\Rightarrow I(t) \geq 0$
Similarly 4^{th} *and* 5^{th} *equation of system 1*

$$\frac{dT}{dt} = \gamma I - (\sigma+\mu)\, T \geq -(\sigma+\mu)\, T$$

Which leads to

$$T(t) = T_0 \exp\left(-\int_0^t (\sigma+\mu)\right) ds \geq 0$$

$\Rightarrow T(t) \geq 0$

$$\frac{dR}{dt} = \sigma T{-}\mu R \geq -\mu R$$

which leads to

$$R(t) = R_0 \exp\left(-\int_0^t \mu ds\right) \geq 0$$

$\Rightarrow R(t) \geq 0$
Hence, the results (S, E, I, T, R) of 1 sustaining the primary conditions $S(t) \geq 0$, $E(t) \geq 0$, $I(t) \geq 0$, $T(t) \geq 0$, *and* $R(t) \geq 0$ *for all* $t \in [0, t_0)$ *are nonnegative in the section* $[0, t_0)$.
Now, we demonstrate that the boundedness of clarifications of system 1.
The positivity of the solutions indicates that
$\frac{dS}{dt} \leq \wedge - \mu S$
From the beyond equation, we can write that $\lim_{t\to\infty} \sup S \leq \frac{\wedge}{\mu}$ *and* $S \leq \frac{\wedge}{\mu}$.
Consider the total populations $N = S + E + I + T + R$.
On differentiation gives $\frac{dN}{dt} \leq \wedge - \mu N$ *which leads to* $\lim_{t\to\infty} \sup N \leq \frac{(\wedge)}{(\mu)}$.
Then, we get $N \leq \frac{\wedge}{\mu}$
$\Rightarrow S + E + I + T + R \leq \frac{\wedge}{\mu}$
Therefore all the solution curves (S, E, I, T, R) *sustaining by the primary conditions are consistently bounded in* R_+^5 *and in the section*
$\Omega = \left\{(S, E, I, T, R) \in R_+^5 : 0 \leq (S, E, I, T, R) \leq \frac{\wedge}{\mu}\right\}$.

3.2 Basic Reproduction Number

A crucial factor for communicable disease is the Basic Reproduction Number (R_0) which is distinct as the middling number of subordinate cases obtained by distinct primary case during the infectious dated in a susceptible populace. With R_0, the epidemic growth rate can be estimated and Stability of model will be analyzed [8]. R_0 Value can be determined through approach of Next Generation Matrix method [4], [13].

$R_0 = FV^{-1}$
Where

$$F = \begin{pmatrix} \beta + \mu \\ 0 \\ 0 \end{pmatrix}$$

and

$$V = \begin{pmatrix} (\alpha + \mu) E \\ \alpha E - (\gamma + \mu) I \\ \gamma I - (\sigma + \mu) T \end{pmatrix}$$

The Jacobian of F and V are dual matrices F and V which determined at an disinfection state $E = 0$, $I = 0$ and $T = 0$, we have

$$F = \begin{pmatrix} 0 & \beta & \mu \\ 0 & 0 & 0 \\ 0 & 0 & 0 \end{pmatrix}$$

and

$$V = \begin{pmatrix} (\alpha + \mu) & 0 & \\ \alpha & (\gamma + \mu) & 0 \\ 0 & -\gamma & (\sigma + \mu) \end{pmatrix}$$

FV^{-1} is $\frac{\beta\alpha}{(\alpha+\mu)(\gamma+\mu)} + \frac{\alpha\sigma\mu}{(\alpha+\mu)(\gamma+\mu)(\sigma+\mu)}$
Hence $R_0 = \frac{\beta\alpha}{(\alpha+\mu)(\gamma+\mu)} + \frac{\alpha\sigma\mu}{(\alpha+\mu)(\gamma+\mu)(\sigma+\mu)}$

3.3 Local Stability of Disease Free Equilibrium

Theorem 2. *For $R_0 < 1$, the Disease-Free Equilibrium point E_0=$(\frac{\triangle}{\mu}, 0, 0, 0, 0)$ was locally asymptotically stable and for R_0 >1, it was unstable [17].*

Proof 2. *The Jacobian matrix corresponding to the structure 1 at disease free equilibrium E_0 is*

$$J(E_0) = \begin{pmatrix} -\mu & 0 & -\beta & 0 & 0 \\ 0 & -(\mu + \alpha) & \beta & 0 & 0 \\ 0 & \alpha & -(\gamma + \mu) & 0 & 0 \\ 0 & 0 & \gamma & -(\sigma + \mu) & 0 \\ 0 & 0 & 0 & \sigma & -\mu \end{pmatrix}$$

The characteristic equation is

$$(\lambda + \mu)^2 (\lambda + (\sigma + \mu)) \left(\lambda^2 + a_1\lambda + a_2\right) = 0$$

Where $a_1 = 2\mu + \alpha + \gamma$ and $a_2 = (\mu + \alpha)(\gamma + \mu) - \alpha\beta$.
There are 5 Eigen values for the Jacobian matrix $J(E_0)$ of which first three are -μ, -μ, -$(\sigma + \mu)$, and the remaining two Eigen values are roots of quadratic equation $(\lambda_2 + a_1\lambda + a_2)$ = 0, which are negative.
Through Routh-Hurwitz criterion [20], all the roots of charateristics equation have destructive real part which revenues steady equilibrium if $a_1 > 0$ and $a_2 > 0$.
Since $\mu > 0$, $\alpha > 0$ and $\gamma > 0$, we have $2\mu + \alpha + \gamma > 0$ that is $a_1 > 0$.
Since $(\mu + \alpha)(\gamma + \mu) - \alpha\beta > 0$ >0 that is $a_2 > 0$.
If R_0 <1, then

$$\frac{\beta\alpha}{(\alpha + \mu)(\gamma + \mu)} + \frac{\alpha\sigma\mu}{(\alpha + \mu)(\gamma + \mu)(\sigma + \mu)(\alpha + \mu)} < 1$$

$$\Rightarrow \frac{\beta\alpha}{(\alpha+\mu)} < \frac{\beta\alpha}{(\alpha+\mu)(\gamma+\mu)} + \frac{\alpha\sigma\mu}{(\alpha+\mu)(\gamma+\mu)(\sigma+\mu)(\alpha+\mu)} < 1$$

$$\Rightarrow \frac{\beta\alpha}{(\alpha+\mu)(\gamma+\mu)} < 1 \Rightarrow \beta\alpha < (\alpha+\mu)(\gamma+\mu)$$

$$\Rightarrow (\mu+\alpha)(\gamma+\mu) - \alpha\beta > 0 thatisa_2 > 0.$$

Therefore, $a_2 > 0$ *if* $R_0 < 1$
Hence by Routh–Hurwitz Criteria, the disease free equilibrium point E_0 *is locally asymptotically stable if* $R_0 < 1$.

3.4 Global Stability of Disease Free Equilibrium

Theorem 3. *The disease-free equilibrium point* $E_0 = (\frac{\triangle}{\mu}, 0, 0, 0, 0)$ *of structure 1 was globally asymptotic stable if* $R_0 < 1$ *[19].*

Proof 3. *It can be detected that from the structure (1), the disease-free sections are S, R and the infected sections are E, I, T. The system of equations (1) will be arranged as*

$$\frac{dU}{dt} = P(U,V), \frac{dV}{dt} = G(U,V), \text{ and } G(U,0) = 0 \tag{2}$$

where $U = (S,R) \in R^2_+$, $V = (A,I,Q,J) \in R^3_+$.
By using the technique introduced by Castillo-Chavez [5], we derived global stability of the disease-free equilibrium point $E_0 = (\frac{\triangle}{\mu}, 0, 0, 0, 0)$. *For the worldwide asymptotic stability of* E_0 *the succeeding two conditions should be satisfied.*
1. $\frac{dU}{dt} = P(U,0)$ *Where* X^* *is world wide asymptotically steady.*
2. $G(U,V) = KV - \hat{G}(U,V)$, $\hat{G}(U,V) \geq 0$, *where* $K = D_V G(U^*,0)$ *is the Metzler Matrix and* $(X,Y) \in \omega$.
If the given system of equations 1 satisfies 2 then the equilibrium point E_0 *is a global asymptotically stable for* $R_0 < 1$.
Hence, the system 1 can be rewritten as

$$P(U,0) = \begin{pmatrix} \wedge - \mu S \\ 0 \end{pmatrix}, K = \begin{pmatrix} (\alpha+\mu) & 0 & 0 \\ \alpha & (\gamma+\mu) & 0 \\ 0 & \gamma & (\sigma+\mu) \end{pmatrix} and$$

$$\hat{G}(U,V) = \begin{pmatrix} \beta I (S_0 - S) \\ 0 \\ 0 \end{pmatrix}$$

Since $S_0 > S$, *by observation,* $\hat{G}((U,V)) \geq 0$ $(U,V) \in \Omega$.
We can say that the matrix K *is* M *matrix by the definition of* M *and also we able to find that* $X^* = (\frac{\triangle}{\mu}, 0)$ *is globally asymptotic stable steady state of the limiting structure* $\frac{dU}{dt} = P(U,0)$.
Since the two conditions are fulfilled, disease-free steady state $E_0 = (\frac{\triangle}{\mu}, 0, 0, 0, 0)$ *of structure of equations 1 is globally asymptotic stable if* $R_0 < 1$.

3.5 Local Stability of Endemic Equilibrium point

We conclude the endemic steady state $X^* = (S^* E^*, I^*, T^*, R^*)$ with their possibility conditions are

$$
\begin{aligned}
S^* &= \frac{\wedge}{\beta I^*+\mu}, \\
E^* &= \frac{\beta S^* I^*}{(\alpha+\mu)}, \\
T^* &= \frac{\gamma I^*}{(\alpha+\mu)}, \\
R^* &= \frac{\sigma T^*}{\mu}, \\
I^* &= \frac{(\wedge\alpha\beta-\mu(\gamma+\mu))}{(\beta(\gamma+\mu(\sigma+\mu)))} = \frac{(\wedge(R_0-1)-\alpha\sigma\mu)}{(\beta(\gamma+\mu)(\sigma+\mu))}
\end{aligned}
$$

Theorem 4. *When $R_0 > 1$,then Endemic Equilibrium point X^* is locally asymptotically steady and unstable if $R_0 < 1$.*

Proof 4. *The Jacobian matrix corresponding to the system 1 at endemic equilibrium point X^* is*

$$
J(X^*) = \begin{pmatrix}
(-\beta I^* + \mu) & 0 & -\beta S^* & 0 & 0 \\
\beta I^* & -(\mu+\alpha) & \beta S^* & 0 & 0 \\
0 & \alpha & -(\gamma+\mu) & 0 & 0 \\
0 & 0 & \gamma & -(\sigma+\mu) & 0 \\
0 & 0 & 0 & \sigma & -\mu
\end{pmatrix}
$$

The characteristic equation is

$$
(\gamma+\mu)(\gamma+(\sigma+\mu))\left(\lambda^3 + b_1\lambda^2 + b_2\lambda + b_3\right) = 0
$$

Where b_1=$\beta I^* + 3\mu + \alpha + \gamma$,
b_2= $(\alpha+\mu)(\gamma+\mu) - \alpha\beta S^* + (\gamma+\mu)(\beta I^* + \mu)$ *and*
$b_3 = (\beta I^* + \mu)((\alpha+\mu)(\gamma+\mu) - \alpha\beta S^*) - \beta^2 S^* I^*$
Hence the first two Eigen values are – μ,-$(\sigma+\mu)$ and remaining three Eigen values are the roots of the $\left(\lambda^3 + b_1\lambda^2 + b_2\lambda + b_3\right)$= 0.
Yet over again if the constants of specific equation $a_1 > 0$, $a_2 > 0$, $a_3 > 0$ and $a_1a_2 > a_3$ are true, formerly by Routh-Hurwitz criterion, altogether the roots of the specific equation have negative real portions and hence a stable equilibrium. Therefore Endemic equilibrium at X^* is locally asymptotically stable if $R_0 > 1$

4 Numerical Simulation

Numerical simulation was performed in order to establish analytical result. We assumed some parameter values and initial conditions of proposed $SEITR$ model and it can be shown table 2.

4.1 Analysis of results

The basic reproduction number for this set of limitation is $R_0 = 2.806$. The dynamical performance of the system will be observed in 2 with the help of MATLAB programming. From Fig. 2, we observed that the dynamics behavior of susceptible, exposed, Infected, treatment and recovered classes. This graph demonstrated that when the treatment rate rose, the infected population decreased and joined either the treatment population or the recovered population.

4.2 Discussion of results

From Fig.3 it was observed that the infected population(Fig.3b), exposed population(Fig.3c) and treatment population(Fig.3d) were decreased while the susceptible population(Fig.3a) was increased whenever the treatment rate increases.

Table 2: Influenza parameters values of the SEITR model

Parameter	Values	Source
β	1.2	[16],[30]
α	0.2	[9],[30]
γ	0.4	[16],[30]
σ	0.1	[16],[30]
μ	0.01	[26],[29]
$S(0)$	1	Assumed
$E(0)$	0.2	Assumed
$I(0)$	0.01	Assumed
$T(0)$	0.4	Assumed
$R(0)$	0.3	Assumed

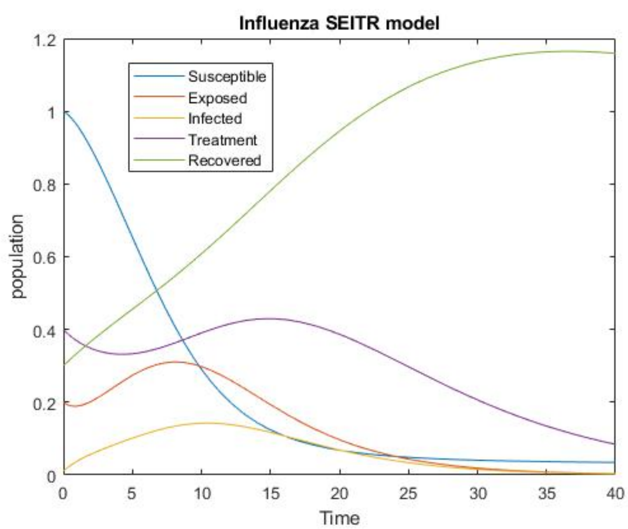

Figure 2: Dynamic behavior various compartments of SEITR model

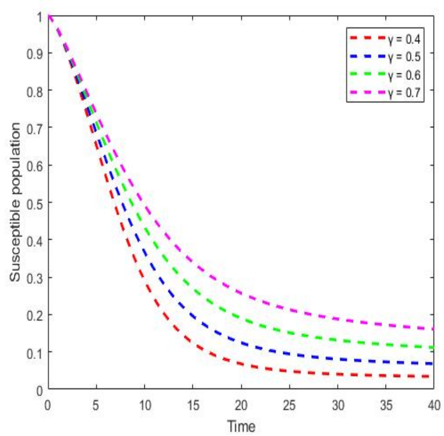

(a)

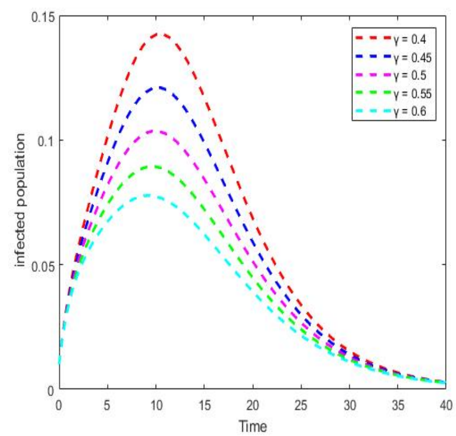

(b)

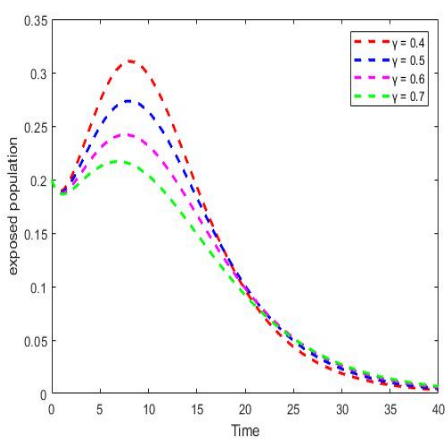

(c)

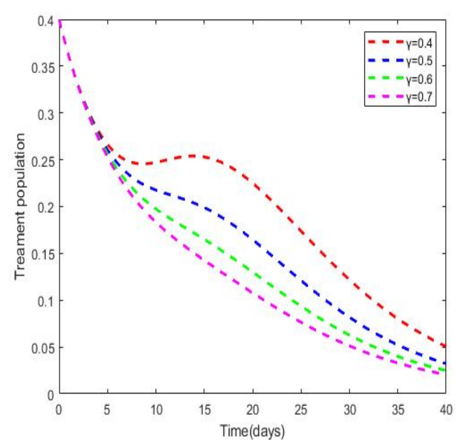

(d)

Figure 3: Effect of treatment rate γ on susceptible, exposed, Infected and treatment population

5 CONCLUSION

The epidemiological models are enabled us a noble knowledge to understanding the spread dynamics of infectious disease in better way. In this article, a five compartment epidemiological model SEITR was proposed and the basic properties were discussed. The basic reproduction number R_0 value was determined. The positivity and uniform boundedness were performed. The existence of disease free equilibrium point E_0 was discussed and showed that it is locally also globally asymptotically stable for $R_0 < 1$. Similarly the endemic equilibrium point X^* be real and local asymptotically stable for $R_0 > 1$. The transmission dynamics of influenza has been observed. The result of treatment rate on the susceptible, exposed, infected and treatment populaces has been examined and it has a positive effect on the infected population. The reproduction number $R_0 = 2.806 > 1$ indicates that the outbreak has gotten out of hand and that there are currently more sick people than ever before. Therefore, the only method to reduce the rate of illness spread is to enhance the rate of treatment, which includes the quick hospitalisation of infections that are dangerously ill. The outcome of the SEITR model on the disease program mechanism can be investigated in next studies. Additionally, future research can be done to ascertain the most effective management strategies for the sickness spread model and the belongings of medications and immunizations on the SEITR model.

References

[1] Anderson. R. M. and May R. M., Infectious Diseases of Humans: Dynamics and Control, Oxford University Press, Oxford, 1991.

[2] Andreasen. V, Lin. J and Levin. S.A, The dynamics of co circulating influenza strains conferring partial cross-immunity. J. Math. Biol., 35, 825-842, 1997.

[3] Attiq ul Rehman, Ram singh, Jagdev Singh, Mathematical analysis of multi-compartmental malaria transmission model with reinfection Chaos, Solitons and Fractals, 163, 2022.

[4] Baojun S. Compute using next generation operator. mtbi, Department of Mathematical Sciences Montclair State University, 12-14, 2013.

[5] Casagrandi. R, Bolzoni. L, Levin. S. A and Andreasen. V, The sirc model and influenza . Math. Biosci. (200) 152-169, 2006.

[6] Chinviriyasit. W, Numerical modelling of the transmission dynamics of influenza, ORSC & APORC, 52-59, 2007.

[7] Coburn. B. J, Wagner B. G. and Blower S., Modeling influenza epidemics and pandemics: insights into the future of swine flu (H1N1), BMC Med, 7(30), 2009.

[8] Dickmann O. and Heeserbeek J. A. P., Mathematical Epidemiology of Infectious Disease: Model Building Analysis and Interpretation, John Wiley, New York, 2000.

[9] Douglas. R, Influenza in man, in: E. Kilbourne (Ed.), The Influenza Viruses and Influenza, Academic Press, New York, USA, 395, 1975.

[10] Earn. D.J.D., Dushoff J. and Levin S.A, Ecology and evolution of the flu, Trends Ecol. Evol., (17) 334-340, 2002.

[11] Eccles. R., Understanding the symptoms of the common cold and influenza, The lancet infectious diseases Vol.5, No.11, 718-25, November 2005.

[12] Gu. Y., Komiya N., Kamiya H., Yasui Y., Taniguchi K., Okabe N., Pandemic A(H1N1) transmission during pre-symptomatic phase, Japan, Emerging infectious diseases, 17(9), September 2011.

[13] Heffernan J.M., Smith R.J. and Wahl L.M, Perspectives on the basic reproductive ratio, Journal of the Royal Society Interface, 2: 281-298, 2005.

[14] Herbert. W. Hethcote, Three basic epidemiological models, Springer - Verlag, NY, 1989.

[15] Hethcote. H.W, The mathematics of infectious diseases, siam rev., 42 599-653, 2000.

[16] Islam, R., Biswas, M. H. A., & Jamali, A. J. U. Mathematical Analysis of Epidemiological Model of Influenza a (H1N1) Virus Transmission Dynamics in Perspective of Bangladesh, GANIT: Journal of Bangladesh Mathematical Society, 37, 39-50, 2018. https://doi.org/10.3329/ganit.v37i0.35724.

[17] Jagdev Singh and Arpita Gupta, Computational analysis of fractional modified Degasperis - Procesi equation with Caputo-Katugampola derivative, AIMS Mathematics, 8(1):194-212, 2022.

[18] Jagdev Singh, Behzad Ganbari, Devendra Kumar, Dumitru Baleanu, Analysis of fractional model of guava for biological pest control with memory effect, Journal of Advanced Research, 32:99-108, 2021.

[19] Jagdev Singh, Devendra Kumar, Dumitru Baleanu, A new analysis of fractional fish farm model associated with Mittag-Leffler type kernel, International Journal of Biomathematics 13(2), 2020.

[20] Jongeun Choi, Lecture on Routh-Hurwitz Stability Criterion, Michigan State University.

[21] Kermack. W. O .and McKendrick A. G, A contribution to the mathematical theory of epidemics, Proc. Roy SocLond, 1927.

[22] Mishra O P, Mishra D K, Spread and control of influenza in two groups: a model, Applied Mathematics and Computation, April,219 (15):7982-7996, 2013.

[23] Murray. E., Alexander M.E., Seyed M., Moghadas S.M., Gergely R. and Jianhong W, A delay differential model for pandemic influenza with antiviral treatment, bull."Math. Biol. 70, 382-396, 2008.

[24] Quirouette C, Younis NP, Reddy MB, Beauchemin CAA (2020) Correction: A mathematical model describing the localization and spread of influenza A virus infection within the human respiratory tract. PLOS Computational Biology 16(11): e1008424. https://doi.org/10.1371/journal.pcbi.1008424

[25] Samuel Abubakar, Bifurcation analysis on the mathematical model of measles disease dynamics, UJAM, 212-216, 2013.

[26] Sanchez Y.G., Sabir Z., Guirao J.L.G. Design of a nonlinear SITR fractal model based on the dynamics of a novel coronavirus (covid -19) Fractals,28(8), 2020.

[27] Srivastav A K, Ghosh M, Analysis of a simple influenza (H1N1) model with optimal control, World Journal of Modelling and Simulation 12(4):307-319, 2016.

[28] Supriya yadav, Devendra Kumar, Jagdev Singh, Dumitru Baleanu, Analysis and Dynamics of Fractional Order Covid-19 Model with Memory Effect, Results in Physics, 24, 2021.

[29] Umar. M, Z. Sabir, M.A.Z. Raja, M. Shoaib, M. Gupta, Y.G. Sánchez, A stochastic intelligent computing with neuro-evolution heuristics for nonlinear SITR system of novel Covid-19, dynamics, Symmetry, 12(10),2020.

[30] Vinod Kumar Bais, and Deepak Kumar, SITR Dynamical Model for Influenza, International Journal of Engineering Technology Science and Research IJETSR,2,2015.

[31] ZhilanFeng, Final and peak epidemic sizes for SEIR models with quarantine and isolation, Mathematical Biosciences and Engineering, 4(4), 2007.

MHD Stagnation Point Flow and Heat Transfer of a Nanofluid Over a Stretching Sheet Fixed in Porous Medium with Effect of Thermal Radiation, Joule Heating and Heat Source/Sink

Ravindra Kumar[1] *Ruchika Mehta*[1*], *Tripti Mehta*[2] *and Sushila*[3]
[1]*Department of Mathematics and Statistics*,
Manipal University Jaipur, Jaipur(Raj.), India
[1]*Department of Mathematics*,
Vivekananda Global University, Jaipur(Raj.), India
[2]*Department of Mathematics*,
S. S. Jain Subodh P. G. College, Jaipur(Raj.), India
[3]*Department of Physics*,
Vivekananda Global University, Jaipur(Raj.), India
ruchika.mehta1981@gmail.com

Abstract

The goal of this research is to see how thermal radiation, joule heating, and heat Source/Sink affect two-dimensional nanofluid stagnation point flow above a stretching sheet fixed in a spongy medium. This research accounts for the magnetic field, and the nonlinear Rosseland approximation is used to calculate heat radiation. The governing equations are converted into a system via similarity transformations in joined nonlinear ordinary differential equations, which are solved numerically using the Runge-Kutta fourth order approach with shooting technique. The numerical results reveal that this method has excellent correctness, good convergence with minimal computational cost, and a lot of promise. The velocity and temperature are also found to increase as a function of the radiation parameter, Eckert number, Brownian motion parameter, Thermophoresis parameter, Biot Number, and thermal buoyancy parameter, as well as the reverse effect in Prandtl numeral. The skin friction, local Nusselt number, and local Sherwood number are increasing functions of the ratio of free stream velocity to stretching sheet velocity parameter, Biot number, Brownian motion parameter, and thermophoresis parameter, with the reverse effect in magnetic parameter, Prandtl number, and permeability parameter.

Keywords: Nanofluid, Stretching Sheet, thermal radiation, joule heating, heat Source/Sink.

1 Introduction:

Nanofluid is a base fluid containing nanometer-sized particles/fibers (water, oil, ethylene glycol, etc.).Al_2O_3, Cu, T_iO_2, Ag, and other materials are commonly utilized for nanoparticles. These liquid combinations were discovered to have excellent assets that could make them useful in a variety of technical and manufacturing applications involving temperature transmission, nuclear reactors, petroleum cells, microelectronics, power production and carrying, space expertise, security and ships, and bony film solar power collectors are only few of the technologies that are being developed. [5] deals with (MHD) nanofluid stream towards a nonlinear extended plane with changeable depth in the company of an electric ground. In the existence of thermal radiation and Joule heating impacts, buoyant MHD nanofluid flow and heat transmission over a stretching sheet are examined [7]. [12] examined the impacts of thermally evolved thermophoresis diffusion and Brownian motion in non-Newtonian nanofluids across an angled extending sheet, as well as the belongings of hotness radiation and chemical response. [14]The influence of thermal radiation on a heat absorbing magneto-viscous nanofluid's dissipative boundary layer flow transversely a holey exponentially overextended pane with thermal slips and Navier's velocity was investigated. When there is a consistent magnetic field present. [15] Entropy generation study of a two-way nanofluid flick stream of Eyringâ€"Powell liquid with warmth and mass transport through an unstable porous stretched sheet was investigated (MHD). [21] The belongings of a magnetic ground and heat rays on the compelled convection stream of CuO-water nano-fluid transversely a stretched pane with a point of stagnation were statistically investigated. The effects of heat radiation on the heat transfer of water-based nanofluids containing exponentially stretched sheets of motile gyrotactic microorganisms were studied by [24]. [26] The authors presented a Form in mathematics for MHD radiative stream of III-grade nanomaterials limited by a nonlinear extending sheet of flexible thickness. [29] investigated the formation of entropy in a II-grade nanofluid MHD stream finished a sheet that is being heated convectively and using nonlinear current radioactivity and viscid .Numerous slip properties on MHD unsteady Maxwell nanofluid stream finished a holey overextended pane with thermal radioactivity and thermo-diffusion in the attendance of chemical response were examined by [1]. In the presence of thermal radiation and a heat source, a 2-way MHD stream of a Jeffery nanofluid transversely a stretched sheet has been quantitatively examined by [2]. In a 2-dimensional accepted convection stream of unstable electrical nanofluid with MHD across a linearly leaky stretched pane, the belongings of suction, as well as current radioactivity, and Joule heating, are investigated by [4]. [18] looked explored the influence of numerous slipups on axisymmetric (MHD) buoyant nano-fluid stream across an extending sheet.[20] The stream of a nanofluid with changeable liquid characteristics done an angled overextended pane in the existence of current energy and chemical response is investigated using unsteady magnetohydrodynamics (MHD). The impact of slip circumstances on the two-way unsteady varied convection stream of electric MHD nanofluid over a stretched sheet in the company of thermal energy, gluey debauchery, and chemical response are the subject of this research. [4]. The effect of nonlinear thermal radiation and spatial and temperature dependent heat generation/absorption on a 3- way MHD Jeffrey liquid stream across a nonlinearly With porous material present, a permeable stretched sheet was investigated. [10]. The current and Joule boiler effect of Casson nanofluid stream with chemical response across an inclined porous stretched surface is investigated in [11]. The effects of buoyancy force on viscoelastic (second grade fluid) magnetized nanofluid were studied by [13]. [19] using a stretched sheet immersed in a porous media generated by suction/blowing, researchers explored the belongings of viscous-Joule boiler, current energy, and warmth production (or absorption) on MHD nanofluid flow. [28] used the power of numerical computing-based Lobatto IIIA method to investigate warmth and mass transmission in 3-D MHD radioactive current of water-based mixture nanofluid across an extended sheet. [30] investigated the three-dimensional border coating stream of Maxwell nanofluid across a extending sheet using magnetohydrodynamic (MHD) warmth and mass transmission. [31] An unsteady magneto-hydrodynamic heat and mass transfer model is used to investigate the heat and mass transfer of a hybrid nanofluid flow across a stretched

2

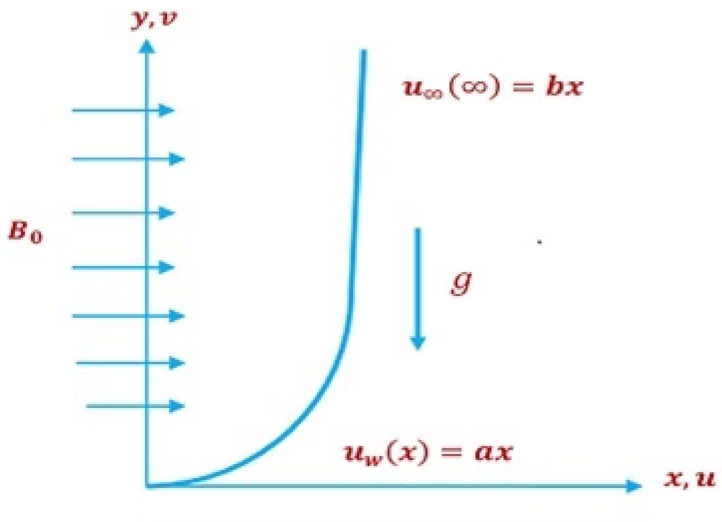

Figure 1: Schematic diagram of the Problem

surface. [32] investigated the heat and mass transfer characteristics of nanofluid flow over a stretched surface embedded in a porous medium in both steady and unsteady cases. [9] examined the effects of solar waves on 2-dimensional a stretched sheet is traversed by nanofluid stagnation-point flow. [16] looked at the heat transport and entropy of an unsteady flow of a non-Newtonian Casson nanofluid. [17] studied for magnetic dipole with stagnation point flow of micropolar nanofluids. [23] warmth and mass transport across a linear extending pane, as well as the essence of nonlinear thermal rays and entropy production for continuous laminar 2-way convective MHD Jeffrey nanofluid stream, were examined. [25]. The effects of convective boundary conditions on MHD Prandtl nanofluid flow over a stretched sheet were investigated.[3]considered the rheological and thermophysical characteristics of a non-Newtonian viscoelastic liquid under stratification over a linearly stretched surface.[27]This pagination's main goal is to outline characteristics of a water-based hybrid nanoliquid flow with single-wall carbon nanotube dispersion.

2 Construction of the Problem:

A steady nanofluid boundary layer flow in two dimensions through an extending sheet is using the speed of $u_w(x) = ax$ wherever a is a constant, as illustrated in Fig.1. A homogenous attractive arena of B_0 upright to the flow direction is supposed to be influenced. Warmth transmission scrutiny is done in the company of viscous dissipation and Joule heating and thermal energy qualities.T_w denotes the convective surface temperature which are based on Fig.1 and T_∞ symbolizes the ambient fluid temperature in the following governing equations. For this nano-fluid flow, the stable border line coat equations for stagnation point flow that is in-compressible:

$$\frac{\partial u}{\partial x} + \frac{\partial v}{\partial y} = 0, \tag{1}$$

$$u\frac{\partial u}{\partial x} + v\frac{\partial u}{\partial y} = u_\infty\frac{\partial u_\infty}{\partial x} + \nu\frac{\partial^2 u}{\partial y^2} - \frac{\sigma {B_0}^2(u-u_\infty)}{\rho} - \frac{\nu}{k}(u-u_\infty) \\ +g\beta_T(T-T_\infty) + g\beta_C(C-C_{\infty)}, \tag{2}$$

Where u_∞ is the free stream velocity, ν means the kinematic viscocity, σ expressions forelectric conduction of liquid, B_0 establishes the unvarying magnetic arena along y-direction, k is used for porosity factor, u and v, respectively, stand for the x- and y-directional velocity components. We have the following border circumstances for the problem under consideration:

$$u = u_w(x) = ax, v = 0, at\ y = 0, and\ u \to u(\infty) = bx, \quad as\ y \to \infty \tag{3}$$

The dimensionless variables are introduced in the form of

$$\eta = \sqrt{\frac{a}{\nu}}y\ , u = \frac{\partial \psi}{\partial y} = axf'(\eta)\ , v = -\frac{\partial \psi}{\partial x} = axf(\eta) \tag{4}$$

Eq. (1) is satisfied in the same way, and Eqs. (2) and (3) can be rewritten as

$$f^{'''} + ff^{''} - f^{'^2} - \ (M+K)(f^{'} - \lambda) + \lambda^2 + \lambda_1\theta + \lambda_2\phi = 0, \tag{5}$$

$$f(0) = 0,\ f^{'}(0) = 1,\ when\ \eta = 0\ and\ f^{'}(\infty) = \lambda,\ as\ \eta \to \infty, \tag{6}$$

where $M = \frac{(\sigma {B_0}^2)}{\rho a}$,is the magnetic restriction, $\lambda = \frac{b}{a}$, represents the share of the rates of unrestricted stream speed to the extending sheet speed, $K = \frac{\nu}{ka}$ is the permeability parameter $\lambda_1 = \frac{G_r}{R_e^2}$ is the thermal buoyancy parameter, where $G_r = g\beta_T(T_w - T_\infty)\frac{x^3}{\nu^2}$ is Grashof numeral, and $Re = \frac{(xU_w)}{\nu}$ is Reynolds number, $\lambda_2 = g\beta_C(C_w - C_\infty)\frac{x^3}{\nu^2}$ is the concentration buoyancy parameter.
Equation of Energy

$$\begin{aligned} u\frac{\partial T}{\partial x} + v\frac{\partial T}{\partial y} = \alpha\frac{\partial^2 T}{\partial y^2} + \frac{\nu}{C_p}(\frac{\partial u}{\partial y})^2 - \frac{1}{\rho c_p}\frac{\partial q_r}{\partial y} + \frac{\sigma {B_0}^2(u-u_\infty)^2}{\rho c_p} \\ + \tau(D_b\frac{\partial T}{\partial y}\frac{\partial C}{\partial y} + \frac{D_T}{T_\infty}(\frac{\partial T}{\partial y})^2) + \frac{Q^*(T-T_\infty)}{\rho c_p} \end{aligned} \tag{7}$$

Equation of Concentration

$$u\frac{\partial C}{\partial x} + v\frac{\partial C}{\partial y} = D_b\frac{\partial^2 C}{\partial y^2} + \frac{D_T}{T_\infty}(\frac{\partial T}{\partial y})^2 \tag{8}$$

where T symbolizes the temperature, C symbolizes the nanoparticles concentration, α is the current diffusivity, D_b and D_T are the Brownian motion coefficient and the thermophoretic dispersal coefficient, correspondingly. $\tau = \frac{(\rho p)_p}{(\rho p)_f}$ is the share of the nanoparticle active warmth size to the base fluid warmth size and q_r states to the radiative warmth flux amount. The radiative heat flux can be calculated using the Rosseland guess for current radiation and applied to optically thick medium as. $q_r = -\frac{4}{3}\frac{\sigma^*}{K^*}\frac{\partial T^4}{\partial y}$ where σ^*, k^* are the Stefan-Boltzman constant and average assimilation coefficient, correspondingly. $T^4 = 4T{T_\infty}^3 - 3T_\infty^4$ is achieved by utilising the Taylor series to expand $T^4$with respect to T_∞while disregarding terms of higher orders. As a result, Eq. (7) is found to be

$$\begin{aligned} u\frac{\partial T}{\partial x} + v\frac{\partial T}{\partial y} = \alpha\frac{\partial^2 T}{\partial y^2} + \frac{\nu}{C_p}(\frac{\partial u}{\partial y})^2 + \frac{16\sigma^* T_\infty^3}{3\rho C_p k^*}\frac{\partial^2 T}{\partial y^2} + \frac{\sigma {B_0}^2(u-u_\infty)^2}{\rho c_p} \\ + \tau(D_b\frac{\partial T}{\partial y}\frac{\partial C}{\partial y} + \frac{D_T}{T_\infty}(\frac{\partial T}{\partial y})^2) + \frac{Q^*(T-T_\infty)}{\rho c_p} \end{aligned} \tag{9}$$

For radiative heat flux modelling, the nonlinear Rosseland guess is used. As an outcome, the relevant convective warmth transport boundary conditions can be presented as.

$$-k\frac{\partial T}{\partial y} = (T - T_W), C = C_w, at\ y = 0, T \to T_\infty,\ C \to C_\infty, as\ \ y \to \infty \tag{10}$$

As a result of specifying the non-dimensional temperature $T = T_\infty + (T_w - T_\infty)\theta(\eta)$ and $C = C_\infty + (C_w - C_\infty)\phi(\eta)$. Eqs. (7) and (8) take the following format:

$$(1 + R_a)\theta^{''} + P_r[f\theta^{'} + ME_c(f^{'} - \lambda)^2 + E_c(f^{''})^2 + (N_b\theta^{'}\phi^{'} + N_t\theta^{'^2}) + \delta\theta\ ] = 0 \tag{11}$$

$$\phi^{''} + L_e f\phi^{'} + \frac{N_t}{N_b}\theta^{''} = 0, \tag{12}$$

and the borderline circumstances

$$\theta^{'}(0) = -(1 - \theta(0))Bi, \phi(0) = 1, \theta(+\infty) \to 0, \phi(+\infty) \to (0), \tag{13}$$

Where $P_r = \frac{\nu}{\alpha}$, is Prandtl number, $R_a = \frac{16\sigma^* T_\infty^3}{3kk^*}$, is radiation parameter, $E_c = \frac{U_w^2}{C_p(T_w - T_\infty)}$, is the Eckert number, $N_b = \frac{\tau D_b(C_W - C_\infty)}{\nu}$,shows the Brownian motion restriction, $N_t = \frac{\tau D_T(T_W - T_\infty)}{\nu T_\infty}$, is thermophoresis restriction,$\delta = \frac{Q^* L}{\rho C_p U_w}$, heat source/sink restriction, $L_e = \dfrac{\nu}{D_b}$, Lewis factor, $Bi = \dfrac{h}{k}\sqrt{\frac{\nu}{a}}$, denotes the Biot number. The three physical measures of our attention are the coefficient of skin friction C_{f_x}, the local Nusselt numberN_{u_x}, and local Sherwood number S_{u_x}, are given as.

$$C_{f_x} = \frac{\tau_w}{\rho U_w^2}, N_{u_x} = \frac{xq_w}{k(T_w - T_\infty)}, S_{u_x} = \frac{xq_m}{D_b(C_w - C_\infty)}, \tag{14}$$

where

$$\tau_w = \mu(\frac{\partial u}{\partial y})_{y=0}, q_w = -k(\frac{\partial T}{\partial y})_{y=0} + (q_r)_{y=0}, q_m = -D_b(\frac{\partial C}{\partial y})_{y=0}, \tag{15}$$

the relations will be.

$$C_{f_x}(R_e)^{\frac{1}{2}} = f^{''}(0),\ N_{u_x}(R_e)^{\frac{-1}{2}} = -(1 + R_a)\theta'(0), S_{u_x}(R_e)^{\frac{1}{2}} = -\phi^{'}(0), \tag{16}$$

The result of equations (4), (11) and (12) jointly through borderline circumstances (5) and (13) is determine through by a systematic numerical method called shooting technique. We translate the nonlinear equivalences into first order regular differential equivalences by labelling the variable quantity i.e.

$f = f_1$, $f^{'} = f_2$, $f^{''} = f_3$, $f^{'''} = f_3^{'}$, $\theta = f_4$, $\theta^{'} = f_5$, $\theta^{''} = f_5'$, $\phi = f_6$,

$\phi^{'} = f_7$, $\phi^{''} = f_7^{'}$, Hence, the system of equations becomes

$$f_1^{'} = f_2, f_2^{'} = f_3, f_3^{'} = [f_2^2 - f_1 f_3 + (M + K)(f_2 - \lambda) - \lambda^2 - \lambda_1 f_4 - \lambda_1 f_6] \tag{17}$$

$$f_4^{'} = f_5, \tag{18}$$

$$f_5^{'} = -(1 + R_a)^{-1} P_r[f_1 f_5 + ME_c(f_2 - \lambda)^2 + E_c f_3^2 + N_b f_5 f_7 + N_t f_5^2 + \delta f_4] \tag{19}$$

$$f_6^{'} = f_7, \tag{20}$$

$$f_7^{'} = -(l_e f_1 f_5 + \frac{N_t}{N_b} f_5^{'}), \tag{21}$$

Subject to the following conditions

$$\begin{gathered} f_1(0) = 0, f_2(0) = 1, f_3(0) = S_1, f_4(0) = (1 + \frac{S_2}{B_i}), f_5(0) = S_2, f_6(0) = 1, \\ f_7(0) = S_3,\ as\ \eta \rightarrow 0\ and\ f_2(\infty) = \lambda, f_4(\infty) = 0, f_6(\infty) = 0,\ as\ \eta \rightarrow \infty \end{gathered} \tag{22}$$

Now fourth order Runge-Kutta way with shooting technique is follow for stepwise integration and calculations are passed out on MATLAB computer software.

3 Influence of Diverse Restrictions

Ordinary differential equations that are nonlinear. (4), (11) and (12) are numerically solved with the borderline circumstances (5) and (13) using the MATLAB software and the shooting and fourth-order Runga-Kutta method. The obtained results demonstrate the impact of non-dimensional controlling parameters, specifically the magnetic field parameter M, Prandtl numeral P_r, radiation restriction R_a, the proportion of the free stream speed to the extending sheet speed restriction λ, Eckert numeral E_c, Thermophoresis restriction N_t, Brownian motion restriction N_b, Biot Numeral B_i, Lewis factor L_e, Permeability restriction K, thermal buoyancy parameter λ_1, Solutal buoyancy parameter λ_2 and Heat Source/Sink δ. Figures 2 and 3 depict the effect of the magnetic field restriction M on the velocity and temperature field distributions.It's worth noting that when M gets higher, the velocity field gets smaller. A resistive sort of force termed Lorentz force is created in the stream when the magnetic field parameter increases, causing a decrease in velocity field curves. It has been pragmatic that an enhance in magnetic parameters raises the temperature. The Lorentz force causes some additional warmth to be created in the flow. When the magnetic field is increased, the momentum layer thickness decreases while the thermal layer thickness increases. The impact of Prandtl number P_r on the supply of speed and temperature ground is exposed in Fig.4 and 5. It is perceived that growing values of P_r results a decline in velocity and temperature field. Figure 6 and 7 exhibits the significance of the radiation parameter R_a on the velocity and temperature, correspondingly. Figures 6 and 7 show that increasing the radiation parameter increases fluid velocity and temperature. The impact of proportion of the free stream speed to the speed of the extending sheet restriction λ on temperature arena is exposed in Fig.9. escalating values of Λ results a decrement in temperature field. The impact of Eckert number E_c, Brownian motion parameter N_b, Thermophoresis parameter N_t, Biot Numeral B_i on the sharing of speed and warmth field is exposed in Fig. 10, 11, 12, 13, 14, 15 16 and 17It has been observed that rising values of E_c, N_b, N_t and B_i results increment in velocity and temperature field.

4 Conclusions

The influence of thermal radiation, Heat Source/Sink, and joule heating on two-dimensional nanofluid stagnation point stream across a extending pane fixed in porous medium is discussed in this study. The controlling PDEs are changed into nonlinear ODEs using similarity transformations, and then These equations are numerically solved . The effects of a variety of non-dimensional characteristics on velocity and temperature fields are discussed and represented using graphs. The

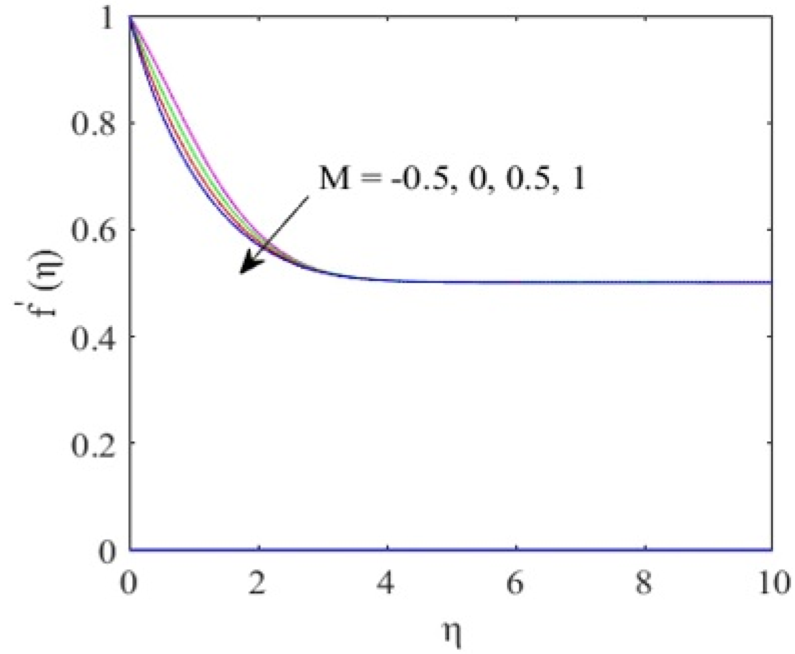

Figure 2: Velocity with η for disparate facts of magnetic restriction M.

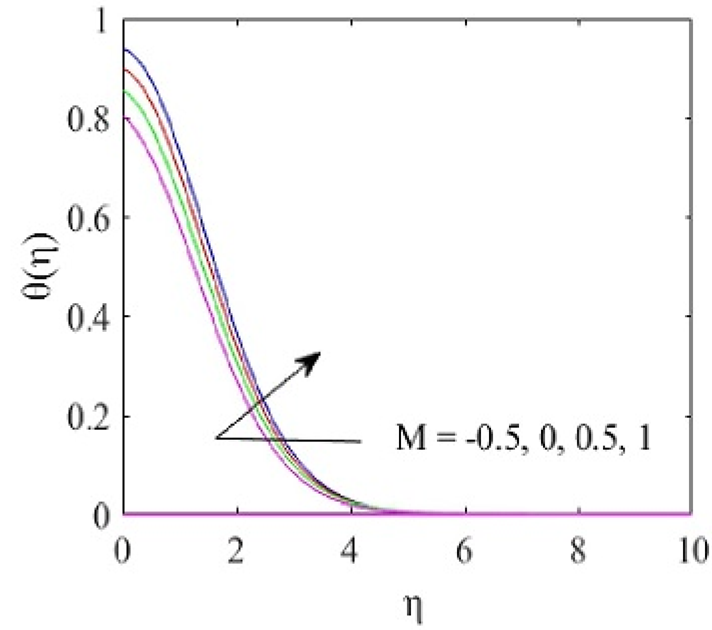

Figure 3: Temperature with η for disparate facts of magnetic restriction M.

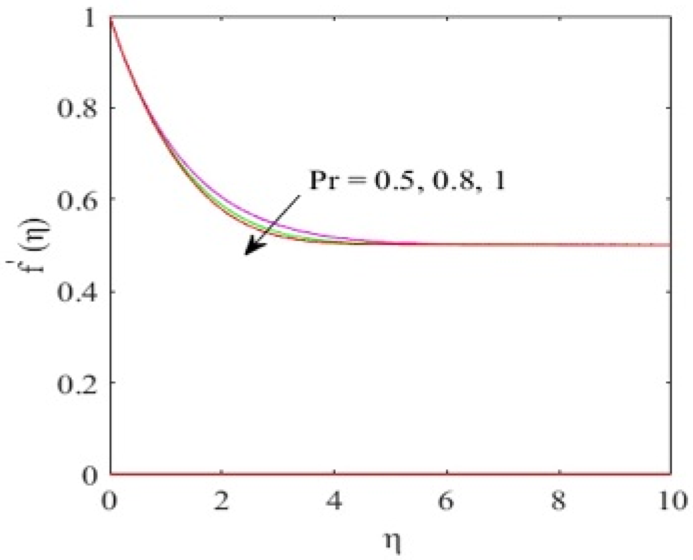

Figure 4: Velocity with η for disparate facts of Prandtl numeral P_r.

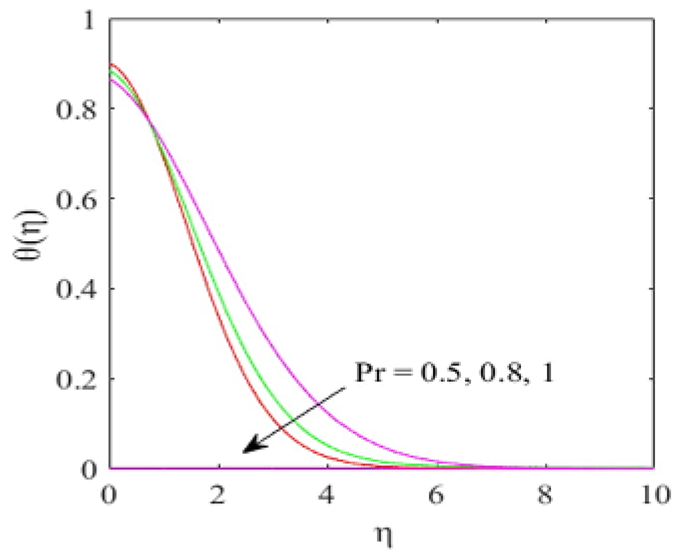

Figure 5: Temperature with η for disparate facts of Prandtl numeral P_r.

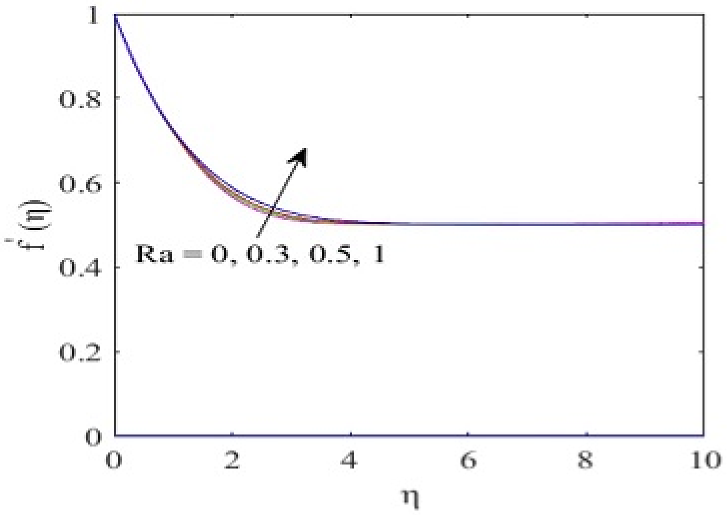

Figure 6: Velocity with η for disparate facts of radiation restriction R_a.

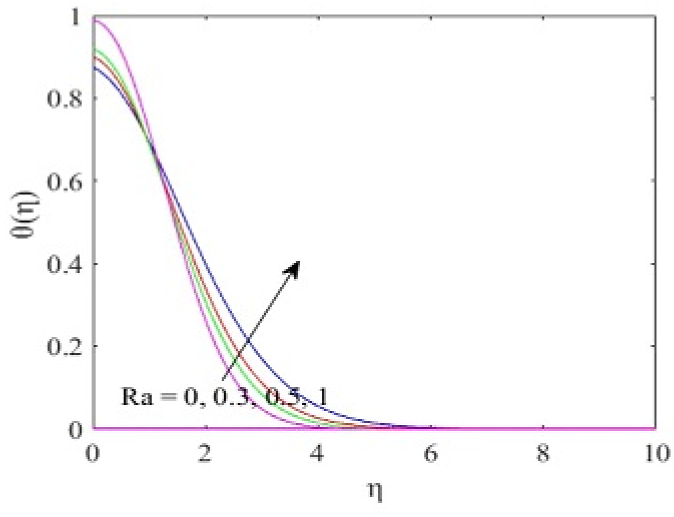

Figure 7: Temperature with η for disparate facts of radiation restriction R_a.

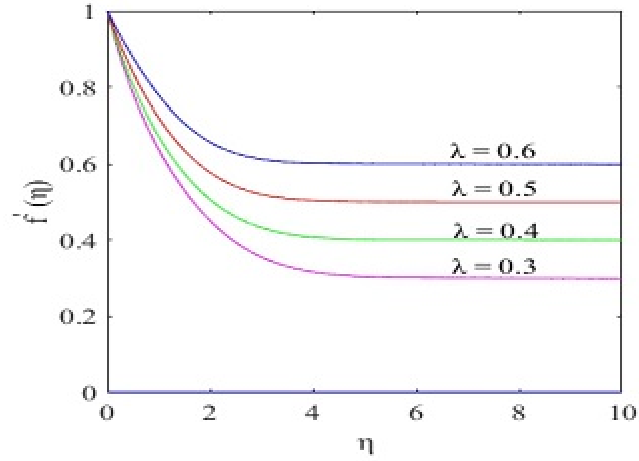

Figure 8: Velocity with η for disparate facts of free stream velocity to stretch sheet restriction velocity ratio of the stretching sheet parameter λ.

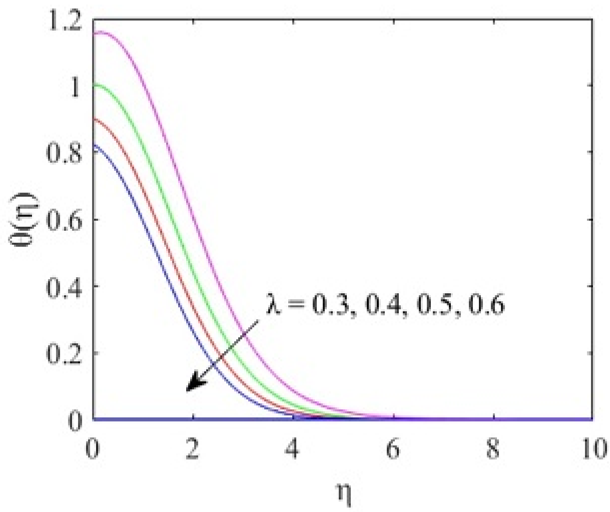

Figure 9: Temperature $\theta(\eta)$ related to η for unlike facts of ratio of the free stream velocity to stretch sheet restriction velocity ratio parameter λ.

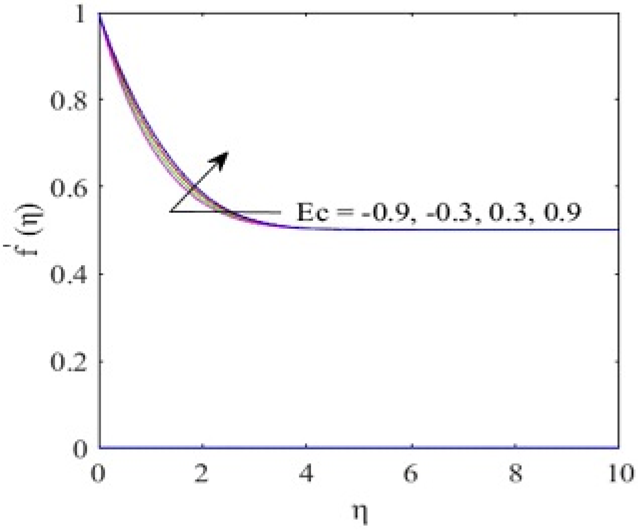

Figure 10: Velocity with η for disparate facts of Eckert numeral E_c.

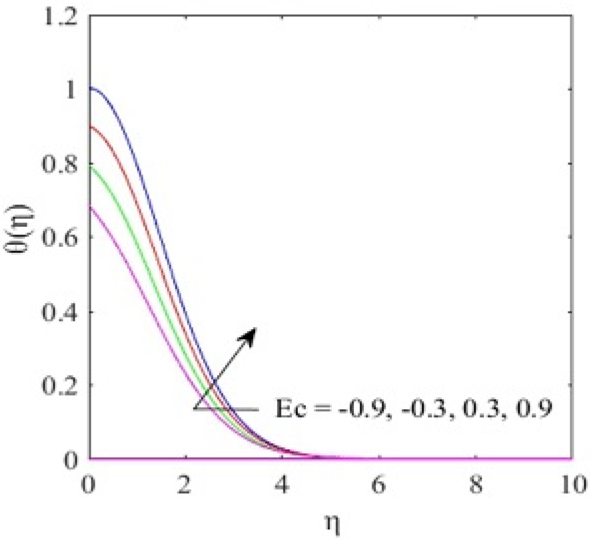

Figure 11: Temperature with η for disparate facts of Eckert numeral E_c.

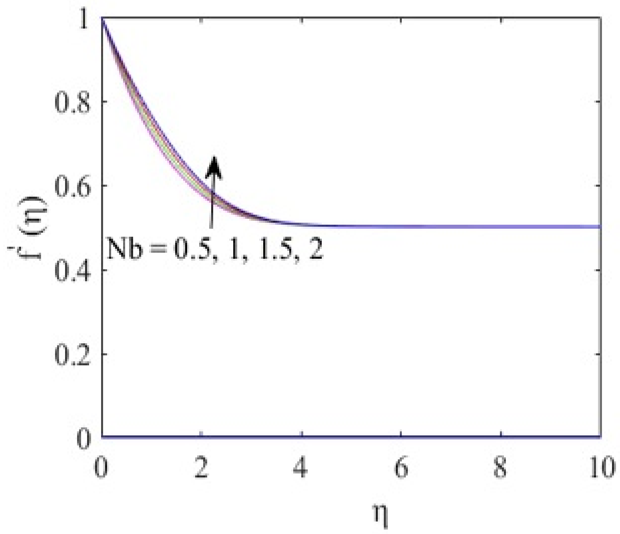

Figure 12: Velocity with η for disparate facts of Brownian motion parameter N_b.

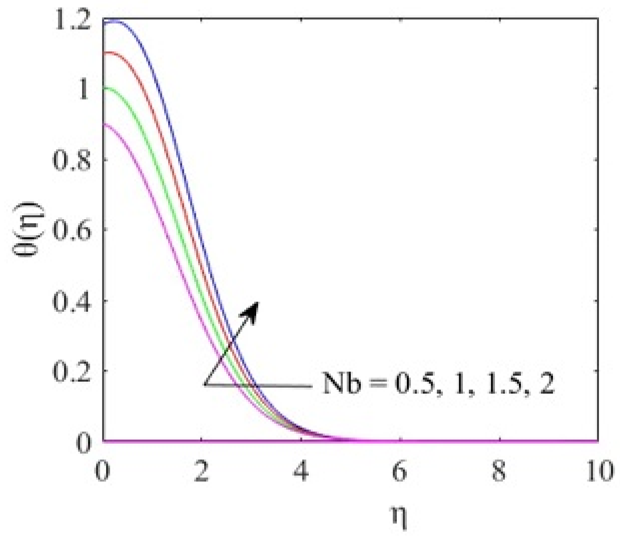

Figure 13: Temperature with η for disparate facts of Brownian motion parameter N_b.

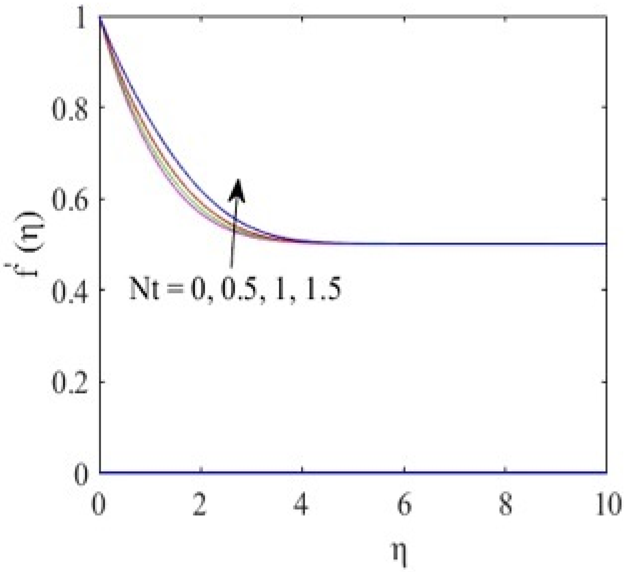

Figure 14: Velocity with η for disparate facts of Thermophoresis parameter N_t.

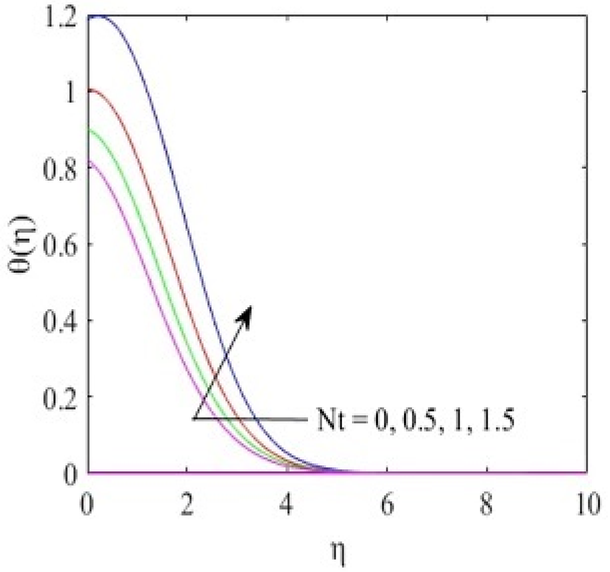

Figure 15: Temperature with η for disparate facts of Thermophoresis parameter N_t.

13

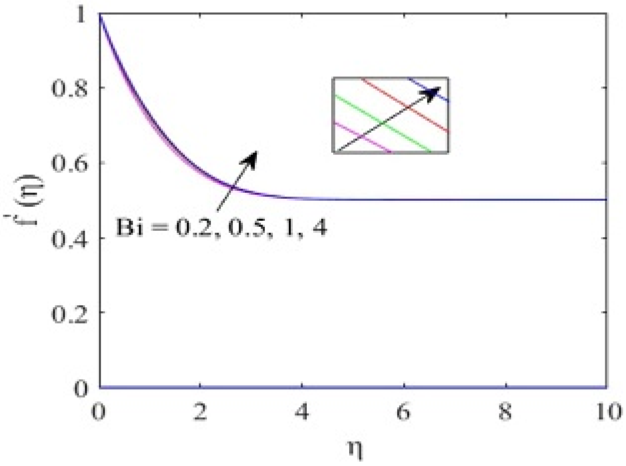

Figure 16: Velocity with η for disparate facts of Biot Numeral Bi.

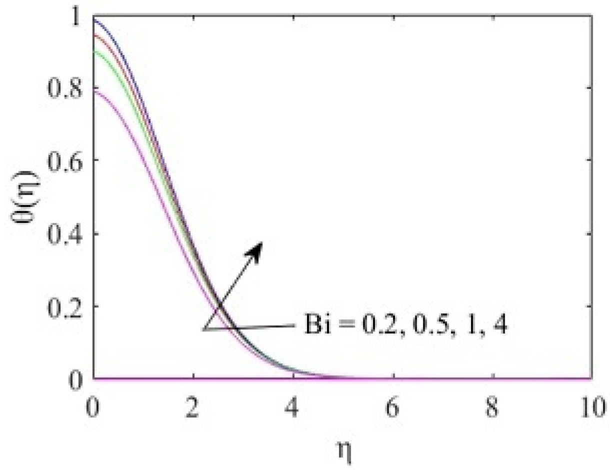

Figure 17: Temperature with η for disparate facts of Biot Numeral Bi.

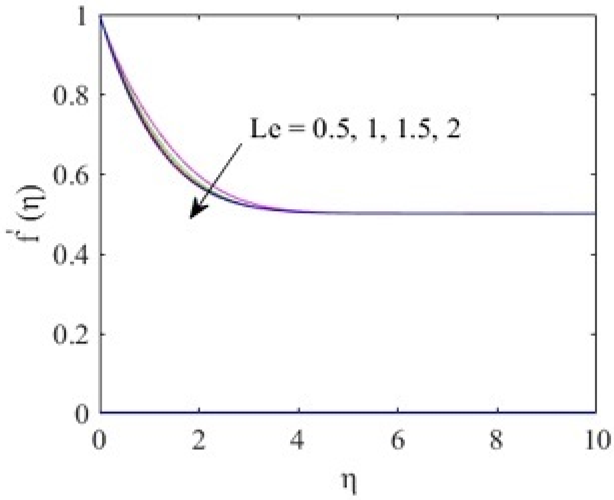

Figure 18: Velocity with η for disparate facts of Lewis factor L_e.

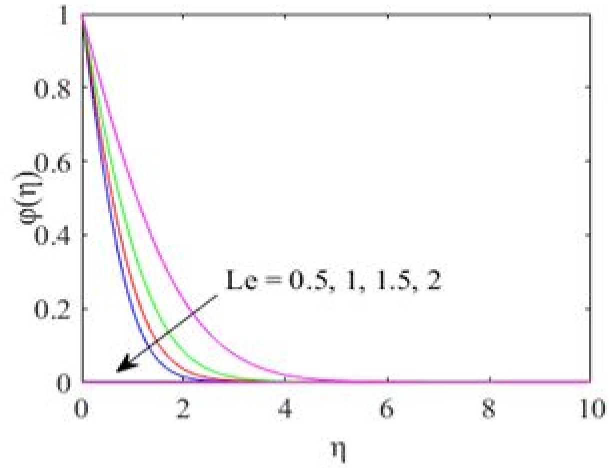

Figure 19: Concentration with η for disparate facts of Lewis factor L_e.

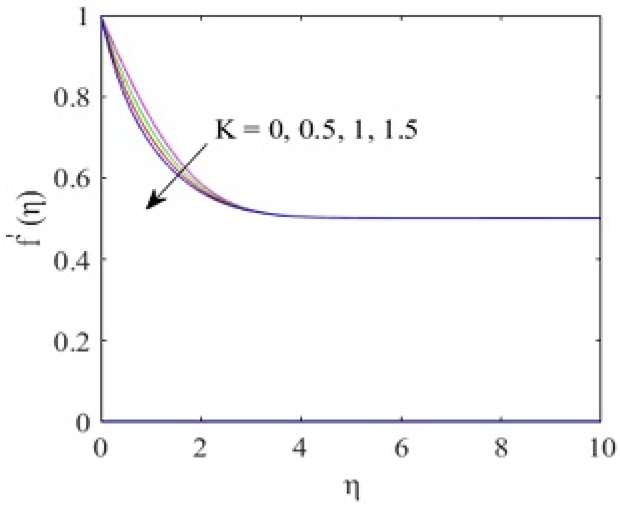

Figure 20: Velocity with η for disparate facts about permeability limitations K.

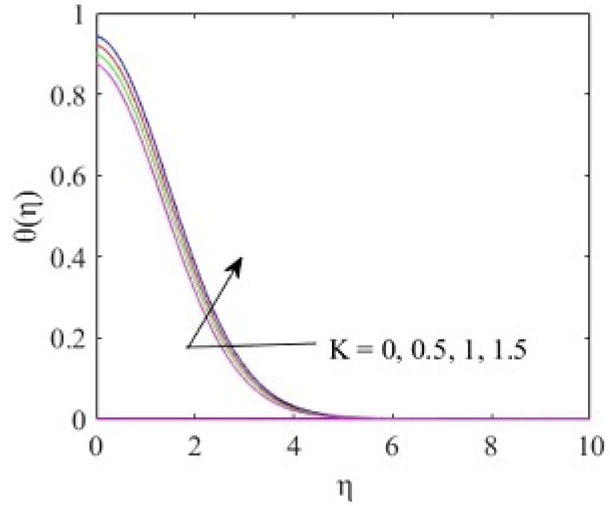

Figure 21: Temperature with η for disparate facts about permeability limitations K.

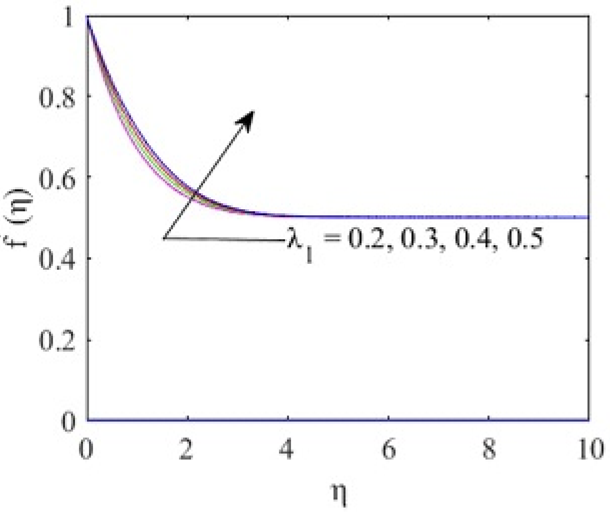

Figure 22: Velocity with η for disparate facts of thermal buoyancy parameter λ_1.

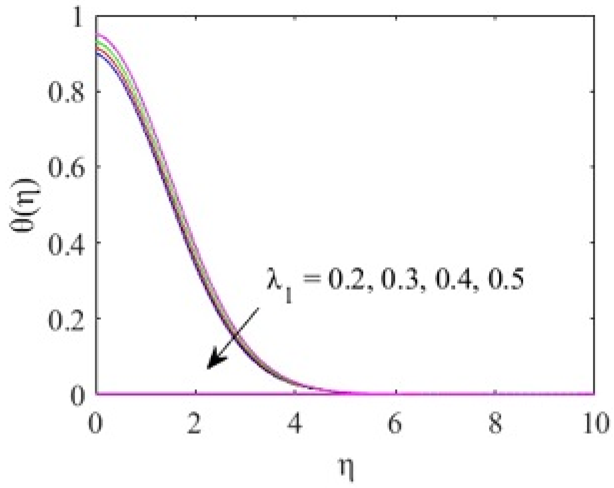

Figure 23: Temperature with η for disparate facts of thermal buoyancy parameter λ_1.

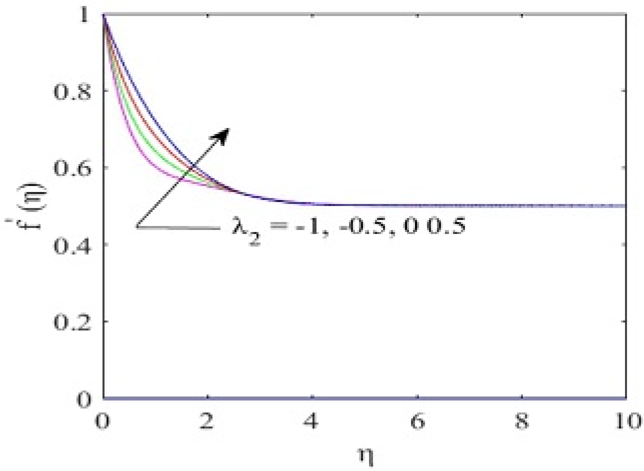

Figure 24: Velocity with η for disparate facts of Solutal buoyancy parameter λ_2.

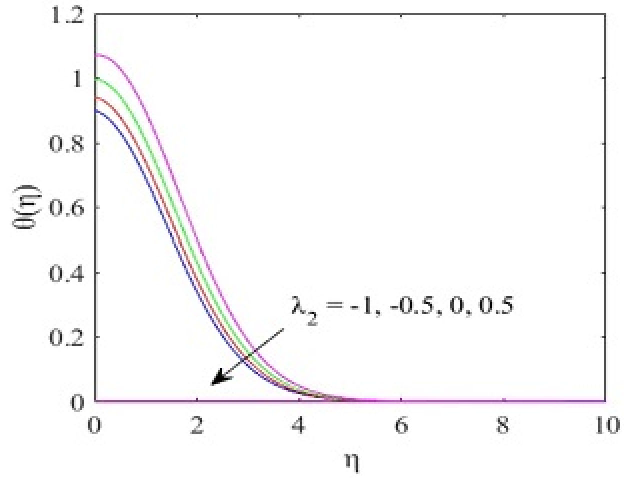

Figure 25: Temperature with η for disparate facts of Solutal buoyancy restriction λ_2.

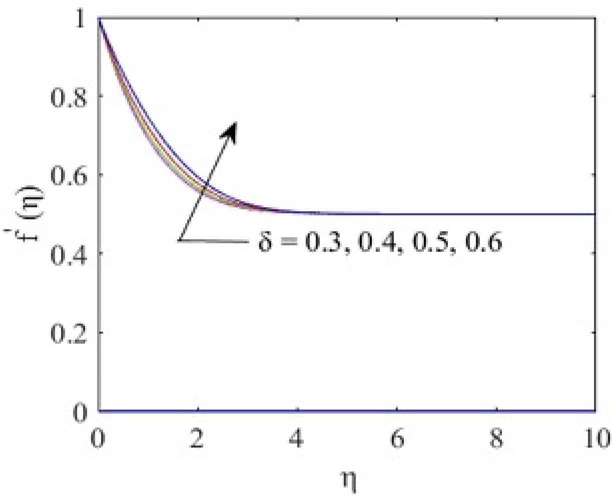

Figure 26: Velocity with η for disparate facts of Heat Source/Sink δ.

Table 1: Encouragement of the three physical dealings are the coefficient of skin friction C_{f_x}, the local Nusselt number N_{u_x} and local Sherwood number S_{u_x}.

Parameter	C_{f_x}	N_{u_x}	S_{u_x}
$M=-0.5$	-0.1951	0.1470	0.7460
$M=0$	-0.2948	0.1080	0.7365
$M=0.5$	-0.3866	0.0749	0.7291
$M=1$	-0.4707	0.0450	0.7222
$P_r=0.5$	-0.3827	0.1008	0.7316
$P_r=0.8$	-0.3861	0.0870	0.7296
$P_r=1$	-0.3866	0.0749	0.7291
$K=0$	-0.2887	0.0930	0.7381
$K=0.5$	-0.3866	0.0749	0.7291
$K=1$	-0.4758	0.0585	0.7217
$K=1.5$	-0.5573	0.0422	0.7160
$\lambda=0.3$	-0.5386	-0.1136	0.7041
$\lambda=0.4$	-0.4778	-0.0015	0.7141
$\lambda=0.5$	-0.3866	0.0749	0.7291
$\lambda=0.6$	-0.2743	0.1320	0.7460
$B_i=0.2$	-0.4161	0.0630	0.7261
$B_i=0.5$	-0.3866	0.0749	0.7291
$B_i=1$	-0.3749	0.0813	0.7315
$B_i=4$	-0.3641	0.0850	0.7326
$\lambda_1=0.2$	-0.5240	0.0369	0.7145
$\lambda_1=0.3$	-0.4762	0.0518	0.7196
$\lambda_1=0.4$	-0.4307	0.0642	0.7251
$\lambda_1=0.5$	-0.3866	0.0749	0.7291
$\lambda_2=-1$	-0.9295	-0.0525	0.6858
$\lambda_2=-0.5$	-0.7493	0.0030	0.7006
$\lambda_2=0.5$	-0.3866	0.0749	0.7291
$E_c=-0.9$	-0.4532	0.2360	0.7191
$E_c=-0.3$	-0.4204	0.1557	0.7241
$E_c=0.3$	-0.3866	0.0749	0.7291
$E_c=0.9$	-0.3546	-0.0021	0.7352
$\delta=0.3$	-0.4505	0.2182	0.7189
$\delta=0.4$	-0.4241	0.1590	0.7231
$\delta=0.5$	-0.3866	0.0749	0.7291
$\delta=0.6$	-0.3283	-0.0563	0.7391
$N_b=0.5$	-0.3866	0.0749	0.7291
$N_b=1$	-0.3519	-0.0014	0.7335
$N_b=1.5$	-0.3180	-0.0732	0.7375
$N_b=2$	-0.2880	-0.1344	0.7406
$N_t=0$	-0.4150	0.1347	0.7225
$N_t=0.5$	-0.3866	0.0749	0.7291
$N_t=1$	-0.3490	-0.0034	0.7398
$N_t=1.5$	-0.2823	-0.1400	0.7571
$R_a=0$	-0.3700	0.0060	0.7301
$R_a=0.3$	-0.3846	0.0527	0.7296
$R_a=0.5$	-0.3866	0.0749	0.7291
$R_a=1$	-0.3879	0.1251	0.7290
$L_e=0.5$	-0.3643	0.0930	0.5055
$L_e=1$	-0.3866	0.0749	0.7291
$L_e=1.5$	-0.4030	0.0696	0.9021
$L_e=2$	-0.4162	0.0681	1.0503

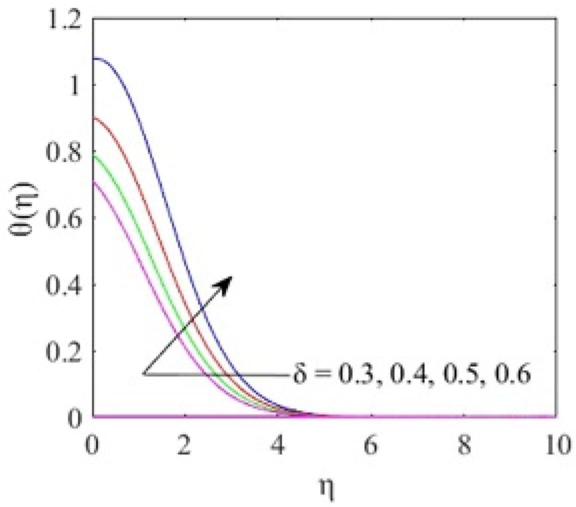

Figure 27: Temperature with η for disparate the Source/Sink facts δ.

table analyses and presents the effect of physical parameters on skin friction, local Nusselt number, and local Sherwood number. The following is a summary of the findings:

- Increasing the magnetic field parameter causes the velocity field to decrease and the temperature distribution to improve.
- The velocity and temperature field both are decrease for Prandtl number but reverse effect is seen in of radiation restriction R_a, Eckert numeral E_c, Thermophoresis limitations N_t,Brownian motion limitations N_b, Biot Numeral B_i and warmth Source/Sink δ.
- The parameter of proportion of the free stream speed to the speed of the stretching sheet λ, decrease the distribution of temperature.
- The Lewis factor decrease the distribution of concentration.
- The Permeability restriction K help to lessening the velocity arena and increase the supply of temperature arena.
- The thermal buoyancy parameter λ_1 an Solutal buoyancy parameter λ_2 help to increase the speed and decrease the temperature field.
- Sherwood number, Skin friction, and Nusselt number are increasing function of proportion of the free stream speed to the speed of the extending sheet restriction λ, Biot Number B_i, thermal buoyancy restriction λ_1 and Solutal buoyancy restriction λ_2 and decreasing function of magnetic field restriction M, Prandtl numeral P_r and Permeability restriction K.
- Skin friction and Sherwood number are increasing function of Eckert number E_c, heat Source/Sink δ, Brownian motion parameter N_b and Thermophoresis parameter N_t. But reverse effect is seen in Nusselt number.

[1] [2] [5] [6] [4] [7] [8] [9] [10] [11] [12] [13] [15] [16] [14] [18] [17] [19] [20] [21] [22] [24] [23] [25] [26] [28] [29] [30] [31] [32] [3] [27]

References

[1] Ali, B., Nie, Y., Khan, S. A., Sadiq, M. T., and Tariq, M. Finite element simulation of multiple slip effects on mhd unsteady maxwell nanofluid flow over a permeable stretching sheet with radiation and thermo-diffusion in the presence of chemical reaction. *Processes 7*, 9 (2019), 628.

[2] Babu, D. H., Ajmath, K., Venkateswarlu, B., and Narayana, P. Thermal radiation and heat source effects on mhd non-newtonian nanofluid flow over a stretching sheet. *Journal of Nanofluids 8*, 5 (2019), 1085–1092.

[3] Bilal, S., Shah, I. A., Akgül, A., Tekin, M. T., Botmart, T., Yahia, I., et al. A comprehensive mathematical structuring of magnetically effected sutterby fluid flow immersed in dually stratified medium under boundary layer approximations over a linearly stretched surface. *Alexandria Engineering Journal 61*, 12 (2022), 11889–11898.

[4] Daniel, Y. S., Aziz, Z. A., Ismail, Z., Bahar, A., and Salah, F. Slip role for unsteady mhd mixed convection of nanofluid over stretching sheet with thermal radiation and electric field. *Indian Journal of Physics 94*, 2 (2020), 195–207.

[5] Daniel, Y. S., Aziz, Z. A., Ismail, Z., and Salah, F. Impact of thermal radiation on electrical mhd flow of nanofluid over nonlinear stretching sheet with variable thickness. *Alexandria Engineering Journal 57*, 3 (2018), 2187–2197.

[6] Daniel, Y. S., Aziz, Z. A., Ismail, Z., and Salah, F. Thermal radiation on unsteady electrical mhd flow of nanofluid over stretching sheet with chemical reaction. *Journal of King Saud University-Science 31*, 4 (2019), 804–812.

[7] Dogonchi, A., and Ganji, D. Effect of cattaneo–christov heat flux on buoyancy mhd nanofluid flow and heat transfer over a stretching sheet in the presence of joule heating and thermal radiation impacts. *Indian Journal of Physics 92*, 6 (2018), 757–766.

[8] Ganesh, N. V., Kameswaran, P., Al-Mdallal, Q. M., Hakeem, A., and Ganga, B. Non-linear thermal radiative marangoni boundary layer flow of gamma al2o3 nanofluids past a stretching sheet. *Journal of Nanofluids 7*, 5 (2018), 944–950.

[9] Ghasemi, S., and Hatami, M. Solar radiation effects on mhd stagnation point flow and heat transfer of a nanofluid over a stretching sheet. *Case Studies in Thermal Engineering 25* (2021), 100898.

[10] Gireesha, B., Umeshaiah, M., Prasannakumara, B., Shashikumar, N., and Archana, M. Impact of nonlinear thermal radiation on magnetohydrodynamic three dimensional boundary layer flow of jeffrey nanofluid over a nonlinearly permeable stretching sheet. *Physica A: Statistical Mechanics and its Applications 549* (2020), 124051.

[11] Goud, B. S., Reddy, Y. D., and Rao, V. S. Thermal radiation and joule heating effects on a magnetohydrodynamic casson nanofluid flow in the presence of chemical reaction through a non-linear inclined porous stretching sheet. *Journal of Naval Architecture and Marine Engineering 17*, 2 (2020), 143–164.

[12] Gupta, S., Kumar, D., and Singh, J. Mhd mixed convective stagnation point flow and heat transfer of an incompressible nanofluid over an inclined stretching sheet with chemical reaction and radiation. *International Journal of Heat and Mass Transfer 118* (2018), 378–387.

[13] Hayat, T., Khan, W., Abbas, S., Nadeem, S., and Ahmad, S. Impact of induced magnetic field on second-grade nanofluid flow past a convectively heated stretching sheet. *Applied Nanoscience 10*, 8 (2020), 3001–3009.

[14] Hussain, S. M., Sharma, R., Seth, G. S., and Mishra, M. R. Thermal radiation impact on boundary layer dissipative flow of magneto-nanofluid over an exponentially stretching sheet. *Int. J. Heat Technol. 36*, 4 (2018), 1163–1173.

[15] Ishaq, M., Ali, G., Shah, Z., Islam, S., and Muhammad, S. Entropy generation on nanofluid thin film flow of eyring–powell fluid with thermal radiation and mhd effect on an unsteady porous stretching sheet. *Entropy 20*, 6 (2018), 412.

[16] Jamshed, W., Goodarzi, M., Prakash, M., Nisar, K. S., Zakarya, M., Abdel-Aty, A.-H., et al. Evaluating the unsteady casson nanofluid over a stretching sheet with solar thermal radiation: An optimal case study. *Case Studies in Thermal Engineering 26* (2021), 101160.

[17] Khan, S. A., Ali, B., Eze, C., Lau, K. T., Ali, L., Chen, J., and Zhao, J. Magnetic dipole and thermal radiation impacts on stagnation point flow of micropolar based nanofluids over a vertically stretching sheet: finite element approach. *Processes 9*, 7 (2021), 1089.

[18] Khan, S. A., Nie, Y., and Ali, B. Multiple slip effects on magnetohydrodynamic axisymmetric buoyant nanofluid flow above a stretching sheet with radiation and chemical reaction. *Symmetry 11*, 9 (2019), 1171.

[19] Mishra, A., and Kumar, M. Thermal performance of mhd nanofluid flow over a stretching sheet due to viscous dissipation, joule heating and thermal radiation. *International Journal of Applied and Computational Mathematics 6*, 4 (2020), 1–17.

[20] Mjankwi, M. A., Masanja, V. G., Mureithi, E. W., and James, M. N. Unsteady mhd flow of nanofluid with variable properties over a stretching sheet in the presence of thermal radiation and chemical reaction. *International Journal of Mathematics and Mathematical Sciences 2019* (2019).

[21] Mohammadein, S., Raslan, K., Abdel-Wahed, M., and Abedel-Aal, E. M. Kkl-model of mhd cuo-nanofluid flow over a stagnation point stretching sheet with nonlinear thermal radiation and suction/injection. *Results in Physics 10* (2018), 194–199.

[22] Muhammad, T., Waqas, H., Farooq, U., and Alqarni, M. Numerical simulation for melting heat transport in nanofluids due to quadratic stretching plate with nonlinear thermal radiation. *Case Studies in Thermal Engineering 27* (2021), 101300.

[23] Pal, D., Mondal, S., and Mondal, H. Entropy generation on mhd jeffrey nanofluid over a stretching sheet with nonlinear thermal radiation using spectral quasilinearisation method. *International Journal of Ambient Energy 42*, 15 (2021), 1712–1726.

[24] Pal, D., and Mondal, S. K. Mhd nanofluid bioconvection over an exponentially stretching sheet in the presence of gyrotactic microorganisms and thermal radiation. *BioNanoScience 8*, 1 (2018), 272–287.

[25] Patil, A. B., Humane, P. P., Patil, V. S., and Rajput, G. R. Mhd prandtl nanofluid flow due to convectively heated stretching sheet below the control of chemical reaction with thermal radiation. *International Journal of Ambient Energy* (2021), 1–13.

[26] Qayyum, S., Hayat, T., and Alsaedi, A. Thermal radiation and heat generation/absorption aspects in third grade magneto-nanofluid over a slendering stretching sheet with newtonian conditions. *Physica B: Condensed Matter 537* (2018), 139–149.

[27] Shah, I. A., Bilal, S., Akgül, A., Tekin, M. T., Botmart, T., Zahran, H. Y., and Yahia, I. S. On analysis of magnetized viscous fluid flow in permeable channel with single wall carbon nano tubes dispersion by executing nano-layer approach. *Alexandria Engineering Journal 61*, 12 (2022), 11737–11751.

[28] Shoaib, M., Raja, M. A. Z., Sabir, M. T., Islam, S., Shah, Z., Kumam, P., and Alrabaiah, H. Numerical investigation for rotating flow of mhd hybrid nanofluid with thermal radiation over a stretching sheet. *Scientific Reports 10*, 1 (2020), 1–15.

[29] Sithole, H., Mondal, H., and Sibanda, P. Entropy generation in a second grade magnetohydrodynamic nanofluid flow over a convectively heated stretching sheet with nonlinear thermal radiation and viscous dissipation. *Results in Physics 9* (2018), 1077–1085.

[30] Sreedevi, P., and Reddy, P. S. Combined influence of brownian motion and thermophoresis on maxwell three-dimensional nanofluid flow over stretching sheet with chemical reaction and thermal radiation. *Journal of Porous Media 23*, 4 (2020).

[31] Sreedevi, P., Sudarsana Reddy, P., and Chamkha, A. Heat and mass transfer analysis of unsteady hybrid nanofluid flow over a stretching sheet with thermal radiation. *SN Applied Sciences 2*, 7 (2020), 1–15.

[32] Sudarsana Reddy, P., and Sreedevi, P. Impact of chemical reaction and double stratification on heat and mass transfer characteristics of nanofluid flow over porous stretching sheet with thermal radiation. *International Journal of Ambient Energy* (2020), 1–11.

J. COMPUTATIONAL ANALYSIS AND APPLICATIONS, VOL. 31, NO. 2, 2023, COPYRIGHT 2023 EUDOXUS PRESS, LLC

Dynamic Mathematical Modelling of Capacitive Pressure Sensors using Different Materials for Healthcare Applications

Suman[1], Deepak Bhatia[1,*] and Devendra Kumar[2]

[1]Department of Electronics Engineering, Rajasthan Technical University, Kota-324010, Rajasthan, India

[2]Department of Mathematics, University of Rajasthan, Jaipur-302004, Rajasthan, India
*Corresponding author: dbhatia@rtu.ac.in

December 30, 2022

Abstract

This paper discusses the principle, design and theoretical dynamical modelling of MEMS capacitive pressure sensors with different material properties results that have been simulated as well as compared. The properties of the material ensure that sensor performance analysis for operating pressure range 0-25kPa. This work discusses Timoshenkos plate deflection theory and follows the pull-in phenomenon. One important factor that could influence the performance of a MEMS capacitive pressure sensor is the structure of the diaphragm. The active area of this sensor is made up of 0.5 mm0.5 mm and the cavity size are 2m. According to the simulations, the optimized parameters have higher linearity and greater sensitivity than the initial parameters. The comparison of results shows that Aluminium material gives the highest deflection and better capacitance sensitivities which is about 88 pF/pa and is more linear with the applied pressure than other materials. The behaviour of the touch mode capacitive pressure sensor in terms of the temperature dependence of capacitance is analysed and repeatability error has been reduced. This configuration of touch mode pressure sensor is promising for the use in health monitoring devices like patient blood pressure due to small pressure fluctuation.

Keywords— Capacitive pressure sensor, Linearity, Sensitivity, Range of Blood pressure, Deflections

1 Introduction

Nowadays CPS (Capacitive pressure sensor) is one of the popular MEMS pressure sensors due to their fast dynamic range and less sensitivity to temperature in comparison with piezoresistive pressure sensors and is widely applied in high-performance applications [4, 27, 5, 13] . The capacitive pressure sensor comprises the thin elastic diaphragm and a sealed cavity between the elastic diaphragm and substrate. The thin diaphragm is allowed to contact the substrate and a pair of plates behave as parallel plate capacitors.

Micromachined MEMS CPS can be classified in different ranges such as low, medium, ultra-low and high. Different ranging of pressure can work for different applications like gentle touches use low- a pressure range (1kPa- 10kPa) [3, 24] ,medium pressure range (10kPa -100kPa) can be used for some pressure or movement of the object that is operated by hands [21] . Ultra-low pressure ranging ($< 1Pa$) is used in the progress of the microphone, and touch screen and finger-print recognition. Above these sensors, the range is also used in commercial products like wearable touch keyboards [29, 30] and household appliances. High-pressure ranges ($> 100kPa$) are used in special applications such as industrial robots, colonoscopes [26], etc. MEMS capacitive pressure sensor has a fast-developed product range with brand-new features in contemporary years and covers the foremost part of the sensor market. With the increasing requirements of some sensing applications, great efforts are devoted to the exploration in the direction of the application range of pressure sensors. The main motive of this studies is to find out suitable material for better sensitivity and good linearity. Sensitivity is the most important parameter to judge the quality of pressure sensors [34]. To achieve good sensitivity, conductivity, stability, reproducibility and resolutions. the main aim is to enhance these performance parameters of capacitive pressure sensors. Particularly these parameters are dominantly determined by different two critical factors which are 1) the materials used for conductive electrodes [15, 31] and 2) the shape and structure of the dielectric layer [22, 20, 7, 8, 6, 19] . But there have some limitations of micromachined capacitive pressure sensors have non-linear output and low sensitivity in terms of capacitance [28] . To address this problem, one way is increasing the diaphragm thickness and another way is to expand the middle of the diaphragm membrane in such a way that the output will be more linear concerning the input but capacitive sensitivity reduces due to increasing the stiffness [25, 17].

Many materials have been used as active and non-active components in pressure design applications because the properties of materials play a very significant role in the behaviour of capacitive pressure sensors. Still, one of the main concerns is Material selection for the diaphragm, with rapid development in the world of research, it is not impossible to discover a new material that can compete with the existing materials. In this paper, firstly different capacitive pressure sensors using different diaphragm membrane materials with their different application are investigated and simulated in the same model. Detailed mathematical modelling and simulation results on various characteristics are presented.

2 Design of Pressure Sensors

The diaphragm and substrate are used as mechanical components in many sensors and are the most important part of the system. The size of the thin diaphragm, material

S.NO	Types of pressure sensors	Measurement	Range
1	Absolute	Atmospheric pressure	101.3 kPa
2	Absolute	In-vivo Blood Pressure	80/120 mm
3	Gauge	Intraocular Pressure	15mm Hg
4	Gauge	Tire pressure	30 Psi
5	Differential	Ventilators	25cm H_2O

Table 1: Types of Pressure Sensors with Specific Range and their Applications [2]

selection of the diaphragm, and substrate depend upon the required applications. Some types of pressure sensors along with their application and their pressure range are given in table 1. The deflection of the diaphragm and sensitivity of the sensor is depending upon according to properties of the materials and pressure mounted on the thin membrane.

The design of the diaphragm membrane and structure of MEMS pressure sensor by using finite element simulation software (FEA). MEMS pressure sensors are generally used to measure one parameter at a time, but the value of parameters changes when they operate in complex environments which create a major task for designing a MEMS pressure sensor to achieve good sensitivity with operational precision and speed in harsh environments.

3 Principle and Mathematics background Modelling of the Capacitive Pressure Sensor

MEMS capacitive pressure is work on the principle of the electromechanics interface. By changing applying the pressure to the top of the diaphragm, the membrane moves towards the direction of the substrate. Then performance occurs in terms of diaphragm deflection with thermal considerations. Due to the symmetric nature of the geometry, only a single geometry is used for the analysis [18, 10]. this model contains a thin membrane that is held at a fixed potential of 5V.

$$\frac{\partial^4 w(x,y)}{\partial x^4} + 2\alpha \frac{\partial^4 w(x,y)}{\partial x^2 \partial y^2} + \frac{\partial^4 w(x,y)}{\partial y^4} = \frac{p}{Dh^3} \tag{1}$$

To avoid any connection between substrate and diaphragm membrane insulation connection is provided. Basically, for designing diaphragm capacitive pressure sensors uses the theory of thin plate and small deflection, where the condition of theory plates uses a $h \approx \frac{a}{10}$ and deflection is $w_{max} \approx \frac{h}{4}$ [32] but in case of circular diaphragm r is taken as radius and where h is the thickness and the rectangular diaphragm is taken a is length and b is width. The mathematical expression for calculating diaphragm deflection with a clamped edge due to applied pressure P are governing the fourth-order differential equation in x-y planes (1).

Where w (x, y) is deflection of diaphragm supported with boundary edge condition, a is side of diaphragm, h is the thickness. The following mathematical expression can be used to determine the capacitance of this structure [12].

$$c_0 = \frac{\varepsilon k A}{d_0} \tag{2}$$

3

Where ε is absolute dielectric permittivity of, k is the relative permittivity of the plates, A is the area of the plates on a squared meters and d0 is the separation between the parallel conducting plates. However, the capacitance cannot be calculated using equation (2) above when the diaphragm's pressure has changed. As a result of uniform pressure being applied, the diaphragm deflects. As can be seen, the deflection with a uniformly loaded square shape plate is utmost at the diaphragm's centre.

$$w_{max} = 0.00126 \frac{L^4 P}{D} \tag{3}$$

Where w_{max} is the maximum deflection, α is the length of the diaphragm membrane, P is the differential pressure, D is the flexural rigidity can be computed by the expression [16, 9, 11] .

$$D = \frac{Eh^3}{12(1 - v^2)} \tag{4}$$

Where h is thickness of membrane, E is modulus of elasticity, ν is Poissons ratio [23]. When above equation number 3 is insert in equation number 2 then, maximum deflection occurs.

$$w_{max} = 0.01512(1 - v^2) \frac{PL^4}{Eh^3} \tag{5}$$

3.1 Measurements of Capacitance

The mentioned relation (6) can use to find out the change in capacitance and sensitivity of the moving diaphragm towards the cavity after changing the load on the top of the diaphragm.

$$c_f = \varepsilon \int \int \frac{dx.dy}{d - w(x, y)}, \tag{6}$$

$$c_f = \frac{\varepsilon}{d} \int \int \frac{dx.dy}{d - w(x, y)}, \tag{7}$$

Taylor series expansion is given in the following equation,

$$\frac{1}{1 + x} = 1 + x + x^2 + x^3, for - 1 < x < 1 \tag{8}$$

Since in this case(w/d=1), therefore formula (8) can be written in the equation (9),

$$c_f = \frac{\varepsilon}{d} \int \int_{-a}^{a} (1 + \frac{w(x, y)}{d} + \frac{w^2(x, y)}{d} + ..) \tag{9}$$

As long as the sensor works with less deflection then, the capacitance, neglecting the higher-order factors, can be calculated by,

$$c_f = \frac{\varepsilon}{d} \int \int_{-a}^{a} (1 + \frac{w(x, y)}{d}) dx.dy \tag{10}$$

By using the binomial expression, the change in capacitance of square shape membrane can be written as [1].

$$c = c_0 (1 + \frac{12.5 P a^4}{2015 dh}) \tag{11}$$

4

Where c is the final calculating capacitance, c_0 is initial capacitance, P is uniform (constant) pressure applied, d is the spacing between the plates and a is the length (size) of the diaphragm. As the zero-pressure capacitance, is given in equations (12),

$$c_0 = \frac{4\varepsilon a^2}{d} \tag{12}$$

Capacitive pressure sensitivity of the square membrane is given by (9).

$$S_A = \frac{49\varepsilon a^6}{2025 d^2 D} \tag{13}$$

3.2 Measurement of Sensitivity

Therefore, Sensitivity of above diaphragm depend upon thickness of membrane and distance between electrodes, influence by applied load and sensitivity of membrane can be expressed as (15).

$$S_c = \frac{dc}{dp} \tag{14}$$

The mechanical sensitivity of a diaphragm is defined as

$$S_M = \frac{dW}{dp} \tag{15}$$

For small deflection, square diaphragm sensitivity is,

$$S_m = \frac{a^2}{3.14h[\frac{4.2Eh^3}{3.14a^2(1-v^2)}]} \tag{16}$$

Thus, the low capacitance will make the device more sensitive. As a result, high displacement will lead to nonlinearity. The segmented or mesh model was created using the FEM (Finite element method) as depicted in figure 2.

4 Simulation Result and Discussion

In this analysis, Diaphragm deflection, capacitance and mechanical sensitivity vary according to the properties and characteristics of materials explained and simulated results of each material are also presented, as well as the equation used for the modelling of pressure to calculate and verify results. The shape of a diaphragm can be square, elliptical and circular but in this paper, the shape of the diaphragm is taken as square and dimensions are $0.5mm \times 0.5mm \times 10\mu m$ made up of different diaphragm material has been examined under the uniform pressure range is 0 to 15kPa, the dimensions of the cavity is 2 m filled with vacuum, silicon is taken substrate is shown in the figure 1 and FEM is used to create the segmented model is depicted in figure 2 and mesh parameter is shown in table 2 and as seen in the diagram boundary condition for the diaphragm deflection of this structure is limited in the z-direction only.

The result shown here in figure 3 is the simulation profile of deformation of the Aluminium membrane at external pressure 15 kPa. The given results proves that maximum deflection is occur at the centre and displacement reduces as moves away from the centre as shown by the vertical line and in order to sustain the linearity moving diaphragm/ plate should not move more than of the distance between the plates. Figure 4. Shows the simulation profile of applied boundary load at 10kPa. The maximum and mean deformations of the square diaphragm membrane at 10 kPa, 3.21 μm and 1.21 μm respectively.

S.NO	Parameter	Size
1	Maximum element size	0.3
2	Minimum element size	0.054
3	Element Growth rate	1.5
4	Curvature factor	0.6
5	Resolution of the regions	0.5
6	Number of iterations	4

Table 2: Mesh Parameter of the Model

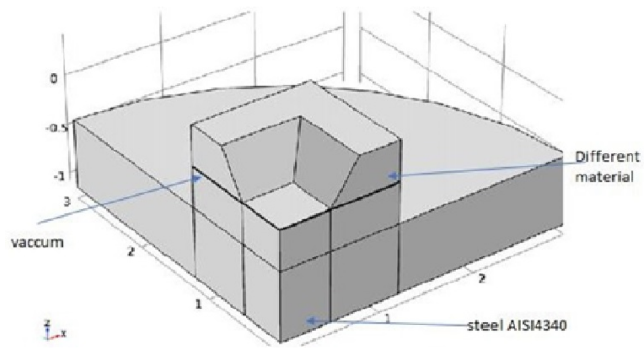

Figure 1: Three -dimensional view of Capacitive Pressure Sensor with different Material

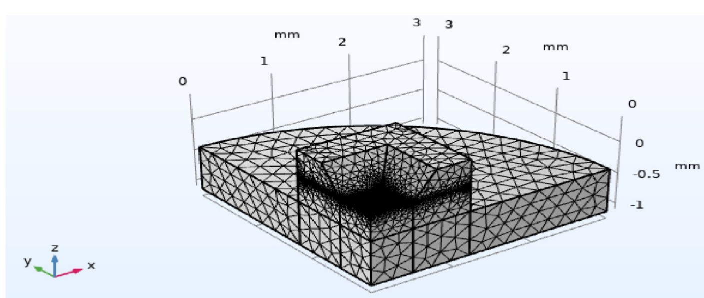

Figure 2: Mesh Model of Capacitive Pressure Sensor

6

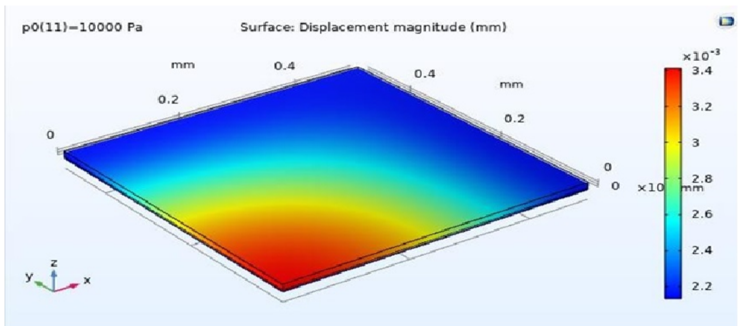

Figure 3: Quadrant Simulation Profile of Deformation of Diaphragm for 0.5mm at 10 kPa pressure

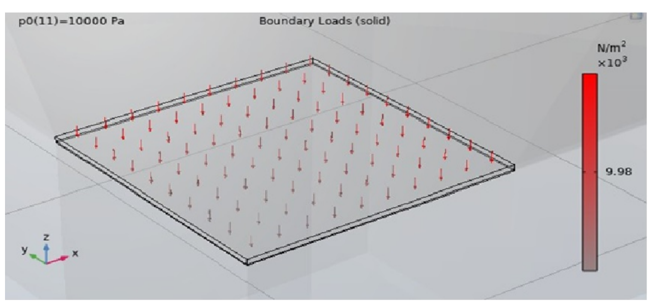

Figure 4: Simulation profile of applied boundary load when applied pressure at 10 kPa

Parameter Name	Value	Units
Youngs modulus	170	GPa
Poissons ratio	0.06	1
Density	2330	Kg/m^3
Relative permittivity	11.7	1
Coefficient of thermal expansion	2.6×10^{-6}	PPM/ $^{\circ}C$

Table 3: Material properties of Si

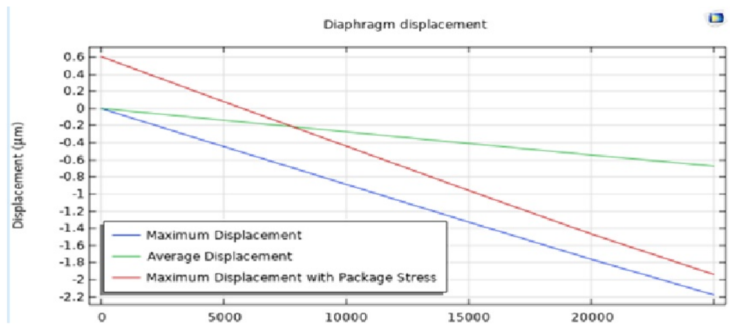

Figure 5: Diaphragm Displacement with Applied Pressure

5 Analysis of Pressure Sensor Performance using Different Materials

Only a few materials are being investigated for capacitive pressure sensors in order to achieve the required application. As three basic requirements of material defined by Mc Donald [33] (a) good electrical and mechanical properties (b) compatible with the fabrication device (c) good intrinsic properties that prevent high stress from developing during processing. Here simulated result of all material is presented.

5.1 Silicon

Silicon material is used as diaphragm material in capacitive pressure sensors due to high melting points and low hysteresis and low thermal expansion. Due to thermal expansion added to the devices, the response of this device is more dependent on the temperature and the capacitive response of the device is nonlinear with gradually increasing the pressure range. the simulated result of capacitance sensitivity is 52.8×10^{-6} pF/Pa and computation time calculated for the whole sensor is 23s. The properties used for the device are shown the table 3 and the graph between diaphragm deflection under applied uniform pressure with and without packaging stress is shown in figure 5.

Parameter Name	Value	Units
Youngs modulus	169	GPa
Poissons ratio	0.22	1
Density	2320	Kg/m^3
Relative permittivity	4.5	1
Coefficient of thermal expansion	2.8×10^{-6}	PPM/$^{\circ}C$

Table 4: Material Properties of Silicon Nanowires

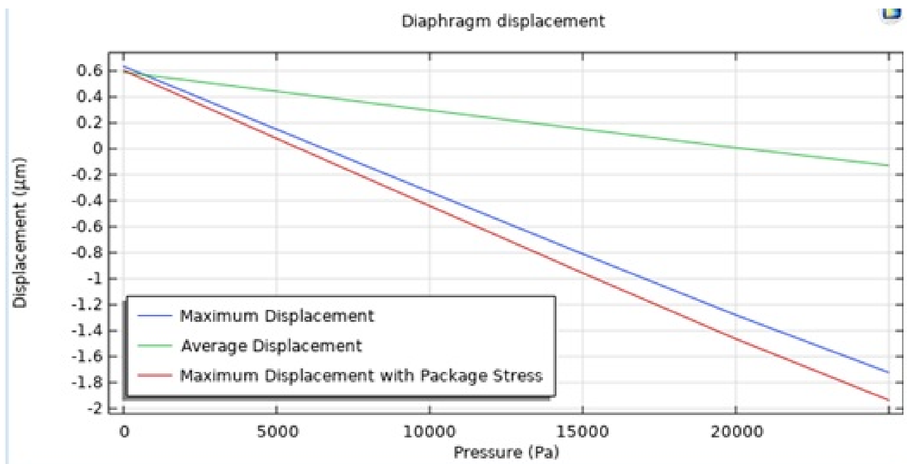

Figure 6: Diaphragm Displacement with Applied Pressure

5.2 Silicon nanowires

Silicon nanowires are used as diaphragm material in capacitive pressure and used low range pressure sensing application that is suitable for blood flow monitoring applications [14]and the simulated result of capacitance sensitivity is 2.3×10^{-6} pF/kPa. The properties used for the device are shown the table 4 and the graph between diaphragm deflection under applied pressure with and without packaging stress is shown in figure 6.

5.3 Titanium

Titanium metal is used as diaphragm material in capacitive pressure and titanium thin films deposited in conjunction with other materials onto a single crystal substrate is being used to create the micro devices. Due to strongest and high fracture toughness, this element is more promising metal substrate. The properties used for the device is shown the table 5 and graph between diaphragm deflection under applied pressure with and without packaging stress is depicted in figure 7.

9

Parameter Name	Value	Units
Youngs modulus	115.7	GPa
Poissons ratio	00.321	1
Density	4506	Kg/m^3
Relative permittivity	89.1	1
Coefficient of thermal expansion	8.5×10^{-6}	PPM/$^{\circ}C$

Table 5: Material Properties of Titanium

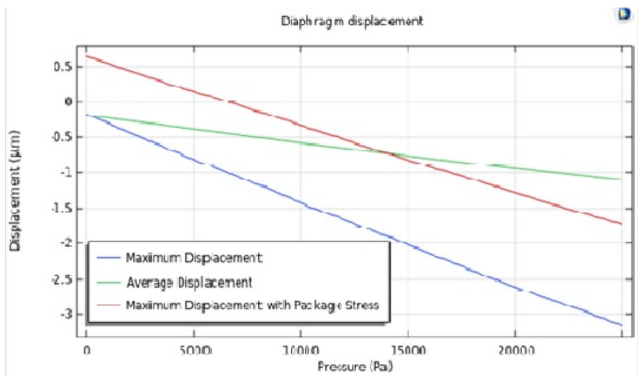

Figure 7: Diaphragm Displacement with Applied Pressure

5.4 Aluminium

Aluminium metal is used as diaphragm material in capacitive pressure and used in IC microelectronics through the integration of CMOS (complementary metal oxide semiconductor) Technology. Capacitive pressure on-chip signal circuitry with aluminium metal gives the highest sensitivity in square shape diaphragms under different pressure ranges. The properties used for the device are shown the table 6 and the graph between diaphragm deflection under applied pressure with and without packaging stress is shown in figure 8.

Parameter Name	Value	Units
Youngs modulus	70	GPa
Poissons ratio	0.35	1
Density	2700	Kg/m^3
Relative permittivity	11.5	1
Coefficient of thermal expansion	25×10^{-6}	PPM/$^{\circ}C$

Table 6: Material Properties of Aluminium

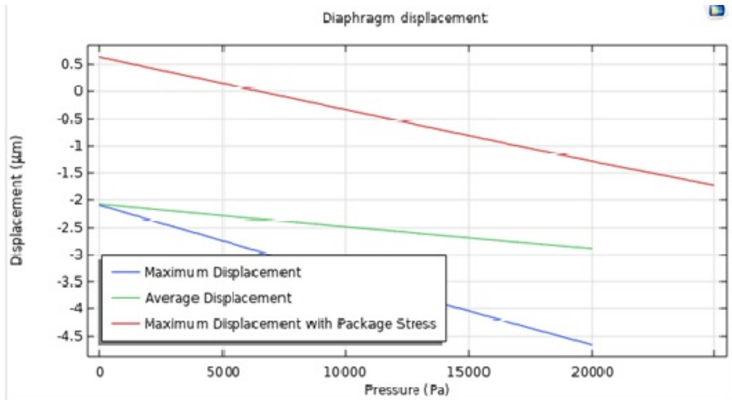

Figure 8: Diaphragm Displacement with Applied Pressure

Parameter Name	Value	Units
Youngs modulus	120	GPa
Poissons ratio	0.34	1
Density	8960	Kg/m^3
Relative permittivity	11.5	1
Coefficient of thermal expansion	25×10^{-6}	PPM/$°C$

Table 7: Material properties of copper

5.5 Copper

Copper metal is used as diaphragm material in capacitive pressure. Although it has good electrical conductivity and high malleable as compared to other materials. it cannot be used in high-pressure applications due to the weak nature of the metal. The properties used for the device are shown in the table 7 and the graph between diaphragm deflection under applied pressure with and without packaging stress is shown in figure 9.

5.6 Comparative Analysis of all Materials

In this paper, different membrane materials were used on the same model and a comparative analysis of touch mode capacitive pressure sensor for different pressure range 0 to 25kPa has been investigated at $10\mu m$ thickness. The average diaphragm deflection and capacitance varied according to the used material properties. The average diaphragm deflection of different membrane materials to different pressure ranges is shown in the figure 10. In, the plots represent that the average deflection of all material is increases with increasing the pressure range in a linear or non-linear manner. On the other hand, among all materials Aluminium material has the highest deflection and more linearity as compared to other materials.

Figure 11. depicts the relationship between the relative capacitance and applied pressure in case of a square diaphragm. This plot represents that the aluminium material has the highest capacitances when compared to other materials. At zero

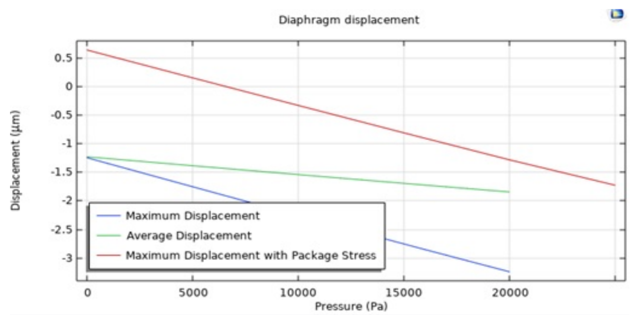

Figure 9: Diaphragm Displacement with Applied Pressure

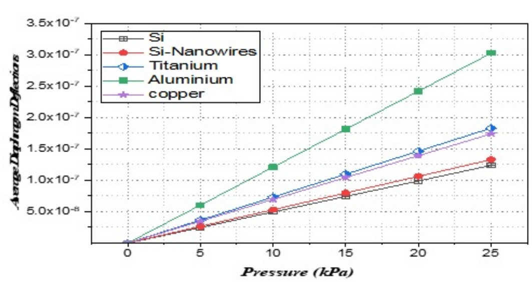

Figure 10: Diaphragm Displacement with Applied Pressure

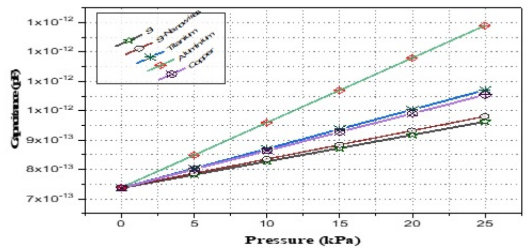

Figure 11: Capacitance changes with Applied Pressure

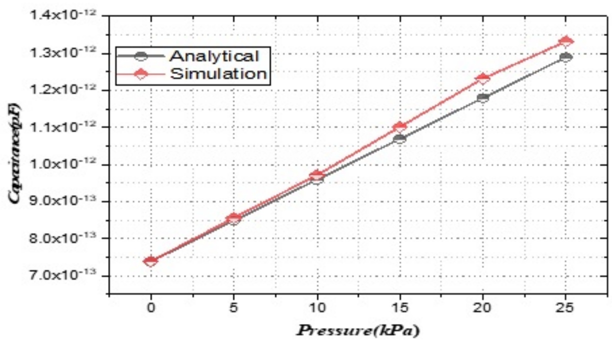

Figure 12: Analytical and Simulation Capacitance with Pressure

applied pressure, the value of capacitances for all the materials is same and gradually increases with applied pressure, but as is shown in the graph, Aluminium material provides better linearity than others materials over the range 0 kPa to 25 kPa

Figure 12 shows the comparison of analytical and simulation results of capacitance with applied pressure of a square diaphragm. This plot indicates that aluminium material provides more accurate and promising result of analytical with simulation result. At 10kPa, the value of capacitance is 9.69×10^{-13} F.

5.7 Sensitivity Analysis

Sensitivity is an important factor for the analysis of the capacitive pressure when membrane deflection and capacitance changes. Here table 8 shows a comparative analysis of the capacitance sensitivity of all Materials of the square diaphragm in which aluminium material provides the highest sensitivity at 10 kPa externally applied pressure is 22×10^{-6} pF/pa (one fourth part of the model) and the overall sensitivity of the model is 88×10^{-6} pF/pa with and without packaging stress.

Material Name	Sensitivity-Quadrant part (pF/pa)	Overall Sensitivity(pF/pa)
Si	9×10^{-6}	36×10^{-6}
Si- Nanowires	9.6×10^{-6}	38.4×10^{-6}
Titanium	13.2×10^{-6}	52.8×10^{-6}
Aluminium	$22.0 \times 1^{0-6}$	88.0×10^{-6}
Copper	12.6×10^{-6}	50.4×10^{-6}

Table 8: Comparative Sensitivity of all Material

6 Conclusion

This paper has described the dynamical modelling of highly sensitive normal and touch mode capacitive pressure sensor was analytically designed and simulated using the finite element method. This sensor comprises of moving top membrane, fixed bottom plate and cavity. In this investigation, the results show that the analytical result is in good agreement with the simulated result. Based on the observed performance its characteristics, accuracy and resolution are improved while repeatability error and computation time are reduced. Aluminium has been found to be more compatible and sensitive than other materials, making it more suitable for the measurement of blood pressure measurement. It also discussed how the reduced cavity size enhanced the sensitivity but this approach is restricted due to pull-in the phenomenon that faces inaccuracies in response time. In addition, these findings open a new route for other medical applications like ICP, IOP.

References

[1] Nisheka Anadkat and M Rangachar. Simulation based analysis of capacitive pressure sensor with comsol multiphysics. *Int. J. Eng. Res. Technol.*, pages 848–852, 2015.

[2] Kirankumar B Balavalad and BG Sheeparamatti. A critical review of mems capacitive pressure sensors. *Sensors & Transducers*, 187(4):120, 2015.

[3] S Bhatter, Kamlesh Jangid, SD Purohit, et al. Fractionalized mathematical models for drug diffusion. *Chaos, Solitons & Fractals*, 165:112810, 2022.

[4] Sung-Pil Chang and Mark G Allen. Demonstration for integrating capacitive pressure sensors with read-out circuitry on stainless steel substrate. *Sensors and Actuators A: Physical*, 116(2):195–204, 2004.

[5] Sarvesh Dubey, Ved Prakash Dubey, Jagdev Singh, Ahmed M. Alshehri, and Devendra Kumar. Computational Study of a Local Fractional Tricomi Equation Occurring in Fractal Transonic Flow. *Journal of Computational and Nonlinear Dynamics*, 17(8), 06 2022. 081006.

[6] Ved Prakash Dubey, Devendra Kumar, Hashim M Alshehri, Sarvesh Dubey, and Jagdev Singh. Computational analysis of local fractional lwr model occurring in a fractal vehicular traffic flow. *Fractal and Fractional*, 6(8):426, 2022.

[7] Ved Prakash Dubey, Devendra Kumar, Hashim M Alshehri, Jagdev Singh, and Dumitru Baleanu. Generalized invexity and duality in multiobjective variational problems involving non-singular fractional derivative. *Open Physics*, 20(1):939–962, 2022.

[8] Ved Prakash Dubey, Devendra Kumar, Jagdev Singh, Ahmed M Alshehri, and Sarvesh Dubey. Analysis of local fractional klein-gordon equations arising in relativistic fractal quantum mechanics. *Waves in Random and Complex Media*, pages 1–21, 2022.

[9] Ved Prakash Dubey, Jagdev Singh, Ahmed M Alshehri, Sarvesh Dubey, and Devendra Kumar. Analysis of local fractional coupled helmholtz and coupled burgers' equations in fractal media. *AIMS Mathematics*, 7(5):8080–8111, 2022.

[10] Ved Prakash Dubey, Jagdev Singh, Ahmed M Alshehri, Sarvesh Dubey, and Devendra Kumar. Forecasting the behavior of fractional order bloch equations appearing in nmr flow via a hybrid computational technique. *Chaos, Solitons & Fractals*, 164:112691, 2022.

[11] Ved Prakash Dubey, Jagdev Singh, Ahmed M Alshehri, Sarvesh Dubey, and Devendra Kumar. A hybrid computational method for local fractional dissipative and damped wave equations in fractal media. *Waves in Random and Complex Media*, pages 1–23, 2022.

[12] BA Ganji and NATERI M SHAMS. Modeling of capacitance and sensitivity of a mems pressure sensor with clamped square diaphragm. 2013.

[13] Xiuchun Hao, Sinya Tanaka, Atsuhiko Masuda, Jun Nakamura, Koichi Sudoh, Kazusuke Maenaka, Hidekuni Takao, and Kohei Higuchi. Application of silicon on nothing structure for developing a novel capacitive absolute pressure sensor. *IEEE Sensors Journal*, 14(3):808–815, 2013.

[14] Wataru Iwasaki, Hirofumi Nogami, Satoshi Takeuchi, Masutaka Furue, Eiji Higurashi, and Renshi Sawada. Detection of site-specific blood flow variation in humans during running by a wearable laser doppler flowmeter. *Sensors*, 15(10):25507–25519, 2015.

[15] Yunsik Joo, Junghwan Byun, Narkhyeon Seong, Jewook Ha, Hyunjong Kim, Sangwoo Kim, Taehoon Kim, Hwarim Im, Donghyun Kim, and Yongtaek Hong. Silver nanowire-embedded pdms with a multiscale structure for a highly sensitive and robust flexible pressure sensor. *Nanoscale*, 7(14):6208–6215, 2015.

[16] Reza Khakpour, Solmaz RM Mansouri, and AR Bahadorimehr. Analytical comparison for square, rectangular and circular diaphragms in mems applications. In *2010 International Conference on Electronic Devices, Systems and Applications*, pages 297–299. IEEE, 2010.

[17] Wen H. Ko. Solid-state capacitive pressure transducers. *Sensors and Actuators*, 10(3):303–320, 1986.

[18] Ali E Kubba, Ahmed Hasson, Ammar I Kubba, and Gregory Hall. A micro-capacitive pressure sensor design and modelling. *Journal of Sensors and Sensor Systems*, 5(1):95–112, 2016.

[19] Shyamsunder Kumawat, S Bhatter, DL Suthar, SD Purohit, and Kamlesh Jangid. Numerical modeling on age-based study of coronavirus transmission. *Applied Mathematics in Science and Engineering*, 30(1):609–634, 2022.

[20] Donguk Kwon, Tae-Ik Lee, Jongmin Shim, Seunghwa Ryu, Min Seong Kim, Seunghwan Kim, Taek-Soo Kim, and Inkyu Park. Highly sensitive, flexible, and wearable pressure sensor based on a giant piezocapacitive effect of three-dimensional microporous elastomeric dielectric layer. *ACS applied materials & interfaces*, 8(26):16922–16931, 2016.

[21] Kin Fong Lei, Kun-Fei Lee, and Ming-Yih Lee. A flexible pdms capacitive tactile sensor with adjustable measurement range for plantar pressure measurement. *Microsystem technologies*, 20(7):1351–1358, 2014.

[22] Tie Li, Hui Luo, Lin Qin, Xuewen Wang, Zuoping Xiong, Haiyan Ding, Yang Gu, Zheng Liu, and Ting Zhang. Flexible capacitive tactile sensor based on micropatterned dielectric layer. *Small*, 12(36):5042–5048, 2016.

[23] Shi-Yu Liu, Jian-Gang Lu, and Han-Ping D Shieh. Influence of permittivity on the sensitivity of porous elastomer-based capacitive pressure sensors. *IEEE Sensors Journal*, 18(5):1870–1876, 2018.

[24] Stefan CB Mannsfeld, Benjamin CK Tee, Randall M Stoltenberg, Christopher V Chen, Soumendra Barman, Beinn VO Muir, Anatoliy N Sokolov, Colin Reese, and Zhenan Bao. Highly sensitive flexible pressure sensors with microstructured rubber dielectric layers. *Nature materials*, 9(10):859–864, 2010.

[25] Manju Mittal, Anurekha Sharma, et al. Virtual prototyping of a mems capacitive pressure sensor for tpms using intellisuite®. In *2012 1st International Symposium on Physics and Technology of Sensors (ISPTS-1)*, pages 25–28. IEEE, 2012.

[26] Lijia Pan, Alex Chortos, Guihua Yu, Yaqun Wang, Scott Isaacson, Ranulfo Allen, Yi Shi, Reinhold Dauskardt, and Zhenan Bao. An ultra-sensitive resistive pressure sensor based on hollow-sphere microstructure induced elasticity in conducting polymer film. *Nature communications*, 5(1):1–8, 2014.

[27] Robert Puers. Capacitive sensors: when and how to use them. *Sensors and Actuators A: Physical*, 37:93–105, 1993.

[28] MJ Sharifi, N Nemati, and A Abedi. A new mems based capacitive differential pressure sensor with acceptable sensitivity and improved linear region. In *2014 22nd Iranian Conference on Electrical Engineering (ICEE)*, pages 29–32. IEEE, 2014.

[29] Ruilong Shi, Zheng Lou, Shuai Chen, and Guozhen Shen. Flexible and transparent capacitive pressure sensor with patterned microstructured composite rubber dielectric for wearable touch keyboard application. *Science China Materials*, 61(12):1587–1595, 2018.

[30] Aarushi Shrivastava, Janki B Sharma, and Sunil D Purohit. Image encryption based on fractional wavelet transform, arnold transform with double random phases in the hsv color domain. *Recent Advances in Computer Science and Communications (Formerly: Recent Patents on Computer Science)*, 15(1):5–13, 2022.

[31] Xingtian Shuai, Pengli Zhu, Wenjin Zeng, Yougen Hu, Xianwen Liang, Yu Zhang, Rong Sun, and Ching-ping Wong. Highly sensitive flexible pressure sensor based on silver nanowires-embedded polydimethylsiloxane electrode with microarray structure. *ACS applied materials & interfaces*, 9(31):26314–26324, 2017.

[32] Stephen Timoshenko, Sergius Woinowsky-Krieger, et al. *Theory of plates and shells*, volume 2. McGraw-hill New York, 1959.

[33] William SN Trimmer. Microrobots and micromechanical systems. *Sensors and actuators*, 19(3):267–287, 1989.

[34] Michael Wehner, Ryan L Truby, Daniel J Fitzgerald, Bobak Mosadegh, George M Whitesides, Jennifer A Lewis, and Robert J Wood. An integrated design and fabrication strategy for entirely soft, autonomous robots. *nature*, 536(7617):451–455, 2016.

TABLE OF CONTENTS, JOURNAL OF COMPUTATIONAL ANALYSIS AND APPLICATIONS, VOL. 31, NO. 2, 2023